# Structural and Stability Investigations of Metal-Organic Frameworks under Humid Conditions for Heat Transformation Applications

Inauguraldissertation

zur Erlangung des Doktorgrades
der mathematisch-naturwissenschaftlichen Fakultät der


vorgelegt von

Dominik Fröhlich
aus Frankenbrunn
Düsseldorf, im November 2016

aus dem Institut für Anorganische Chemie und Strukturchemie
der Heinrich-Heine-Universität Düsseldorf

Gedruckt mit der Genehmigung der
mathematisch-naturwissenschaftlichen Fakultät der
Heinrich-Heine-Universität Düsseldorf

Referent: Prof. Dr. Christoph Janiak
Korreferent: Prof. Dr. Walter Frank

Tag der mündlichen Prüfung: 24.01.2017

Die vorliegende Arbeit wurde in der Zeit von April 2013 bis November 2016 am Institut für anorganische Chemie und Strukturchemie der Heinrich-Heine-Universität Düsseldorf, Abteilung bioanorganische Chemie, am Lehrstuhl von Prof. Dr. Christoph Janiak angefertigt. Die praktischen Arbeiten wurden am Fraunhofer-Institut für solare Energiesysteme ISE, Freiburg, im Bereich Thermische Anlagen und Gebäudetechnik, in der Abteilung Thermisch aktive Materialien und solare Kühlung, in der Gruppe Sorptionstechnik – Materialentwicklung und –Charakterisierung ausgeführt.

# Kurzzusammenfassung

Metallorganische Gerüstverbindungen (MOFs) erhalten eine immer größere Aufmerksamkeit von Wissenschaft und Industrie, was an ihrem hohen Potential für unterschiedlichste Anwendungen liegt. Etwa Gasspeicherung, Gastrennung, Katalyse oder was in dieser Arbeit besonders im Fokus ist: Wärmetransformationsanwendungen. Hiermit können bedeutend effizienter Heizsysteme entwickelt werden. Stand der Technik bei diesen Anlagen sind klassische hydrophile Sorptionsmaterialen wie SilicaGel oder Zeolithe. Diese Materialien könnten von MOFs, aufgrund ihrer extrem hohen Porosität, Wasseraufnahmekapazität und Varietät abgelöst werden.

Da MOFs eine noch relativ neue Materialienklasse ist, gilt es deren Eigenschaften anwendungsbezogen zu untersuchen. Es sind noch kaum Untersuchungen bezüglich Langzeitstabilität oder Adsorptionscharakteristik dieser Materialien gegenüber Wasser bekannt.

Innerhalb dieser Arbeit wurden Aluminiumfumarat und CAU-10-H als äußerst vielversprechende MOFs identifiziert und wurden genauer untersucht. Aluminiumfumarat konnte mittels Direktkristallisation auf einen Untersuchungskörper beschichtet werden. 4.500 Wasserdampf Ad-/Desorptionszyklen wurden unbeschadet überstanden, anschließend wurde ein Wärmeübertrager damit beschichtet und erzielte eine maximale Kühlleistung von 2900 W. CAU-10-H wurde mit Hilfe eines Silicophen Binders beschichtet und überstand 10.000 Wasserdampf Ad-/Desorptionszyklen mit unverminderter Adsorptionskapazität. Auch wurde die Syntheseroute optimiert, vom Milligram- in den Kilogrammaßstab, um Material effizienter herzustellen und damit einen Wärmeübertrager zu beschichten. Zur Aufklärung des Sorptionsverlaufs konnte die Kristallstruktur des beladenen MOFs gelöst werden.

Um ein tieferes Verständnis der Wassersorption, und damit der Stabilität der Materialien, zu erlangen wurden neue *in situ* Methoden entwickelt. Zu der schon etablierten *in situ* thermogravimetrischen Untersuchung, wurde *in situ* PXRD (Pulverröntgendiffraktometrie) sowie *in situ* DRIFTS (diffuse Reflexions-Fouriertransformationsinfrarotspektroskopie) Analytik entwickelt.

Des Weiteren wurde die Sorption von Methanol an verschiedenen UiO-66 MOFs und deren Stabilität während Methanolsorption untersucht.

# Abstract

Metal organic frameworks (MOFs) are gaining more and more attention from science and industry. This is due to their huge potential for various applications, for example gas storage and separation, catalysis or, what is in focus of this work, sorption based heat transformation. By using MOFs much more efficiently heating and cooling systems, as well as energy storage systems, could be developed. State of the art are classical hydrophilic sorption materials, like silica gel or zeolites. They could be replaced by MOFs, because of their extreme high porosity and variety.

MOFs are a rather new class of material and there are almost no studies about long term stability or adsorption characteristic. Therefore their properties should be studied application oriented.

Aluminium-fumarate (Al-fumarate) and CAU-10-H are among the most promising MOFs and were thoroughly analysed. It was possible to coat Al-fumarate via direct crystallization. It was proven that the coating withstands 4.500 water vapor ad-/desorption cycles while keeping its crystal structure. Afterwards, a full scale heat exchanger was coated and got a gross cooling power of 2900 W. CAU-10-H was coated via a silicophen binder and has contained its sorption capacity after 10.000 water vapor ad-/desorption cycles. The yield of the syntheses was optimized, from milligram to kilogram scale, in order to coat a heat exchanger efficiently. To reveal the sorption mechanism, the crystal structure of the water loaded MOF was solved.

To gain a deeper understanding of the water sorption and therefore the stability of the materials, new *in situ* analytic technics have been developed. On top of the established *in situ* thermogravimetrical analysis, a *in situ* PXRD (powder x-ray diffraction) and *in situ* DRIFTS (diffuse reflectance infrared fourier transform spectroscopy) analysis was developed.

Furthermore the sorption of methanol, on various MOFs, as well as their stability during cyclic methanolsorption, was examined.

# Eidesstattliche Versicherung / Erklärung

Ich versichere an Eides Statt, dass die vorliegende Dissertation von mir selbstständig und ohne unzulässige fremde Hilfe unter Beachtung der „Grundsätze zur Sicherung guter wissenschaftlicher Praxis an der Heinrich-Heine-Universität Düsseldorf“ erstellt worden ist.

Gleichzeitig erkläre ich, weder diese Dissertation, noch andere, vergleichbare Werke einer anderen Fakultät vorgelegt zu haben.

Schließlich erkläre ich, bislang keine erfolglosen oder erfolgreichen Promotionsversuche unternommen zu haben.

Düsseldorf, am 30. November 2016

(Unterschrift)

# Danksagung

Ich bedanke mich herzlich bei Herrn Prof. Dr. C. Janiak für die Möglichkeit, diese Dissertation in seinem Arbeitskreis anfertigen zu können und für die wertvolle und trotz der räumlichen Distanz, immer schnelle und kompetente Hilfe.

Bei Herrn Prof. Dr. W. Frank bedanke ich mich für die Übernahme des Zweitgutachtens.

Vielen Dank an Dr. Stefan Henninger, meinem Betreuer am Fraunhofer ISE, für die vielen Diskussionen, Unterstützung bei Problem, aber auch für die großen Freiheit beim Forschen.

Darüber hinaus geht großer Dank an die ganze Arbeitsgruppe „Sorptionstechnik – Materialentwicklung und -charakterisierung“. Durch das großartige Arbeitsklima, konnte ich jeden Tag mit einem Lachen auf die Arbeit fahren. Im speziellen Philipp Hügenell für das das tolle Büroklima und die vielen Physisorptioinsmessungen. Max Baumgartner für Hilfe beim Basteln, spezielle TG Messungen und zahllose Feierabendaktionen. Harry Kummer für gute Diskussionen und die gute Laune. Phillip Bendix für die Hilfe bei Beschichtungen sowie gemeinsamen sportliche Aktivitäten. Albina Holz für die vielen Synthesen im Labor, gewissenhafte Büroarbeiten sowie beste Verpflegung. Tobias Helling für die Bastelaktionen am DRIFTS und die häufigen Partyeinladungen, welche ich leider meistens ausschlagen musste. Raffael Wolff für die sehr motivierte Arbeit im Labor, sowie Raphael Zachmann für die vielen TG-Zyklierungen. Gunther Munz dafür, dass er immer wusste wo was ist sowie kreative Lösungen für Aufbauten. Sebastian Ernst für die gemeinsamen Konferenzbesuche und Lina Rustam für Hilfe im Labor und die leckeren Muffins. Ganz besonders möchte ich mich bei Felix Jeremias bedanke für die vielen motivierenden Diskussionen und gute Ideen.

Darüber hinaus bei Helge Reinsch von der Uni Kiel für die vielen hilfreichen Diskussionen, den Rietveldkurs , sowie neue Projektideen.

Beim Bundesministerium für Wirtschaft und Energie sowie bei der Fraunhofer-Gesellschaft bedanke ich mich für die Finanzierung meiner Arbeit im Rahmen der Projekte MOF2MARKET bzw. HARVEST.

Am meisten bedanke ich mich bei Eltern, Familie und meinen vielen Freunden.

# Table of Contents

# 1 Introduction[a]

With almost 9 billion tons of oil equivalent in 2011,[1] the worldwide final energy consumption is still growing, thus raising concerns about future energy supplies, resources, and environmental impacts. Buildings account for 20% to 50% of the final energy consumption.[2] Thus, the efficient use of energy for heating and cooling of buildings is a key issue towards a sustainable and secure energy supply in the future. Electrical power shortage due to grid overload is a well-known phenomenon already, and will probably increase with increasing demand for air conditioning in the emerging economies.

By the end of 2011, a total capacity of 234.6 GWth of solar thermal collectors was in operation. During summer time, collectors often produce more heat than needed for domestic hot water, thus, stagnation occurs at the same time when cooling demand increases. Low temperature heat (<150 °C) is also available as a by-product of various industrial processes, but often simply rejected to the environment. As the cooling demand usually increases during the same period of the year, the use of thermally driven chillers is a promising alternative. This holds true even more for applications where heat rejection and cooling demand are independent of the season. Prime examples are data centres, where waste heat from power generation can be used for cooling of the computing systems.

Out of the different possibilities for thermally driven systems, solid sorption systems are seen as a very promising method. They are customizable, promise low-maintenance and use comparatively benign refrigerants like water or methanol.

[a] This section is based on the following publication: "Water and methanol adsorption on MOFs for cycling heat transformation processes" *New J. Chem.*, 2014, **38**, 1846-1852, DOI: 10.1039/c3nj01556d.

## 1.1 Introduction to Sorption-based Heat Transformation

### 1.1.1 Working Principle and Working Cycle

Adsorption heat pumps and chillers feature a two-step process, which is depicted in Fig. 1. The first figure of merit is the working fluid exchange within the thermodynamic cycle and the second is the adsorption and evaporation enthalpy of the used gas–solid working pair (adsorptive–adsorbent). Thus, water as a working fluid is a natural choice because it is non-toxic, easily available and, above all, has a high evaporation enthalpy of 2500 kJ $kg^{-1}$. Open systems, e.g., desiccant cooling systems, can also be realized based on water sorption. A minor drawback of closed systems with water as a refrigerant is the low vapor pressure of 1.0 to 6.0 kPa under typical cooling conditions. Hence, besides the fact that the systems need to be vacuum tight, the mass transport may be limited due to the underlying diffusion regime. Consequently, short-chain alcohols like methanol and ethanol or ammonia are also of interest due to their higher evaporation pressures at low temperatures. They were already investigated in combination with, e.g., activated carbons.[3] Moreover, these refrigerants are of principle interest for heat pump applications, as low temperature sources below 0 °C, e.g., ambient air, can be used for evaporation. While ammonia is not appropriate for indoor use due to the high toxicity and compatibility problems, methanol is a good alternative to water, although it may be unstable at temperatures above 120 °C.[4]

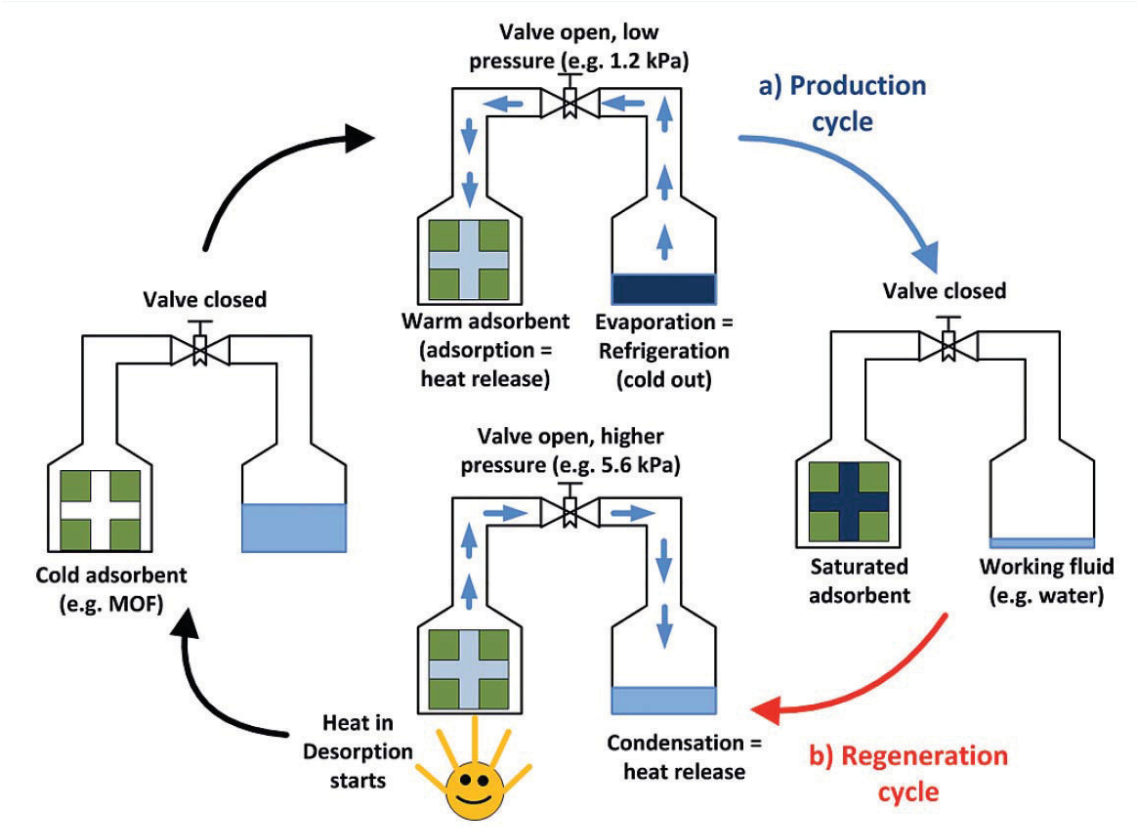


Figure 1 Illustration of the basic heat pump process. (Figure taken from ref.[5] Copyright © 2001 Wiley-VCH Verlag GmbH & Co. KGaA)

The basic ad-/desorption process starts with a freshly regenerated desorbed MOF in one chamber and an adsorption fluid, e. g. water in another chamber, separated by a valve. The system is under vacuum, respectively water vapor pressure. After the valve is opened, water vapor is adsorbed by the MOF, where adsorption heat is generated. Simultaneously, water evaporates, to restore in the atmosphere what is adsorbed, cools down trough evaporation and is taking up evaporation heat. When the adsorbent/MOF is saturated, it is regenerated by heat for desorption. The water desorbs, and releases heat while condensation. When the MOF is cold, the cycle can start again.

## 1.2 Working Pairs

Choosing the appropriate adsorbent is governed by several figures of merit: as the thermal mass of the adsorbent has to be costly chilled down and reheated during every working cycle, the porosity should be as high as possible for better efficiency. Depending on the boundary conditions given by the application (desired evaporation and condensation temperatures, and available regeneration temperature), adsorption–desorption must take place at appropriate relative pressures $p/p_0$.

The hydrothermal multi-cycle stability is another key issue, as several thousand adsorption–desorption cycles will be performed during the lifetime of an AHP or a TDC.

Most porous materials were originally developed for different applications and thus they feature adsorption characteristics not matching the demands of heat transformation processes. However, within the last decade several exciting improvements have been made with the development of new porous materials like aluminophosphates (AlPOs), silica-aluminophosphates (SAPOs) and metal–organic frameworks (MOFs).[6,7]

### 1.2.1 Silica Gels and Zeolites

The present generation of adsorption chillers mostly uses silica gels as adsorbents, and finding improved silica gels for heat pumping and cooling applications has been a research priority for many years.[8]

The key problem of silica gels, synthesized either by polymerization of silicic acid, $Si(OH_4)$, or aggregation of colloidal silica particles, is that most of the water adsorption occurs at too high relative pressures. Thus, the working fluid exchange over the cycle is only a small part of the total working capacity. Various modifications were investigated to overcome this issue, such as increasing the amount of silanol groups on the surface or reducing the pore sizes. The silica gels showing the strongest water adsorption at low pressures were found to be those that have very small pores (microporous silica) and contain trace impurities like aluminium or other metals.[9]

Among the various zeolitic adsorbents, only zeolites with large pore volumes need to be considered for adsorptive cooling cycles. These are primarily the commercially available zeolites of types A, X, and Y. Zeolites X and Y both belong to the faujasite (FAU) crystal structure type, are the most commonly available synthetic zeolites and have been considered for adsorptive heat pumping and cooling cycles since the 1980s.[10] Zeolites feature a comparatively high maximum water adsorption capacity, but the strong hydrophilicity significantly reduces the fluid exchange within the cycle for desorption temperatures below 140 °C.[11]

Several modifications, either by ion exchange or de-alumination, were investigated to reduce the required desorption temperatures. In addition, the fabrication of materials without the use of any adhesive was investigated to reduce the inactive parts of, e.g., shaped materials.[12]

### 1.2.2 AlPO and SAPO

Zeolite-like crystalline aluminophosphates (AlPO) and silicaaluminophosphates (SAPO) are considered for heat transformation within the last decade, with the potential to overcome the aforementioned problems of the classical adsorbents.[13] AlPO-5, AlPO-17, AlPO-18 and APO-TRIC were identified as the most promising members of this family.[14] Their adsorption behaviour changes from hydrophobic to hydrophilic at a characteristic $p/p_0$, which leads to the desired s-shape adsorption isotherms.[15] In addition, they can provide a higher maximum water uptake capacity than zeolites.

Modification of the structure and the sorption properties can be realized by isomorphous substitution of metal atoms in the framework. This leads to a negatively charged framework, so a charge-balancing extra-framework cation is introduced, increasing the polarity and, hence, the hydrophilicity of the framework. Consequently, silica-aluminophosphates, SAPOs, are typically more hydrophilic than AlPOs. In fact, SAPO-34, which is among the best-known compounds, still shows an s-shaped isotherm, with the steep increase of the isotherm shifted towards lower p/p0. These characteristics show the excellent suitability of AlPOs and SAPOs for heat transformation applications. Due to the

templated syntheses, these materials are unfortunately very expensive, and their adsorption capacity remains so far limited.

### 1.2.3 MOFs

Crystalline, three-dimensional and porous metal–ligand coordination networks with metal nodes and bridging organic ligands (Fig. 2) are called metal–organic frameworks (MOFs). Typically, they feature a uniform pore structure throughout the crystalline framework.[16] The pore size, shape and chemical nature of the inner pore surface can be tuned by variation of the organic ligands. This new class of porous materials is being investigated for numerous potential applications[17,18,19] such as for gas storage[20] and separation processes, drug delivery, heterogeneous catalysis, and, recently, water sorption for heat transformation[5,21–23,24,25,26] which was first suggested by Aristov. MOFs initially contain solvent molecules or linker residues inside the pores. After synthesis of the material, the pores have to be emptied through washing and evacuation procedures (activated) to give accessible micropore volumes with BET surface areas ranging typically between 1000 and 4000 $m^2\ g^{-1}$. Pore apertures or channel diameters of MOFs range from 0.3 to 3.4 nm with pore volumes of up to 1.5 or 2 $cm^3\ g^{-1}$. Water stability is, however, a problem for MOFs. Many are not stable at all or appear water stable only because of their hydrophobicity.[27]

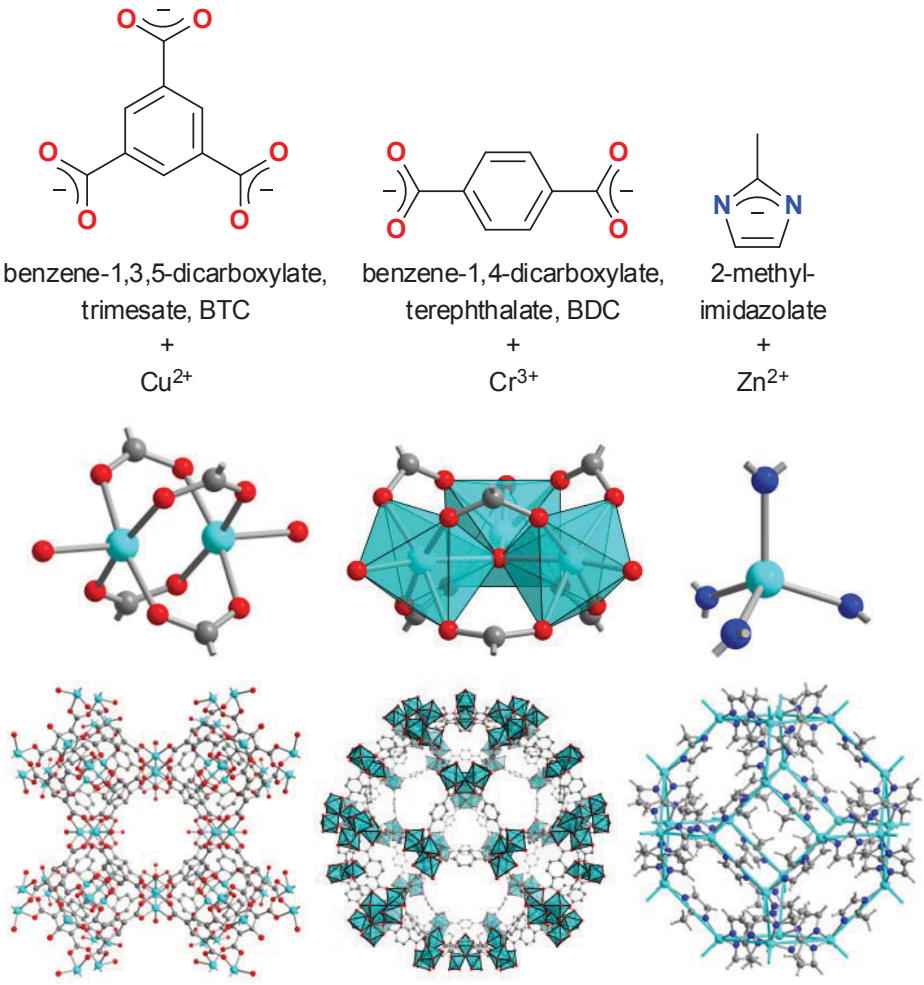


Figure 2 Prototypical linkers with selected metal nodes and secondary building units in corresponding MOFs (with acronyms). For ZIF-8 the sodalite cage is highlighted. (Figure taken from ref.[28] Copyright 2014 Royal Society of Chemistry)

## 1.3 Adsorption Characteristics of MOFs

### 1.3.1 MOFs with Water as a Working Fluid

One of the first MOFs tested for reversible water sorption in the realm of heat transfer was the mixed-ligand MOF ISE-1 ([$Ni_3(\mu_3$-BTC)$_2(\mu_4$-BTRE)$_2$(m-$H_2O)_2$], BTRE = bis(triazolyl)ethane) with a crystal water content of about 30 wt% which can be reversibly removed over at least 10 cycles.[29] The group of Férey introduced a series of porous materials, known as MILs (for Material Institute Lavoisier), comprised of three- and four-valent metal ions ($Ti^{4+}$, $Cr^{3+}$, $Fe^{3+}$, $Al^{3+}$), and aromatic di- and tri-carboxylate linkers.[19,30] MIL materials form under quite harsh synthesis conditions in water (pH < 1, T > 150 °C) so good hydrothermal stability can be anticipated. MILs can accept water in the range of 1.0–1.5 g $g^{-1}$ for MIL-101Cr (Fig. 3), 0.6–0.7 g $g^{-1}$ for MIL-100Cr, 0.65–0.75 g $g^{-1}$ for MIL-100Fe and 0.5 g $g^{-1}$ for MIL-100Al.[21,26,31]

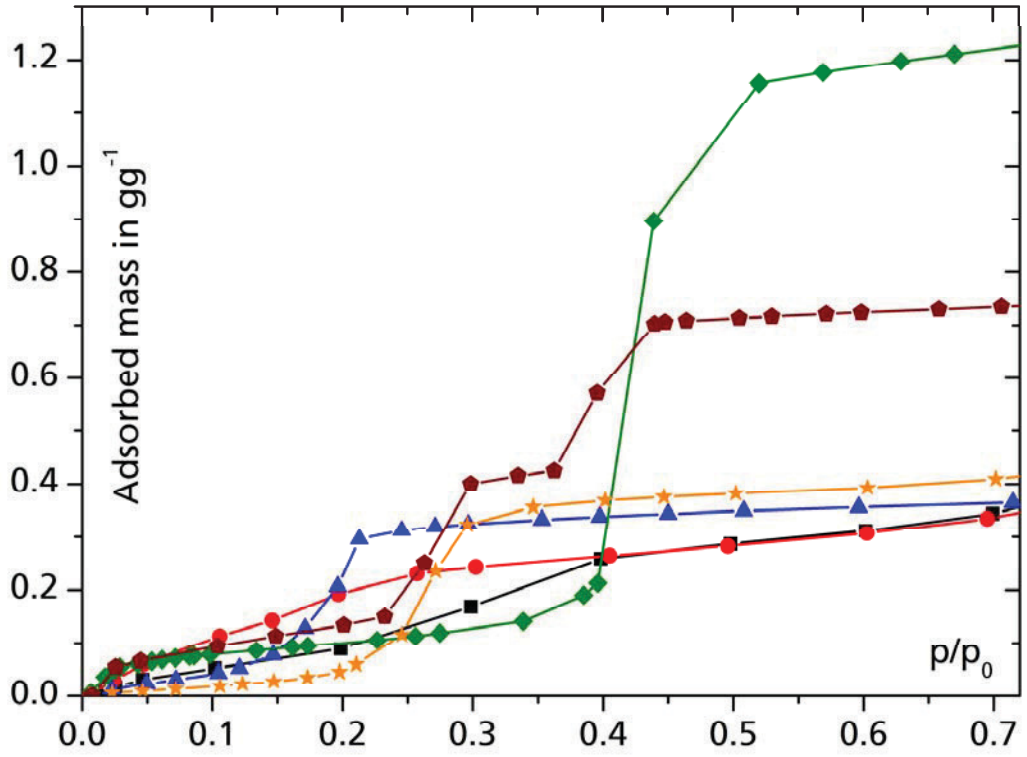


Figure 3 Water adsorption isotherms for selected MOFs at 25°CC: UiO-66 (-■-),[22] H2N-UiO-66 (-●-),[22] H2N-MIL-125 (-▲-),[22] MIL-101Cr (-◆-),[26] Al-fumarate (-★-)[32] and MIL-100(Fe) (-⬟-).[21] (Figure taken from ref.[28] Copyright 2014 Royal Society of Chemistry)

In contrast to zeolites, MOFs typically exhibit s-shaped water adsorption isotherms. The water uptake capacity of MOFs is not only determined by the available porosity, but also by the hydrophobicity/hydrophilicity of the ligand, the hydrogen-bonding capabilities of functional groups and a possible structural transition of the adsorbent material.[33] In order to tune the water uptake to lower $p/p_0$ values, the organic linker can be modified with hydrophilic amino- or hydroxo-groups (cf. Fig. 3). A nice example was illustrated with the replacement of hydrophobic 2-methylimidazolate in MAF-4 (ZIF-8) by hydrophilic 3-methyl-1,2,4-triazolate in MAF-7 (Fig. 4).[25]

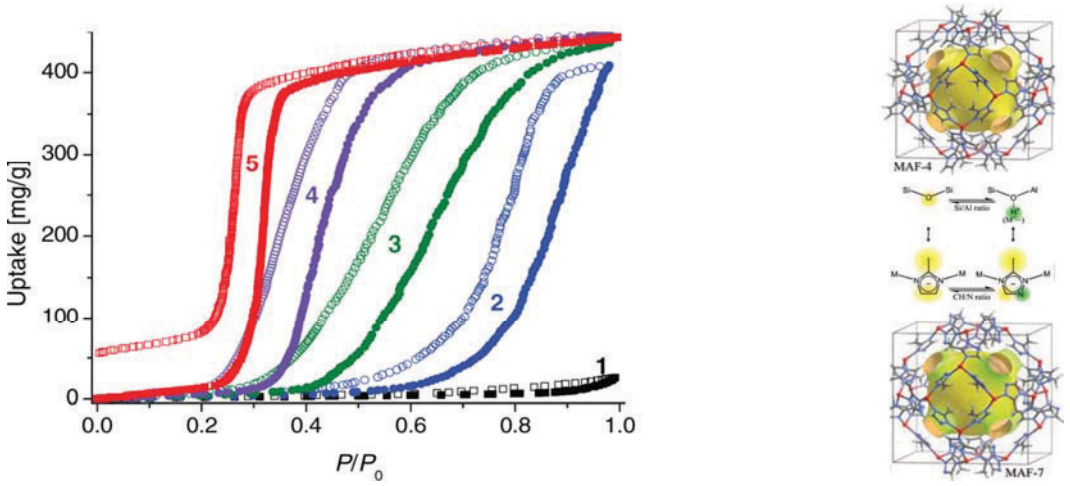


Figure 4 Water adsorption of MAF 4-7. (Figure taken from ref.[25] Copyright © 2011 Wiley-VCH Verlag GmbH & Co. KGaA)

### 1.3.2 MOFs with Methanol as a Working Fluid

A large share of potentially interesting MOFs exhibit desirable properties like a high initial working fluid uptake, but cannot be used in water-based heat pump processes due to their inherent lack of multicycle hydrothermal stability.[5] Thus, the working fluid methanol may be a good prospect for hydrothermally unstable materials. Chromium terephthalate MIL-53Cr was one of the first MOFs investigated with methanol as an adsorptive and exhibited a loading lift of 0.53 g $g^{-1}$, with the main uptake occurring at relative pressures as low as $p/p_0 < 0.20$.[34] MIL-101Cr is among the most interesting MOFs when it comes to heat transformation, mainly because of its stability and high porosity ($S_{BET} > 3000$ $m^2$ $g^{-1}$).[26,35] While water uptake is negligible at relative pressures lower than $p/p_0 <$

0.4 (cf. Fig. 3), it turned out that 1.0 g $g^{-1}$ of MeOH are already adsorbed at this pressure (Fig. 4). Well-examined copper trimesate HKUST-1 features a type-I adsorption isotherm for MeOH and exhibits a loading lift of approx. 0.5 g $g^{-1}$ (Fig. 4). As the substance is commercially available and turned out to retain its crystallinity even after several thousands of adsorption–desorption cycles (see the Stability characteristics of MOFs section below), it is among the most promising candidates for MeOH based appliances.

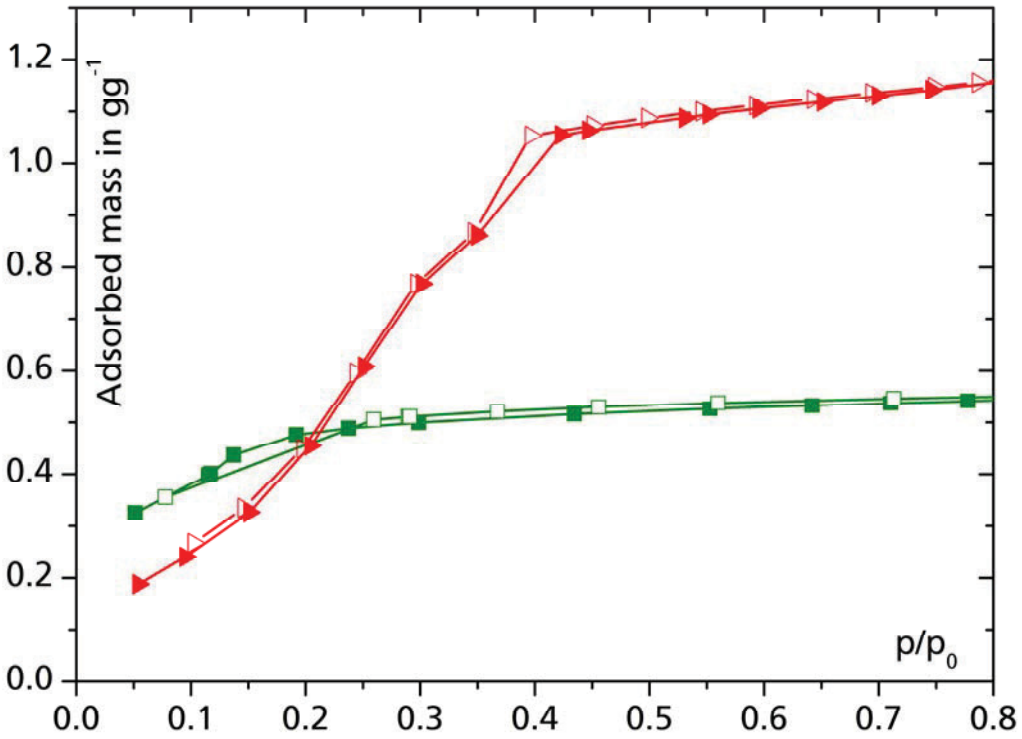


Figure 5 Methanol adsorption isotherms acquired at 25 °C for selected MOFs: HKUST-1 (■) and MIL-101Cr (►). Adsorption is depicted with full symbols, desorption with empty symbols. (Figure taken from ref.[28] Copyright 2014 Royal Society of Chemistry)

## 1.4 Stability Characteristics of MOFs

One of the key challenges for the applicability of any adsorbent in a heat transformation process is to achieve its permanent stability towards cyclic adsorption of the working fluid. The search for hydrothermally stable MOFs, however, is of general interest for a lot of different industrial applications, where at least traces of water are usually present.[27] The hydrothermal stability of a given MOF depends on the inertness of the coordinative metal–linker bond against hydrolysis and on the hydrophobicity of the framework. Hence, binding energies, coordination geometries, d-configurations and steric effects play important roles. The first estimation of hydrothermal stability can be based on coordination chemistry principles for the metal–linker combination. As a result, the stability increases from Zn(II) carboxylate MOFs over Cu(II) to Cr(III) carboxylate MOFs. Hydrothermal stability can also be improved by shielding the metal–linker bond from water vapor using sterically demanding and hydrophobic linkers. However, as in many cases, an aqua ligand or a free coordination site on the metal atom serves as an anchor for water cluster formation, hydrophilicity is usually strongly reduced in such cases, and the MOF may not adsorb any water at all.[36] For example, zinc imidazolate ZIF-8 is hydrothermally stable because no water is adsorbed.[37] A zinc trimesate (and other MOFs) showed increased hydrothermal stability when water adsorption is prevented due to interpenetration or pore blocking.[38] For use in adsorption heat pumps/chillers, hydrothermal stability cannot be deduced merely by retrieving the MOF from an aqueous suspension without structural damage but needs to be verified through a larger number of water vapor adsorption–desorption cycles (Fig. 5). The difference in cyclic hydrothermal stability may be explained by the phase change enthalpy released at the adsorption site, i.e., at the framework itself. Corresponding values have been calculated to lie in the range of ligand displacement energies. Furthermore, water molecules are actively being conveyed towards and away from the porous material during cyclic adsorption–desorption processes. Thus, the probability of M–L bond hydrolysis increases and pores are stressed by the alternating forces created through cavitation and capillary forces. MIL-101Cr, MIL-100Al, Fe, aluminium fumarate and some 4th group MOFs are among the most stable compounds examined so far (Fig. 5).

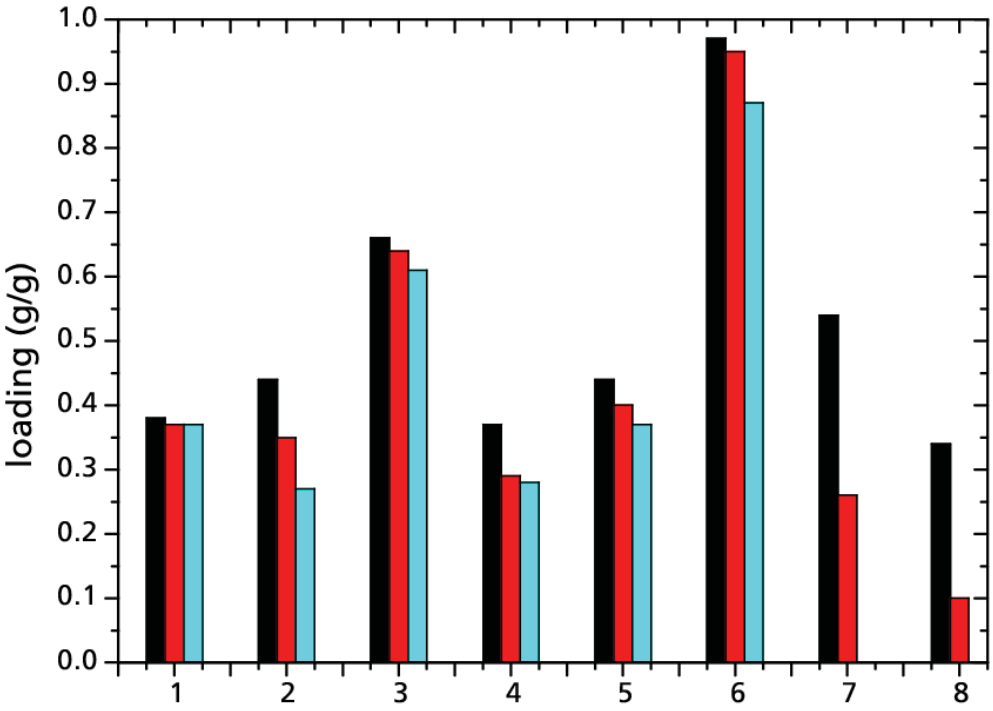


Figure 6 Water loading spread measured on aluminium fumarate (1),[32] UiO-66-$NH_2$ (2),[22] MIL-100(Fe) (3)[21] and (Al) (4),[21] H2N-MIL-125 (5),[22] MIL-101(Cr) (6),[26] HKUST-1 (7)[5] and Basolite F300 (8)[5] after activation (■), after 20 adsorption–desorption cycles with water vapor (■), and after 40 adsorption– desorption cycles (■). (Figure taken from ref.[28] Copyright 2014 Royal Society of Chemistry)

## 1.5 Shaping for Optimized Heat and Mass Transport

Clearly, the maximum power of an adsorption heat pump or chiller depends proportionally on how much working fluid can be adsorbed and desorbed at a given time. Sorption kinetics is governed by two main aspects,[39] the first being mass transport towards and away from the adsorption site by inter- and intracrystalline transport phenomena, which are subject to the laws of molecular, Knudsen or surface diffusion. Possibilities for improvement include, among others, decreasing the diffusion path lengths, for example by the employment of nanocrystals and by optimization of the outer surface of the adsorber.[40] The second, even more important aspect is conveyance of heat of adsorption, i.e., the thermal coupling between the adsorption site and the heat exchanger. Current AHPs/TDCs feature either packed-bed or coated heat exchanger concepts. In principle, packed-bed adsorbers prepared from MOFs can also be made, as pellets are available. Upon the transition from silica gel to zeolites with their working fluid uptake in the range of 0.2 to 0.4 g $g^{-1}$, coated heat exchangers prepared via direct crystallization have proven superior to packed beds already.[7,18,41] However, since heat conductivities of packed-bed adsorbers are usually inferior[42] due to point-like thermal contacts, MOF packed beds are being examined mainly for applications where heat transfer comes second to capacity, e.g., storage and separation of non-polar adsorptives like $CH_4$, $N_2$, $H_2$ or $CO_2$.[43] In the case of heat pumps/chillers, a much higher heat flow must be ensured.[44] With their higher capacities, MOF-based adsorbents require to be shaped even more into 100–200 mm thick, sturdy, thermally well coupled and fully accessible coatings. Procedures for the preparation of such layers are scarce, as research on MOF coatings is mainly focused on delicate applications like sensing, luminescence, gas separation, etc., which require thin (<1 mm), oriented, even monocrystalline films grown on functionalized substrates.[45] One recent approach is the thermal gradient method, based on the significant temperature dependence of crystal growth, thus allowing for direct crystallisation just on the surface. The method is beneficial for the preparation of coated heat exchangers, as these are made for the purpose of internal heating. Indeed, coatings of representative MOFs like HKUST-1 and aluminium fumarate can be synthesized on different

metallic substrates, with rates of approximately 50 mm $h^{-1}$ (see Fig. S4 in ESI†).[32,46] In the future, binder-based MOF coatings may also prove valuable.

## 1.6 *In Situ* Experiments

To study structural changes during adsorption, *in situ* experiments are extremely beneficial.

The ability to obtain real time, *in situ* information about the sample degradation during ad-/desorption and the possibility to observe the sorption mechanism over the course of the reaction offers unique and valuable insights into the process.

### 1.6.1 Thermogravimetric

To determine the hydrothermal cycle stability via weight, the uptake capacity, as well as the sorption time, is measured with a magnetic balance in an environment controlled chamber.

To gain detailed knowledge about the ad-/desorption behavior during the cycles, the sample weight is constantly measured The advantage of this analysis is, that the loading point is very sensible to changes in the sorption properties of the sample, and therefore stability of the material. This *in situ* cycle adsorption characteristic delivers information about the loss in uptake capacity as well as the adsorption kinetics.

### 1.6.2 DRIFTS

Diffuse reflectance Fourier transform infrared spectroscopy (DRIFTS) is in detail described by A. Drochner and H. Vogel,[47] and M. Mitchell.[48]

In comparison to common infrared transmission spectroscopy DRIFTS offers the following advantages for the study of porous materials:

- The sample does not need to be pressed into a tablet with KBr.
- The unaltered sample allows gas diffusion and can be exposed *in situ* to different kind of gasses under wet and dry conditions.
- Temperature and pressure can also be adjusted *in situ.*

Thus it is possible to study the surface chemistry, as well as the interior of high surface powders with infrared spectroscopy.

Hence, this technique provides a powerful approach for the study of porous materials.

The underlying principle of this spectroscopic technique is based on the different kinds of interactions when the IR beam interacts with the sample. Diffuse Fresnel and the specular Fresnel reflection, as well as the Kubelka-Munk diffuse reflectance play a role. Latter interacts with the surface of the material and also penetrates the material (Figure 7). DRIFTS uses this share of the reflected light, since it contains the chemical information of the material. It is collected via a parabolic mirror which focuses it to the detector. The other types of reflection are excluded by the geometry of the mirror.

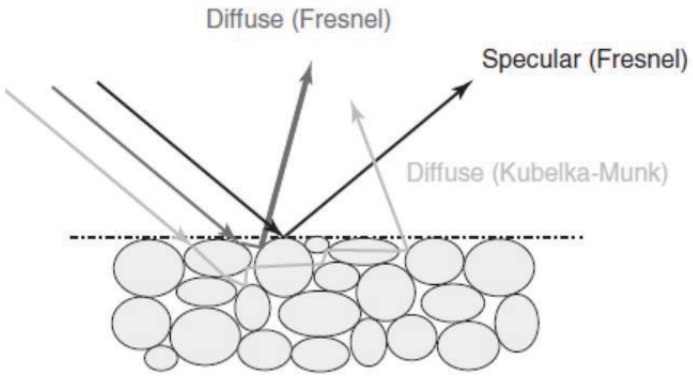


Figure 7 Schematic diagram of different kinds of IR interactions happens while DRIFTS measurments. (Figure taken from ref.[49] Copyright © 2012 Wiley-VCH Verlag GmbH & Co. KGaA)

Due to the transmission of the IR beam through the particles on the Kubelka-Munk path, the emitted light gives the same spectrum as a usual transmission spectrum, but the intensities of the single bands can differ. The reason for that can be found in the path passed by the IR ray which can differ compared to a usual transmission experiment. If the sample has a low extinction coefficient, the IR beam can propagate more easily throughout the sample. More pronounced bands are the result. The opposite is the case for samples with a high extinction coefficient (Figure 8).

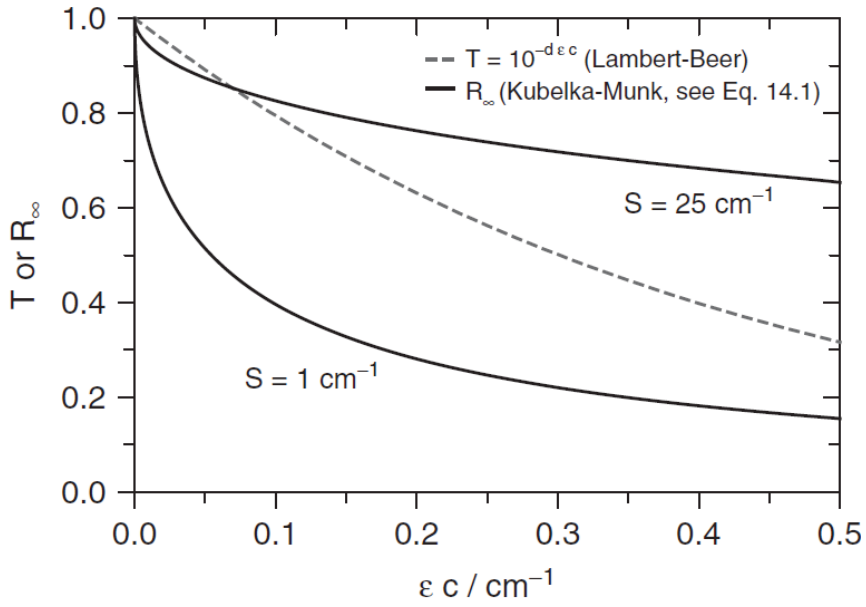


Figure 8 Lambert–Beer transmission (T) and Kubelka–Munk reflectance (R∞) as a function of the absorption module K (divided by 2 · ln(10)) for different values of the scattering module S. (Figure taken from ref.[47] Copyright © 2012 Wiley-VCH Verlag GmbH & Co. KGaA)

The different kinds of reflected IR beam are collected via a parabolic mirror which focuses it to the detector.

Due to the nature of this analysis, it is possible to study reactions of the sample, for example ad-/desorption, or hydrolysis. This can be achieved because the temperature of the cell can be chosen between 25°C and 800°C as well as the gas atmosphere, which could be nearly all type of gasses, for example $N_2$, $H_2O$, MeOH, $CH_4$, $CO_2$… as well as vacuum.

### 1.6.3 Non-Ambient Powder X-Ray Diffraction

Crystalline materials are mostly analyzed by X-ray diffraction, which is usually carried out under ambient conditions. It is also possible to control the environment, while carrying out the diffraction experiments, in a special X-ray chamber, in which the atmosphere is controllable, for example the temperature or gas atmosphere.

Therefore it is possible to observe structural transition of the crystalline material. This could be a phase transition, for example during water adsorption[50], or a loss of crystallinity because of decomposition.

# 2 Scope of Work

Commercial available and state of the art adsorption heat pumps and chillers are using silica gel as adsorbent and water as working fluid. Also, there is some recent work with SAPOs and AlPOs as adsorbents.

MOFs got in focus, because of their high porosity and uptake capacity, for example MIL-101(Cr) with 1.3 g(water)/g(material) at $p/p_0$ = 0.55.[26] As well as their variety of chemical composition or tunable hydrophilicity and thereby the relative pressure of the water sorption, like the CAU-10[51] or MAF[37] series. Hydrothermal stability is playing a key role in this field of application. First initial short hydrothermal cycle tests[21,22], which proofs for the applicability[5,23] of MOFs in this technology, have also recently been published. There is some promising work about hydrothermal stability, for example from Low et. Al.[27]

Since first tests to use MOFs in heat pumps are promising, it is important to examine these materials more closely. Therefore the aim of this thesis was based on water stable MOFs for heat pump applications.

This includes enhanced stability tests, as well as a deeper knowledge of the ad-/desorption mechanism. This should be done with *in situ* techniques, for example already developed hydrothermal gravimetric ad- and desorption cycles. Too that it would be favorable to develop new techniques like *in situ* PXRD or DRIFTS ad-/desorption cycles, because these analytical methods are commonly used in MOF characterization. Therewith, the long term stability of a material should be better predictable.

Once stable candidates are found, it is important to upscale the synthesis from the milligram to kilogram scale for enhanced experiments. After accomplishing a stable material in a large scale, the next step is to shape the material from powder to a coating or monolith, because powders are not useable in most applications. With a sufficient coating a real scale heat exchanger should be coated and tested under application conditions.

# 3 Cumulative Part

In section 3.1 to 3.4, the published and submitted work of thesis is presented in a chronological order and in cumulative form. Each of the following publications stands for itself and with a separate list of references. Before each section of this cumulative part a short overview of the publication is given as well as the share of work of the author in each case.

Additional results that have not yet been published in peer-reviewed journals yet are given in section 4.

*Note:* Reference numbers within the publication copies in this chapter correspond to the reference libraries at the end of each publication, and not to the general reference library.

## 3.1 Advancement of Sorption-Based Heat Transformation by a Metal Coating of Highly-Stable, Hydrophilic Aluminium Fumarate MOF

Felix Jeremias, Dominik Fröhlich, Christoph Janiak and Stefan K. Henninger

*RSC Adv.*, **2014**, *4*, 24073-24082
DOI: 10.1039/c4ra03794d

In this publication we examine the MOF aluminum fumarate. It can be produced economically in high yield from aluminum sulfate and fumaric acid via a precipitation and spin drying process. This fact, and cheap educts, make it a very cost effective MOF, and therefore, the possibility to use it in an heat pump application should be examined.
As it will be shown, the water sorption properties as well as the stability of this MOF is very interesting for heat pump applications. For this reason we developed a direct crystallization coating procedure for a good thermal coupling as well as deeper pore analysis, heat of adsorption and *in situ* thermogravimetric stability investigations. Also, for the first time *in situ* PXRD/humidity ad-/desorption experiments with a MOF had been done.

Author´s share of work:
- Setup and interpretation of *in situ* (TG and PXRD) experiments,
- writing of the stability chapter,
- proofreading of the whole manuscript.

RSC Advances

PAPER

View Article Online
View Journal | View Issue



Cite this: *RSC Adv.*, 2014, **4**, 24073

# Advancement of sorption-based heat transformation by a metal coating of highly-stable, hydrophilic aluminium fumarate MOF†

Felix Jeremias,[ab] Dominik Fröhlich,[ab] Christoph Janiak*[a] and Stefan K. Henninger*[b]

Received 25th April 2014
Accepted 13th May 2014

DOI: 10.1039/c4ra03794d

www.rsc.org/advances

The distinctive water sorption properties of microporous aluminium fumarate (s-shaped isotherm, narrow hysteresis, loading >0.3 g $g^{-1}$ at a relative pressure as low as $p/p_0 = 0.3$ under realistic working conditions) permit a large advancement of MOF-based sorption heat transformation processes, especially as we demonstrate that the favourable sorption properties are accompanied by an unprecedented cyclic hydrothermal stability. With regard to the application of heat transformation, where unhindered heat and mass transfer are crucial for fast ad-/desorption cycles and a high power density, the question of proper shaping was also addressed. A 300 μm thick, polycrystalline, thermally well coupled and highly accessible coating of microporous aluminium fumarate was deposited on a metal substrate *via* the thermal gradient approach, and found to be stable for the first 4500 ad-/desorption cycles with water vapour.

## 1 Introduction

Metal–organic frameworks (MOFs) receive continuous attention due to their unsurpassed porosity and chemical variability, which both originate from the inherent, molecular cluster-linker concept.[1] Substantial progress can be expected from their introduction into the fields of gas storage,[2,3] gas[4] and liquid[5] separation processes, drug delivery,[6] heterogeneous catalysis[7] and other applications,[8] but especially for sorption-based heat transformation purposes.

Thermally driven adsorption chillers (TDCs) or adsorption heat pumps (AHPs) pose an alternative to traditional air conditioners, heat pumps or condensing boilers operating on electricity or fossil fuels. Driven by solar or waste heat, TDCs/AHPs can help to minimize primary energy consumption. They are based on the evaporation of coolants, preferably water, and consecutive adsorption at a microporous material under specific conditions.

This technology has gained more and more interest during the last years, because it allows waste heat, which would otherwise be simply released to the environment, to be used for cooling applications, or stored, *e.g.*, for heating in winter. Additionally, the process can be operated in heat-pump mode: as additional thermal energy from the environment can be used for heating, less fuel is required.[9–11] It is clear that the performance, efficiency and range of use of a sorption-based heat pump, or chiller, drastically depend on the performance of the applied sorption material. MOFs are of high interest for the use as adsorbents, as they can surpass classical materials like silica gels or zeolites in terms of fluid uptake capacity and also offer the potential for tuning the microporosity and hydrophilicity through their variable building blocks depending on the specific heat transformation application. MOFs are being increasingly investigated for this purpose because of their high porosities, tunable hydrophilicities, and inherent, narrow pore size distributions which result in a sharp loading step. However, low hydrophilicity, insufficient hydrothermal stability and a pricey production still impede their commercial success in this and related fields.[9,12–18]

While the chemical properties of a MOF material can be tailored to meet the specifications of a particular task,[19] harsh environmental conditions and especially the presence of water vapour often result in irreversible structural transformations and rapid loss of porosity especially in well-established and examined materials: copper trimesate HKUST-1 (although it is synthesized in aqueous solution), zinc terephthalate MOF-5, and even zirconium aminoterephthalate $H_2$N-UiO-66 show framework disintegration under humid working conditions.[15,20,21] The decomposition process has been found to commence at the metal-linker coordination bond in most cases.[21] The collection of better water-stable MOFs includes many zeolitic imidazolate frameworks (ZIFs)[22] and a few other

[a]*Institut für Anorganische Chemie und Strukturchemie, Universität Düsseldorf, 40204 Düsseldorf, Germany. E-mail: janiak@uni-duesseldorf.de*

[b]*Department of Thermally Active Materials and Solar Cooling, Fraunhofer Institute for Solar Energy Systems (ISE), Heidenhofstr. 2, 79110 Freiburg, Germany*

† Electronic supplementary information (ESI) available: $N_2$ adsorption isotherm, PXRD (literature, bulk μp-AF and coated sheets), heat capacity and FT-IR spectrum of bulk μp-AF, PXRD of the top and bottom layer of the coating, desorption isobar of sheet 2, individual diffractograms for the *in situ* ad-/desorption study, and crystal structures of related MIL-53. See DOI: 10.1039/c4ra03794d

azolate-derived compounds,[16,23] MOFs based on Cr(III) (such as MIL-101),[14] or use 4th group metal clusters,[15,24] some MOFs that employ phosphonates as linkers,[25] and so on. However, hydrothermal stability is often achieved by hydrophobicity, which can easily be deduced from the comparatively late rise of the water sorption isotherm. This is the case, *e.g.*, for many ZIFs, metal azolate–carboxylate MOFs,[26] and to some extent also MIL-101.

Suitable equilibrium sorption characteristics are a necessary requirement for any MOF application, but when it comes to fast, cyclic adsorption processes, unhindered heat and mass transfer have to be ensured as well. Hence, the MOF cannot be used as a powder, but must be fabricated into a device. While elaborate procedures are available for the production of custom-made, yet low-capacity μm-films, *e.g.*, by means of direct or seeded growth,[27] electrochemical synthesis,[28] microwave-induced[29] or self-assembled monolayer (SAM-) assisted deposition,[30] results are scarce when it comes to high-capacity, sturdy, firmly adhering films or membranes which are at the same time highly accessible and thermally well coupled to the substrate. Such films are necessary for high-turnover applications in the field of gas sorption, catalysis *etc.*, where substantial amounts of heat have to be delivered or dissipated, with sorption-based heat transformation being an especially challenging task for the material because of the recurring ad- and desorption cycles (Fig. 1).

Microporous aluminium fumarate (abbreviated as μp-AF in this publication) keeps appearing in the patent literature since 2007,[31,32] and it distinguishes from other MOFs especially by the fact that it can be easily prepared from inexpensive reagents *via* a water-based precipitation approach. This also means that at least some water stability can be anticipated. Gas separation, $H_2$ or methane storage, and storage and release of liquid agents have been named as possible applications for μp-AF, for which it may be marketed by BASF as Basolite™ A520.[31,33] These facts all point out that μp-AF can become one of the commercially most important MOFs, but, curiously enough, publications in scientific journals remain scarce.[33,34]

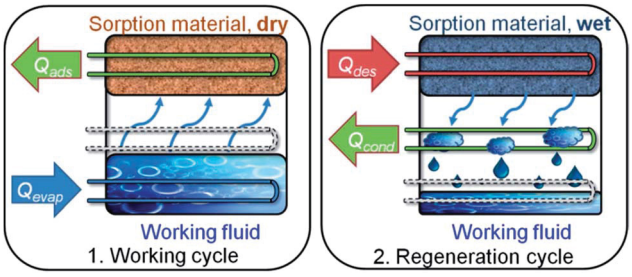


Fig. 1 Working principle of a sorption heat pump/chiller. (1) Working cycle: a working fluid (typically $H_2O$ due to the high evaporation enthalpy of 44 kJ $mol^{-1}$) is evaporated at low pressure by application of evaporation heat $Q_{evap}$, and adsorbed at a microporous material, releasing adsorption heat $Q_{ads}$. (2) Regeneration cycle: when the adsorbent is saturated, driving heat $Q_{des}$ is applied for desorption of the working fluid. The vapour then condenses at a cooler, and condensation heat $Q_{des}$ is released. Energy is now stored until reinitiation of the working cycle. Note: low temperature (*T*) heat is depicted in blue, medium *T* heat in green and high *T* heat in red. Copyright by the Royal Society of Chemistry, reproduced by permission of the authors of ref. 13.

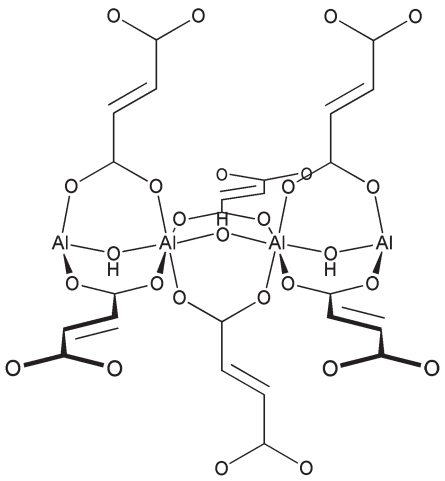

Scheme 1 Probable building block in μp-AF based on the analogy to MIL-53.

Structurally, μp-AF resembles MIL-53, as it also consists of infinite Al–OH–Al chains connected by fumarate linkers (Scheme 1).[35] From this comparison, a 3D structure consisting of [Al(OH)($O_2C$–CH=CH–$CO_2$)] with rhombohedral channels is probably formed (see Fig. S8 in ESI†).[31]

Here, a MOF-based material with promising properties (capacity, sorption behaviour, multi-cycle stability), and also a method for the production of a coating on a metallic substrate are presented. In this contribution, we demonstrate the unprecedented water-stability and hydrophilicity of μp-AF and fabricate this MOF into a thermally well coupled coating on aluminium metal sheets, *e.g.*, for use on heat exchangers in sorption-based heat transformation applications.

## 2 Experimental

### 2.1 Synthesis of bulk-μp-AF

Although a convenient water-based precipitation approach for the synthesis of microporous aluminium fumarate, μp-AF is known, a different patent procedure using dimethyl formamide as the solvent was chosen because of the alleged better reaction control, and adaptability towards the fabrication of MOF coatings.[31] In a 1000 mL round bottom flask, 26.9 g (108 mmol) of aluminium chloride hexahydrate (p.a., Merck) and 15.4 g (133 mmol) of fumaric acid (≥99.5%, Carl Roth) were dissolved in 550 mL of freshly distilled dimethyl formamide (≥99.5%, Carl Roth). The turbid, yellowish mixture was stirred at 130 °C for 4 days. After cooling, the snow-white precipitate was filtered off and stirred twice in redist. acetone (1 h and 24 h, 200 mL each), and twice in redist. ethanol (1 h and 24 h, 200 mL each). The solid was then dried in air at 80 °C. Yield: 15.4 g (90% based on Al). IR, neat (ATR), 3385, 1593, 1471, 1419, 1212, 1152, 1005, 985, 804, 713, 694, 646, 483 $cm^{-1}$ (see Fig. S4†). $C_4H_3O_5Al$ (158.04) calc. C 30.40, H 1.91%; found C 30.91, H 2.82.

 

### 2.2 Thermal gradient coating

**2.2.1 Aluminium substrate sheet preparation.** Aluminium sheets (50 × 50 × 1.0 $mm^3$) were sanded on both sides, etched in sodium hydroxide solution (140 g $L^{-1}$, 65 °C, 90 s), deoxidized in diluted nitric acid (13%, RT, 30 s) and dried in air at 60 °C. Directly prior to use, both sheets were clamped to a custom-made aluminium heating cartridge equipped with a surface thermocouple,[17] and the whole assembly was deoxidized again with diluted $HNO_3$ and carefully rinsed using water and dimethyl formamide. The accessible surface of each sheet was 13 $cm^2$.

**2.2.2 Coating synthesis.** For a typical synthesis, a solution of $Al(NO_3)_3 \cdot 9H_2O$ (Merck, 20.08 g) and fumaric acid (Carl Roth, 10.68 g) in freshly distilled dimethyl formamide (Carl Roth, 200 mL) was filled into a stainless steel beaker (65 mm inner diameter) thermostated to 30 °C. Using a custom-made aluminium heating apparatus as described in the literature,[17] the Al substrate sheet was immersed into the solution and heated to a temperature of 145 °C for 3 h. After cooling, the Al sheet was carefully removed, rinsed with and soaked overnight in DMF, then rinsed with and soaked overnight in ethanol, finally dried in air at 50 °C. Coating yield was 147 mg (11.3 mg $cm^{-2}$) for sheet 1, 172 mg (13.2 mg $cm^{-2}$) for sheet 2.

**2.2.3 Protective coating.** At RT, 10.0 mL of Silikophen® P 50/300 (Evonik Industries) were dissolved in 30.0 mL of xylene (*o*/*m*/*p*, technical grade). Sheet 2 was dipped into the solution, removed after 20 s, and dried over night at RT in air. The sample was then tempered according to the following program (ramp time/temperature/hold time): 60 min/50 °C/120 min; 180 min/105 °C/120 min; 120 min/250 °C/180 min; 300 min/RT. Total mass increase was 33.1 mg, which equals a varnish content in the μp-AF layer of 19% assuming that the silicone resin accumulates mainly at the rough μp-AF surface, not at the backside.

### 2.3 Analytics: procedure and instrumentation

$N_2$ adsorption isotherms were obtained on a Quantachrome® Nova @ 77 K, after vac. degassing (120 °C/24 h). $H_2O$ adsorption isotherms: obtained on a Quantachrome® Hydrosorb, after vac. degassing (120 °C/24 h). $H_2O$ adsorption isobars and powder cycle stability were examined in a Setaram™ TGA-DSC-111. A humidified argon gas flow (40 °C, 76.3% relative humidity) was generated by a Setaram™ WetSys humidity controller and passed through the sample chamber, while the temperature of the sample chamber itself was varied. For multi-cycle ad-/desorption experiments, the temperature of the sample chamber was varied between 40 °C and 140 °C with a cycle time of 5 h. X-ray diffractograms were acquired on a Bruker D8 Advance with DaVinci™, using a Cu anode tube at 40 kV/40 mA, with a Ni filter and constant sample illumination spot size (broadness: 12 mm); step size 0.02°, 1.0 s per step, Cu-Kα radiation. A rotating sample holder was used for powders. A MRI humidity chamber was used for controlled humidity experiments (Fig. 2d), where a humidified $N_2$ gas flow was passed over the sample at atmospheric pressure. Before each scan, the sample was allowed to equilibrate for 90 min. A Newport stage with three axes was used for coated sheets. IR

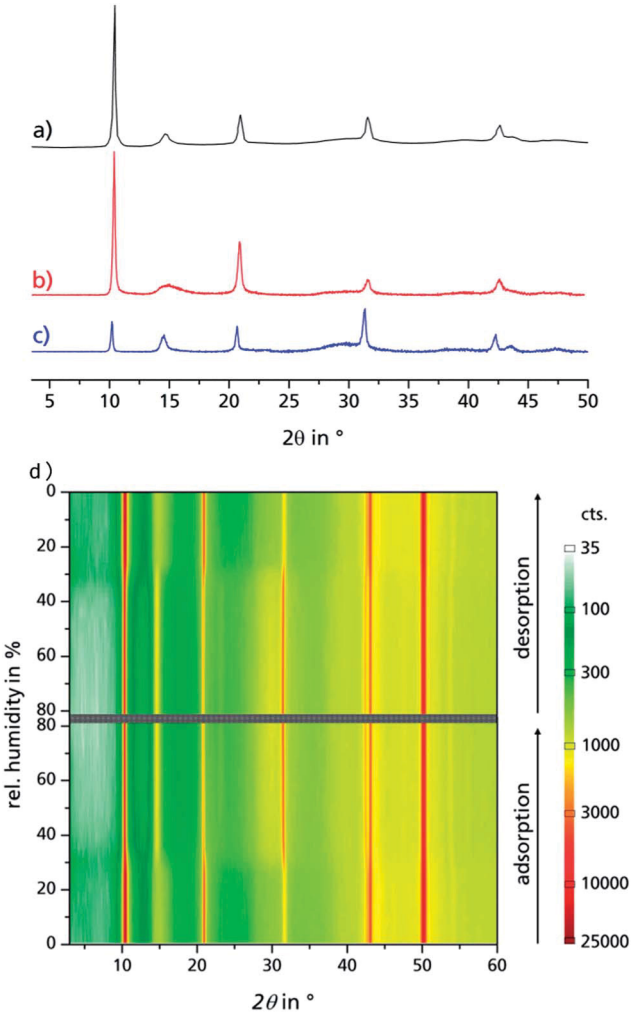


Fig. 2 PXRD of bulk μp-AF as extracted from patent literature (a), dried μp-AF (stored at 120 °C under vacuum for 24 h (b)) and hydrated μp-AF (stored under 100% water vapour atmosphere overnight, (c)). (d) Reversible structural transition observed by *in situ* PXRD in a humidity chamber at 313 K. See Fig. S5 in the ESI† for the individual diffractograms.

spectra were obtained on a PerkinElmer™ SpectrumTwo FTIR equipped with a diamond ATR unit. Multi-cycle stability tests of coated samples: in order to investigate the adsorption/desorption cycle stability of μp-AF over 1500 and another 3000 adsorption/desorption cycles, multi-cycle experiments were conducted in a special apparatus under pure water vapour atmosphere (1300 Pa), where the samples were clamped to a heating/cooling plate, with the temperature alternating between 125 °C and 20 °C for 90 seconds each. Hence, relative vapour pressure values of $p/p_0 = 0.006$ or, respectively, $p/p_0 = 0.55$, are generated and the main loading lift of μp-AF is covered. Microscopic images were obtained on a Keyence® VHX reflected-light microscope. Scanning electron microscope images were obtained on a FEI™ QUANTA 400 MK-II (25 kV, ET-detector). Heat capacity of bulk aluminium fumarate was determined using a SETARAM™ SenSys evo DSC calorimeter. Heat conductivity and contact resistance were obtained on a

NETZSCH LFA 457 laser flash analysis apparatus under vacuum. For the investigation of bulk aluminium fumarate, a pellet (Ø = 12.7 mm, forming pressure = 13 kN) was prepared. For investigation of the coating, a 10 × 10 $mm^2$ cut was used. Samples were coated with graphite on both sides and dehumidified at 120 °C prior to measurement. A Cowan 2-layer approach with regard to heat loss and pulse correction was applied. Heat capacity and thermal conductivity of the Al substrate were obtained from the Netzsch database, the heat capacity of the coating was calculated from the regression function given in the ESI.† For each temperature step, three values were taken, the given values are calculated as the arithmetic average. The calculation of the thermal conductivity was performed using the Netzsch software algorithm, which is based on the work by Hartmann *et al.*[36]

# 3 Results and discussion

## 3.1 Bulk μP-AF

Aluminium chloride hexahydrate reacts with fumaric acid in dimethyl formamide (DMF) at 130 °C under formation of aluminium fumarate, [Al(OH)($O_2$C–CH=CH–$CO_2$)] in high yield. The product was verified by positively matching the powder X-ray diffractograms of both dried and rehydrated μp AF with the pattern given for genuine Basolite™ A520 in the literature (Fig. 2a–c).[31]

**3.1.1 Pore analysis and $H_2O$ adsorption behaviour.** $N_2$ adsorption analysis yielded a BET surface of $S_{BET}$ = 1021 $m^2$ $g^{-1}$, and a micropore volume of $V_{pore}$ = 0.48 $cm^3$ $g^{-1}$ (literature:[33] $S_{Langmuir}$ = 1000–1200 $m^2$ $g^{-1}$, see ESI† for details).

Water adsorption isotherms were acquired in a temperature range between 298 K and 333 K, leading to a maximum water vapour uptake of approx. 0.45 g $g^{-1}$. The isotherms show a very favorable s-shape, with a steep increase in a narrow pressure range ($p/p_0$ = 0.2–0.3) (Fig. 3). The desorption hysteresis is small compared to other, comparably hydrophilic MOFs like iron or aluminium trimesate, MIL-100 (Fe, Al)[13] or zirconium aminoterephthalate $H_2$N-UiO-66.[15] The $H_2O$ loading of 0.45 g $g^{-1}$ correlates well to the micropore volume of 0.48 $cm^3$ $g^{-1}$ determined from $N_2$ sorption experiments for a solvent of density 1 g $cm^{-3}$, so that the micropores are filled at high $p/p_0$. This points to a high uniformity and hydrophilicity of the inner pore surface, without particularly hydrophobic sites. However, the conditions inside a thermally driven chiller can be considered to be *isobaric* rather than *isothermal*, due to the cyclic heating and cooling process. With the intent to simulate conditions close to reality, adsorption isobars were acquired at a partial water vapour pressure of 1.2 kPa (corresponding to an evaporator temperature of 10 °C), while desorption was examined at 5.6 kPa (corresponding to a condenser temperature of 35 °C) (see Fig. 3). During adsorption, the main loading lift of μp-AF occurs at $p/p_0$ < 0.3, permitting a medium temperature level of approx. 30 °C. The main desorption step occurs already between a relative pressure range of 0.4 > $p/p_0$ > 0.25, corresponding to a desorption ("driving") temperature of as low as 65 °C – a level which can be easily produced from solar or (surplus) district heat. These properties fit excellently to the demands typically anticipated for a thermally driven chiller.[12,37] From *in situ* ad-/desorption PXRD analysis of μp-AF (Fig. 2d and S5 in ESI†), we could find evidence that the structure is reversibly deformed during the transition. Based on the structural analogy between μp-AF (Basolite™ A520) and MIL-53, the aluminium fumarate framework can also be assumed to be a flexible, 'breathing'-type network adapting to guest molecules, that is, it can assume different shapes and porosities depending on the guest's presence or absence.[35,38] In the case of water as a guest molecule, however, the observed structural change in μp-AF was minor (see Fig. 2).

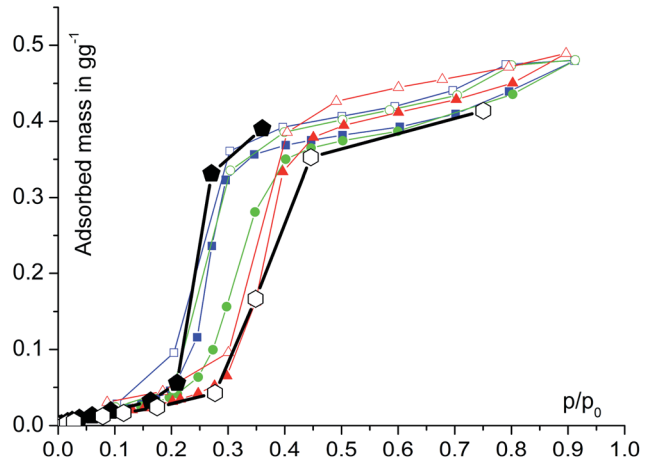


Fig. 3 Water sorption *isotherms* of bulk μp-AF, acquired at 25 °C water $p_0$ = 3.17 kPa, (■), 40 °C ($p_0$ = 7.39 kPa, (●) and 60 °C $p_0$ = 19.95 kPa, (▲), and *isobars* at 1.2 kPa (⬟) and 5.6 kPa (○). Adsorption is depicted with filled, desorption with empty symbols.

**3.1.2 Differential heat of adsorption.** The specific heat of adsorption $\Delta H_{ads}$ is a very important figure of merit especially for energy transformation applications. From a set of adsorption isotherms acquired at different temperatures, $\Delta H_{ads}$ can be calculated using a modified form of the Clausius–Clapeyron eqn (1):[39]

$$\frac{dp}{dT} = \frac{\Delta H_{ads}}{T \cdot \Delta V_{ads}} \quad (1)$$

with the approximation that the vapour volume change upon adsorption, $\Delta V_{ads}$, can be expressed using the ideal gas law, integration of the formula yields eqn (2):

$$\ln \frac{p}{p_0} = \frac{-\Delta H_{ads}}{R \cdot T} + c \quad (2)$$

The adsorption enthalpy for a specific amount of adsorbate can now be calculated from a dataset of different temperatures $T_1, T_2, \ldots, T_n$, required to obtain adsorption of this amount, and the corresponding absolute pressures $p_1, p_2, \ldots, p_n$, as the points $P_n(\ln(p_n/p_0)|1/T_n)$ will describe a straight line with the slope $-\Delta H_{ads}/R$. Values between isotherm data points were interpolated by straight lines, and $\Delta H_{ads}$ was calculated over the whole adsorption range (Fig. 4).

For the largest part of the adsorbed amount, the differential adsorption enthalpy $\Delta H_{ads}$ remains constantly about 10% above

 

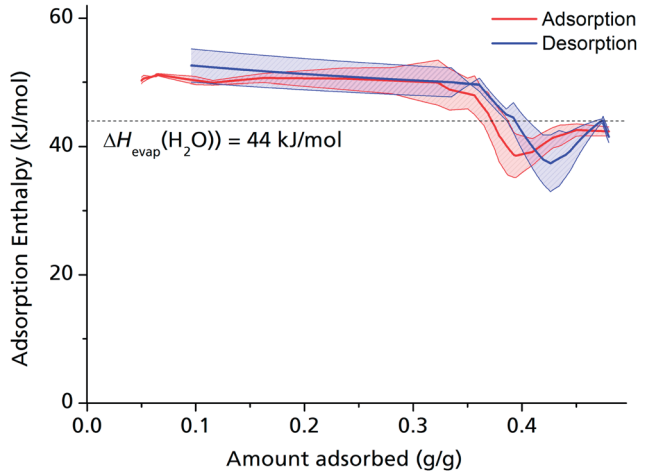


Fig. 4 Heat of adsorption for μp-AF–water, calculated from 298 K, 313 K and 333 K isotherms. The shaded area indicates the standard deviation of the respective linear fits through the points $P_1$, $P_2$, $P_3$.

the evaporation enthalpy of water, which is a value in the range typically found for medium hydrophilic zeolites or silica gels.[11,40] This points to a uniform, comparatively hydrophilic internal surface, with water molecules accumulating homogeneously along the channel walls. This behaviour differs considerably from that of, *e.g.*, MIL-100 or MIL-101, where strong coordinative bonds are established between the first adsorbed $H_2O$ molecules and the highly polar, hydrophilic metal ion clusters,[13] but makes sense given that μP-AF does not contain metal ion clusters, but infinite Al–O–Al–O chains running along the channel walls.

$\Delta H_{ads}$ drops substantially below the evaporation enthalpy of water when the pores are almost completely filled, which means that a simultaneous, endothermic process must take place at this point, such as the reversible deformation of the framework that can be deducted from the *in situ* PXRD measurements (Fig. 2). Another possible endothermic process, which may be responsible for the drop of adsorption enthalpy at high adsorbed amounts, which is not easy to detect, is the rearrangement of already adsorbed water molecules towards a closer, yet energetically less favourable configuration upon pore filling.

**3.1.3 Heat capacity and conductivity.** The heat capacity of dry bulk μp-AF is between 1.05 J $g^{-1}$ $K^{-1}$ and 1.35 J $g^{-1}$ $K^{-1}$ in the temperature range between 50 °C and 145 °C (see Fig. S3 in ESI†). These values are in accordance with those measured for other MOFs, where heat capacities range from 0.8 J $g^{-1}$ $K^{-1}$ to 1.2 J $g^{-1}$ $K^{-1}$.[41]

For the pressed pellet, the thermal conductivity in this temperature range lies around 0.12 W $m^{-1}$ $K^{-1}$.

**3.1.4 Multicycle water sorption stability test.** A metal–organic framework compound is often called "water-stable" when the powder can be recovered from water or from water–DMF mixtures without structural change as proven by powder X-ray diffraction.[5,22,42] In the cyclic operational mode of sorption heat transformation appliances, the sorption material is subjected to numerous ad-/desorption cycles with simultaneous cyclic thermal stress. Under these conditions, hydrothermal stability is a crucial aspect and, therefore, has to be investigated separately *via* multi-cycle ad-/desorption experiments. Under the cycling conditions heat transfer to and from the sample is limited. The thermodynamic water sorption equilibrium is not completely reached within the individual cycles. Consequently, a 20 h thermodynamic analysis cycle was run before the cycling experiment and after every 20 cycles the equilibrium $H_2O$ uptake capacity of the material was determined.

Judged from the longer analysis cycles during the multi-cycle ad-/desorption experiments in Fig. 5, the adsorption capacity remains within the range to be expected from the volumetric measurements: 0.37 g $g^{-1}$ after 20, 0.38 g $g^{-1}$ after 40, 0.37 g $g^{-1}$ after 60 and 0.37 g $g^{-1}$ after 80 cycles. While the framework seems to lose approx. 6% of its weight during the first 20 cycles, this seems to have no impact on the sorption capacity itself. The decrease in dry mass indicates a further activation effect due to water sorption cycles. This post-activation phenomenon can be explained by stepwise removing of fumaric acid, which apparently could not be fully cleaved from the narrow and highly polar channels of μp-AF by the initial washing procedure. During cycling however, the desorbing water vapour is likely to entrain the high-boiling, yet poorly water-soluble fumaric acid in a way similar to steam distillation.

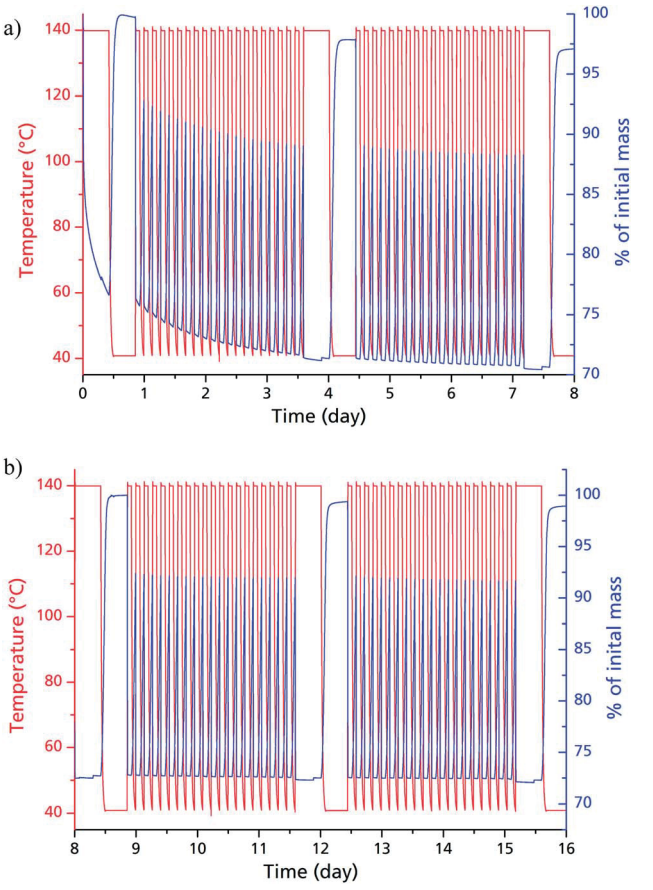


Fig. 5 Thermogravimetric adsorption/desorption cycling experiments for 40 cycles (a), and another 40 cycles (b) of bulk μp-AF. Long segments at the beginning, in the middle and at the end of each experiment were conducted to determine the equilibrium loading of the sample.

### 3.2 μp-AF@Al coating

**3.2.1 Coating synthesis.** When performing thermal gradient synthesis, the temperature of the solution of aluminium nitrate and fumaric acid is maintained at 30 °C by active chilling, only the substrate itself is heated. Due to the arising temperature gradient, the MOF crystals form a layer covering only the very surface, with a growth rate of approx. 100 μm $h^{-1}$. Simply applying the original procedure for thermal gradient synthesis[17] to μp-AF did not yield the desired result. We found that several parameters had to be changed in order to obtain a sufficiently thick coating in a reasonable amount of time.

*Replacement of the $Al^{3+}$-source.* As chloride anions are known to provoke corrosion of the most common metallic substrates, *e.g.*, copper, aluminium, and also stainless steel alloys, the aluminium chloride used in the original synthesis procedure[31] was replaced by an equimolar amount of aluminium nitrate nonahydrate.

*Increase of reactant concentration.* In order to speed up layer growth and obtain sufficiently thick layers, we doubled the concentrations of reactants (aluminium nitrate nonahydrate and fumaric acid) for a second run, compared to the original procedure.

*Protective lacquer.* For increased mechanical stability, one sample was additionally furnished with a protective lacquer. An industry-standard, highly water vapour permeable silicone-resin varnish was chosen for this purpose (Evonik Silikophen® P50/300).

*Reaction temperature.* We found that it was necessary to set the temperature of the substrate to 145 °C compared to 130 °C for the batch synthesis in order to obtain an evenly distributed coating. The temperature of the cooling jacket was set to 30 °C.

Under the conditions given above, a uniform coating of μp-AF could be deposited on pretreated aluminium sheets (Fig. 6 and 7). As can be seen from the polished cross-section (see Fig. 7d), the coating consists of a macroporous and structured top layer with a thickness of approx. 280 μm (top-down view in Fig. 7b). Applying moderate force, the top layer can be removed with a spatula, exposing a denser and firmly adhering bottom layer with a thickness of only 20 μm (Fig. 7c). Both layers consist of crystalline μp-AF, as proven by PXRD (see Fig. S6 in ESI†).

The gravimetric density of the μp-AF coating (determined by measuring and weighing a flake removed from the substrate) is $\rho_{coating} = 0.61$ g $cm^{-3}$.

**3.2.2 Crystal structure and multicycle stability of μp-AF coating.** From comparison of PXRD measurements of both sheet 1 and 2 (Fig. 8) with the PXRD for bulk μp-AF (Fig. 2 and S2 in ESI†), it can be seen that the single crystalline phase within the coating can be ascribed to μp-AF.[34] The main peak at $2\theta = 10.5°$, however, is comparatively more intense, which suggests that a preferred orientation of crystallites is present. Such a behavior is well-known for polycrystalline layers, and can be

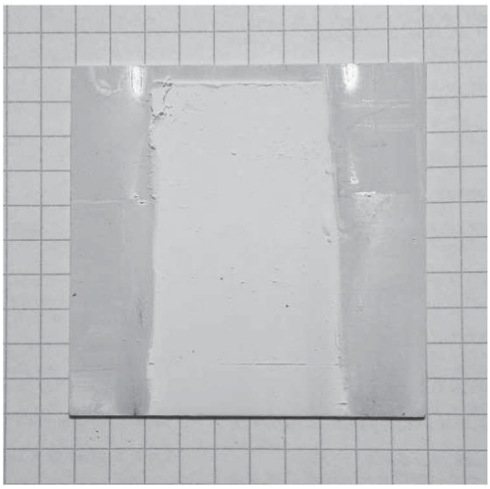

Fig. 6 Representative image of an μp-AF@Al coated aluminium sheet. Edges were covered by mounting clamps during coating synthesis.

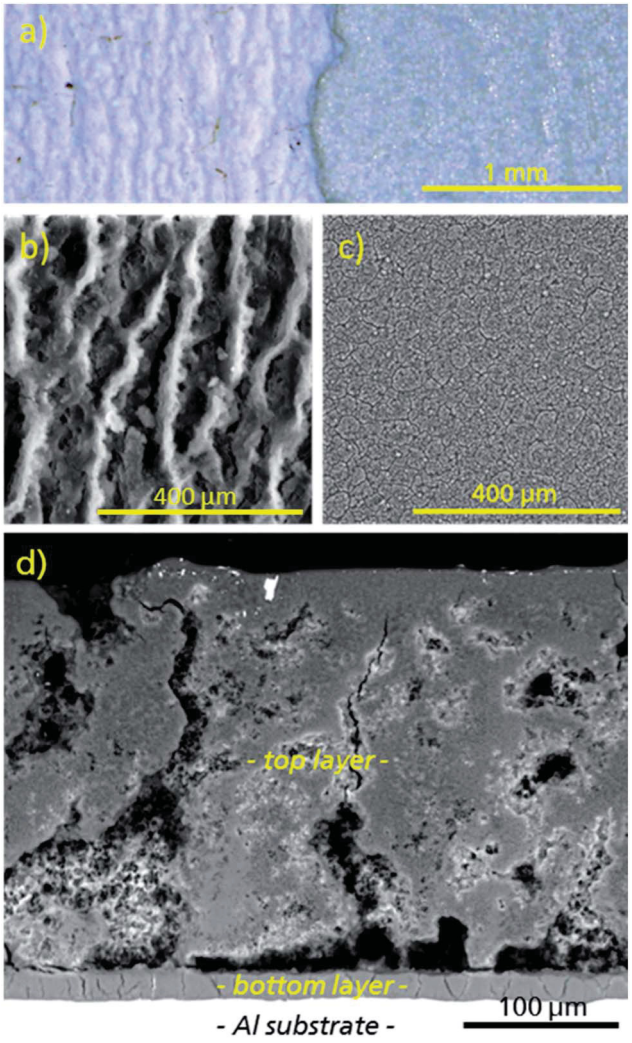


Fig. 7 (a) Representative optical microscope image of the μp-AF@Al coating in top-down view, with the top layer being removed in the right part of the image in order to expose the bottom layer. The different structures can be seen in (b) (SEM image of the top-down view of the top layer) and (c) (SEM image of the top-down view of the bottom layer), and in the polished cross-section of the whole coating (d).

 

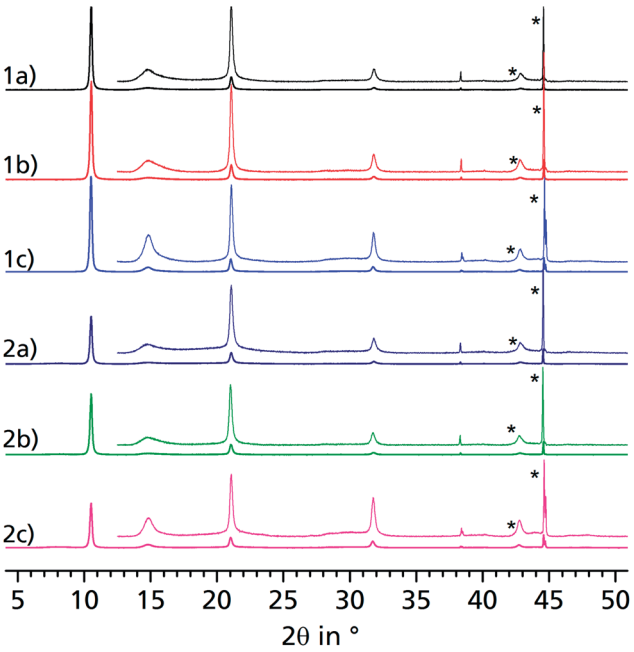


Fig. 8 PXRD of two representative μp-AF@Al sheets 1 and 2, each before cycling (a), after 1500 (b) and 4500 (c) ad-/desorption cycles with water vapour. Sheet 2 has been covered with the silicon resin. Insets are multiplied by the factor of 6 for better visualization. Peaks marked with an asterisk (★) are caused by the Al substrate.

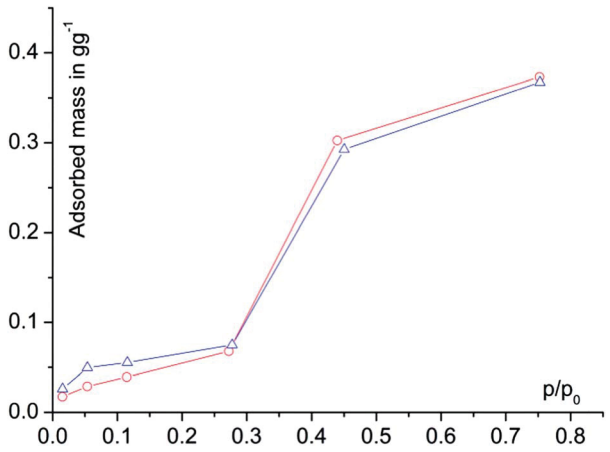


Fig. 9 Equilibrium water desorption isobars of a representative μp-AF@Al coating after 1500 (○) and 4500 cycles (△). Isobars were acquired gravimetrically under pure water vapour atmosphere, at $p_{H_2O}$ = 5.6 kPa, with 140 °C ≥ $T$ ≥ 40 °C. Samples were degassed at 150 °C under vacuum for 12 h prior to measurement, and loaded with water vapour for 8 h. Adsorbed mass is based on the amount of μp-AF coating.

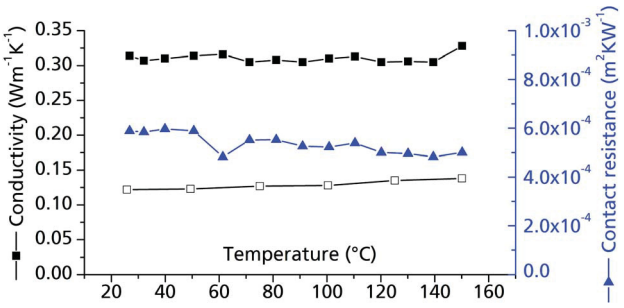


Fig. 10 Thermal conductivity of μp-AF. Measurements were conducted on bulk μp-AF (pellet, ∅ = 12.68 mm, $h$ = 1.71 mm, forming pressure = 13 kN; $\rho$ = 0.714 g cm$^{-3}$, empty symbols) and a μp-AF@Al coated sheet with protective layer (filled symbols). For the $c_p$ values, the curve determined for bulk μp-AF was used in both cases (see Fig. S3 in ESI†).

explained by evolutionary selection (van-der-Drift growth).[43] Compared to sheet 1, reflections of sheet 2 are less intense, because the sample was varnished with silicon resin.

When comparing the diffractograms of the coated sheets before cycling, after 1500 and after 4500 cycles, no weakening or broadening of the reflections can be seen in both cases. In fact, the intensity and sharpness of the reflections at $2\theta = 14.9°$ and 31.8° increases. This can be explained by recrystallization/rearrangement phenomena during cycling, and also by a post-activation procedure as described above for bulk μp-AF.

After 1500 and 4500 cycles, the desorption isobar for the μp-AF coating in Fig. 9 corresponds well to the isobar acquired for bulk μp-AF (Fig. 3). Also, the $H_2O$ capacity of 0.37 g g$^{-1}$ from the desorption *isobar* corresponds to the equilibrium loading in the multi-cycle experiments of bulk μp-AF (Fig. 5). This is an excellent water uptake value as to the best of our knowledge, so far, no other MOF has shown such a stability towards the first 4500 ad/desorption cycles with water vapor (*cf.* Fig. 8).

Sheet 2 was additionally covered with silicone resin and features the same shape of the isotherm after 4500 cycles, but with a smaller relative load, due to the additional weight added to the coating by the silicone resin (see Fig. S7 in ESI†).

**3.2.3 Thermal conductivity and contact resistance of the coating.** These two parameters directly determine the dissipation of the heat of adsorption. This correlates directly to the kinetics and hence to the performance of the finished adsorber. The conductivity of the μp-AF@Al coating (Fig. 10) lies in a range of 0.33 to 0.31 W m$^{-1}$ K$^{-1}$, which is approx. 3 times higher than for the pressed pure Al-fumarate powder sample, despite its slightly lower density ($\rho_{coating}$ = 0.61 cm$^3$ g$^{-1}$, *vs.* $\rho_{pellet}$ = 0.71 cm$^3$ g$^{-1}$). The high thermal conductivity of the layer can be explained with the high uniformity of the layer and the fact that crystallites seem to be highly intergrown (*cf.* Fig. 7). For comparison, a packed zeolite 4 Å bed features a thermal conductivity of 0.09 W m$^{-1}$ K$^{-1}$ when no additives are used,[44] and a silica gel packing about 0.2 W m$^{-1}$ K$^{-1}$.[45] An activated carbon bed has a conductivity of 0.15 to 0.5 W m$^{-1}$ K$^{-1}$.[46] On the other hand, the conductivity of monocrystalline MOF-5 has even been reported as low as 0.35 W m$^{-1}$ K$^{-1}$.[47] The comparatively high thermal conductivity for the μp-AF@Al coating can be traced to the highly intergrown crystals within the coated sample (Fig. 7), so that intercrystalline heat transport is facilitated.

The contact resistance between the MOF layer and the resin coating is about 5.1 × 10$^{-4}$ m$^2$ K W$^{-1}$ in the examined temperature range (Fig. 10). For comparison, this value equals

the contact resistance between a similar combination of materials (activated carbon pressed to an aluminium bronze surface, but with a pressure of 1.0 MPa) and is hence a very acceptable value for a MOF–metal interface.[48]

# 4 Conclusions

The thorough investigation of the water sorption properties of μp-AF show that this remarkable MOF may be employed as a promising adsorbent for heat transformation applications. The maximum water exchange of 0.35 g $g^{-1}$ is certainly lower than in other MOFs such as UiO-66 (ref. 15) or MIL-100,[13] but it can be fully utilized under realistic, isobaric working conditions due to the hydrophilicity of μp-AF. The characteristic, steep s-shape of the isotherm in a relative pressure band of $0.2 < p/p_0 < 0.35$ has not been observed for other water-stable MOFs before. In this context, μp-AF can be compared best to modern, hydrophilic, zeotype adsorbents such as AlPO-18 or AlPO-4.[40] In terms of cyclic hydrothermal stability, μp-AF surpasses other hydrophilic MOFs, even other aluminium carboxylates such as MIL-100(Al).[13]

μp-AF can already be produced comparatively cost-efficiently *via* a simple precipitation reaction. This is in contrast to, *e.g.*, the template-based AlPO-18 synthesis, or various hydro-/solvothermal synthesis routes required for other MOFs. μp-AF is also free of harmful components such as heavy metals or critical organic compounds. Aluminium salts are approved as EU food additives (E520-523), as well as several fumarates (E365-368).

The way towards the application has been cleared further by the successful preparation of a thick, thermally well coupled μp-AF coating on a metallic substrate *via* the thermal gradient approach, and its hydrothermal stability proven for 4500 ad-/desorption cycles, renders this material very interesting also for other applications such as catalysis or gas storage.

The chemically versatile C=C-bond of the fumarate linker can be a valuable anchor for further tailoring of μp-AF by post-synthetic modifications (for example, it might serve as a complex ligand after hydroxylation, or directly *via* the π-bond electrons). This topic should be investigated in the future, in order to render μp-AF more versatile also for highly specific applications.

# Acknowledgements

Funding by the Federal German Ministry of Economics (BMWi) under grant-# 0327851A/B, and by the Fraunhofer Society under grant-# MAVO 824 704 is gratefully acknowledged. Part of this project is also funded by DFG grant Ja466/25-1 to CJ. This work is dedicated to Prof. Christel Marian on the occasion of her 60th birthday.

# Notes and references

1 J. R. Long and O. M. Yaghi, *Chem. Soc. Rev.*, 2009, **38**, 1213–1214; M. O'Keeffe and O. M. Yaghi, *Chem. Rev.*, 2012, **112**, 675–702; C. Janiak and J. K. Vieth, *New J. Chem.*, 2010, **34**, 2366–2388.

2 R. J. Kuppler, D. J. Timmons, Q.-R. Fang, J.-R. Li, T. A. Makal, M. D. Young, D. Yuan, D. Zhao, W. Zhuang and H.-C. Zhou, *Coord. Chem. Rev.*, 2009, **253**, 3042–3066; M. P. Suh, H. J. Park, T. K. Prasad and D. W. Lim, *Chem. Rev.*, 2012, **112**, 782–835; H. Wu, Q. Gong, D. H. Olson and J. Li, *Chem. Rev.*, 2012, **112**, 836–868; L. J. Murray, M. Dincă and J. R. Long, *Chem. Soc. Rev.*, 2009, **38**, 1294–1314.

3 J. A. Mason, M. Veenstra and J. R. Long, *Chem. Sci.*, 2014, **5**, 32–51; R. Sathre and E. Masanet, *RSC Adv.*, 2013, **3**, 4964–4975; J. Liu, P. K. Thallapally, B. P. McGrail, D. R. Bown and J. Liu, *Chem. Soc. Rev.*, 2012, **41**, 2308–2322; H. Amrouche, B. Creton, F. Siperstein and C. Nieto-Draghi, *RSC Adv.*, 2012, **2**, 6028–6035.

4 J. R. Li, J. Sculley and H. C. Zhou, *Chem. Rev.*, 2012, **112**, 869–932; Z. Zhang, Y. Zhao, Q. Gong, Z. Li and J. Li, *Chem. Commun.*, 2013, **49**, 653–661; H. B. Tanh Jeazet, C. Staudt and C. Janiak, *Dalton Trans.*, 2012, **41**, 14003–14027; X. Y. Chen, V.-T. Hoang, D. Rodrigue and S. Kaliaguine, *RSC Adv.*, 2013, **3**, 24266–24279; G. Férey, C. Serre, T. Devic, G. Maurin, H. Jobic, P. L. Llewellyn, G. De Weireld, A. Vimont, M. Daturi and J. S. Chang, *Chem. Soc. Rev.*, 2011, **40**, 550–562; J.-R. Li, Y. Ma, M. C. McCarthy, J. Sculley, J. Yu, H.-K. Jeong, P. B. Balbuena and H.-C. Zhou, *Coord. Chem. Rev.*, 2011, **255**, 1791–1823; N. Hara, M. Yoshimune, H. Negishi, K. Haraya, S. Hara and T. Yamaguchi, *RSC Adv.*, 2013, **3**, 14233–14236; J. H. Yoon, D. Kim, X. Song, S. Han, J. Shin, S. B. Hong and M. Soo Lah, *RSC Adv.*, 2012, **2**, 11566–11573; M. Fischer, F. Hoffmann and M. Fröba, *RSC Adv.*, 2012, **2**, 4382–4396; L. Ge, A. Du, M. Hou, V. Rudolph and Z. Zhu, *RSC Adv.*, 2012, **2**, 11793–11800.

5 K. A. Cychosz and A. J. Matzger, *Langmuir*, 2010, **26**, 17198–17202; Y.-X. Tan, Y.-P. He, M. Wang and J. Zhang, *RSC Adv.*, 2014, **4**, 1480–1483.

6 P. Horcajada, R. Gref, T. Baati, P. K. Allan, G. Maurin, P. Couvreur, G. Férey, R. E. Morris and C. Serre, *Chem. Rev.*, 2012, **112**, 1232–1268.

7 J. Lee, O. K. Farha, J. Roberts, K. A. Scheidt, S. T. Nguyen and J. T. Hupp, *Chem. Soc. Rev.*, 2009, **38**, 1450–1459; M. Yoon, R. Srirambalaji and K. Kim, *Chem. Rev.*, 2012, **112**, 1196–1231; M. A. Gotthardt, A. Beilmann, R. Schoch, J. Engelke and W. Kleist, *RSC Adv.*, 2013, **3**, 10676–10679; Y. Fu, D. Sun, M. Qin, R. Huang and Z. Li, *RSC Adv.*, 2012, **2**, 3309–3314.

8 A. U. Czaja, N. Trukhan and U. Muller, *Chem. Soc. Rev.*, 2009, **38**, 1284–1293; G. Férey, *Dalton Trans.*, 2009, 4400–4415; M. J. Prakash and M. S. Lah, *Chem. Commun.*, 2009, 3326–3341; C. Hou, Q. Xu, Y. Wang and X. Hu, *RSC Adv.*, 2013, **3**, 19820–19823; J. F. Guo, C. M. Li, X. L. Hu, C. Z. Huang and Y. F. Li, *RSC Adv.*, 2014, **4**, 9379–9382.

9 F. Jeremias, D. Fröhlich, C. Janiak and S. K. Henninger, *New J. Chem.*, 2014, **38**, 1846–1852; C. Janiak and S. K. Henninger, *Nachr. Chem.*, 2013, **61**, 520–523.

10 Y. I. Aristov, *Appl. Therm. Eng.*, 2013, **50**, 1610–1618; R. Wang and R. Oliveira, *Prog. Energy Combust. Sci.*, 2006, **32**, 424–458; Y. I. Aristov, *Int. J. Refrig.*, 2009, **32**, 675–686; L. G. Gordeeva, A. Freni, Y. I. Aristov and G. Restuccia, *Ind. Eng. Chem. Res.*,

 

2009, **48**, 6197–6202; Y. I. Aristov, *J. Chem. Eng. Jpn.*, 2007, **40**, 1242–1251; Y. I. Aristov, M. M. Tokarev, A. Freni, I. S. Glaznev and G. Restuccia, *Microporous Mesoporous Mater.*, 2006, **96**, 65–71; Y. I. Aristov, B. Dawoud, I. S. Glaznev and A. Elyas, *Int. J. Heat Mass Transfer*, 2008, **51**, 4966–4972; Y. I. Aristov, G. Restuccia, G. Cacciola and V. N. Parmon, *Appl. Therm. Eng.*, 2002, **22**, 191–204.

11 N. C. Srivastava and I. W. Eames, *Appl. Therm. Eng.*, 1998, **18**, 707–714.

12 S. K. Henninger, F. Jeremias, H. Kummer and C. Janiak, *Eur. J. Inorg. Chem.*, 2012, 2625–2634.

13 F. Jeremias, A. Khutia, S. K. Henninger and C. Janiak, *J. Mater. Chem.*, 2012, **22**, 10148–10151.

14 J. Ehrenmann, S. K. Henninger and C. Janiak, *Eur. J. Inorg. Chem.*, 2011, 471–474.

15 F. Jeremias, V. Lozan, S. Henninger and C. Janiak, *Dalton Trans.*, 2013, **42**, 15967–15973.

16 S. K. Henninger, H. A. Habib and C. Janiak, *J. Am. Chem. Soc.*, 2009, **131**, 2776–2777.

17 F. Jeremias, S. K. Henninger and C. Janiak, *Chem. Commun.*, 2012, **48**, 9708–9710.

18 A. Rezk, R. Al-Dadah, S. Mahmoud and A. Elsayed, *Int. J. Heat Mass Transfer*, 2012, **55**, 7366–7374.

19 A. Khutia, H. U. Rammelberg, T. Schmidt, S. Henninger and C. Janiak, *Chem. Mater.*, 2013, **25**, 790–798; H. Jasuja, J. Zang, D. S. Sholl and K. S. Walton, *J. Phys. Chem. C*, 2012, **116**, 23526–23532; S. M. Cohen, *Chem. Rev.*, 2012, **112**, 970–1000; G. Akiyama, R. Matsuda, H. Sato, A. Hori, M. Takata and S. Kitagawa, *Microporous Mesoporous Mater.*, 2012, **157**, 89–93.

20 P. Küsgens, M. Rose, I. Senkovska, H. Fröde, A. Henschel, S. Siegle and S. Kaskel, *Microporous Mesoporous Mater.*, 2009, **120**, 325–330.

21 M. Taddei, A. Ienco, F. Costantino and A. Guern, *RSC Adv.*, 2013, **3**, 26177–26183; J. J. Low, A. I. Benin, P. Jakubczak, J. F. Abrahamian, S. A. Faheem and R. R. Willis, *J. Am. Chem. Soc.*, 2009, **131**, 15834–15842.

22 K. S. Park, Z. Ni, A. P. Cote, J. Y. Choi, R. Huang, F. J. Uribe-Romo, H. K. Chae, M. O'Keeffe and O. M. Yaghi, *Proc. Natl. Acad. Sci. U. S. A.*, 2006, **103**, 10186–10191.

23 A. Demessence, D. M. D'Alessandro, M. L. Foo and J. R. Long, *J. Am. Chem. Soc.*, 2009, **131**, 8784–8786.

24 J. H. Cavka, S. Jakobsen, U. Olsbye, N. Guillou, C. Lamberti, S. Bordiga and K. P. Lillerud, *J. Am. Chem. Soc.*, 2008, **130**, 13850–13851; C. Gomes Silva, I. Luz, F. X. Llabres i Xamena, A. Corma and H. Garcia, *Chem.–Eur. J.*, 2010, **16**, 11133–11138; D. Feng, Z.-Y. Gu, J.-R. Li, H.-L. Jiang, Z. Wei and H.-C. Zhou, *Angew. Chem.*, 2012, **124**, 10453–10456.

25 J. M. Taylor, R. K. Mah, I. L. Moudrakovski, C. I. Ratcliffe, R. Vaidhyanathan and G. K. Shimizu, *J. Am. Chem. Soc.*, 2010, **132**, 14055–14057; C. Serre, N. Stock, T. Bein and G. Férey, *Inorg. Chem.*, 2004, **43**, 3159–3163.

26 V. Colombo, C. Montoro, A. Maspero, G. Palmisano, N. Masciocchi, S. Galli, E. Barea and J. A. Navarro, *J. Am. Chem. Soc.*, 2012, **134**, 12830–12843.

27 J. Liu, F. Sun, F. Zhang, Z. Wang, R. Zhang, C. Wang and S. Qiu, *J. Mater. Chem.*, 2011, **21**, 3775; S. Kayaert, S. Bajpe, K. Masschaele, E. Breynaert, C. E. A. Kirschhock and J. A. Martens, *Thin Solid Films*, 2011, **519**, 5437–5440; P. Falcaro, A. J. Hill, K. M. Nairn, J. Jasieniak, J. I. Mardel, T. J. Bastow, S. C. Mayo, M. Gimona, D. Gomez, H. J. Whitfield, R. Ricco, A. Patelli, B. Marmiroli, H. Amenitsch, T. Colson, L. Villanova and D. Buso, *Nat. Commun.*, 2011, **2**, 237; A. Schoedel, C. Scherb and T. Bein, *Angew. Chem., Int. Ed.*, 2010, **49**, 7225–7228; V. V. Guerrero, Y. Yoo, M. C. McCarthy and H.-K. Jeong, *J. Mater. Chem.*, 2010, **20**, 3938; A. Centrone, Y. Yang, S. Speakman, L. Bromberg, G. C. Rutledge and T. A. Hatton, *J. Am. Chem. Soc.*, 2010, **132**, 15687–15691; H. Guo, G. Zhu, I. J. Hewitt and S. Qiu, *J. Am. Chem. Soc.*, 2009, **131**, 1646–1647; J. Gascon, S. Aguado and F. Kapteijn, *Microporous Mesoporous Mater.*, 2008, **113**, 132–138.

28 N. Campagnol, T. Van Assche, T. Boudewijns, J. Denayer, K. Binnemans, D. De Vos and J. Fransaer, *J. Mater. Chem. A*, 2013, **1**, 5827; T. R. C. Van Assche, G. Desmet, R. Ameloot, D. E. De Vos, H. Terryn and J. F. M. Denayer, *Microporous Mesoporous Mater.*, 2012, **158**, 209–213; S. A. Silkin, V. I. Petrenko and A. I. Dikusar, *Surf. Eng. Appl. Electrochem.*, 2010, **46**, 1–8; R. Ameloot, L. Pandey, M. Van der Auweraer, L. Alaerts, B. F. Sels and D. E. De Vos, *Chem. Commun.*, 2010, **46**, 3735–3737; R. Ameloot, E. Gobechiya, H. Uji-i, J. A. Martens, J. Hofkens, L. Alaerts, B. F. Sels and D. E. De Vos, *Adv. Mater.*, 2010, **22**, 2685–2688; R. Ameloot, L. Stappers, J. Fransaer, L. Alaerts, B. F. Sels and D. E. De Vos, *Chem. Mater.*, 2009, **21**, 2580–2582; A. Doménech, H. García, M. T. Doménech-Carbó and F. Llabrés-i-Xamena, *Electrochem. Commun.*, 2006, **8**, 1830–1834.

29 Y. Yoo and H. K. Jeong, *Chem. Commun.*, 2008, 2441–2443.

30 D. Zacher, O. Shekhah, C. Wöll and R. A. Fischer, *Chem. Soc. Rev.*, 2009, **38**, 1418–1429; C. Scherb, R. Koehn and T. Bein, *J. Mater. Chem.*, 2010, **20**, 3046.

31 C. Kiener, U. Müller and M. Schubert, Germany Pat. WO 2007/118841 A2, 2007.

32 C. Kiener, U. Müller and M. Schubert, *US Pat.* 12/297,666, 2012; E. Leung, U. Müller, N. Trukhan, H. Mattenheimer and G. Cox, *US Pat.* 13/249,943, 2012.

33 B. Yilmaz, N. Trukhan and U. Müller, *Chin. J. Catal.*, 2012, **33**, 3–10.

34 M. Gaab, N. Trukhan, S. Maurer, R. Gummaraju and U. Müller, *Microporous Mesoporous Mater.*, 2012, **157**, 131–136.

35 T. Loiseau, C. Serre, C. Huguenard, G. Fink, F. Taulelle, M. Henry, T. Bataille and G. Férey, *Chem.–Eur. J.*, 2004, **10**, 1373–1382; C. Serre, F. Millange, C. Thouvenot, M. Noguès, G. Marsolier, D. Louër and G. Férey, *J.Am. Chem. Soc.*, 2002, **124**, 13519–13526.

36 G. Langer, J. Hartmann and M. Reichling, *Rev. Sci. Instrum.*, 1997, **68**, 1510.

37 Y. I. Aristov, *Appl. Therm. Eng.*, 2012, **42**, 18–24; B. B. Saha, A. Chakraborty, S. Koyama, K. Srinivasan, K. C. Ng, T. Kashiwagi and P. Dutta, *Appl. Phys. Lett.*, 2007, **91**, 111902.

38 J. Liu, F. Zhang, X. Zou, G. Yu, N. Zhao, S. Fan and G. Zhu, *Chem. Commun.*, 2013, **49**, 7430–7432.

39 J. Rouquerol, F. Rouquerol and K. S. W. Sing, *Adsorption by Powders and Porous Solids*, Academic Press, San Diego, 1998.

40 S. K. Henninger, F. P. Schmidt and H. M. Henning, *Appl. Therm. Eng.*, 2010, **30**, 1692–1702.
41 B. Mu and K. S. Walton, *J. Phys. Chem. C*, 2011, **115**, 22748–22754.
42 M. Kandiah, M. H. Nilsen, S. Usseglio, S. Jakobsen, U. Olsbye, M. Tilset, C. Larabi, E. A. Quadrelli, F. Bonino and K. P. Lillerud, *Chem. Mater.*, 2010, **22**, 6632–6640; V. Guillerm, F. Ragon, M. Dan-Hardi, T. Devic, M. Vishnuvarthan, B. Campo, A. Vimont, G. Clet, Q. Yang, G. Maurin, G. Férey, A. Vittadini, S. Gross and C. Serre, *Angew. Chem., Int. Ed.*, 2012, **51**, 9267–9271.
43 A. Van der Drift, *Philips Res. Rep.*, 1967, **22**, 267.
44 L. Pino, Y. Aristov, G. Cacciola and G. Restuccia, *Adsorption*, 1997, **3**, 33–40.
45 J. M. Gurgel and R. P. Klüppel, *Chem. Eng. J. Biochem. Eng. J.*, 1996, **61**, 133–138.
46 D. Menard, X. Py and N. Mazet, *Chem. Eng. Process.*, 2007, **46**, 565–572.
47 B. L. Huang, Z. Ni, A. Millward, A. J. H. McGaughey, C. Uher, M. Kaviany and O. Yaghi, *Int. J. Heat Mass Transfer*, 2007, **50**, 405–411.
48 M. Khandelwal and M. M. Mench, *J. Power Sources*, 2006, **161**, 1106–1115.

 

**† Electronic Supplementary Information**

# Advancement of sorption-based heat transformation by a metal coating of highly-stable, hydrophilic aluminium fumarate MOF

Felix Jeremias,[a,b] Dominik Fröhlich,[a,b] Christoph Janiak[a,*] and Stefan K. Henninger[b,*]

a) Institut für Anorganische Chemie und Strukturchemie, Universität Düsseldorf, 40204 Düsseldorf, Germany
b) Department of Thermally Active Materials and Solar Cooling, Fraunhofer Institute for Solar Energy Systems (ISE), Heidenhofstr. 2, 79110 Freiburg, Germany

## Nitrogen sorption isotherm for bulk µp-AF

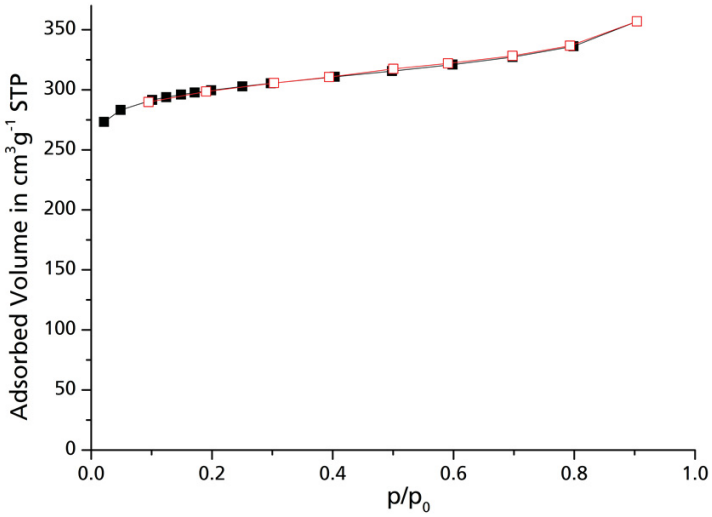


**Figure S1:** Nitrogen adsorption isotherm of bulk aluminum fumarate (filled squares: adsorption, empty squares: desorption). Acquired at 77 K, after 24 h of vacuum degassing at 120 °C.

**PXRD comparison**

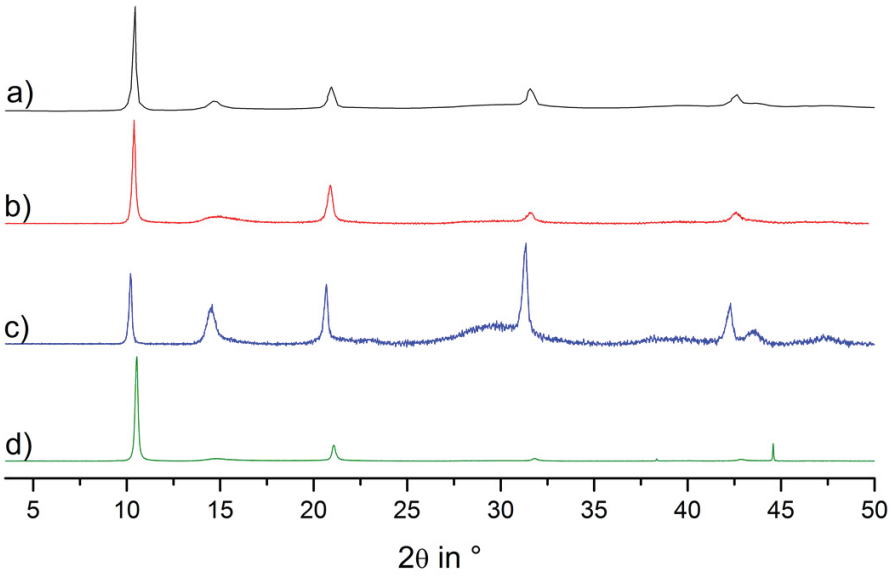


**Figure S2:** Powder X-ray diffractograms for µp-AF from patent literature (a), for the prepared bulk sample in dry (b) and wet (c) condition, and the coated sheet *1* (d). All diffractograms are normalized to the highest reflection.

**Heat Capacity of bulk µp-AF**

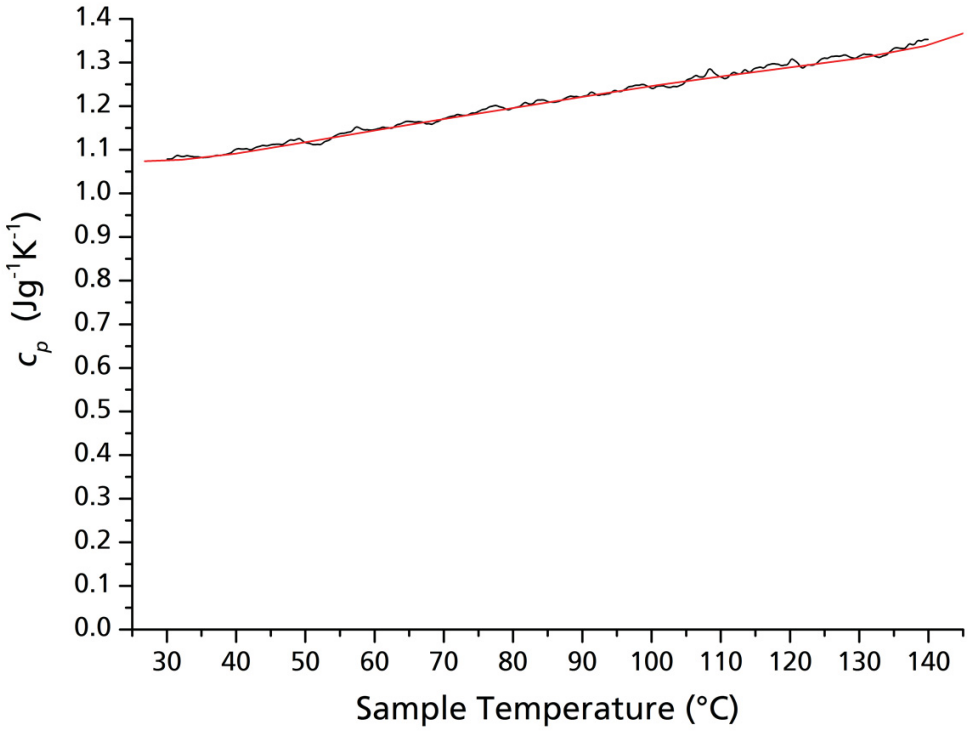


**Figure S3:** Measured $c_p$ values (black) and interpolation (red), which was used for the conductivity measurements.

**FT-IR of bulk µp-AF**

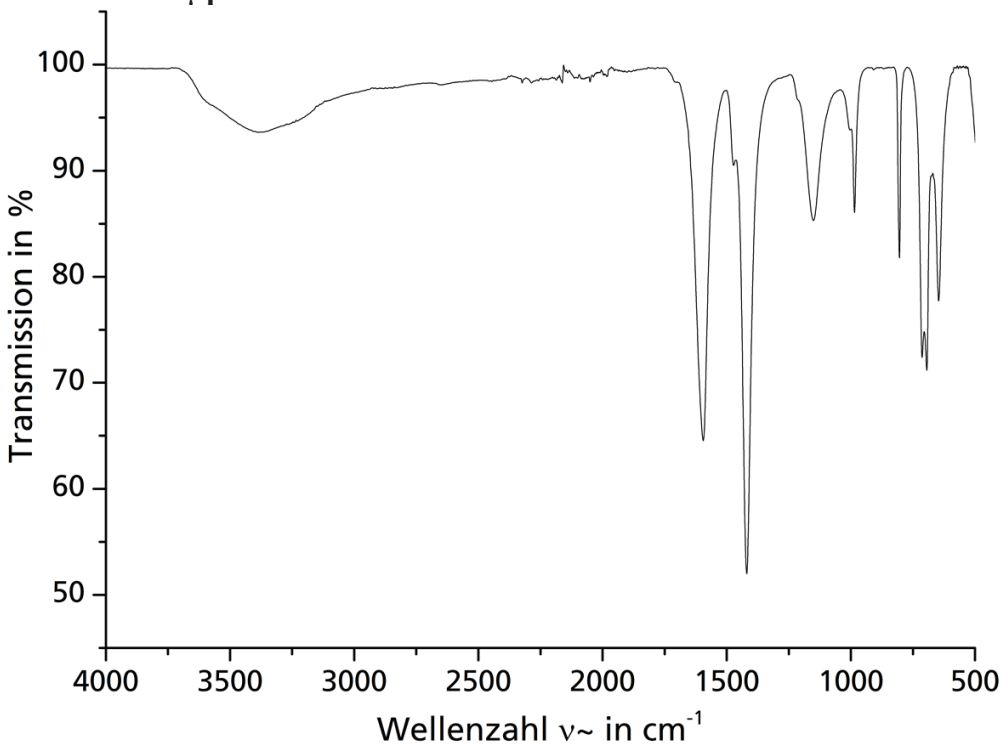


**Figure S4:** FT-IR spectrum (ATR) of bulk µp-AF.

**In-situ PXRD: Individual diffractograms**

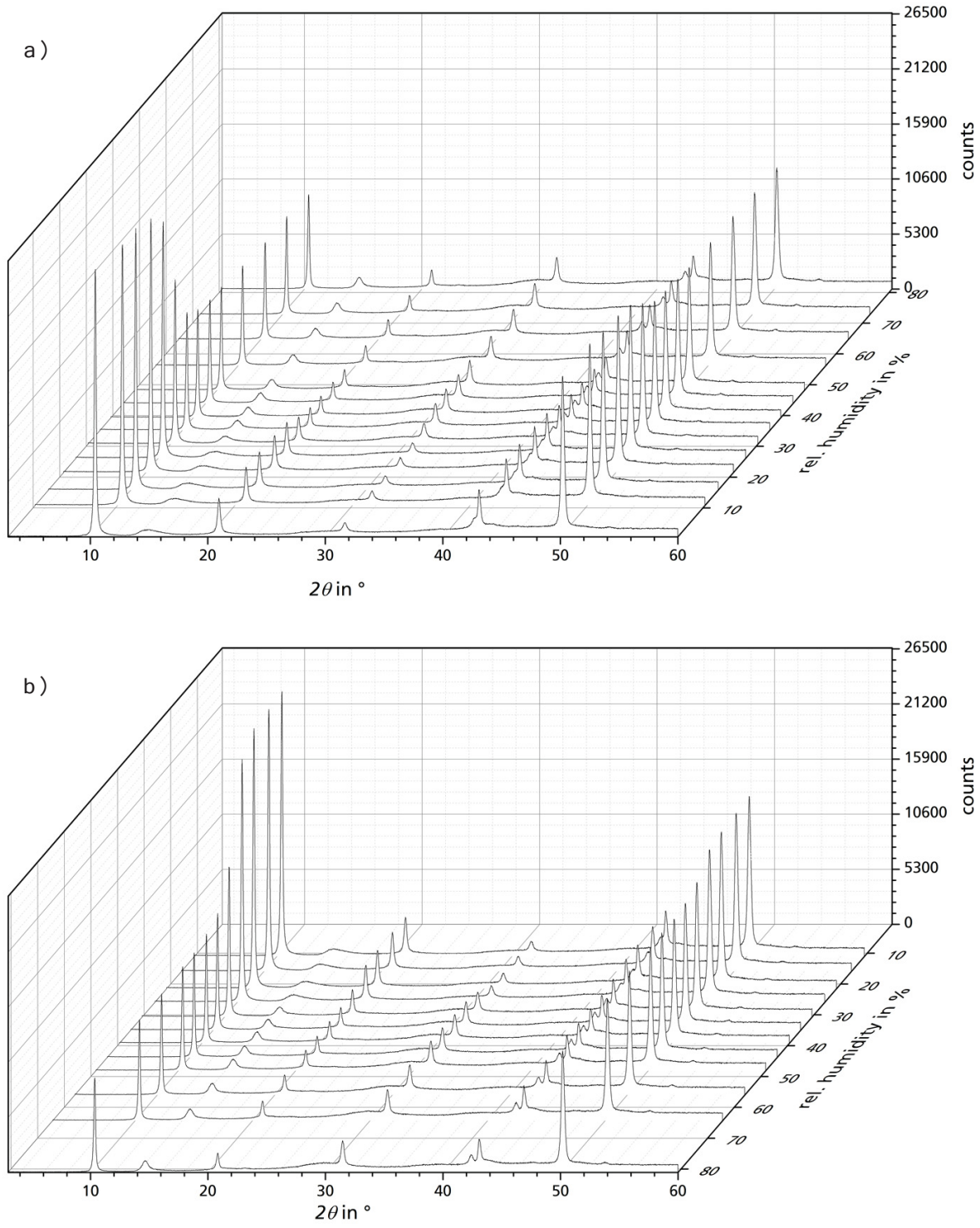


**Figure S5:** Waterfall plots of the individual diffractograms acquired during adsorption (a) and desorption (b). Cu-Kα radiation, 0.02°/step, 1.0 s/step.

**PXRD of top and bottom layer**

Part of the top layer was manually removed, ground in an agate mortar and examined by PXRD analysis, and the substrate with the remaining bottom layer was also examined by PXRD.

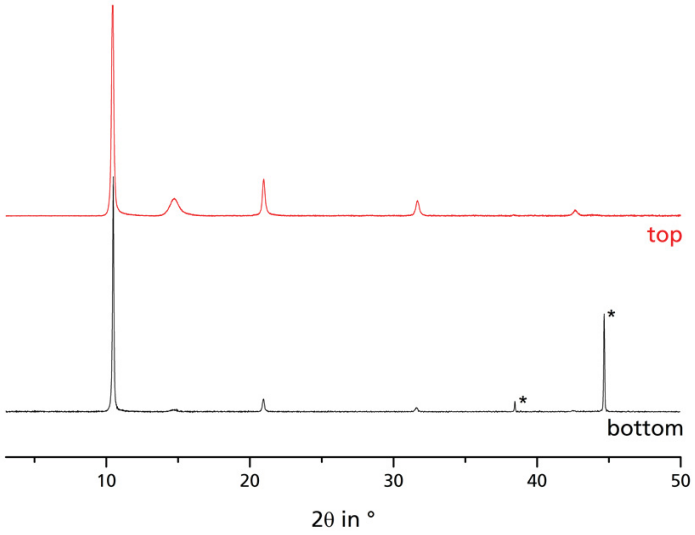


**Figure S6:** PXRD (Cu-Kα) of the top and bottom layers of the thermal gradient coating. Peaks marked with an asterisk (*) are due to the Al substrate under the bottom layer.

**Desorption isobar of the coated sheet**

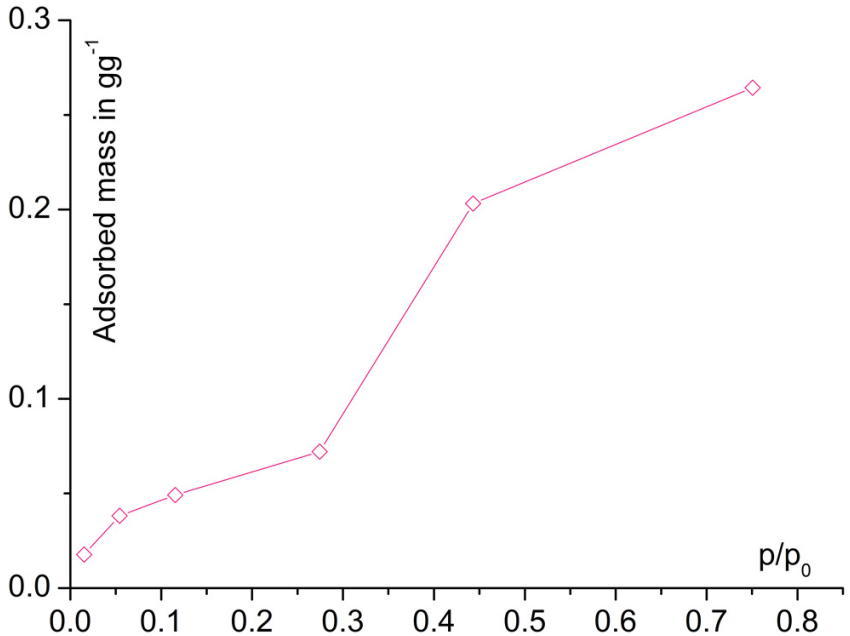


**Figure S7:** Representative desorption isobar of the µp-AF coated sheet of aluminum fumarate, after application of the protective lacquer and after completing 4500 ad-/desorption cycles with water vapor.

**Packing diagram of MIL-53**

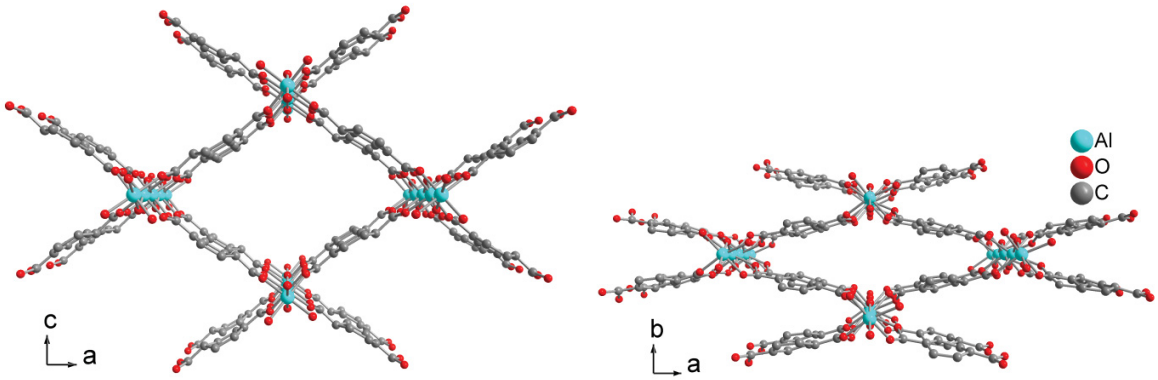


(a) MIL-53as = MIL-53ht, large pore; (b) MIL-53lt, narrow pore

**Figure S8:** Section of the packing diagram of [Al(BDC)(μ-OH)], MIL-53 with a flexible, 'breathing' network adapting to guest molecules. Each benzene-1,4-dicarboxylate ligand bridges between four Al atoms. The hydroxido-bridging occurs along the metal chains in the *b* direction. The channels can contain guest molecules in the as-synthesized structure (MIL-53as) (a, guest molecules not shown) or be empty after a thermal guest removal in the identical activated high-temperature, large pore structure MIL-53ht. Cooling down to room temperature with adsorption of water from air then transforms the structure into the low-temperature, narrow pore form MIL-53lt (b). Hydrogen atoms are not shown (CSD-Refcodes SABVOH and SABWAU).

## 3.2 Multicycle Water Vapour Stability of Microporous Breathing MOF Aluminium Isophthalate CAU-10-H

Dominik Fröhlich, Stefan K. Henninger and Christoph Janiak
*Dalton Trans.* **2014**, *43*, 15300-15304.
DOI: 10.1039/c4dt02264e

In the search for new water adsorption materials CAU-10-H came into focus. It shows an extremely steep s-shaped isotherm and has cheap raw products, being aluminium sulfate and isophthalic acid. After a multi temperature water adsorption study via isotherms, a PXRD humidity experiment was undertaken. It is observed that there is a reversible, breathing like, structural change, which takes part at ad-/desorption of the material. 100 *in situ* thermogravimetric ad-/desorption cycles as well as 700 *ex situ* experiments under open system conditions where performed. The material remained stable in both experiments.

Author´s share of work:

- planning and performing of all practical work,
- writing the manuscript and drawing of the figures expect fig. 1 (done by Mr. Janiak)
- editing of the manuscript regarding the reviewer´s comments.

Dalton Transactions



COMMUNICATION

View Article Online
View Journal | View Issue



Cite this: *Dalton Trans.*, 2014, **43**, 15300

Received 25th July 2014,
Accepted 23rd August 2014

DOI: 10.1039/c4dt02264e

www.rsc.org/dalton

# Multicycle water vapour stability of microporous breathing MOF aluminium isophthalate CAU-10-H

Dominik Fröhlich,[a,b] Stefan Kai Henninger*[a] and Christoph Janiak*[b]

**The hydrothermal stability of aluminium hydroxide isophthalate MOF CAU-10-H was proven, under humid multi-cycling conditions. Detailed *in situ* thermogravimetric measurements and *in situ* powder X-ray diffraction analysis during water ad-/desorption were used. A reversible structural change during adsorption was detected and thereby exemplified the robustness of breathing-like MOFs over 700 water vapour ad/desorption cycles. In combination with high water adsorption capacity, hydrophilic CAU-10-H is the first breathing-like MOF with a structural change which is a promising candidate for the use in heat transformation processes.**

Metal–organic frameworks (MOFs) receive continuous attention due to their high potential for various applications[1] based on their designable and high microporosity.[2] With this new generation of porous materials, significant improvements in gas storage,[3] separation processes,[4] or sorption based heat transformation applications[5] are possible. Thermally driven systems like adsorption chillers (AC), adsorption heat pumps (AHP) or solid desiccant cooling (SDC) are gaining more and more attention as a promising approach to energy efficient heating and cooling.[6,7] However, the relatively low stability under non-inert conditions, especially the often poor long-lasting water vapour stability of MOFs is a critical issue for numerous industrial processes. With regard to the use in ACs, AHP and SDC and their inherent sorption processes, the water vapour stability must be guaranteed over several thousand up to hundreds of thousand cycles. Although several MOFs are claimed as moisture stable, stability often originates from the hydrophobic character of the compound.[8,9] Typically, water stability tests consist of stirring the material in boiling water.[10] Unfortunately, stability tests with liquid water give no clear evidence regarding the use under water vapour conditions. Whereas under liquid conditions the pores are instantly completely filled with water which remains there during the whole process, this is not the case for cyclic water vapour sorption processes in which pores get filled and emptied many times. Furthermore, during water ad- and desorption processes a phase change from gaseous to the adsorbed phase accompanied by enthalpy exchange (heat of ad- and desorption) to and from the framework occurs. This leads to additional energetic stress to the coordinative metal–ligand bonds as the enthalpy of ad-/desorption is within the range of the activation energy for ligand displacement. In addition, pore stress due to guest–host hydrogen-bonding interactions accompanied by a possible breathing of the framework can occur.[7] Additionally, thermal stress is applied due to heating and cooling of the materials during the heat transformation process for typical temperatures in the range of 20 up to 150 °C. Thus, the evaluation of the multi-cycle hydrothermal stability is of great importance. At present, it is not clear if 'breathing' MOFs, which undergo a phase transition while ad-/desorption, are sufficiently stable to withstand a large number of gas sorption cycles in the presence of water vapour.

'Breathing' in MOFs refers to the motion of a flexible framework adapting to guest molecules, that is, a reversible swelling or shrinking with atomic displacements which can reach several Å.[11] The most famous 'breathing' MOF is MIL-53 which adapts a large pore and a narrow pore form, depending of the host–guest interactions.[11,12] Therefore, we subjected a hydrophilic breathing-like MOF to multi-cycling experiments with water vapour.

Recently, the development of a series of hydrophilic aluminium MOFs was reported by Stock *et al.*[13] which were tested for their hydrothermal stability by stirring in aqueous media at different pH values and solvothermal conditions. The microporous aluminium isophthalate CAU-10-H (*cf.* Fig. 1) shows a water adsorption isotherm of beneficial s-shape with the main loading lift occurring at a comparatively low relative pressure ($0.15 < p/p_0 < 0.25$) (*cf.* Fig. 2).[13] Especially for the use in heat pump applications, the adsorption at low relative water vapour pressure is of great interest.

[a]*Fraunhofer Institute for Solar Energy Systems ISE, Heidenhofstrasse 2, 79110 Freiburg, Germany. E-mail: Dominik.Froehlich@ise.fraunhofer.de, stefan.henninger@ise.fraunhofer.de; Fax: +49 761 4588913; Tel: +49 761 45885817*
[b]*Institut für Anorganische Chemie und Strukturchemie, Heinrich-Heine-Universität Düsseldorf, Universitätsstr. 1, 40225 Düsseldorf, Germany. E-mail: janiak@uni-duesseldorf.de; Tel: +49 211 8112286*

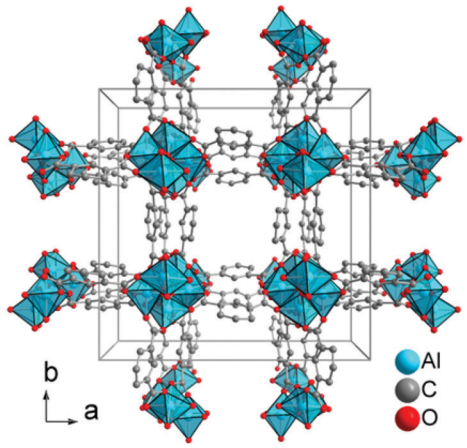


Fig. 1 Section of the packing diagram of CAU-10-H. The structure was redrawn with Diamond[14] using the CIF-file supplied with ref. 13.

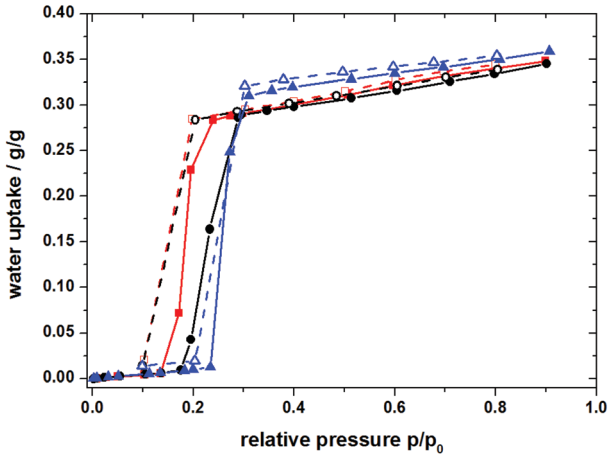


Fig. 2 Water ad-/desorption isotherm of CAU-10-H at different temperatures. 25 °C adsorption —■—, 25 °C desorption – □ –, 40 °C adsorption —●—, 40 °C desorption – o –, 60 °C adsorption —▲—, 60 °C desorption – △ –.

MOFs which were previously investigated for cyclic water sorption processes, such as Cr-MIL-101 showed high absolute water adsorption capacities albeit at a high $p/p_0$ (>0.7) because of their limited hydrophilicity.[5] With more hydrophilic compounds, the usable loading lift for AC or AHP applications should be shifted to lower $p/p_0$ (<0.4).

To evaluate the application oriented hydrothermal stability towards water vapour sorption the aluminium isophthalate CAU-10-H was synthesized according to the literature procedure by Stock *et al.*[13] In detail, 200 mg of 1,3-benzenedicarboxylic acid (1,3-$H_2$BDC, 1.20 mmol) dissolved in 1 mL of *N*,*N*-dimethylformamide (DMF) and 800 mg $Al_2(SO_4)_3{\cdot}18H_2O$ dissolved in 4 mL $H_2O$ were placed in a 37 mL Teflon-lined steel-autoclave for 12 h at 135 °C. After cooling to room temperature, the product was filtered and purified by washing three times *via* simultaneous sonication in 10 mL of water. The white solid was first dried for 24 h at 50 °C and afterwards activated for 24 h at 120 °C in vacuum.

Initial water adsorption isotherms where obtained on a *Quantachrome® Hydrosorb*, after vacuum degassing (120 °C/24 h) at 25 °C, 40 °C and 60 °C (*cf.* Fig. 2). Stability to water was tested by *in situ* X-ray analysis under different humidity conditions. Diffractograms were acquired on a Bruker D8 Advanced diffractometer, with Cu-Kα radiation, combined with an MRI TC-humidity chamber, coupled to a humidified nitrogen flow generated by an Ansyco® humidifier. A diffractogram was measured bidirectional at every 5% relative humidity (r.H.) between 0% r.H. and 90% r.H. at a constant temperature of 40 °C (*cf.* Fig. 3). The short time *in situ* thermogravimetric cycling test was performed on a *Setaram™ TGA-DSC-111* with a humidified argon gas flow at 40 °C (*cf.* Fig. 4). The sample temperature was varied between 40 °C and 140 °C, whereas the gas flow temperature and relative humidity was kept constant at 40 °C and 76.3% r.H. corresponding to a water vapour pressure of 5.6 kPa. A fixed-time procedure was used, where a full cycle consisted of a desorption step with heating from 40 °C to 140 °C with a heating rate of 20 K $min^{-1}$ followed by an isothermal step for 90 min for complete desorption and finally cooling down to 40 °C with 20 K $min^{-1}$ where water adsorption takes place. To keep the experiment at a reasonable time scale, equilibrium measurements are only performed for the first and the last cycle, holding the sample at 40 °C for 20 h. Hence the complete experiment with 100 cycles took about 15 days. To expand the hydrothermal stress experiments a newly developed apparatus for powders and granules was used. Two alternating air streams are passed through the

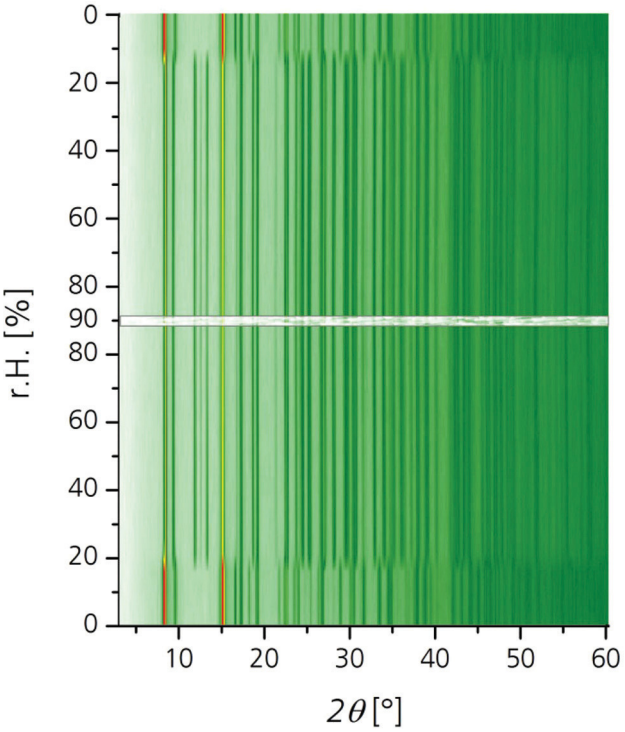


Fig. 3 Powder X-ray diffraction (PXRD) carpet plot showing a reversible structural change upon water ad- and desorption around 20% r.H. (red: high intensity, yellow: middle intensity, green: low intensity).

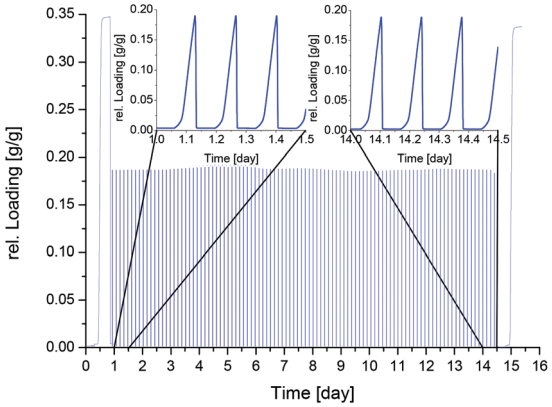


Fig. 4 Thermogravimetric cycling test of CAU-10-H at constant humidity.

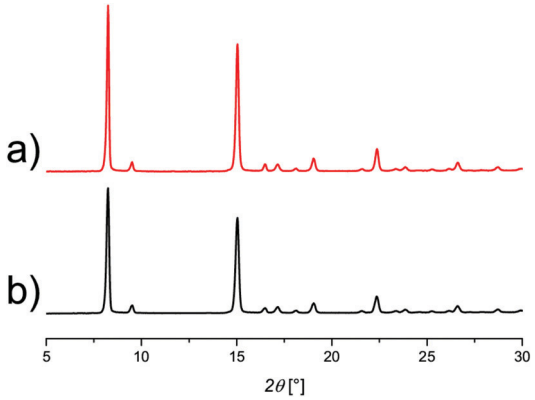


Fig. 5 Powder X-ray diffractogram of activated sample (a) and after 700 water sorption cycles (b), both recorded under dry conditions.

sample. Desorption is achieved by a hot air stream at 120 °C at 0% r.H., whereas adsorption is realized with a humidified air stream at 40 °C and 85% r.H. The streams are controlled by mass-flow-controllers and operated at 12 L $min^{-1}$. This corresponds to a total water impact of 0.4 g $H_2O$ $min^{-1}$ or a water excess of around six times compared to the maximum water uptake of the sample with a cycling time of 20 minutes and a sample amount of around 4 g. This allows faster cycles under open system conditions.

The performed hydrothermal stability tests do not exactly reproduce any particular cycle, but are a good profile of the general underlying temperatures and humidity in open and closed systems. Although, within closed cycle systems, addition stress occurs due to the vacuum or low vapour pressure, we assume that the main weakness is due to the coordinative metal–ligand bonds, which must withstand the repetitive hydrophilic attack of water. This is reflected by the chosen test conditions as a good first approximation.

The specific surface area of CAU-10-H is $S_{BET}$ = 525 $m^2$ $g^{-1}$ (635 $m^2$ $g^{-1}$ in ref. 13) with a pore volume of 0.27 $cm^3$ $g^{-1}$ (0.25 $cm^3$ $g^{-1}$ in ref. 13). The volumetric water sorption isotherms show a sigmoidal shape with a steep rise at a low relative pressure ($0.15 < p/p_0 < 0.25$) (Fig. 2). Adsorption and desorption isotherms were measured at 25 °C, 40 °C and 60 °C. Nearly no hysteresis was observed at 25 °C and 60 °C in our water sorption experiments. However, a slight difference between the adsorption and desorption path for the isotherm measured at 40 °C is visible, which can be directly related to the corresponding phase transition visible within the PXRD experiments.

The diffraction patterns of the *in situ* PXRD at 40 °C show a significant structural change at the step from 15 to 20% r.H. (*cf.* Fig. 3). At this point the positions and the ratio of the intensity of the major reflections change. This can be attributed to a structural change, akin to breathing effects with water as guest molecule similar to MIL-53.[15] The shifts in the reflections at about 20% r.H. correspond to the steep water uptake in the adsorption isotherm. As saturation is achieved at a relative pressure of 25% r.H. the structural change is complete. Upon desorption the structure changes back to the initial state at 20% r.H. This coincides excellent with the desorption path of the isotherm, where desorption starts at the same r.H. of $p/p_0$ = 0.2 (Fig. 2). This supports the assumption, that the structural change during ad- and desorption of water is a completely reversible process and structural integrity and crystallinity is preserved. Thus, a good hydrothermal stability for the use in cyclic water sorption applications can be expected.

Based on the good results of the *in situ* PXRD analysis, hydrothermal stability was evaluated by short time *in situ* thermogravimetric cycling tests in a humid atmosphere, as described above (*cf.* Fig. 4). In these experiments, long equilibration times are often needed, because the heat and mass transfer to the sample is limited by thermal coupling and geometry of the crucible. After 100 ad-/desorption cycles, there was no visible change in adsorption dynamics, also the dry weight remained constant. The adsorption capacity remains constant before and after cycling with an uptake at the thermodynamic equilibrium of 0.34 g $g^{-1}$ (Fig. 4 before day 1 and after day 15).

To expand the stability testing CAU-10-H was also exposed to a high excess of water, with a rapid humid gas flow as described above. After 700 ad-/desorption cycles the material was removed and analysed again by PXRD. As can be seen in Fig. 5 no irreversible structural change or degradation was observed.

## Conclusions

The MOF CAU-10-H exhibits a fully reversible structural change like a 'breathing' effect upon water ad- and desorption. The water adsorption characteristics of CAU-10-H show a high hydrophilicity with a steep and characteristic s-shaped adsorption isotherm already at a low relative humidity around $p/p_0$ = 0.2.

With regard to possible applications in sorptive heat transformation processes, hydrothermal stability was tested by short and long-term cycle tests. Even after 700 ad-/desorption cycles, no degradation of crystallinity was observed, despite considerable phase transition activity of the material.

 

It is important to note that the hydrothermal stability of CAU-10-H unlike other MOFs such as ZIF-8 is not achieved by hydrophobicity as CAU-10-H is a hydrophilic MOF.

In summary, the advantageous adsorption characteristics combined with an exceptional hydrothermal stability render the CAU-10-H material suitable for the use in thermally driven heat pumps, chillers or dehumidification applications. Although boundary conditions vary strongly with the specific application closed *versus* open AC/AHP, cooling *versus* heat pump or dehumidification (SDC), the initial multicycle water vapor stability has been proven by this contribution. Thus, corresponding tests which are closer to specific application conditions may now follow.

## Acknowledgements

Funding by the Fraunhofer Society under grant-# MAVO 824 704 and by the University of Düsseldorf through its strategic research fund (SFF) is gratefully acknowledged. We thank the State of Baden-Württemberg for funds of the "Baden-Württemberg Research Program Securing a Sustainable Living Environment (BWPLUS) under grant BWE 12001 which supported the stability investigations.

## Notes and references

1 C. Janiak, *Dalton Trans.*, 2003, 2781–2804; A. U. Czaja, N. Trukhan and U. Muller, *Chem. Soc. Rev.*, 2009, **38**, 1284–1293; M. J. Prakash and M. S. Lah, *Chem. Commun.*, 2009, 3326–3341; C. Janiak and J. K. Vieth, *New J. Chem.*, 2010, **34**, 2366–2388.

2 J. R. Long and O. M. Yaghi, *Chem. Soc. Rev.*, 2009, **38**, 1213–1214; K. Biradha, *New J. Chem.*, 2010, **34**, 2353–2354; H. C. Zhou, J. R. Long and O. M. Yaghi, *Chem. Rev.*, 2012, **112**, 673–674; S. Kitagawa and S. Natarajan, *Eur. J. Inorg. Chem.*, 2010, 3685–3685.

3 J. R. Li, R. J. Kuppler and H. C. Zhou, *Chem. Soc. Rev.*, 2009, **38**, 1477–1504; M. P. Suh, H. J. Park, T. K. Prasad and D. W. Lim, *Chem. Rev.*, 2012, **112**, 782–835; H. Wu, Q. Gong, D. H. Olson and J. Li, *Chem. Rev.*, 2012, **112**, 836–868; L. J. Murray, M. Dinca and J. R. Long, *Chem. Soc. Rev.*, 2009, **38**, 1294–1314.

4 J.-R. Li, Y. Ma, M. C. McCarthy, J. Sculley, J. Yu, H.-K. Jeong, P. B. Balbuena and H.-C. Zhou, *Coord. Chem. Rev.*, 2011, **255**, 1791–1823; G. Férey, C. Serre, T. Devic, G. Maurin, H. Jobic, P. L. Llewellyn, G. De Weireld, A. Vimont, M. Daturi and J. S. Chang, *Chem. Soc. Rev.*, 2011, **40**, 550–562; H. B. Tanh Jeazet, C. Staudt and C. Janiak, *Dalton Trans.*, 2012, **41**, 14003–14027; K. Hunger, N. Schmeling, H. B. Tanh Jeazet, C. Janiak, C. Staudt and K. Kleinermanns, *Membranes*, 2012, **2**, 727–763; H. B. Tanh Jeazet, C. Staudt and C. Janiak, *Chem. Commun.*, 2012, **48**, 2140–2142; J.-R. Li, J. Sculley and H.-C. Zhou, *Chem. Rev.*, 2012, **112**, 869–932; Z. Zhang, Y. Zhao, Q. Gong, Z. Li and J. Li, *Chem. Commun.*, 2013, **49**, 653–661; B. Zornoza, C. Tellez, J. Coronas, J. Gascon and F. Kapteijn, *Microporous Mesoporous Mater.*, 2013, **166**, 67–78; G. X. Dong, H. Y. Li and V. K. Chen, *J. Mater. Chem. A*, 2013, **1**, 4610–4630.

5 C. Janiak and S. K. Henninger, *Chimia*, 2013, **67**, 419–424; S. K. Henninger, F. Jeremias, H. Kummer and C. Janiak, *Eur. J. Inorg. Chem.*, 2012, 2625–2634; G. Akiyama, R. Matsuda, H. Sato, A. Hori, M. Takata and S. Kitagawa, *Microporous Mesoporous Mater.*, 2012, **157**, 89–93; G. Akiyama, R. Matsuda and S. Kitagawa, *Chem. Lett.*, 2010, **39**, 360–361; F. Jeremias, A. Khutia, S. K. Henninger and C. Janiak, *J. Mater. Chem.*, 2012, **22**, 10148–10151; P. Küsgens, M. Rose, I. Senkovska, H. Fröde, A. Henschel, S. Siegle and S. Kaskel, *Microporous Mesoporous Mater.*, 2009, **120**, 325–330; J. Ehrenmann, S. K. Henninger and C. Janiak, *Eur. J. Inorg. Chem.*, 2011, **2011**, 471–474; Y.-K. Seo, J. W. Yoon, J. S. Lee, Y. K. Hwang, C.-H. Jun, J.-S. Chang, S. Wuttke, P. Bazin, A. Vimont, M. Daturi, S. Bourrelly, P. L. Llewellyn, P. Horcajada, C. Serre and G. Férey, *Adv. Mater.*, 2012, **24**, 806–810; S. K. Henninger, H. A. Habib and C. Janiak, *J. Am. Chem. Soc.*, 2009, **131**, 2776–2777; A. Khutia, H. Urs Rammelberg, T. Schmidt, S. Henninger and C. Janiak, *Chem. Mater.*, 2013, **25**, 790–798; F. Jeremias, V. Lozan, S. Henninger and C. Janiak, *Dalton Trans.*, 2013, **42**, 15967–15973; F. Jeremias, D. Fröhlich, C. Janiak and S. K. Henninger, *RSC Adv.*, 2014, **4**, 24073–24082.

6 Y. I. Aristov, *J. Chem. Eng. Jpn.*, 2007, **40**, 1242–1251; Y. I. Aristov, *Appl. Therm. Eng.*, 2013, **50**, 1610–1618; Y. I. Aristov, *Int. J. Refrig.*, 2009, **32**, 675–686; L. G. Gordeeva, A. Freni, Y. I. Aristov and G. Restuccia, *Ind. Eng. Chem. Res.*, 2009, **48**, 6197–6202; Y. I. Aristov, *J. Chem. Eng. Jpn.*, 2007, **40**, 1242–1251; Y. I. Aristov, M. M. Tokarev, A. Freni, I. S. Glaznev and G. Restuccia, *Microporous Mesoporous Mater.*, 2006, **96**, 65–71; B. Dawoud and Y. Aristov, *Int. J. Heat Mass Transfer*, 2003, **46**, 273–281; Y. I. Aristov, G. Restuccia, G. Cacciola and V. N. Parmon, *Appl. Therm. Eng.*, 2002, **22**, 191–204; N. C. Srivastava and I. W. Eames, *Appl. Therm. Eng.*, 1998, **18**, 707–714; R. Wang and R. Oliveira, *Prog. Energy Combust. Sci.*, 2006, **32**, 424–458; Y. I. Aristov, *Appl. Therm. Eng.*, 2012, **42**, 18–24; B. B. Saha, A. Chakraborty, S. Koyama, K. Srinivasan, K. C. Ng, T. Kashiwagi and P. Dutta, *Appl. Phys. Lett.*, 2007, **91**, 111902; B. B. Saha, S. Jribi, S. Koyama and Yu. I. Aristov, *Int. J. Heat Mass Transfer*, 2009, **52**, 516–524; R. E. Critoph, Z. Tamainot-Telto and S. J. Metcalf, *Int. J. Refrig.*, 2009, **32**, 1212–1229; J. V. Veselovskaya, R. E. Critoph and R. N. Thorpe, *Appl. Therm. Eng.*, 2010, **30**, 1188–1192; K. Habib, B. B. Saha, A. Chakraborty, S. T. Oh and S. Koyama, *Appl. Therm. Eng.*, 2013, **50**, 1582–1589; A. A. Askalany, M. Salem, I. M. Ismael, A. H. H. Ali, M. G. Morsy and B. B. Saha, *Renewable Sustainable Energy Rev.*, 2013, **19**, 565–572.

7 F. Jeremias, D. Fröhlich, C. Janiak and S. Henninger, *New J. Chem.*, 2014, **4**, 24073–24082.

8 J.-P. Zhang, A.-X. Zhu, R.-B. Lin, X.-L. Qi and X.-M. Chen, *Adv. Mater.*, 2011, **23**, 1268–1271.

9 J. J. Low, A. I. Benin, P. Jakubczak, J. F. Abrahamian, S. A. Faheem and R. R. Willis, *J. Am. Chem. Soc.*, 2009, **131**, 15834–15842.
10 C. Heering, I. Boldog, V. Vasylyeva, J. Sanchiz and C. Janiak, *CrystEngComm*, 2013, **15**, 9757–9768.
11 G. Feréy and C. Serre, *Chem. Soc. Rev.*, 2009, **38**, 1380–1399; M. Alhamami, H. Doan and C.-H. Cheng, *Materials*, 2014, **7**, 3198–3250.
12 C. Serre, F. Millange, C. Thouvenot, M. Noguès, G. Marsolier, D. Louër and G. Feréy, *J. Am. Chem. Soc.*, 2002, **124**, 13519–13526.
13 H. Reinsch, M. A. van der Veen, B. Gil, B. Marszalek, T. Verbiest, D. de Vos and N. Stock, *Chem. Mater.*, 2013, **25**, 17–26; H. Reinsch, S. Waitschat and N. Stock, *Dalton Trans.*, 2013, **42**, 4840–4847.
14 K. Brandenburg, *Diamond (Version 3.2), crystal and molecular structure visualization, Crystal Impact*, K. Brandenburg & H. Putz Gbr, Bonn, Germany, 2007–2012.
15 T. Loiseau, C. Serre, C. Huguenard, G. Fink, F. Taulelle, M. Henry, T. Bataille and G. Feréy, *Chem. – Eur. J.*, 2004, **10**, 1373–1382.

## 3.3 Water Adsorption Behaviour of CAU-10-H: a Thorough Investigation of its Structure–Property Relationships

Dominik Fröhlich, Evangelia Pantatosaki, Panagiotis D. Kolokathis, Karen Markey, Helge Reinsch, Max Baumgartner, Monique A. van der Veen, Dirk E. De Vos, Norbert Stock, George K. Papadopoulos, Stefan K. Henninger and Christoph Janiak

*J. Mater. Chem. A*, **2016**, *4*, 11859-11869.
DOI: 10.1039/c6ta01757f

Aluminium isophthalate CAU-10-H exhibits water adsorption characteristics which make it a promising adsorbent for application in heat-exchange processes. Herein, we prepared a stable coating of this MOF and evaluated its long-term stability under closed-cycle conditions for 10 000 water adsorption and desorption cycles, which are typical lifetimes for adsorption heat storage (AHS) applications. No degradation of the adsorption capacity could be observed which makes CAU-10-H the most stable MOF under these humid cycling conditions reported until now. Moreover, thermophysical properties like thermal conductivity and heat of adsorption were directly measured. In order to identify the structural features associated with the adsorption behavior, the structural differences between the dry and the water loaded CAU-10-H were studied by Rietveld refinements and second harmonic generation (SHG) microscopy. The observed transition of space group symmetry from $I4_1$ to $I4_1/amd$ between the humid and dry forms is induced by the adsorption/desorption of water into/out of the MOF channels. This originates from a torsional motion around the C–C bond between the carboxylate groups and the aromatic ring in half of the linker molecules. These observations are in excellent agreement with molecular dynamics simulations which confirm the energetic benefit of this transition.

*Author's share of work:*

- idea,
- organization of joint work from all groups,
- stability tests,
- design and development of the *in-situ* PXRD setup,
- writing of the stability parts of manuscript and putting parts from coauthors together,
- implementation of the reviewers' comments.

Journal of Materials Chemistry A

PAPER

View Article Online
View Journal | View Issue



Cite this: J. Mater. Chem. A, 2016, 4, 11859

# Water adsorption behaviour of CAU-10-H: a thorough investigation of its structure–property relationships†

Dominik Fröhlich,[ab] Evangelia Pantatosaki,[c] Panagiotis D. Kolokathis,[c] Karen Markey,[d] Helge Reinsch,[e] Max Baumgartner,[a] Monique A. van der Veen,[f] Dirk E. De Vos,[d] Norbert Stock,[e] George K. Papadopoulos,[cg] Stefan K. Henninger*[a] and Christoph Janiak*[b]

Received 27th February 2016
Accepted 27th June 2016

DOI: 10.1039/c6ta01757f

www.rsc.org/MaterialsA

Aluminium isophthalate CAU-10-H [Al(OH)(benzene-1,3-dicarboxylate)]·$n$H$_2$O exhibits water adsorption characteristics which make it a promising adsorbent for application in heat-exchange processes. Herein we prepared a stable coating of this MOF and evaluated its long-term stability under closed-cycle conditions for 10 000 water adsorption and desorption cycles, which are typical lifetimes for adsorption heat storage (AHS) applications. No degradation of the adsorption capacity could be observed which makes CAU-10-H the most stable MOF under these humid cycling conditions reported until now. Moreover, thermophysical properties like thermal conductivity and heat of adsorption were directly measured. In order to identify the structural features associated with the adsorption behaviour, the structural differences between the dry and the water loaded CAU-10-H were studied by Rietveld refinements and second harmonic generation (SHG) microscopy. The observed transition of space group symmetry from $I4_1$ to $I4_1/amd$ between the humid and dry forms is induced by the adsorption/desorption of water into/out of the MOF channels. This originates from a torsional motion around the C–C bond between the carboxylate groups and the aromatic ring in half of the linker molecules. These observations are in excellent agreement with molecular dynamics simulations which confirm the energetic benefit of this transition.

## Introduction

Metal–organic frameworks (MOFs) have been extensively studied with regard to various potential applications.[1] Due to their high porosity, they hold promise as storage and release adsorbents.[2] Their variable composition and tunable surface chemistry[3] make these solids interesting materials for catalysis.[4] MOFs have as well been incorporated into sensing devices.[5] A possible application which came into focus, because of the promising application, is the use of MOFs as adsorbents in adsorption heat transformation, *i.e.*, adsorption heat pumps (AHPs) and adsorption chillers (ACs).[6–8]

For a good performance of AHPs or ACs, the (water) vapor uptake should occur in a pressure range between 0.1 and 0.4 $p/p_0$. The adsorption capacity should be higher than 0.2 g g$^{-1}$ with a steep adsorption step and a small hysteresis for not losing sensible heat. The regeneration temperature should not be higher than 120 °C and cycle stability under these adsorption/desorption conditions should guarantee a material lifetime of several years.

Compared to classical compression chillers, adsorption systems are thermally driven. By the adsorption into a porous material the working fluid is removed from the gas phase and subsequently evaporation from the liquid reservoir takes place. Hence, in analogy to an electrically driven compressor used in refrigerators it can be seen as a "thermal compressor".[9–11] In order to remove the working fluid from the porous material, heat is used as driving energy. Compared to absorption systems

[a]Fraunhofer Institute for Solar Energy Systems ISE, Heidenhofstrasse 2, 79110 Freiburg, Germany. E-mail: stefan.henninger@ise.fraunhofer.de; Fax: +49 761 4588913; Tel: +49 761 45882117
[b]Institut für Anorganische Chemie und Strukturchemie, Heinrich-Heine-Universität Düsseldorf, Universitätsstr. 1, 40225 Düsseldorf, Germany. E-mail: janiak@uni-duesseldorf.de; Tel: +49 211 8112286
[c]School of Chemical Engineering, National Technical University of Athens, 9 Heroon Polytechniou Street, 157 80 Athens, Greece
[d]KU Leuven Centre for Surface Chemistry and Catalysis, University of Leuven, Celestijnenlaan 200f, 3001 Leuven, Belgium
[e]Institute of Inorganic Chemistry, Christian-Albrechts-University Kiel, Max-Eyth-Str. 2, D-24118 Kiel, Germany
[f]Catalysis Engineering, Department of Chemical Engineering, Delft University of Technology, van der Maasweg 9, 2629Hz Delft, The Netherlands
[g]Institute for Medical Engineering and Science, Massachusetts Institute of Technology, Cambridge, Massachusetts 02139, USA

† Electronic supplementary information (ESI) available: CAU-10-H synthesis and characterization details, Rietveld refinement, modelling details and CIF files reported in this paper. CCDC 1454066 and 1454067. For ESI and crystallographic data in CIF or other electronic format see DOI: 10.1039/c6ta01757f

(*e.g.* salt solutions), low temperature heat can be used in adsorption systems.[12] By the use of recently developed MOFs as porous materials, driving temperatures below 75 °C seem to be manageable, thus allowing access to lower energy driving sources. However, while several compounds were investigated regarding their water vapour sorption characteristics,[8,13–20] it was also observed that only very few materials withstand the harsh conditions imposed during repeated water adsorption and desorption cycles, which is a prerequisite for their applicability.[7,20] Long-term multi-cycle water stability is mainly observed for MOFs of the MIL-series.[14–19,21] For example, aluminium fumarate can be subjected to 4500 adsorption/desorption cycles without decomposition.[22] Another MOF showing promising stability is the aluminium isophthalate CAU-10-H (Fig. 1); it shows a small reversible structural change during adsorption and no loss in crystallinity or porosity after 700 water vapour adsorption/desorption cycles.[23] Remarkably, both materials are based on infinite chains of $AlO_6$-octahedra and exhibit square shaped one-dimensional channels.[24,25] The underlying mechanism and the structure dependence caused by the adsorption of guest molecules are not yet fully understood. With regard to the intended application in a sorption chiller or a heat pump, further investigations need to be conducted, namely shaping and further stability tests under a closed water vapour atmosphere, accompanied by evaluation of the thermophysical properties.

Thus, herein we report a detailed analysis of this promising MOF including heat capacity ($c_p$), thermal conductivity and long-term stability measurements, as well as further structural analysis by means of *in situ* powder X-ray diffractometry (PXRD) during water adsorption studies, Rietveld refinement and second harmonic generation microscopy. Experimental investigations are complemented by molecular simulations in order to understand the structural transition and structure–property relationships.

Furthermore, we present an appropriate binder based coating of CAU-10-H on a metallic layer, which has been exposed to an application-oriented multi-cycle water adsorption/desorption test of 10 000 cycles, which is to the best of our knowledge currently the highest water vapour sorption cycle number a MOF has successfully withstood.

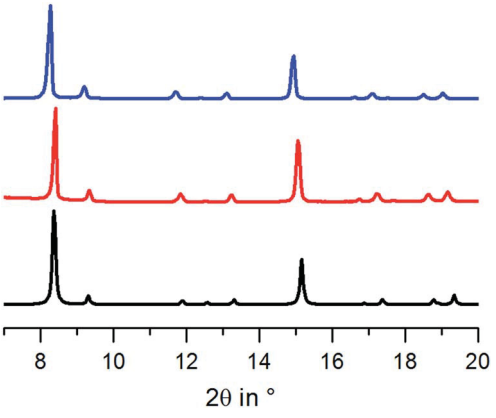


Fig. 1 PXRD patterns of CAU-10-H after coating (red), after 10 000 cycles (blue). For comparison, the simulated PXRD pattern of the hydrated structure is shown (black).

# Experimental

## Sample preparation

CAU-10-H was synthesized and activated according to an adapted literature procedure[24] using $Al_2(SO_4)_3 \cdot 18H_2O$ as the metal source (Bernd Kraft) and isophthalic acid (Aldrich Chemistry). In contrast to the standard procedure, a round bottom glass flask has been used to prepare larger amounts of CAU-10-H (see ESI† for details).

Coatings were prepared following a previously published procedure,[26] slightly modified and adapted for use with CAU-10-H. 2.085 g of dehumidified CAU-10-H were mixed with 1.408 g of Silikophen® P 50/300 and 6.437 g of xylene. The resulting dispersion was stirred and homogenised in an ultra-sonic bath for 20 min. Subsequently, the dispersion was manually applied with a pipette on 50 × 50 $mm^2$ aluminium plates (AlMg3 alloy). After drying at RT, the coated plates were heated to 200 °C and cured at this temperature for 2 h. The achieved coating has a mass of 0.253 g with a thickness of approximately 300 μm (see Fig. S1 and S2 in the ESI† for SEM images of the coating).

## Characterization

**Pore volume and surface area.** The pore volume and surface area were obtained by $N_2$ adsorption isotherm analysis performed on a Quantachrome® Nova at 77 K, after vacuum degassing (120 °C/24 h).

**Powder X-ray diffraction (PXRD) analysis.** Powder X-ray diffraction (PXRD) analysis was performed on a Bruker D8 Advance diffractometer with DaVinci™ design, using Cu-Kα radiation from a Cu anode tube at 40 kV/40 mA with a Ni filter in Bragg Brentano geometry. An MRI TC-humidity chamber, coupled to a humidified nitrogen flow generated by an Ansyco® humidifier, was used for controlled humidity and *in situ* PXRD cycle experiments. An XYZ Newport stage was used for coated sheets.

***In situ* PXRD.** *In situ* PXRD cycle experiments were done with the sample held at 40 °C and cycled between a wet (40% r.H.) and dry (0% r.H.) nitrogen flow. After every cycle, the powder diffractogram was recorded.

**High-resolution PXRD data for Rietveld refinement.** High-resolution PXRD data for Rietveld refinement were acquired from samples which were loaded into capillaries and sealed either under ambient conditions (hydrated form) or sealed after evacuation at 0.1 mbar and heating to 200 °C (dry form). The data were collected using a STOE Stadi-P diffractometer equipped with a Mythen detector using monochromated Cu Kα1 radiation. The software used for indexing and refinements was TOPAS.[27] The structural data for this paper have been deposited with the Cambridge Crystallographic Data Center (CCDC-numbers 1454066 and 1454067).

***In situ* second harmonic generation (SHG) microscopy.** *In situ* second harmonic generation (SHG) microscopy was used to study structural phase transitions upon desorption and

 

adsorption. A customized inverted wide-field Olympus microscope which is described elsewhere[28,29] coupled to a femtosecond pulsed InSight DeepSee laser operating at a wavelength of 800 nm was used. For the *in situ* adsorption and desorption, a RH95 Linkam Humidity controller was mounted on the microscope.

**Water adsorption characteristics.** Water adsorption characteristics were measured as isotherms and isobars using a custom-built Rubotherm thermobalance with enhanced measuring load and cell geometry to allow measurements on coated samples (for details see ref. 26).

**Hydrothermal cycle stability.** Hydrothermal cycle stability was investigated by short cycle experiments under isobaric conditions (5.6 kPa $H_2O$ vapour) between 140 °C and 40 °C within the Rubotherm thermobalance. This allowed the *in situ* detection of possible initial degradation during the first cycles. Advanced long term hydrothermal stability to 10 000 full cycles was acquired within a custom-made closed cycle apparatus, consisting of a vacuum chamber under a pure water vapour atmosphere of 1.2 kPa. The samples are fixed on a heat exchanger plate connected to an alternating flow of hot and cold water in order to enable heating at 120 °C and cooling at 20 °C within 90 seconds.

Prior to and after the treatment, the water uptake of the samples at 40 °C and 5.6 kPa was measured within the thermobalance to identify possible loading degradation.

### Computer modelling

The unit cell of CAU-10-H was calculated by means of the PXRD data to obtain the fractional coordinates and their occupancy probabilities. Then, implementation of the symmetry operations of the $I4_1/amd$ crystallographic space group led to the final unit cell atomic coordinates. Molecular dynamics (MD) simulations were conducted on both the dehydrated and water-loaded CAU-10-H up to 20 ns at 300 K in the isothermal constant-stress ensemble (*N*, **S**, *T*) to account for the sorbent cell's volume and shape fluctuations according to a combination of the isenthalpic constant-stress method of Parrinello and Rahman,[30] and the thermostat algorithm of Nosé.[31] However, results based on the Andersen conventional isobaric algorithm,[32] wherein only the pressure tensor is taken into account, namely crystal transformations remain inhibited, are also presented in the ESI† for comparison. The calculated structure was modelled as a fully flexible framework; the parameters for the potential functions are detailed in the ESI.† Furthermore, regarding the particular mobility of the ligands of the material, two model options were tested: a stiff version by imposing torsional potentials on them, and another one enabling quasi-free rotation around the C–C bonds of the linker carboxylate groups (Fig. S5 in ESI†). However, only the latter version predicts the structural transition of the CAU cell upon water adsorption; also, it captures the linker dynamics upon water adsorption with respect to the second harmonic generation (SHG) microscopy experiments of this work. Although the scope of the modelling work of this article is not the derivation of a strict force field for this sorbent, one could conclude that a realistic representation for its linkers definitely opts for flexible states. The guest water interactions were described by the SPC/E model.[33] The water model was kept rigid by constraining the two bond lengths and the angle between them by means of the SHAKE[34] algorithm.

## Results

### Water uptake and stability characteristics under closed system conditions

Coating preparation was successful as the crystal structure of CAU-10-H is preserved, as proven by PXRD measurements (Fig. 1). Furthermore, the sample showed good accessibility for water, as the maximum water uptake of the coated sample was determined at 0.26 g $g^{-1}$ (g water per g of coating (CAU-10-H + binder)) at $p/p_0 = 0.76$ (Fig. 2).

This corresponds approximately to 76–79% of the maximum pure powder capacity (*i.e.* 0.33–0.34 g $g^{-1}$) at maximal loading. This is in good agreement with the MOF content of approximately 76 wt% within the coating calculated from the initial composition. Thus, it can be concluded that the coating formulation does not impede the accessibility of the micropores.

With regard to hydrothermal stability, cycle experiments were first performed in the thermobalance, as strong degradation of MOFs typically occurs during the initial cycles.[22] Thus, the coated samples were tested under closed-system conditions.

A very small degradation is visible in these 7 cycles, as shown in Fig. 3. The maximal water sorption capacity in the beginning is 0.264 g $g^{-1}$ whereas after 7 cycles 0.261 g $g^{-1}$ is observed. The total capacity loss amounts to 0.003 g $g^{-1}$, 2.3%. In addition, the dry mass decreases from 0.253 g to 0.252 g which leads to a very small loss of 0.001 g or 0.4%. This can be attributed to a small rearrangement in the crystal or occupation of active sites by water which is then bound too strong to free these sites under cycle conditions. Also the loss in dry mass could be due to the sublimation of unreacted linkers under cycle conditions. This effect is stabilized after some cycles.

Following these very promising initial results, the sample passed 10 000 water adsorption/desorption cycles in the

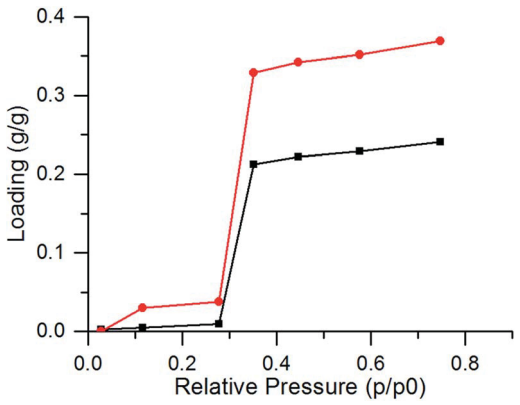


Fig. 2 Water desorption isobar at 5.6 $kPa_{H_2O}$ of CAU-10-H powder (red) and coated AlMg3-plate (black).

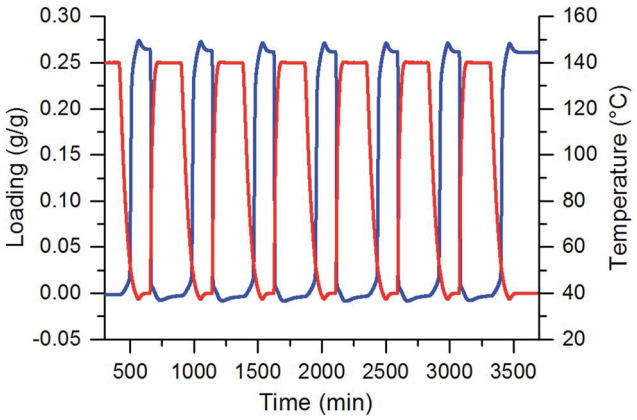


Fig. 3 *In situ* hydrothermal cycles of the CAU-10-H coatings under a pure water vapour atmosphere at 5.6 kPa. The sample was thermally cycled between 40 °C and 140 °C. Loading in blue and temperature in red.

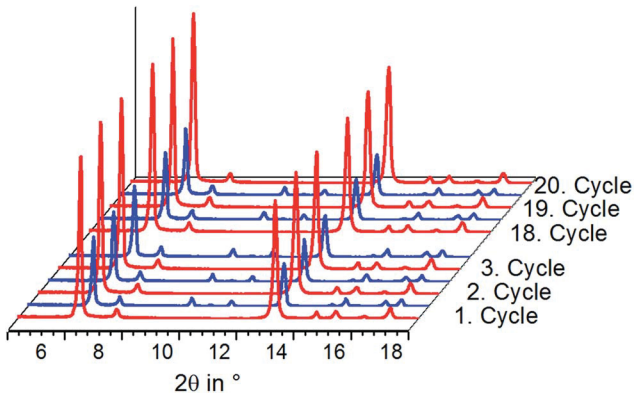


Fig. 5 20 adsorption (blue)/desorption (red) cycles of CAU-10-H with *in situ* XRD observation. For clarity, only the first 3 cycles and last 3 cycles are shown.

custom-made cycle test rig. In contrast to the thermobalance, this setup does not allow an *in situ* determination of the water uptake. Thus, the uptake capacity was measured after 1000, 5000 and 10 000 cycles within the thermobalance. No loss of uptake capacity, within the measurement error, was observed (see Fig. 4).

In addition, the powder X-ray diffractogram before and after 10 000 adsorption/desorption cycles showed that all reflections are preserved and no change in crystallinity is visible (Fig. 2).

### *In situ* PXRD structural stability investigation upon water adsorption/desorption

With regard to the known structural change upon adsorption of guest molecules, especially water, adsorption/desorption experiments were conducted under *in situ* PXRD observation (Fig. 5). After 20 cycles, there are no changes in the PXRD pattern; the reflections of the material show the same intensity as those of the fresh powder. In addition, no increase of amorphous background is visible.

These results are in line with the cycling results by thermogravimetry leading to the conclusion that there is no degradation of the material.

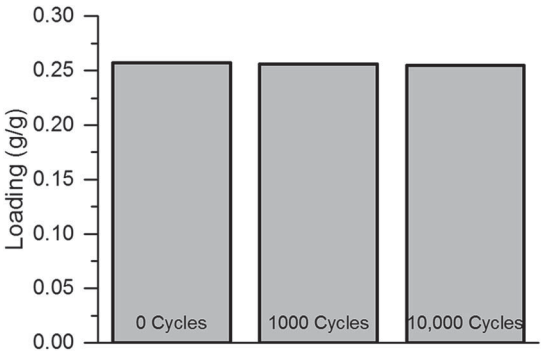


Fig. 4 Comparison of the uptake capacity prior to cycle treatment, after 1000 and after 10 000 adsorption/desorption cycles.

### Rietveld refinements of the wet and dry structures

The *in situ* measurements at different relative humidity values unambiguously prove a phase transition between the known non-centrosymmetric form of CAU-10-H and a not yet reported dry, centrosymmetric conformation. Although the structure of hydrated CAU-10-H has been reported previously, the structure was revaluated since better PXRD data could be obtained. In the light of these results, high-resolution PXRD data were analyzed and crystal structures of the dry and wet forms were obtained by Rietveld refinement, taking also into account the results of SHG-microscopy (see below). For details on the experimental procedure, please see ESI.†

The most relevant parameters of the refinement are summarized in Table 1. The asymmetric units, relevant bond distances and the final Rietveld plots are given in the ESI.†

### *In situ* SHG structural transition observation upon water desorption and adsorption

Using Second Harmonic Generation (SHG) microscopy, non-centrosymmetric to centrosymmetric transitions can be observed, as only non-centrosymmetric crystals generate an SHG signal, whereas centrosymmetric structures cannot.[35] To study the effect of guest water molecules on the crystal structure, the SHG intensity of CAU-10-H was recorded *in situ* upon variation of relative humidity. Fig. 6 shows clearly that a phase transition occurs upon adsorption and desorption of water. The

Table 1 Final parameters of the Rietveld refinements

| CAU-10-H | -$H_2O$ | -dry |
|---|---|---|
| Space group | $I4_1$ | $I4_1/amd$ |
| $a = b$ [Å] | 21.2928(4) | 21.5214(7) |
| $c$ [Å] | 10.7305(3) | 10.3218(4) |
| $V$ [Å$^3$] | 4865.0(2) | 4780.7(4) |
| $R_{WP}$/% | 6.8 | 4.3 |
| $R_{Bragg}$/% | 3.2 | 0.6 |
| GoF | 1.54 | 1.03 |
| Wavelength | Cu K$\alpha_1$ | Cu K$\alpha_1$ |

centrosymmetric to non-centrosymmetric phase transition sets in at 20% relative humidity. This value corresponds to the water adsorption starting point on the adsorption isotherm, as reported by Reinsch *et al.*[24] Therefore, it can be concluded that adsorbed water molecules cause the structure to be organized non-centrosymmetrically, whereas the absence of $H_2O$ leaves the structure centrosymmetric.

## Structure description

The framework structure of CAU-10-H is formed by the interconnection of fourfold helical chains of *cis*-corner sharing $\{AlO_6\}$ octahedra by isophthalate linker molecules (1,3-benzenedicarboxylate). Four oxygen atoms in each polyhedron originate from four different coordinating carboxylate groups while two *cis* standing hydroxide ions induce the helical shape of the inorganic building unit. The organic moieties connect each chain to four adjacent inorganic units and thus square shaped one dimensional channels are formed (Fig. 7).

Adjacent chains in the framework exhibit different orientations; thus, half the helices are $4_1$ helices while the other half represents $4_3$ helices. Due to the high symmetry of the structure, all linker molecules are arranged in an identical fashion. They are arranged pairwise with centroid–centroid distances between the aromatic rings of 3.62(2) Å, indicating $\pi$-stacking interactions between the aromatic moieties. The resulting minimum diagonal distance of the channels based on the vdW-radii of the framework is thus approximately 3.6 Å.

Upon dehydration/rehydration, no bonds are broken and the observed phase transition can be attributed to conformational changes which result from coordination of water molecules. The differences in the crystal structures and, thus, in space group symmetry are due to slight rotations around the C–C bond of the carboxylate groups. These torsions are much stronger in the hydrated form compared to the dry form. Although the accuracy of the refined structure is limited due to the absence of single crystal diffraction data, this can be well observed in the refined crystal structures. In the structure of CAU-10-H, only half a linker molecule is present in the asymmetric unit and the averaged value for the O–C–C–C torsion angle is 13.5°. In the crystal structure of CAU-10-H-$H_2O$ (Fig. 8), two complete linker molecules are present in the asymmetric unit. For one of the molecules, this angular tension is apparently relaxed and O–C–C–C torsion angles with average values of 14.3° and 2.5° are observed. The other linker molecule is more stressed than in the dry state and the O–C–C–C angles amount up to 33.5° and 33.8°. These latter linker molecules also point more strongly into the framework channels narrowing their minimum distance from 3.6 Å to only 2.4 Å. This is also accompanied by the slight tilting of the inorganic building units around their symmetry axis.

This structural change is induced by the adsorption of water molecules. These are found close to the bridging OH-groups (shortest O–O distance 2.80(2) Å and 2.94(2) Å) but also close to coordinating carboxylate oxygen atoms (2.85(2) Å and 2.95(2) Å).

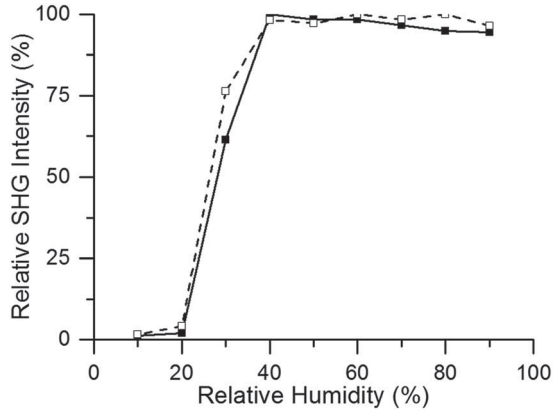


Fig. 6 *In situ* SHG intensity measurement at 26 °C of CAU-10-H with increasing relative humidity of $H_2O$ (adsorption branch, solid line) and subsequent decreasing relative humidity of $H_2O$ (desorption branch, dashed line).

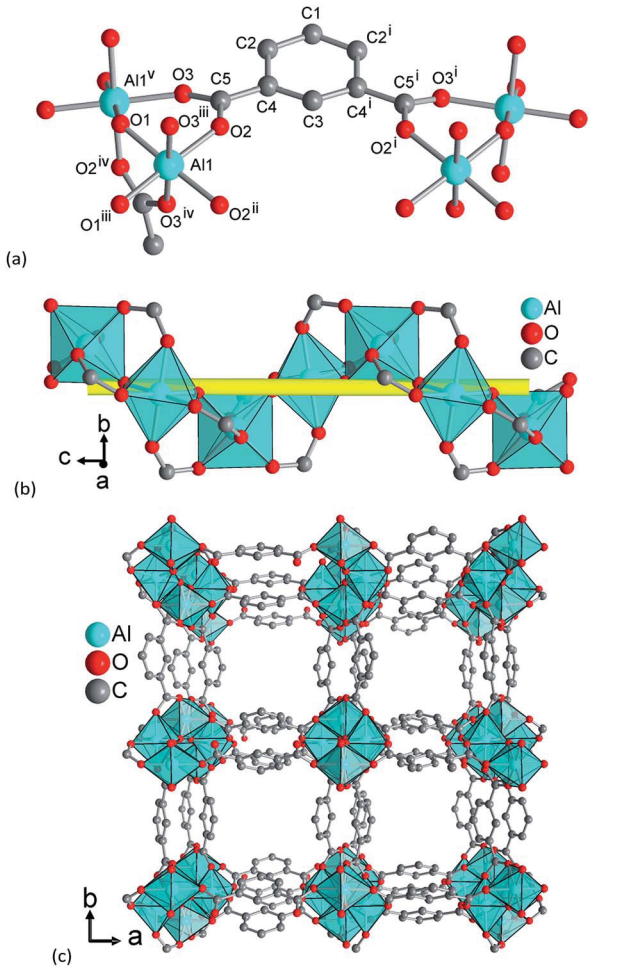


Fig. 7 Structural elements in CAU-10-H dry: (a) extended asymmetric unit with full Al coordination spheres and full ligand bridging mode. Symmetry transformations (i) = $1-x, y, z$; (ii) = $x, -y, -z$; (iii) = $0.25+y, 0.25-x, -0.25+z$; (iv) = $0.25+y, -0.25+x, 0.25-z$; (v) = $0.25y, -0.25+x, 0.25+z$. (b) The inorganic building unit, a fourfold helical chain of *cis* vertex-sharing $AlO_6$ polyhedra winding around the fourfold axis (yellow line). (c) The 3D framework structure exhibiting square shaped one dimensional channels.

Several other close proximities can be observed between the guest molecules inside the pores (for details see ESI†). These structural changes affect the unit cell parameters and upon hydration the unit cell volume is increased by ≈1.7% due to an anisotropic expansion. While the *a* and *b* parameters decrease upon hydration from 21.52 to 21.29 Å, the *c* axis is expanded from 10.32 to 10.73 Å.

## Thermophysical characteristics

**Heat capacity and conductivity of the coated material.** The heat capacity and conductivity of CAU-10-H have been measured for the powder as pressed pellets and for the coated sample (Fig. 9).

The heat capacity for the pure powder is in the range of 1.3 J $g^{-1}$ $K^{-1}$ at RT up to 1.7 J $g^{-1}$ $K^{-1}$ at 150 °C, which is higher compared to the reported literature data for MOFs.[22,36,37] The thermal conductivity has been determined to be 0.08 W $m^{-1}$ $K^{-1}$ and the diffusivity to be 0.07 $mm^2$ $s^{-1}$ showing the characteristics of a porous material. These values are lower for the coated sample, with a heat capacity of 1.25 J $g^{-1}$ $K^{-1}$, a thermal conductivity of 0.03 W $m^{-1}$ $K^{-1}$ and a diffusivity of 0.05 $mm^2$ $s^{-1}$. This is probably because the binder lowers the thermophysical characteristics of the coated material compared to the pure material.

**Heat of adsorption.** The isosteric heat $\Delta H$ was calculated from the adsorption isotherms reported by Fröhlich *et al.*,[23] using the Clausius–Clapeyron equation,[38]

$$\Delta H = -R\frac{\mathrm{d}\ln(p)}{\mathrm{d}(1/T)}$$

where $R$ is the universal gas constant, $p$ is the numerical value of the equilibrium pressure and $T$ is the temperature in K.

For the calculation, the three isotherms were transformed into a form with the relative loading in mol $H_2O$ over absolute pressure in Pa. The loading of the first isotherm was split into 1000 steps. For each step, pressures of the three isotherms with the same loading were calculated using linear interpolation between the measurement points, resulting in a list with 1000 loadings and the corresponding three pressures. For every step, the natural logarithm of the three pressures was plotted against the reciprocal temperatures of the isotherms $1/T$, and a linear fit between the points was made. The slope of this straight line is $\Delta H_{ads}/R$. Fig. 10 shows the calculated heat of adsorption and desorption against the loading in g $g^{-1}$. $\Delta H_{ads}$ starts at approximately 56 kJ $mol^{-1}$ at low loadings, with a plateau of slightly over 50 kJ $mol^{-1}$ between 0.06 and 0.28 g $g^{-1}$, and falls under the evaporation enthalpy of $H_2O$ when capillary pore condensation begins. The calculated heat of desorption $\Delta H_{des}$ shows a similar shape with higher values between 60 kJ $mol^{-1}$

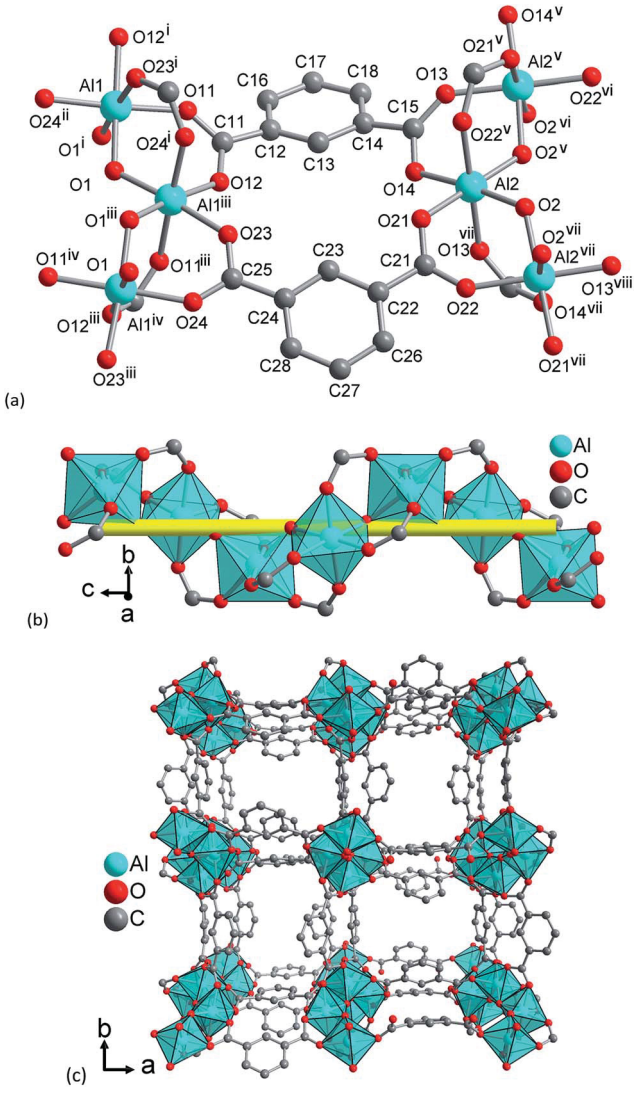


Fig. 8 Structural elements in CAU-10-H $H_2O$: (a) extended asymmetric unit with full Al coordination spheres and full ligand bridging mode. Symmetry transformations (i) = 0.5 − *y*, *x*, −0.25 + *z*; (ii) = 0.5 − *x*, 0.5 − *y*, −0.5 + *z*; (iii) = *y*, 0.5 − *x*, 0.25 + *z*; (iv) = 0.5 − *x*, 0.5 − *y*, 0.5 + *z*; (v) = 0.5 + *y*, 1 − *x*, −0.25 + *z*; (vi) = 1.5 − *x*, 0.5 − *y*, −0.5 + *z*; (vii) = 1 − *y*, −0.5 + *x*, 0.25 + *z*; (viii) = 1.5 − *x*, 0.5 − *y*, 0.5 + *z*. (b) The inorganic building unit, a fourfold helical chain of *cis* vertex-sharing $AlO_6$ polyhedra winding around the fourfold axis (yellow line). (c) The 3D framework structure exhibiting square shaped one dimensional channels. Crystal water molecules are omitted for clarity.

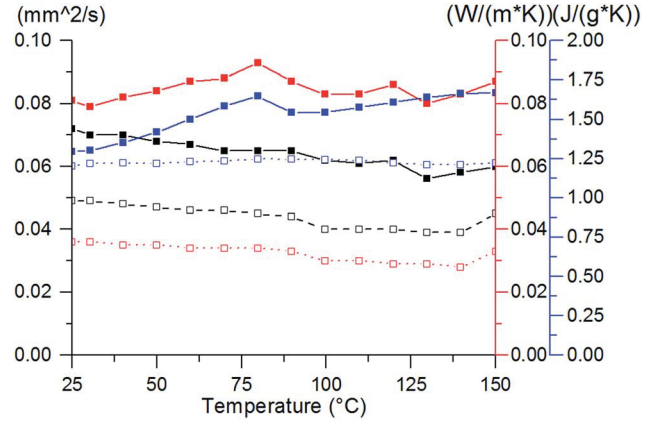


Fig. 9 Diffusivity in $mm^2$ $s^{-1}$ (black), thermal conductivity in W $m^{-1}$ $K^{-1}$ (red) and heat capacity in J $g^{-1}$ $K^{-1}$ (blue) of CAU-10-H (solid line) and coated CAU-10-H (dashed lines).

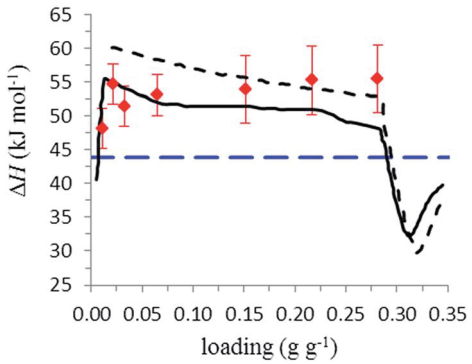


Fig. 10 Isosteric heats: calculated from experimental adsorption (solid line) and desorption (short dashed line) isotherms and computed during MD simulations (see text below and red points); the long dashed line points to the evaporation enthalpy of $H_2O$ at STP.[39]

and 52 kJ mol$^{-1}$ between 0.03 and 0.28 g g$^{-1}$. The decrease in $\Delta H_{ads}$ above 0.28 g g$^{-1}$ is due to a change from adsorption to pore condensation. The rise in $\Delta H_{ads}$ before 0.03 g $^{-1}$ is accounted by uncertainties in the measurement.

### Molecular dynamics computer simulations

The simulated IR spectrum of CAU-10-H was computed by means of the Fourier transform of the correlation function of the dipole moment vectors[40] using the quasi free modelling for the linkers; the latter option proved to be in acceptable agreement with the experimentally measured spectrum (Fig. S9†). Details on adapting the Dreiding generic force field to this sorbent with respect to the experimental spectrum and the derivation of the partial charges of the host atoms are given in the ESI.†

The molecular dynamics revealed a "flapping" motion of the benzene rings around the C–C bonds of the linker carboxylate groups (Fig. S5†), thus taking conformations between two extrema with the one being almost parallel (state I) and the other being vertical (state II) to the channel axis, so that conformations of the linkers approaching the state I or II can widen or narrow, respectively, the effective path-width of the channels.

In Fig. 11, the correlation probabilities between the dihedral angles $\varphi_1$ and $\varphi_2$ denoting the motion of the carboxylate group relative to the aromatic ring (Fig. S5†) are presented, over the total number of ligands (sixteen ligands per unit cell), for both the bare and water-loaded materials at 0.032 and 0.303 g g$^{-1}$. It is shown that in the dry material the most probable conformations are achieved when the aromatic rings tend to lie almost parallel along the $z$-direction. It is worth mentioning that simulation can predict a spectrum of angle values in addition to the experimentally measured average of 13.5°.

The above situation changes gradually upon water adsorption, in the sense that the increasing guest concentration gives rise to two distinct sets of conformations between the vicinity of states I and II separated by a lower probability region, thus forming a free energy barrier of about $3k_BT$, where $k_B = 1.3806 \times 10^{-23}$ J K$^{-1}$ is the Boltzmann constant; presumably this is

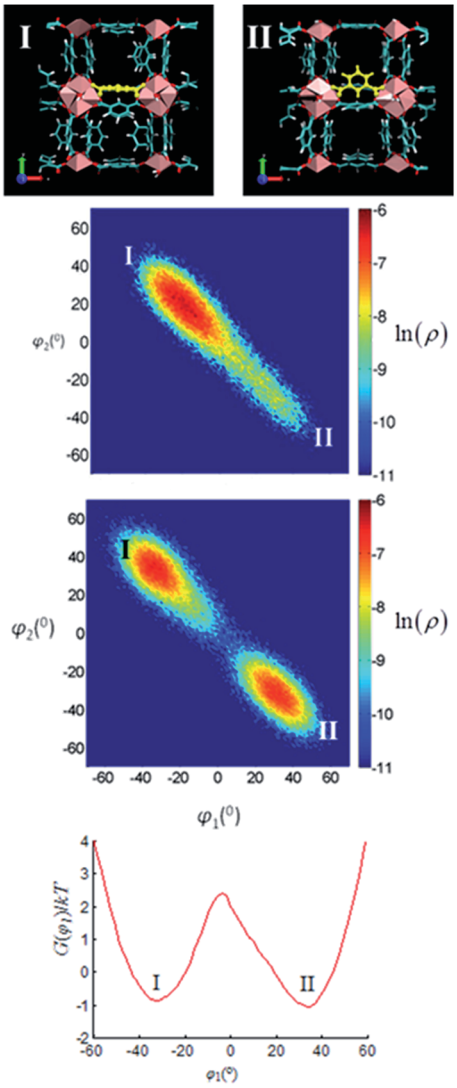


Fig. 11 MD calculations: correlation probabilities of the dihedral angles $\varphi_1$ and $\varphi_2$ for the CAU-10-H ligands attaining two conformation extrema (top), for the dry (middle), and the water-loaded material at 0.303 g g$^{-1}$ (bottom); Gibbs free energy profile of the transition I to II (most bottom).

a consequence of steric hindrance phenomena at higher loadings up to saturation. Furthermore, the Gibbs free energy profile, $G(\varphi_a)$, $a = 1, 2$, shown in the same figure for the first dihedral, was calculated over a sequence of angles between states I and II by

$$G(\varphi_a) = -k_B T \ln[\rho(\varphi_a)/\rho] + \text{const}$$

where

$$\rho(\varphi_a) = \frac{\int \delta(\varphi_a - \varphi_o) \exp\left[-\left[\mathcal{V}(\mathbf{r}^N) + PV\right]/k_B T\right] d\mathbf{r}^N}{\int \exp\left[-\left[\mathcal{V}(\mathbf{r}^N) + PV\right]/k_B T\right] d\mathbf{r}^N}$$

The vector $\mathbf{r}^N$ constitutes the sampled configurational space through the set of $N$ total degrees of freedom for the system guest plus host. The above ratio is actually a mean value of

a delta distribution, sampled over the states of the ($N$, $P$, $T$) ensemble under the prescribed pressure, $P$ (loading), and $T$, therefore defining the probability density, $\rho(\varphi_a)$, $a = 1, 2$, of having a ligand conformation at the angle $\varphi_o$, with dimensions [rad$^{-1}$]; this quantity is normalized by the uniform probability density, $\rho = 1/\omega$, over the totally sampled angle, $\omega$, so that to become dimensionless in the logarithm.

The MD simulations in the $N$, **S**, $T$ ensemble by means of the quasi free ligand version predict an anisotropic structural transition of the unit cell upon water adsorption. In particular, the unit cell contracts in the [100] and [010] directions and expands at the same time in the [001] direction, resulting in a volume increase of approximately 1.9% close to saturation. This finding may be attributed to the aforementioned ligand preferred conformation with increasing water loading. The average unit cell edges were calculated for the water uptakes of 0.005, 0.011, 0.022, 0.032, 0.065, 0.151, 0.216, 0.281, 0.303 and 0.368 g g$^{-1}$ as illustrated in Fig. 12. It is also observed that at saturation where the system becomes much congested the unit cell starts expanding, thus explaining the predicted increase of the $a$ and $b$ axes. The variation of the three angles of the unit cell shown in the same figure was also recorded during the run, showing no deviation from the 90 degrees on the average for a fully equilibrated MD trajectory.

We found that the guest molecules are primarily adsorbed in the proximity of the $AlO_6$ polyhedra *via* hydrogen bonding to the O1 and H7 atoms of the bridging OH groups and the O2 and O3 oxygen atoms of the carboxylate groups (see Fig. S5 and calculated radial distribution functions in Fig. S10†). As loading increases further, the guest–guest interactions dominate as a result of the hydrogen bonding, therefore, giving rise to water clusters which may exert steric effects on the linkers that alter their position (Fig. 11, S11 and S12†); this phenomenon leads to a distortion of the CAU framework. It must be stressed here that the anisotropic structural transition is not observed when imposing torsional potential on all dihedral angles controlling the motion of the CAU-10-H linkers (see Fig. S7 and S8†). This finding supports the result that this anisotropic structural transition of the CAU cell can be mainly attributed to the ligand reorientations upon water sorption. The predicted isosteric heats of water from MD in the CAU sorbent were calculated after developing a Widom type scheme[41] using the following equation for the loadings shown in Fig. 10.

$$\Delta H = k_B \left(\frac{\partial \ln f_b}{\partial (1/T)}\right)_P + \frac{\langle \Delta \mathscr{V}(\mathbf{r}_t; \mathbf{r}^N) \exp[-\Delta \mathscr{V}(\mathbf{r}_t; \mathbf{r}^N)/k_B T]\rangle_W}{\langle \exp[-\Delta \mathscr{V}(\mathbf{r}_t; \mathbf{r}^N)/k_B T]\rangle_W} - k_B T$$

$\mathbf{r}_t$ represents the degrees of freedom of the test water molecule and $\Delta\mathscr{V}(\mathbf{r}_t; \mathbf{r}^N)$ stands for the potential energy change of the system energy, $\mathscr{V}(\mathbf{r}^N, \boldsymbol{\psi}^N)$, upon the insertion of a test sorbate molecule.

In other words, the above equation entails: firstly, an ensemble average of the change in potential energy (and its Boltzmann factor) brought about by the random insertion of a "ghost" (test) water molecule, namely, interacting with the host atoms and guest molecules without perturbing the current configuration; the average is carried out over the states (snapshots) of the system as they are created during the MD trajectory. And secondly, evaluation of a spatial integral over a sequence of random insertions and orientations of this test molecule within the current CAU volume is carried out at each state. The described averages are denoted by $\langle \ldots \rangle_W$. $f_b$ is the fugacity of the bulk phase; at low pressures it becomes pressure, hence the derivative in the above equation decays.

It must be stressed that in our simulations the equation above represents the configurational part of the differential heat of sorption since it is related to the configurational part of internal energy, namely the potential energy, $\mathscr{V}$.

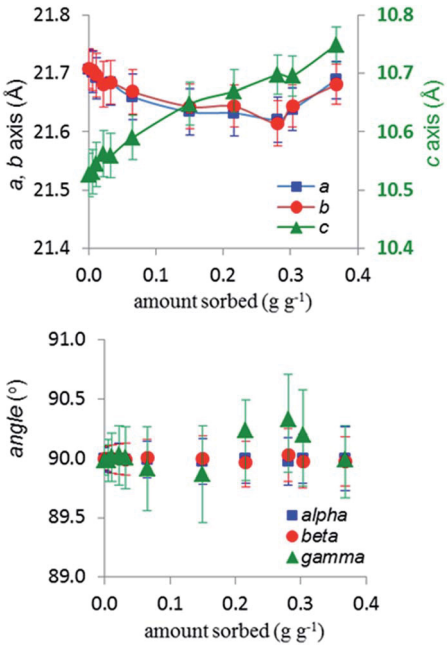


Fig. 12 Computed length evolution of the $a$, $b$ and $c$ axes (top), and $\alpha$, $\beta$, and $\gamma$ angles of the CAU-10-H unit cell (bottom), induced by the water adsorption during an MD trajectory, as a function of loading for 0.005, 0.011, 0.022, 0.032, 0.065, 0.151, 0.216, 0.281, 0.303 and 0.368 g g$^{-1}$.

## Cooling performance

The water adsorption data were transformed according to the Dubinin–Astakhov approach leading to the following equation for the equilibrium loading capacity as a function of the adsorption potential:[42]

$$x = x_{max} \exp\left[-\left(\frac{A}{E}\right)^n\right]$$

where the adsorption potential is given by

$$A = RT \ln\left(\frac{p_0}{p}\right)$$

The transformation leads to a fairly smooth characteristic curve with a steep step between 200 J g$^{-1}$ and 250 J g$^{-1}$ of the adsorption potential. By the use of this rough thermodynamic

 

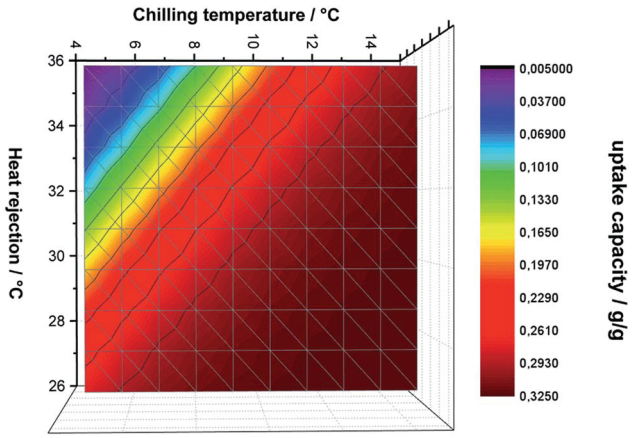


Fig. 13 Projection of the uptake capacity *versus* the chilling and heat rejection temperatures, showing a very broad plateau with maximum uptake capacity for a large range of boundary conditions.

model, the potential of the working pair water/CAU-10-H has been evaluated under different boundary conditions.

At first, the sensitivity of the uptake capacity with regard to the desorption conditions, *i.e.*, the condenser and desorption temperatures, was calculated. As shown in Fig. 13, the CAU-10-H can be easily regenerated by a very low desorption temperature. Even at a high condenser temperature of 35 °C, a desorption temperature less than 75 °C is sufficient to completely dry the material. With lower condenser temperature, the required driving temperatures decrease with a minimum of 70 °C at a condenser temperature of 27 °C.

In addition to the desorption conditions, the sensitivity for the adsorption conditions, *i.e.* the heat rejection and the chilling temperatures (evaporator), was evaluated. As can be seen in Fig. 14, CAU-10 performs best either at heat rejection

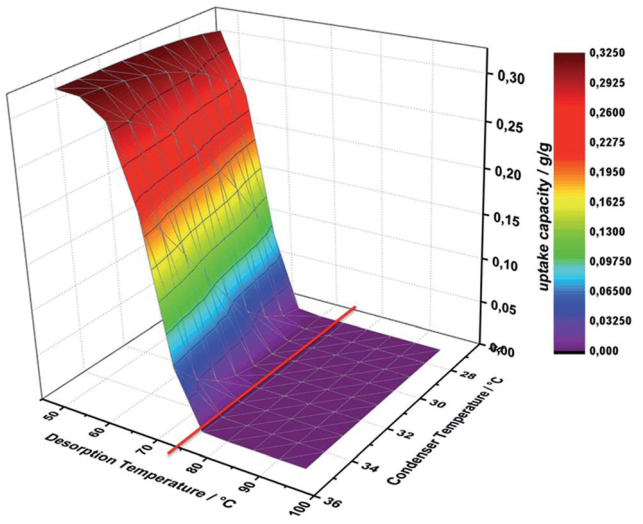


Fig. 14 Calculation of uptake capacity *vs.* desorption temperature and condensing temperature. As illustrated by the red line, CAU-10-H can be completely dried at all typical condenser temperatures used in cooling application with a desorption temperature less than 75 °C.

temperatures below 30 °C and/or for evaporator temperatures above 10 °C with almost the maximum uptake of approximately 0.32 g $g^{-1}$. Surprisingly, nearly the whole uptake capacity can be achieved with heat rejection temperatures below 30 °C for almost the whole range of chilling temperatures. In addition, the full uptake can be achieved even at a very high heat rejection temperature of 35 °C, if the chilling temperatures can be increased above temperatures of 12 °C. Thus, this working pair is highly interesting for very low driving heat cooling applications.

As this field of application is not accessible by current state-of-the-art materials, CAU-10-H clearly closes a gap, thus allowing new adsorption chilling applications.

## Conclusions

The results described herein demonstrate that CAU-10-H remains stable during several thousand adsorption and desorption cycles with water as working fluid.

Due to its thermophysical characteristics, it is a suitable adsorbent for application in adsorptive cooling application with water as the working fluid. The water uptake of 0.26 g $g^{-1}$ for the coated sample (0.34 g $g^{-1}$ for the bulk) is lower compared to that of other very good performing and stable MOFs, like aluminium-fumarate coating (0.35 g $g^{-1}$). Other MOFs with higher water capacities like UiO-66 (0.45 g $g^{-1}$) or MIL-100 (Fe 0.65 g $g^{-1}$, Al 0.36 g $g^{-1}$) lack stability upon cycling. The successful coating procedure, the high stability up to 10 000 cycles under working conditions, the nearly perfect shape of the isotherm and the high uptake capacity make CAU-10-H the best performing MOF for heat pump applications reported until now.

For a successful market introduction, it will be necessary to develop an industrially more feasible and scalable route for its synthesis. The structural transition which was characterised in detail indicates that the flexibility of this material is dominated by a torsional motion within the linker molecule, which nevertheless does not lower the stability of the MOF. Since this is the second MOF demonstrating such long-term stability and since the first MOF with such properties (aluminium fumarate) is also based on $Al^{3+}$, we assume that Al-based MOFs are the most promising MOF adsorbents for application in water based heat pumps. One major challenge in the future will be the development of better MOF adsorbents in which the stability is preserved while the capacity and therefore the amount of converted energy are increased.

## Acknowledgements

The authors would like to thank Linkam for lending them the demo version of the RH95 Humidity Controller. Financial support from the German Federal Ministry of Education and Research and the Greek General Secretariat of Research and Technology within the German-Greek joint project WASSER-MOD under grant 03SF0469B, and the project Optimat under grant 03SF0492A/C as well as support by the Fraunhofer Zukunftsstiftung under grant HARVEST are gratefully

acknowledged. Georg Hagelstein is thanked for the SEM measurements. Also Albina Holz and Konstantin Gradwohl are thanked for their work in the laboratory. KM and DDV are grateful to Belspo for funding in the IAP project Functional Supramolecular Systems. MvdV and DDV are grateful for the financial support from the Hercules Foundation. GKP acknowledges the supercomputing centre of the Greek General Secretariat of Research and Technology, "ARIS".

## Notes and references

1 (*a*) C. Janiak and J. K. Vieth, *New J. Chem.*, 2010, **34**, 2366–2388; (*b*) A. U. Czaja, N. Trukhan and U. Muller, *Chem. Soc. Rev.*, 2009, **38**, 1284–1293; (*c*) C. Janiak, *Dalton Trans.*, 2003, 2781.

2 (*a*) H. Wu, Q. Gong, D. H. Olson and J. Li, *Chem. Rev.*, 2012, **112**, 836–868; (*b*) L. J. Murray, M. Dincă and J. R. Long, *Chem. Soc. Rev.*, 2009, **38**, 1294–1314; (*c*) J. R. Li, R. J. Kuppler and H. C. Zhou, *Chem. Soc. Rev.*, 2009, **38**, 1477–1504; (*d*) M. P. Suh, H. J. Park, T. K. Prasad and D. W. Lim, *Chem. Rev.*, 2012, **112**, 782–835.

3 M. Eddaoudi, D. F. Sava, J. F. Eubank, K. Adil and V. Guillerm, *Chem. Soc. Rev.*, 2015, **44**, 228–249.

4 A. Corma, H. Garcia and F. X. Llabres i Xamena, *Chem. Rev.*, 2010, **110**, 4606–4655.

5 O. Shekhah, J. Liu, R. A. Fischer and C. Wöll, *Chem. Soc. Rev.*, 2011, **40**, 1081–1106.

6 (*a*) Y. I. Aristov, B. Dawoud, I. S. Glaznev and A. Elyas, *Int. J. Heat Mass Transfer*, 2008, **51**, 4966–4972; (*b*) M. F. de Lange, K. J. F. M. Verouden, T. J. H. Vlugt, J. Gascon and F. Kapteijn, *Chem. Rev.*, 2015, **115**, 12205–12250; (*c*) S. K. Henninger, F. Jeremias, H. Kummer and C. Janiak, *Eur. J. Inorg. Chem.*, 2012, 2625–2634; (*d*) C. Janiak and S. K. Henninger, *Chimia*, 2013, **67**, 419–424; (*e*) J. Canivet, A. Fateeva, Y. Guo, B. Coasne and D. Farrusseng, *Chem. Soc. Rev.*, 2014, **43**, 5594–5617.

7 F. Jeremias, D. Fröhlich, C. Janiak and S. K. Henninger, *New J. Chem.*, 2014, **38**, 1846–1852.

8 S. K. Henninger, H. A. Habib and C. Janiak, *J. Am. Chem. Soc.*, 2009, **131**, 2776–2777.

9 (*a*) J. V. Veselovskaya, R. E. Critoph, R. N. Thorpe, S. Metcalf, M. M. Tokarev and Y. Aristov, *Appl. Therm. Eng.*, 2010, **30**, 1188–1192; (*b*) Z. Tamainot-Telto, S. J. Metcalf and R. E. Critoph, *Int. J. Refrig.*, 2009, **32**, 727–733; (*c*) A. A. Askalany, M. Salem, I. M. Ismael, A. H. H. Ali, M. G. Morsy and B. B. Saha, *Renewable Sustainable Energy Rev.*, 2013, **19**, 565–572; (*d*) K. Habib, B. B. Saha, A. Chakraborty, S. T. Oh and S. Koyama, *Appl. Therm. Eng.*, 2013, **50**, 1582–1589; (*e*) Y. I. Aristov, *Appl. Therm. Eng.*, 2012, **42**, 18–24; (*f*) R. Wang and R. Oliveira, *Prog. Energy Combust. Sci.*, 2006, **32**, 424–458; (*g*) B. B. Saha, A. Chakraborty, S. Koyama and Y. I. Aristov, *Int. J. Heat Mass Transfer*, 2009, **52**, 516–524; (*h*) B. B. Saha, A. Chakraborty, S. Koyama, K. Srinivasan, K. C. Ng, T. Kashiwagi and P. Dutta, *Appl. Phys. Lett.*, 2007, **91**, 111902.

10 (*a*) L. G. Gordeeva, A. Freni, Y. I. Aristov and G. Restuccia, *Ind. Eng. Chem. Res.*, 2009, **48**, 6197–6202; (*b*) Y. I. Aristov, M. M. Tokarev, A. Freni, I. S. Glaznev and G. Restuccia, *Microporous Mesoporous Mater.*, 2006, **96**, 65–71; (*c*) B. Dawoud and Y. Aristov, *Int. J. Heat Mass Transfer*, 2003, **46**, 273–281; (*d*) Y. I. Aristov, *Int. J. Refrig.*, 2009, **32**, 675–686; (*e*) I. A. Simonova, A. Freni, G. Restuccia and Y. I. Aristov, *Microporous Mesoporous Mater.*, 2009, **122**, 223–228; (*f*) Y. I. Aristov, *J. Chem. Eng. Jpn.*, 2007, **40**, 1242–1251; (*g*) Y. I. Aristov, *Appl. Therm. Eng.*, 2013, **50**, 1610–1618.

11 (*a*) Y. I. Aristov, G. Restuccia, G. Cacciola and V. N. Parmon, *Appl. Therm. Eng.*, 2002, **22**, 191–204; (*b*) N. C. Srivastava and I. W. Eames, *Appl. Therm. Eng.*, 1998, **18**, 707–714.

12 R. Z. Wang, Z. Z. Xia, L. W. Wang, Z. S. Lu, S. L. Li, T. X. Li, J. Y. Wu and S. He, *Energy*, 2011, **36**, 5425–5439.

13 (*a*) T. Birsa Čelič, M. Mazaj, N. Guillou, E. Elkaïm, M. El Roz, F. Thibault-Starzyk, G. Mali, M. Rangus, T. Čendak, V. Kaučič and N. Zabukovec Logar, *J. Phys. Chem. C*, 2013, **117**, 14608–14617; (*b*) G. W. Peterson, J. B. DeCoste, T. G. Glover, Y. Huang, H. Jasuja and K. S. Walton, *Microporous Mesoporous Mater.*, 2013, **179**, 48–53; (*c*) H. Jasuja and K. S. Walton, *Dalton Trans.*, 2013, **42**, 15421–15426; (*d*) H. Jasuja, J. Zang, D. S. Sholl and K. S. Walton, *J. Phys. Chem. C*, 2012, **116**, 23526–23532; (*e*) G. E. Cmarik, M. Kim, S. M. Cohen and K. S. Walton, *Langmuir*, 2012, **28**, 15606–15613; (*f*) P. M. Schoenecker, C. G. Carson, H. Jasuja, C. J. J. Flemming and K. S. Walton, *Ind. Eng. Chem. Res.*, 2012, **51**, 6513–6519; (*g*) F. Jeremias, V. Lozan, S. Henninger and C. Janiak, *Dalton Trans.*, 2013, **42**, 15967–15973; (*h*) M. F. de Lange, C. P. Ottevanger, M. Wiegman, T. J. H. Vlugt, J. Gascon and F. Kapteijn, *CrystEngComm*, 2015, **17**, 281–285.

14 J. J. Low, A. I. Benin, P. Jakubczak, J. F. Abrahamian, S. A. Faheem and R. R. Willis, *J. Am. Chem. Soc.*, 2009, **131**, 15834–15842.

15 J. Ehrenmann, S. K. Henninger and C. Janiak, *Eur. J. Inorg. Chem.*, 2011, 471–474.

16 A. Khutia, H. U. Rammelberg, T. Schmidt, S. Henninger and C. Janiak, *Chem. Mater.*, 2013, **25**, 790–798.

17 M. Wickenheisser and C. Janiak, *Microporous Mesoporous Mater.*, 2015, **204**, 242–250.

18 M. Wickenheisser, A. Herbst, R. Tannert, B. Milow and C. Janiak, *Microporous Mesoporous Mater.*, 2015, **215**, 143–153.

19 M. Wickenheisser, T. Paul and C. Janiak, *Microporous Mesoporous Mater.*, 2016, **220**, 258–269.

20 N. C. Burtch, H. Jasuja and K. S. Walton, *Chem. Rev.*, 2014, **114**, 10575–10612.

21 F. Jeremias, A. Khutia, S. K. Henninger and C. Janiak, *J. Mater. Chem.*, 2012, **22**, 10148–10151.

22 F. Jeremias, D. Fröhlich, C. Janiak and S. K. Henninger, *RSC Adv.*, 2014, **4**, 24073–24082.

23 D. Fröhlich, S. K. Henninger and C. Janiak, *Dalton Trans.*, 2014, **43**, 15300–15304.

24 H. Reinsch, M. A. van der Veen, B. Gil, B. Marszalek, T. Verbiest, D. de Vos and N. Stock, *Chem. Mater.*, 2013, **25**, 17–26.

25 E. Alvarez, N. Guillou, C. Martineau, B. Bueken, B. Van de Voorde, C. Le Guillouzer, P. Fabry, F. Nouar, F. Taulelle,

 

D. de Vos, J.-S. Chang, K. H. Cho, N. Ramsahye, T. Devic, M. Daturi, G. Maurin and C. Serre, *Angew. Chem., Int. Ed.*, 2015, **54**, 3664–3668.

26 H. Kummer, G. Füldner and S. K. Henninger, *Appl. Therm. Eng.*, 2015, **85**, 1–8.

27 *Topas Academics 4.2, Coelho Software*, 2007.

28 M. A. van der Veen, B. F. Sels, D. E. De Vos and T. Verbiest, *J. Am. Chem. Soc.*, 2010, **132**, 6630–6631.

29 M. A. van der Veen, J. van Noyen, B. F. Sels, P. A. Jacobs, T. Verbiest and D. E. De Vos, *Phys. Chem. Chem. Phys.*, 2010, **12**, 10688–10692.

30 M. Parrinello and A. Rahman, *J. Appl. Phys.*, 1981, **52**, 7182.

31 S. Nosé, *J. Chem. Phys.*, 1984, **81**, 511.

32 (*a*) H. C. Andersen, *J. Chem. Phys.*, 1980, **72**, 2384; (*b*) E. Pantatosaki, G. Megariotis, A.-K. Pusch, C. Chmelik, F. Stallmach and G. K. Papadopoulos, *J. Phys. Chem. C*, 2012, **116**, 201–207.

33 H. J. C. Berendsen, J. R. Grigera and T. P. Straatsma, *J. Phys. Chem.*, 1987, **91**, 6269–6271.

34 J.-P. Ryckaert, G. Ciccotti and H. J. Berendsen, *J. Comput. Phys.*, 1977, **23**, 327–341.

35 T. Verbiest, K. Clays and V. Rodriguez, *Second-order nonlinear optical characterization techniques. An introduction*, CRC Press, Boca Raton, 2009.

36 M. Kandiah, M. H. Nilsen, S. Usseglio, S. Jakobsen, U. Olsbye, M. Tilset, C. Larabi, E. A. Quadrelli, F. Bonino and K. P. Lillerud, *Chem. Mater.*, 2010, **22**, 6632–6640.

37 V. Guillerm, F. Ragon, M. Dan-Hardi, T. Devic, M. Vishnuvarthan, B. Campo, A. Vimont, G. Clet, Q. Yang, G. Maurin, G. Férey, A. Vittadini, S. Gross and C. Serre, *Angew. Chem., Int. Ed.*, 2012, **51**, 9267–9271.

38 P. W. Atkins, *Physikalische Chemie*, Wiley-VCH, Weinheim, 3rd edn, 2001.

39 R. H. Perry, D. W. Green and J. O. Maloney, *Perry's Chemical Engineers' Handbook*, McGraw-Hill, New York, 7th edn, 1997.

40 R. G. Gordon, in *Advances in Magnetic Resonance*, Elsevier, 1968, vol. 3, pp. 1–42.

41 P. D. Kolokathis, E. Pantatosaki and G. K. Papadopoulos, *J. Phys. Chem. C*, 2015, **119**, 20074–20084.

42 (*a*) S. K. Henninger, M. Schicktanz, P. Hügenell, H. Sievers and H.-M. Henning, *Int. J. Refrig.*, 2012, **35**, 543–553; (*b*) F. Stoeckli, *Russ. Chem. Bull.*, 2001, **50**, 2265–2272; (*c*) M. Dubinin, *J. Colloid Interface Sci.*, 1967, **23**, 487–499.

# Electronic Supplementary Material (ESI)

## Water adsorption behaviour of CAU-10-H: A thorough investigation of its structure-property relationships

Dominik Fröhlich[a,b], Evangelia Pantatosaki[c], Panagiotis D. Kolokathis[c], Karen Markey[d], Helge Reinsch[e], Max Baumgartner[a], Monique A. van der Veen[f], Dirk E. De Vos[d], Norbert Stock[e], George K. Papadopoulos[c,g], Stefan K. Henninger[a,*] and Christoph Janiak[b,*]

a. Fraunhofer Institute for Solar Energy Systems ISE, Heidenhofstrasse 2, 79110 Freiburg, Germany; Fax: 49 761 4588913; Tel: +49 761 45882117
b. Institut für Anorganische Chemie und Strukturchemie, Heinrich-Heine-Universität Düsseldorf, Universitätsstr. 1, 40225 Düsseldorf, Germany, Tel.: +49 211 8112286,
c. School of Chemical Engineering, National Technical University of Athens, 9 Heroon Polytechniou Street, 157 80 Athens, Greece
d. Centre for Surface Chemistry and Catalysis, University of Leuven, Kasteelpark Arenberg 23, 3001 Leuven, Belgium
e. Institute of Inorganic Chemistry, Christian-Albrechts-University Kiel, Max-Eyth-Str. 2, D-24118 Kiel, Germany
f. Catalysis Engineering, Department of Chemical Engineering, Delft University of Technology, 2826 Delft, The Netherlands
g. Institute for Medical Engineering and Science, Massachusetts Institute of Technology, Cambridge, Massachusetts 02139, USA

Emails

1) dominik.froehlich@ise.fraunhofer.de
2) evpanta@chemeng.ntua.gr
3) tkolokathis@yahoo.gr
4) Karen.Markey@biw.kuleuven.be
5) hreinsch@ac.uni-kiel.de
6) max.baumgartner@ise.fraunhofer.de
7) M.A.vanderVeen@tudelft.nl
8) dirk.devos@biw.kuleuven.be
9) stock@ac.uni-kiel.de
10) gkpap@chemeng.ntua.gr
*11) stefan.henninger@ise.fraunhofer.de
*12) janiak@uni-duesseldorf.de

## 1) Synthesis of CAU-10-H:

CAU-10-H was synthesized from 505 g (0.75 mol) of aluminium sulfate hydrate ($Al_2(SO_4)_3 \cdot 18H_2O$) dissolved in 2.5 L of $H_2O$, and 132 g (0.79 mol) isophthalic acid dissolved in 625 mL of DMF. The two solutions were combined in a 5 L round bottom flask. The combined mixture was heated under reflux for 117 h. After cooling down the precipitate was filtered, redispersed for washing in 3 L of $H_2O$ by sonication and stirring. The dispersion was filtered again and dried for 4 days at 100 °C and after this activated for 2 days at 120°C in vacuum. The total yield was 150 g (91 %) CAU-10-H. Surface area $S_{BET}$ = 564$m^2g^{-1}$ and pore volume 0.26 $cm^3g^{-1}$.

## 2) SEM images of the coating:

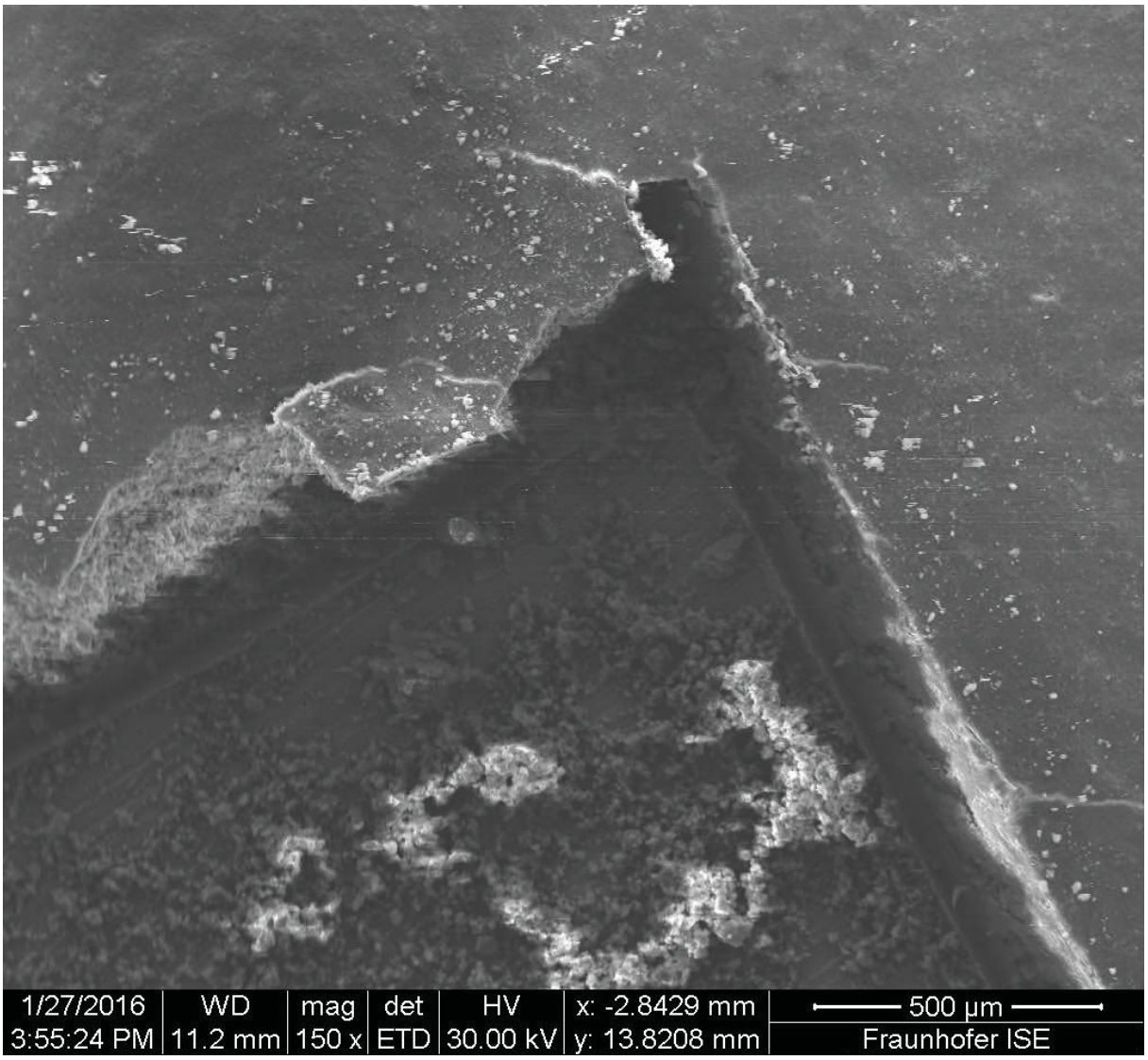


**Fig. S1** SEM image of cross-section of CAU-10-H coating. Part of the coating was removed to get a better impression on the uniformity and thickness of the coating.

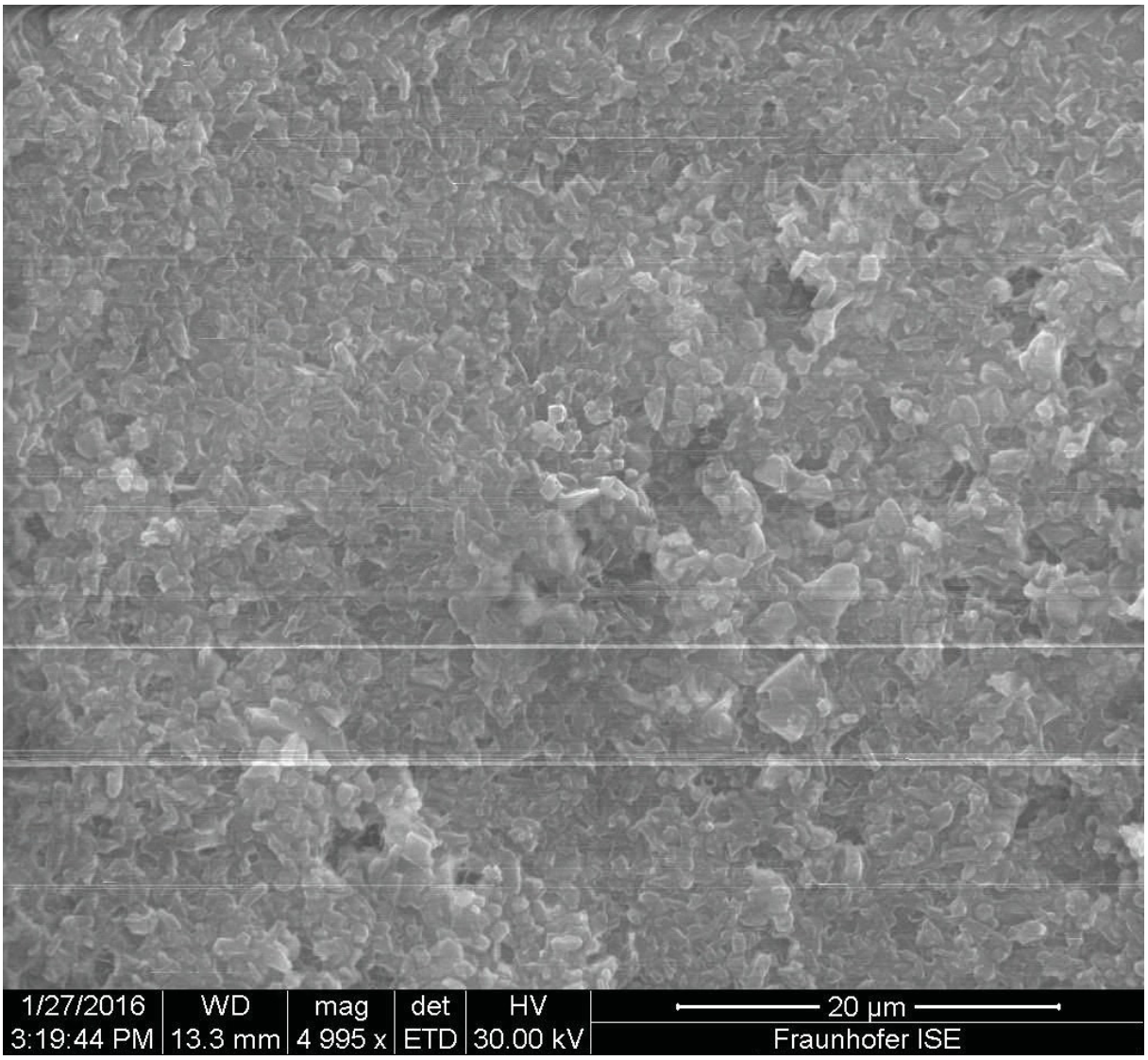


**Fig. S2** SEM image of the CAU-10-H coating.

### 3) Experimental section for capillary PXRD measurements

The in-situ measurements at different relative humidity values unambiguously proved a phase transition between the known non-centrosymmetric form of CAU-10-H and a not yet reported dry, centrosymmetric conformation. In the light of these results, high-resolution PXRD data was analysed and crystal structures of the dry and the wet form were obtained by Rietveld refinement. The samples were loaded in capillaries and sealed either under ambient conditions after filtration (hydrated form) or after evacuation at 0.1 mbar and heating to 200 °C (dried form). The data was collected using a STOE Stadi-P diffractometer equipped with a Mythen detector using monochromated $CuK_{\alpha 1}$ radiation. The software used for indexing and refinements was TOPAS.

The extinction conditions for the dried form are in agreement with the space group $I4_1/amd$ and thus the crystal structure of the isostructural CAU-10-$CH_3$ was utilised as a starting model for Rietveld

refinement. The functional groups were removed from the structural model and the positions of all other atoms could be successfully refined after employing restraints.

Although the structure of hydrated CAU-10-H has been reported previously, the structure was revaluated since better PXRD data could be obtained. Hence for the structure determination of the hydrated form the already reported crystal structure data[1] was taken as a starting model. Initially the position of the linker molecules was optimised by force-field methods using Materials Studio. This first model was used in the Rietveld refinement. Additional electron density found by Fourier Synthesis was attributed to water molecules inside the pores and subsequently their occupancy was also refined. The carbon backbones of the linker molecules were refined as rigid bodies and all other atoms were freely refined using restraints until convergence was achieved. The determination of the position of water molecules is usually very challenging using solely in-house PXRD data. For an ultimate proof, it would be advisable to measure neutron diffraction data on deuterated samples. Nevertheless, in the absence of such data the obtained position and the observed distances are in good agreement with expected values for moderate to strong hydrogen bonds. The residual electron density could be attributed to seven independent oxygen atoms representing water molecules.

The most relevant crystallographic data is summarised in Table S1 and the asymmetric units are given in Figures S3 and S4. Relevant bond distances are given in Tables S2 and S3. The final Rietveld plots are given in Figures S5 and S6.

**Table S1** Final parameters of the Rietveld refinements.

| CAU-10-H | Hydrated | Dry |
|---|---|---|
| space group | $I4_1$ | $I4_1/amd$ |
| $a = b$ [Å] | 21.2928(4) | 21. 5214(7) |
| $c$ [Å] | 10.7305(3) | 10. 3218(4) |
| V [Å$^3$] | 4865.0(2) | 4780.7(3) |
| $R_{WP}$ / % | 6.8 | 4.3 |
| $R_{Bragg}$ / % | 3.2 | 0.6 |
| GoF | 1.54 | 1.03 |
| wavelength | Cu K$\alpha_1$ | Cu K$\alpha_1$ |

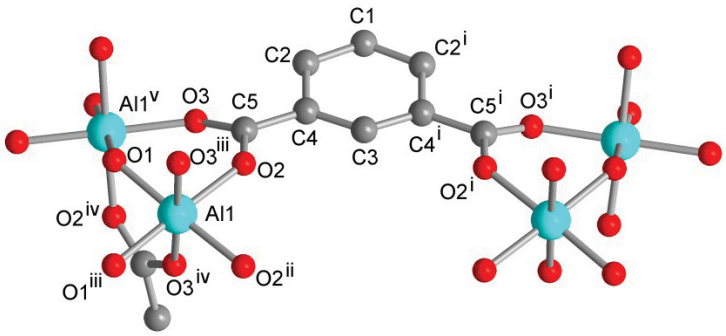


**Figure S3** Extended asymmetric unit of CAU-10H-dry with full Al coordination spheres and full ligand bridging mode. Symmetry transformations i = 1–x, y, z; ii = x, –y, –z; iii = 0.25+y, 0.25–x, –0.25+z; iv = 0.25+y, –0.25+x, 0.25–z; v = 0.25–y, –0.25+x, 0.25+z; selected distances and angles are given inTable S2.

**Table S2** Relevant bond distances (Å) and angles (°) for CAU-10-H-dry.[a]

| | | | |
|---|---|---|---|
| Al1-O1(O1$^{iii}$) | 1.855(9) | O2-C5 | 1.252(13) |
| Al1-O3$^{iii,iv}$ | 1.888(11) | O3-C5 | 1.282(13) |
| Al1-O2(O2$^{ii}$) | 1.903(11) | C1-C2 | 1.400(11) |
| | | C2-C4 | 1.405(12) |
| O1-Al1-O1$^{iii}$ | 88.853(3) | C3-C4 | 1.384(12) |
| O1-Al1-O3$^{iii}$ | 88.2 (3) | C4-C5 | 1.471(11) |
| O1-Al1-O3$^{iv}$ | 91.0(3) | | |
| O1-Al1-O2 | 92.3(3) | | |
| O1-Al1-O2$^{ii}$ | 178.0(3) | | |
| O3$^{iii}$-Al1-O3$^{iv}$ | 178.9(5) | | |
| O3$^{iii}$-Al1-O2 | 90.7(4) | | |
| O3$^{iii}$-Al1-O2$^{ii}$ | 90.1(4) | | |
| O2-Al1-O2$^{ii}$ | 86.5(4) | | |
| Al1-O1-Al1$^{v}$ | 126.657(4) | | |

[a] Symmetry transformations: ii = x, –y, –z; iii = 0.25+y, 0.25–x, –0.25+z; iv = 0.25+y, –0.25+x, 0.25–z; v = 0.25–y, –0.25+x, 0.25+z

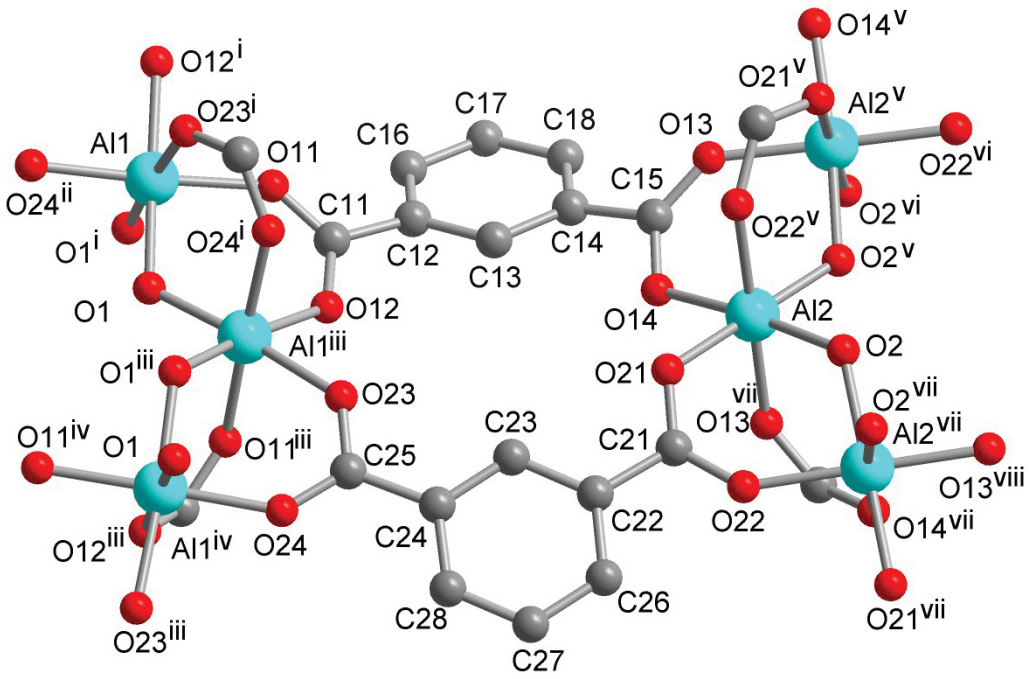


**Figure S4** Extended asymmetric unit of CAU-10H-$H_2O$ with full Al coordination spheres and full ligand bridging mode. Symmetry transformations i = 0.5–y, x, –0.25+z; ii = 0.5–x, 0.5–y, –0.5+z; iii = y, 0.5–x, 0.25+z; iv = 0.5–x, 0.5–y, 0.5+z; v = 0.5+y, 1–x, –0.25+z; vi = 1.5–x, 0.5–y, –0.5+z; vii = 1–y, –0.5+x, 0.25+z; viii = 1.5–x, 0.5–y, 0.5+z; selected distances and angles are given in Table S3. Crystal water guest molecules are not shown.

**Table S3** Relevant bond distances (Å) and angles (°) for CAU-10-H-$H_2O$ including potential hydrogen bonds. Distances within the rigid bodies were not refined and therefore are given without standard uncertainties.[a]

| | | | |
|---|---|---|---|
| Al1-O1 | 1.871(16) | C14-C15 | 1.467 |
| Al1-O1$^{i}$ | 1.875(15) | C16-C17 | 1.393 |
| Al1-O24$^{ii}$ | 1.897(10) | C17-C18 | 1.393 |
| Al1-O12$^{i}$ | 1.903(12) | O13-C15 | 1.237(7) |
| Al1-O11 | 1.906(10) | O14-C15 | 1.236(9) |
| Al1-O23$^{i}$ | 1.967(12) | | |
| O11-C11 | 1.238(9) | Al2-O13$^{vii}$ | 1.890(11) |
| O12-C11 | 1.264(9) | Al2-O2$^{v}$ | 1.906(14) |
| C11-C12 | 1.467 | Al2-O22$^{v}$ | 1.920(11) |
| C12-C13 | 1.401 | Al2-O21 | 1.921(13) |
| C12-C16 | 1.415 | Al2-O2$^{iv}$ | 1.923(15) |
| C13-C14 | 1.401 | Al2-O14 | 1.964(12) |
| C14-C18 | 1.415 | O21 C21 | 1.221(8) |

| | | |
|---|---|---|
| O22 | C21 | 1.300(8) |
| C21 | C22 | 1.479 |
| C22 | C23 | 1.408 |
| C22 | C26 | 1.415 |
| C23 | C24 | 1.408 |
| C24 | C28 | 1.415 |
| C24 | C25 | 1.479 |
| C26 | C27 | 1.392 |
| C27 | C28 | 1.392 |
| O23 | C25 | 1.283(9) |
| O24 | C25 | 1.239(9) |

| | |
|---|---|
| O1-Al1-O1$^{i}$ | 92.2(6) |
| O1-Al1-O24$^{ii}$ | 89.2(6) |
| O1-Al1-O12$^{i}$ | 173.3(7) |
| O1-Al1-O11 | 94.2(6) |
| O1-Al1-O23$^{i}$ | 86.6 (5) |
| O1$^{i}$-Al1-O24$^{ii}$ | 92.2 (6) |
| O1$^{i}$-Al1-O12$^{i}$ | 94.6(5) |
| O1$^{i}$-Al1-O11 | 87.6 (5) |
| O1$^{i}$-Al1-O23$^{i}$ | 175.7 (6) |
| O24$^{ii}$-Al1-O12$^{i}$ | 90.4(6) |
| O24$^{ii}$-Al1-O11 | 176.6 (5) |
| O24$^{ii}$-Al1-O23$^{i}$ | 91.8 (6) |
| O12$^{i}$-Al1-O11 | 86.2 (5) |
| O12$^{i}$-Al1-O23$^{i}$ | 86.7(5) |
| O11-Al1-O23$^{i}$ | 88.4(5) |

| | |
|---|---|
| O13$^{vii}$-Al2-O2$^{v}$ | 92.1 (5) |
| O13$^{vii}$-Al2-O22$^{v}$ | 179.2(6) |
| O13$^{vii}$-Al2-O21 | 88.2(4) |
| O13$^{vii}$-Al2-O2 | 88.1(5) |
| O13$^{vii}$-Al2-O14 | 87.5(5) |
| O2$^{v}$-Al2-O22$^{v}$ | 87.9(5) |
| O2$^{v}$-Al2-O21 | 179.1(6) |
| O2$^{v}$-Al2-O2 | 89.6(6) |
| O2$^{v}$-Al2-O14 | 93.2(5) |
| O22$^{v}$-Al2-O21 | 91.8(4) |
| O22$^{v}$-Al2-O2 | 92.7(5) |
| O22$^{v}$-Al2-O14 | 91.7(5) |
| O21-Al2-O2 | 89.6(5) |
| O21-Al2-O14 | 87.6 (5) |
| O2-Al2-O14 | 174.9(6) |

Potential hydrogen bonds (Å):

| | |
|---|---|
| Og1-Og2 | 2.728(23) |
| Og1-O1 | 2.944(18) |
| Og2-Og3 | 2.766(21) |
| Og2-Og7 | 3.052(50) |
| Og2-Og3 | 3.145(25) |
| Og3-Og7 | 3.018(46) |
| Og3-Og4 | 3.084(24) |
| Og4-O2 | 2.798(20) |
| Og4-O21 | 2.954(20) |
| Og4-O2 | 3.095(21) |
| Og5-O12 | 2.879(19) |
| Og5-Og6 | 3.016(22) |
| Og5-Og7 | 3.068(26) |
| Og5-O23 | 3.129(21) |
| Og6-Og7 | 2.727(54) |
| Og6-Og6 | 2.894(18) |

Symmetry transformations

i = 0.5–y, x, –0.25+z; ii = 0.5–x, 0.5–y, –0.5+z; iii = y, 0.5–x, 0.25+z; iv = 0.5–x, 0.5–y, 0.5+z; v = 0.5+y, 1–x, –0.25+z; vi = 1.5–x, 0.5–y, –0.5+z; vii = 1–y, –0.5+x, 0.25+z; viii = 1.5–x, 0.5–y, 0.5+z.

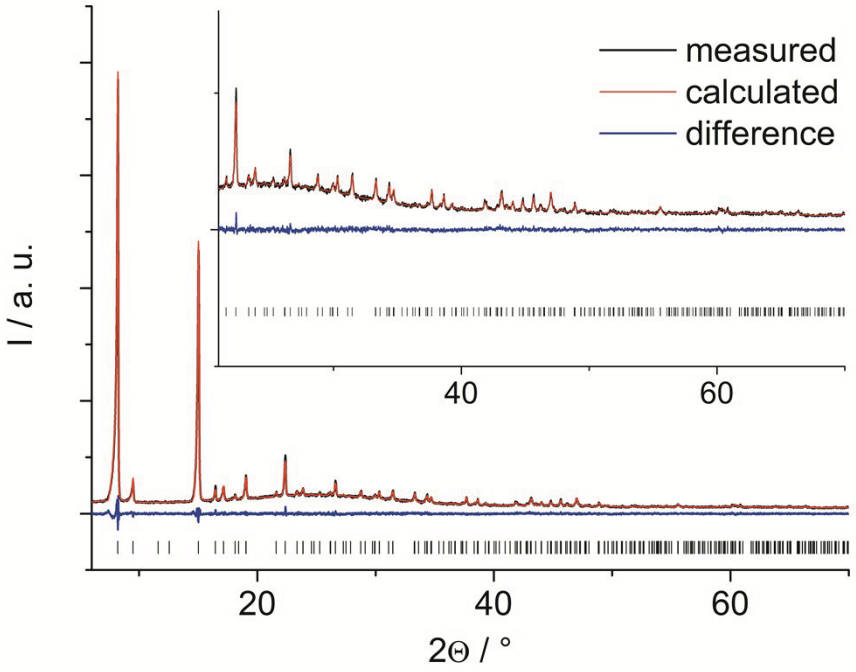


**Figure S5** Final Rietveld Plot for CAU-10-H-dry. The black line is the experimental data, the red line gives the calculated fit, the blue line is the difference curve. Vertical bars mark the Bragg reflection positions.

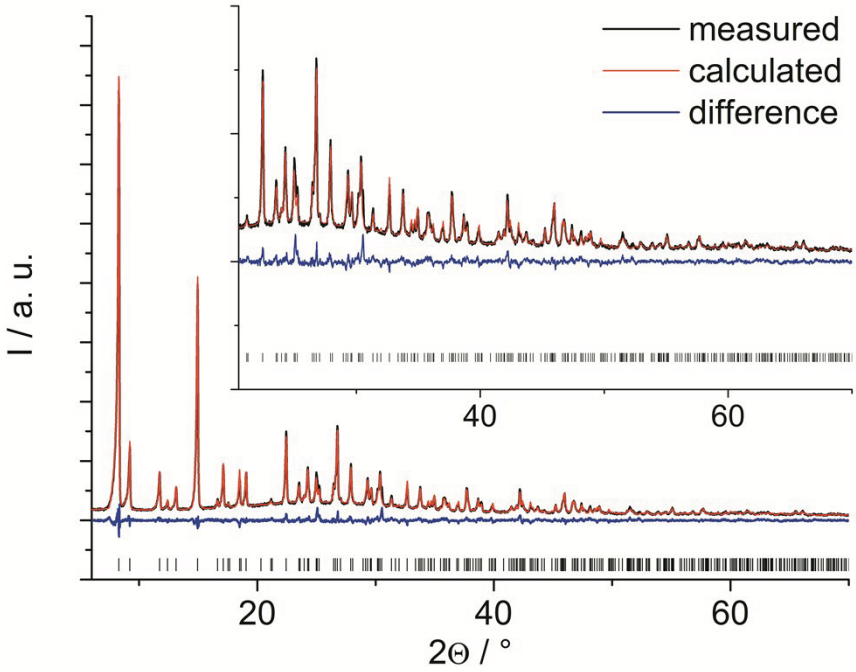


**Figure S6** Final Rietveld Plot for CAU-10-H-$H_2O$. The black line is the experimental data, the red line gives the calculated fit, the blue line is the difference curve. Vertical bars mark the Bragg reflection positions.

Crystallographic Information Files (CIFs):

```
data_
_chemical_name_mineral CAU10dry
_cell_length_a  21.52137(72)
_cell_length_b  21.52137(72)
_cell_length_c  10.32179(44)
_cell_angle_alpha 90
_cell_angle_beta  90
_cell_angle_gamma 90
_cell_volume 4780.74(38)
_symmetry_space_group_name_H-M I41/amdz
loop_
_symmetry_equiv_pos_as_xyz
        '-x, -y, -z'
        '-x, y, z'
        '-x+1/2, -y, z+1/2'
        '-x+1/2, y, -z+1/2'
        '-y+1/4, -x+1/4, -z-1/4'
        '-y+1/4, x-1/4, z+1/4'
        '-y-1/4, -x+1/4, z-1/4'
        '-y-1/4, x-1/4, -z+1/4'
        'y+1/4, -x+1/4, z-1/4'
        'y+1/4, x-1/4, -z+1/4'
        'y-1/4, -x+1/4, -z-1/4'
        'y-1/4, x-1/4, z+1/4'
        'x, -y, -z'
        'x, y, z'
        'x+1/2, -y, z+1/2'
        'x+1/2, y, -z+1/2'
        '-x+1/2, -y+1/2, -z+1/2'
        '-x+1/2, y+1/2, z+1/2'
        '-x, -y+1/2, z'
        '-x, y+1/2, -z'
        '-y-1/4, -x-1/4, -z+1/4'
        '-y-1/4, x+1/4, z-1/4'
        '-y+1/4, -x-1/4, z+1/4'
        '-y+1/4, x+1/4, -z-1/4'
        'y-1/4, -x-1/4, z+1/4'
        'y-1/4, x+1/4, -z-1/4'
        'y+1/4, -x-1/4, -z+1/4'
        'y+1/4, x+1/4, z-1/4'
        'x+1/2, -y+1/2, -z+1/2'
        'x+1/2, y+1/2, z+1/2'
        'x, -y+1/2, z'
        'x, y+1/2, -z'
```

loop_
_atom_site_label
_atom_site_type_symbol
_atom_site_symmetry_multiplicity
_atom_site_fract_x
_atom_site_fract_y
_atom_site_fract_z
_atom_site_occupancy
_atom_site_B_iso_or_equiv
Al1 Al 16 0.31840(42) 0 0 1 0.74(12)
O1 O 16 0.25684(37) 0.00684(37) 0.125 1 0.74(12)
O2 O 32 0.38279(48) 0.00937(40) 0.12478(72) 1 0.74(12)
O3 O 32 0.33677(37) 0.06753(49) 0.27693(79) 1 0.74(12)
C1 C 32 0.5 0.08862(93) 0.4789(17) 1 0.74(12)
C2 C 32 0.44355(22) 0.07462(54) 0.41817(74) 1 0.74(12)
C3 C 32 0.5 0.0373(10) 0.2334(18) 1 0.74(12)
C4 C 16 0.44385(28) 0.05337(55) 0.28952(74) 1 0.74(12)
C5 C 16 0.38363(36) 0.03863(56) 0.22955(87) 1 0.74(12)

data_
_chemical_name_mineral **CAU10H2O**
_cell_length_a 21.29280(42)
_cell_length_b 21.29280(42)
_cell_length_c 10.73045(29)
_cell_angle_alpha 90
_cell_angle_beta 90
_cell_angle_gamma 90
_cell_volume 4865.01(23)
_symmetry_space_group_name_H-M I41
loop_
_symmetry_equiv_pos_as_xyz
'-x+1/2, -y+1/2, z+1/2'
'-y, x+1/2, z+1/4'
'y+1/2, -x, z-1/4'
'x, y, z'
'-x, -y, z'
'-y+1/2, x, z-1/4'
'y, -x+1/2, z+1/4'
'x+1/2, y+1/2, z+1/2'
loop_
_atom_site_label
_atom_site_type_symbol
_atom_site_symmetry_multiplicity
_atom_site_fract_x

_atom_site_fract_y
_atom_site_fract_z
_atom_site_occupancy
_atom_site_B_iso_or_equiv
Al1 Al 8 0.25543(34) 0.31384(35) 0.24427(82) 1 1.04(11)
Al2 Al 8 0.68023(32) 0.24569(33) 0.49332(85) 1 1.04(11)
O1 O 8 0.24869(46) 0.25942(44) 0.3805(14) 1 1.04(11)
O2 O 8 0.74159(40) 0.24565(42) 0.6248(14) 1 1.04(11)
O11 O 8 0.34296(32) 0.29910(39) 0.2213(15) 1 1.04(11)
O12 O 8 0.37685(52) 0.23623(38) 0.36955(86) 1 1.04(11)
C11 C 8 0.3840027 0.2652319 0.2677798 1 1.04(11)
C12 C 8 0.4441725 0.2638812 0.2012799 1 1.04(11)
C13 C 8 0.5006852 0.2601662 0.2677391 1 1.04(11)
C14 C 8 0.5577711 0.2687669 0.2051014 1 1.04(11)
C15 C 8 0.6164345 0.2752286 0.2755989 1 1.04(11)
C16 C 8 0.4452378 0.2729684 0.07067272 1 1.04(11)
C17 C 8 0.5020659 0.279699 0.00779776 1 1.04(11)
C18 C 8 0.5581572 0.277825 0.07447133 1 1.04(11)
O13 O 8 0.65747(27) 0.31092(38) 0.2350(10) 1 1.04(11)
O14 O 8 0.61520(41) 0.23827(41) 0.36435(83) 1 1.04(11)
O21 O 8 0.61510(55) 0.23349(31) 0.61487(83) 1 1.04(11)
O22 O 8 0.66472(30) 0.17040(42) 0.74989(87) 1 1.04(11)
C21 C 8 0.6168703 0.1874452 0.6826409 1 1.04(11)
C22 C 8 0.5579917 0.1683365 0.7451753 1 1.04(11)
C23 C 8 0.4992116 0.1899503 0.7029915 1 1.04(11)
C24 C 8 0.4436339 0.1675857 0.7585928 1 1.04(11)
C25 C 8 0.381207 0.1858979 0.710291 1 1.04(11)
C26 C 8 0.5605369 0.1251226 0.845279 1 1.04(11)
C27 C 8 0.5056948 0.103576 0.9015392 1 1.04(11)
C28 C 8 0.4476166 0.1243813 0.8585278 1 1.04(11)
O23 O 8 0.37952(50) 0.22270(41) 0.61569(86) 1 1.04(11)
O24 O 8 0.33152(34) 0.16816(47) 0.7590(13) 1 1.04(11)
Og1 O 8 0.15210(78) 0.16123(66) 0.3571(21) 1.000(23) 1.04(11)
Og2 O 8 0.05963(71) 0.07394(87) 0.3881(22) 0.759(19) 1.04(11)
Og3 O 8 -0.07003(67) 0.07315(78) 0.4043(17) 1.000(24) 1.04(11)
Og4 O 8 0.65907(81) 0.32458(79) 0.8033(18) 1.000(23) 1.04(11)
Og5 O 8 0.44584(79) 0.12564(78) 0.4407(20) 1.000(25) 1.04(11)
Og6 O 8 0.43204(58) -0.00025(55) 0.5665(14) 1.000(27) 1.04(11)
Og7 O 8 0.5 0 0.3511(57) 0.209(31) 1.04(11)

## 4) Modelling details of CAU-10-H

For the derivation of the partial charges of the CAU-10-H the Electronegativity Equalization Method (EEM) was employed following the approach described in a previous work[2]. Three parameters were used for each atom as input to the EEM to compute the partial charges in CAU-10-H; electronegativity, hardness, and gamma factor (see Table S4). These parameters were taken from analogous parameters of the aluminum-based carboxylate MOF, the MIL-100(Al), since these two MOFs consist of similar atom types. These EEM parameters were calculated on a small cluster of MIL-100(Al) so as to obtain the same partial charges as the ones derived by Density Functional Theory computations on the same cluster[3]. The implementation of the EEM for the unit cells of CAU-10-H resulted in the mean values for the partial charges shown in Table S4.

The above partial charges were employed in a fully flexible model for CAU-10-H used in the Molecular Dynamics simulations. The initial parameters for bonded and dispersion interactions were taken from Dreiding[4]; then the following modifications were made in order to achieve the best possible matching with the IR spectrum of the crystal:

(*i*) The equilibrium bond distances, $r_{IJ}^0$ , (Table S5) and angle values, $\theta_J^0$, (Table S6) were taken from the crystallographic data provided by the University of Kiel.

(*ii*) Except of the bond Al-O1 (that contributes to the stability of the chain of the cis-connected corner-sharing aluminium polyhedra), which was made stronger by shortening its equilibrium bond distance and increasing its force constant (see Table S5); it is worth mentioning that crystallography shows that this bond is slightly shorter that the rest Al-O bonds of the $AlO_6$ polyhedra.

(*iii*) The dispersion parameters for the bridging OH atoms (O1 and H7) were distinguished from the other oxygens and hydrogen atoms of CAU on the basis of their different electron charge (see Table S4); the charges on the O1 and H7 imply that the electrons of the hydrogen atom are shifted closer to the oxygen atom and, consequently the hydrogen atom is behaving like a point charge allowing for the proximity of other electronegative atoms (guest water oxygens) towards the creation of hydrogen bonding. To properly account for this, we used the dispersion parameters of the SPC/E model for the O1 and H7 which has been shown to describe well the formation of hydrogen bonds in liquid water[5].

(*iv*) The torsional potential for the four dihedral angles (O2-C6-C5-C1, O2-C6-C5-C3, O3-C6-C5-C1, O3-C6-C5-C3) was zeroed (see Fig. S5 for notation); these angles control the rotation

of the carboxylate group relative to the aromatic ring. Zeroing them enabled the quasi free rotation of the linkers. The quasi free rotation of the linker has been showed to better capture the host dynamics in our previous work on ZIF-8[6]. To verify the validity of our choice regarding the particular mobility of the linkers, a stiff version was also tested by imposing torsional potentials on them as dictated by Dreiding (see Table S7). This latter stiff model version for the linkers did not satisfactorily reproduce the experimental IR spectrum, it did not capture the linker dynamics upon water adsorption (Fig. S7) with respect to the Second Harmonic Generation (SHG) microscopy experiments of this work, and did not predict the structural transition of CAU cell upon water adsorption (Fig. S8, bottom). So, one could conclude that a realistic representation for CAU-10-H linkers definitely opts for flexible states.
All remaining parameters were left the same as in the Dreiding force field. The final parameters are given in Tables S4-S8. The notation of the framework atoms is shown in Fig. S5.

The potential interaction energy was computed as a sum of bonded and non-bonded energy terms:

$U = U_{bonded} + U_{nonbonded}$

where $U_{bonded} = U_{bonds} + U_{angles} + U_{torsions}$

and $U_{nonbonded} = U_{dispersion} + U_{electrostatic}$

The form of these terms is given below.

Bond stretch: $E_{IJ} = \frac{1}{2} k_{IJ} \left( r_{IJ} - r_{IJ}^0 \right)^2$, for atom *I* bonded to atom *J*

Angle bend: $E_{IJK} = \frac{1}{2} k_{IJK} \left( \theta_{IJK} - \theta_J^0 \right)^2$, for two bonds *IJ* and *JK*

Proper torsion: $E_{IJKL} = \frac{1}{2} V_{JK} \left\{ 1 - \cos\left[ n_{JK} \left( \varphi - \varphi_{JK}^0 \right) \right] \right\}$, for two bonds *IJ* and *KL* connected via a common bond *JK*

Improper torsion: $E_{IJKL} = K \left[ 1 - \cos \Psi \right]$, $\Psi^0 = 0^o$ , for an atom *I* bonded to exactly three other atoms, *J*, *K*, *L*, and planar equilibrium geometry. The angle is between the IL bond and JIK plane.

The dispersion interaction cutoff was 1.0 nm. The Lorentz−Berthelot rules were applied for describing guest−host interactions. Electrostatic interactions were computed through a particle-mesh Ewald summation code.

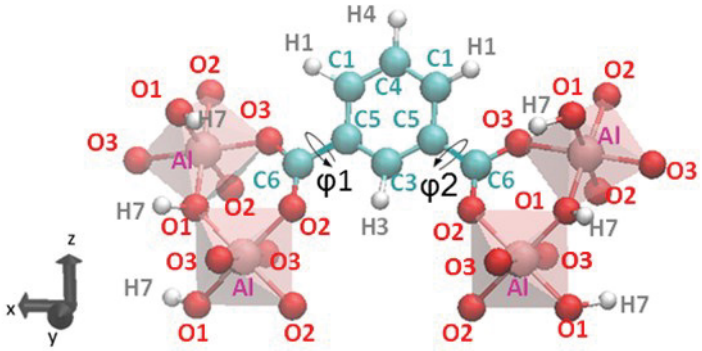


**Fig. S5** CAU-10-H atom notation; definition of the dihedrals O2-C6-C5-C1 ($\varphi_1$ and $\varphi_2$) denoting the motion of the carboxylate group relative to the aromatic ring.

**Table S4** Non-bonded and EEM parameters for the CAU-10-H atoms.

| atom type | atom | $\varepsilon$ (kcal/mol) | σ (Å) | EEM type | $\chi$ (eV/e) | $2\eta$(eV/e$^2$) | $\gamma$(A$^{-3}$) | partial charge (*e*) |
|---|---|---|---|---|---|---|---|---|
| Al | Al | 0.3100 | 3.9110 | Al | 0.8707 | 12.0000 | 0.5443 | 1.7116 |
| O1 | O | 0.1554 [a] | 3.1656[a] | OH | 11.380 | 16.6244 | 1.0898 | -1.1303 |
| O2 | O | 0.0957 | 3.0332 | OT | 7.2560 | 16.6244 | 1.0898 | -0.5997 |
| O3 | O | 0.0957 | 3.0332 | OT | 7.2560 | 16.6244 | 1.0898 | -0.5883 |
| C1 | C | 0.0951 | 3.4730 | CAR2 | 5.7396 | 14.0000 | 0.9000 | -0.1785 |
| C3 | C | 0.0951 | 3.4730 | CAR2 | 5.7396 | 14.0000 | 0.9000 | -0.2173 |
| C4 | C | 0.0951 | 3.4730 | CAR2 | 5.7396 | 14.0000 | 0.9000 | -0.0993 |
| C5 | C | 0.0951 | 3.4730 | CAR | 4.9896 | 14.0000 | 0.9000 | -0.0237 |
| C6 | C | 0.0951 | 3.4730 | CT | 3.7426 | 14.0000 | 0.9000 | 0.7103 |
| H1 | H | 0.0152 | 2.8464 | HAR | 3.0656 | 20.1678 | 0.8910 | 0.1820 |
| H3 | H | 0.0152 | 2.8464 | HAR | 3.0656 | 20.1678 | 0.8910 | 0.2157 |
| H4 | H | 0.0152 | 2.8464 | HAR | 3.0656 | 20.1678 | 0.8910 | 0.1580 |
| H7 | H | 0.0000[a] | --- [a] | HOH | 4.3178 | 19.2186 | 0.8203 | 0.3574 |

[a] SPC/E parameters for the O1 and H7 atoms of the bridging OH group

**Table S5** Bond stretch parameters for the CAU-10-H.

| *I-J* | $k_{IJ}$ (kcal/mol/Å²) | $r_{IJ}^0$ (Å) |
|---|---|---|
| C1-C4 | 1050 | 1.39 |
| C1-C5 | 1050 | 1.39 |
| C3-C5 | 1050 | 1.39 |
| C1-H1 | 700 | 1.02 |
| C3-H3 | 700 | 1.02 |
| C4-H4 | 700 | 1.02 |
| C5-C6 | 700 | 1.47 |
| Al-O1 | 2800 | 1.70 |
| Al-O2 | 700 | 1.90 |
| Al-O3 | 700 | 1.89 |
| O1-H7 | 700 | 1.00 |
| O2-C6 | 700 | 1.25 |
| O3-C6 | 700 | 1.28 |

**Table S6** Angle bend parameters for the CAU-10-H.

| *I-J-K* | $k_{IJK}$ (kcal/mol/rad²) | $\theta_J^0$ (degrees) |
|---|---|---|
| C1-C4-C1 | 100 | 120 |
| C4-C1-C5 | 100 | 120 |
| C1-C5-C3 | 100 | 120 |
| C5-C3-C5 | 100 | 120 |
| C3-C5-C1 | 100 | 120 |
| C5-C1-C4 | 100 | 120 |
| C1-C4-H4 | 100 | 120 |
| C1-C4-H4 | 100 | 120 |
| C4-C1-H1 | 100 | 120 |
| C5-C1-H1 | 100 | 120 |

| | | |
|---|---|---|
| C1-C5-C6 | 100 | 120 |
| C3-C5-C6 | 100 | 120 |
| C5-C3-H3 | 100 | 120 |
| C5-C3-H3 | 100 | 120 |
| C3-C5-C6 | 100 | 120 |
| C1-C5-C6 | 100 | 120 |
| C5-C1-H1 | 100 | 120 |
| C4-C1-H1 | 100 | 120 |
| O1-Al-O1 | 100 | 90 |
| O2-Al-O2 | 100 | 90 |
| O3-Al-O3 | 100 | 180 |
| O1-Al-O2 | 100 | 180 |
| O1-Al-O2 | 100 | 90 |
| O1-Al-O3 | 100 | 90 |
| O2-Al-O3 | 100 | 90 |
| Al-O2-C6 | 100 | 130.4 |
| Al-O3-C6 | 100 | 136.6 |
| O2-C6-C5 | 100 | 117.1 |
| O3-C6-C5 | 100 | 117.1 |
| O2-C6-O3 | 100 | 120 |
| Al-O1-Al | 100 | 126.6 |

**Table S7** Torsion interaction parameters for the CAU-10-H.

| *I-J-K-L* | $V_{JK}$ (kcal/mol) | $n_{JK}$ | $\varphi^0_{JK}$ (degrees) |
|---|---|---|---|
| C4-C1-C5-C3 | 25 | 2 | 0 |
| C1-C5-C3-C5 | 25 | 2 | 0 |
| C5-C3-C5-C1 | 25 | 2 | 0 |
| C3-C5-C1-C4 | 25 | 2 | 0 |
| C5-C1-C4-C1 | 25 | 2 | 0 |
| C1-C4-C1-C5 | 25 | 2 | 0 |
| C4-C1-C5-C6 | 25 | 2 | 0 |
| C1-C5-C3-H3 | 25 | 2 | 0 |
| C5-C3-C5-C6 | 25 | 2 | 0 |
| C3-C5-C1-H1 | 25 | 2 | 0 |
| C5-C1-C4-H4 | 25 | 2 | 0 |
| C1-C4-C1-H1 | 25 | 2 | 0 |
| C5-C1-C4-H4 | 25 | 2 | 0 |
| C1-C4-C1-H1 | 25 | 2 | 0 |
| C4-C1-C5-C6 | 25 | 2 | 0 |
| C1-C5-C3-H3 | 25 | 2 | 0 |
| C5-C3-C5-C6 | 25 | 2 | 0 |
| C3-C5-C1-H1 | 25 | 2 | 0 |
| H4-C4-C1-H1 | 25 | 2 | 0 |
| H1-C1-C4-H4 | 25 | 2 | 0 |
| H1-C1-C5-C6 | 25 | 2 | 0 |
| H3-C3-C5-C6 | 25 | 2 | 0 |
| H3-C3-C5-C6 | 25 | 2 | 0 |
| H1-C1-C5-C6 | 25 | 2 | 0 |
| O2-C6-C5-C1 | 5 | 2 | 0 |
| O2-C6-C5-C3 | 5 | 2 | 0 |
| O3-C6-C5-C1 | 5 | 2 | 0 |
| O3-C6-C5-C3 | 5 | 2 | 0 |

**Table S8** Improper torsion interaction parameters for CAU-10-H.

| *I-J-K-L* (central *I*) | $K$ (kcal/mol/rad$^2$) |
|---|---|
| C4-C1-C1-H4 | 40 |
| C1-C5-C4-H1 | 40 |
| C5-C3-C1-C6 | 40 |
| C3-C5-C5-H3 | 40 |
| C5-C1-C3-C6 | 40 |
| C1-C4-C5-H1 | 40 |
| C6-O2-O3-C5 | 40 |

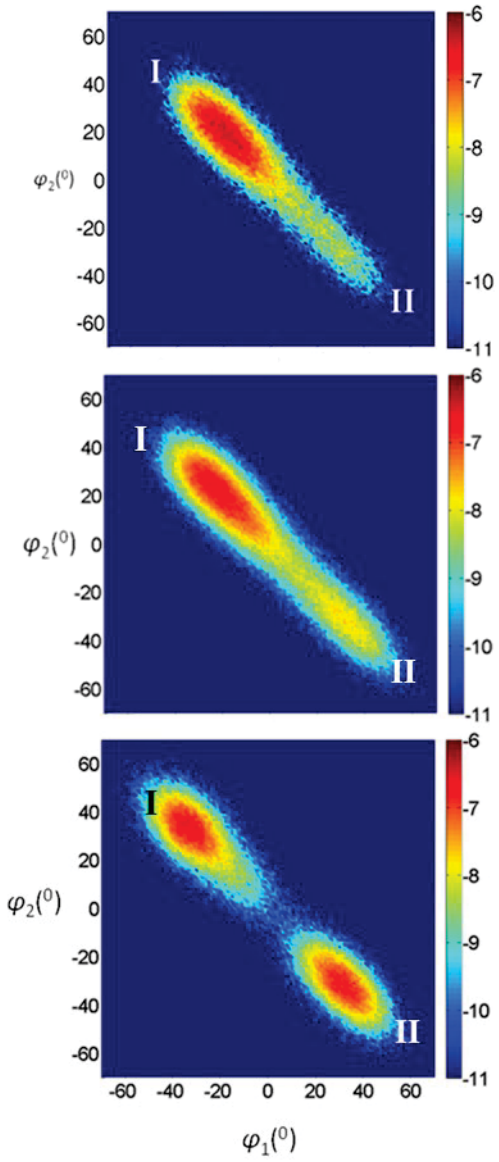


**Fig. S6** Correlation probabilities calculated by MD of the dihedral angles $\varphi_1$ and $\varphi_2$ for the CAU-10-H linkers, for the model option enabling quasi-free rotation of the linkers, for the dehydrated (top), and the water-loaded CAU-10-H at loadings of 0.032 (middle) and 0.303 $gg^{-1}$ (bottom). Colour code: low (blue) to high (red) probability values (in natural logarithmic scale). See analogous figure in the article, illustrating only the dehydrated (top) and the loading of 0.303 $gg^{-1}$ (bottom).

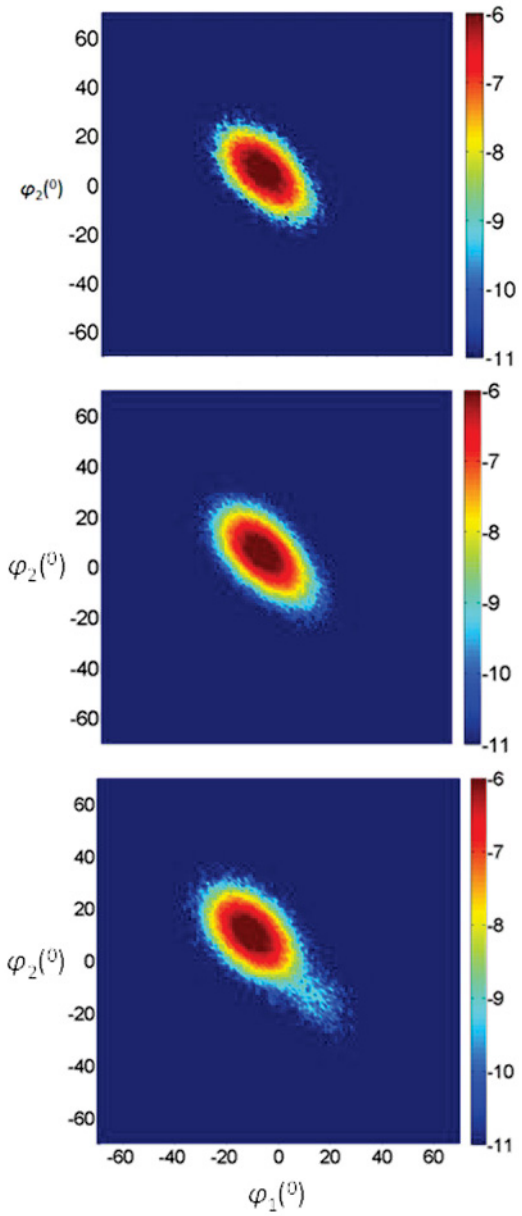


**Fig. S7** Correlation probabilities calculated by MD for the dihedral angles $\varphi_1$ and $\varphi_2$, for the model option imposing torsional potentials on the linkers, for the dehydrated (top), and the water-loaded CAU-10-H at loadings of 0.032 (middle) and 0.303 $gg^{-1}$ (bottom). Colour code: low (blue) to high (red) probability values (in natural logarithmic scale).

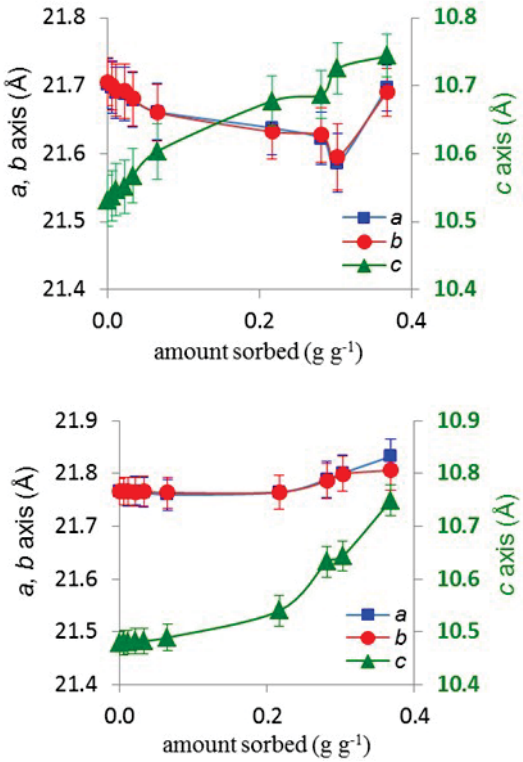


**Fig. S8** Simulated length evolution of the *a*, *b* and *c* axes of the CAU-10-H crystal unit cell induced by the water adsorption during an MD trajectory, as a function of loading: 0.005, 0.011, 0.022, 0.032, 0.065, 0.216, 0.281, 0.303 and 0.368 $gg^{-1}$, using the Andersen conventional isobaric algorithm in MD simulations, for the two model options: enabling quasi-free rotation of the linkers (top) and imposing torsional potentials on them (bottom).

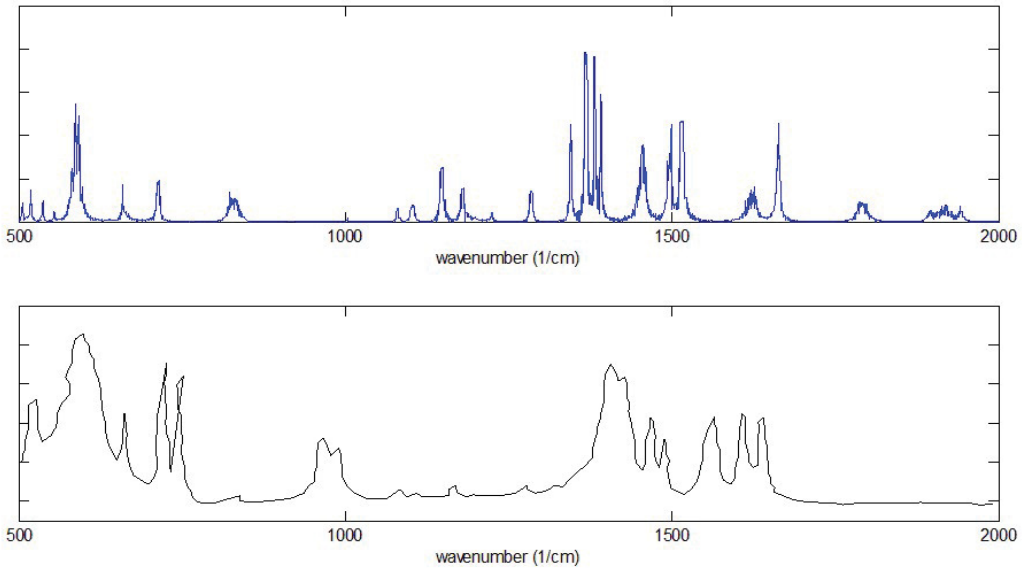


**Fig. S9** Computed (top) and measured[1] (bottom) IR spectra of CAU-10-H.

*We note that we have not simulated an identical IR spectrum with the measured one as this is extremely difficult and practically impossible although we tried hard because of the many degrees of freedom of the mobile CAU system of atoms. For this reason we also added error bars to all modelling experiments (Fig. 10 and Fig. 12 in paper). Also the spectrum is what we found from the last stage Fourier post-MD-processing namely raw results with no smoothening or fitting job on them. The alternative route of deriving ad hoc quantum mechanical parameters and then fitting for CAU-10-H is completely out of scope of this work because we cannot perform ab initio calculations of this type. Concluding we tried to make a reasonable adjustment of parameters, however; so that our modelling results will be reproducible.*

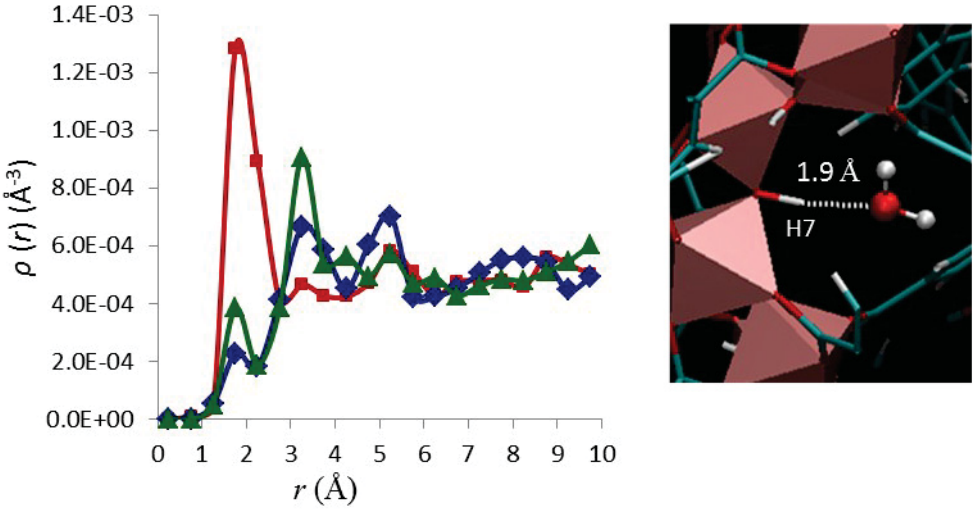


**Fig. S10** Density distribution functions of the guest water oxygens calculated with respect to the hydrogen atom (H7) of the bridging OH group (squares) and the O2 (rhombi) and O3 (triangles) oxygens of the carboxylate groups (see Fig. S5 for atoms notation) at low loading 0.011 $gg^{-1}$; on the right is depicted a snapshot from MD simulations showing the distance between the H7 atom of the bridging OH group and a guest water molecule.

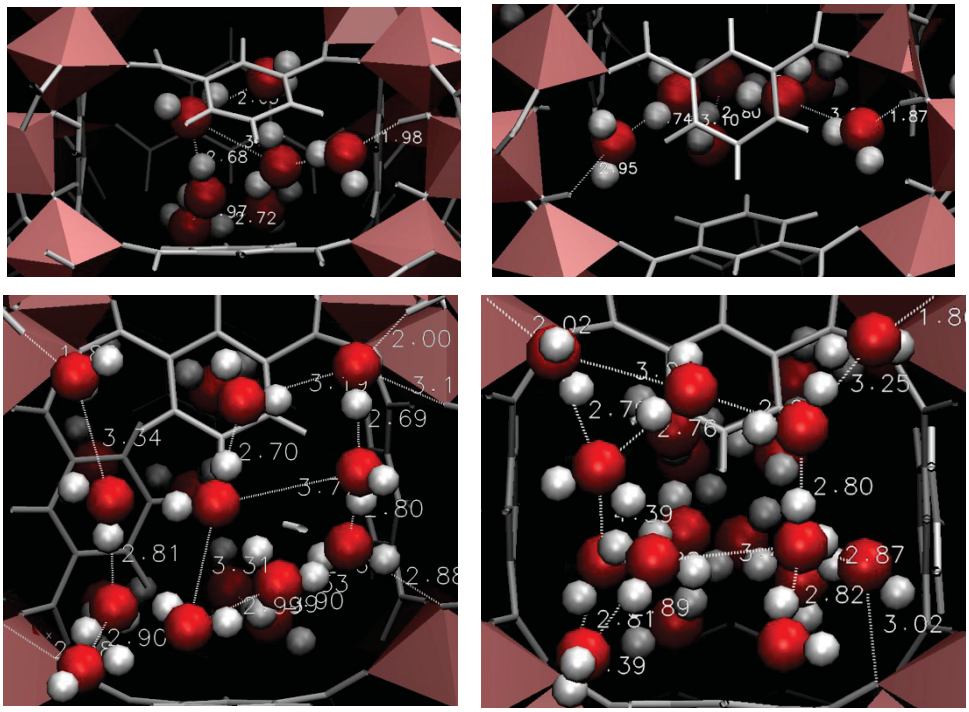


**Fig. S11** Indicative snapshots form MD simulation depicting the formation of water clusters at 0.065 (top, middle) and 0.216 $gg^{-1}$ loadings (bottom); colour code: aluminium polyhedra (pink), water molecule (H: white and O: red), linker and bridging OH group (grey).

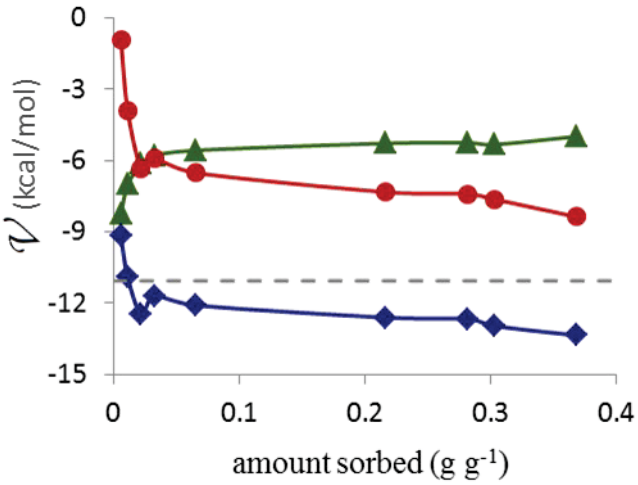


**Fig. S12** Guest−guest (circles) and guest−host (triangles) components of the total potential energy (rhombi) in the water/CAU-10-H system at 300 K as a function of loading; the dashed line points to the energy of liquid water at 300 K computed via the SPC/E model.

References

1. H. Reinsch, M. A. van der Veen, B. Gil, B. Marszalek, T. Verbiest, D. de Vos and N. Stock, *Chem. Mater.*, 2013, **25**, 17.
2. P. D. Kolokathis, E. Pantatosaki and G. K. Papadopoulos, *J. Phys. Chem. C*, 2015, **119**, 20074-20084.
3. Details provided in forthcoming publication by Pantatosaki et al.
4. S. L. Mayo, B. D. Olafson and W. A. Goddard, J. Phys. Chem., 1990, 94, 8897.
5. J. M. Sorenson, G. Hura, R. M. Glaeser and T. Head-Gordon, *J. Chem. Phys.* **2000**, *113*, 9149-9161.
6. E. Pantatosaki, G. Megariotis, A.-K. Pusch, C. Chmelik, F. Stallmach and G. K. Papadopoulos, *J. Phys. Chem.* C, **2012**, *116*, 201–207.

## 3.4 CAU-10 Synthesis Patent

Dominik Fröhlich, Dirk Nielinger, Albina Holz, Helge Reinsch, Norbert Stock, Stefan K. Henninger

WO 2017/046417 A1

After CAU-10-H showed such outstanding properties[52], we searched for a faster and easier way to produce it in large quantities, than the standard solvothermal synthesis in a autoclave at 140 °C.

We found a way to scale up the synthesis. This new method can be performed in a vessel at standard pressure and temperatures in the range of 100 °C within 6 hours. This resulted in a patent application.

Using this synthesis method, CAU-10-H can be produced in kilogram scale.

*Author's share of work:*

- idea of upscaling
- starting of collaboration with CAU-Kiel
- supervision of lab work

There are different possibilities for the synthesis of MOFs; most of them are solvothermal synthesized. For this a metal salt and an organic compound are suspended in a solvent or solvent mixture and the reaction mixture is heated in a pressure reactor. For the very promising MOF CAU-10-H the components would comprise isophtalic acid and aluminium sulfate in a 1:4 water:DMF suspension, which gets heated at 135°C in a teflon autoclave for 12 h. When it comes to terms of upscaling, this way of synthesis leads to several major drawbacks. The reaction must take place at 135 °C, therefore it is under pressure and has to be maintained in a pressure reactor. This hinders the reaction control, and as well raises the costs enormous when it comes to upscaling.

It would be preferable to develop a method that uses different reaction conditions, that lead to a shorter reaction time, less harmful and more environment friendly chemicals, and also takes smaller effort in terms of equipment.

All of this could be achieved. The reaction solvent was changed from DMF-$H_2O$ to alkaline water. The reaction temperature and pressure could be decreased from 135 °C to 100 °C, the vessel type could be changed from closed teflon to open glass, respectively reflux conditions. Also the reaction time could be decreased from 12 h to 6 h. This results in direct economic advantages in the large-scale implementation of the manufacturing process. Another advantage is that the washing procedure is reduced, as well as no vacuum thermal activation is required to remove residual DMF. The environment-friendliness of the process could also be enhanced, because the residues of the synthesis batch can be fed to the sewage treatment plant without further after treatment.

(12) NACH DEM VERTRAG ÜBER DIE INTERNATIONALE ZUSAMMENARBEIT AUF DEM GEBIET DES PATENTWESENS (PCT) VERÖFFENTLICHTE INTERNATIONALE ANMELDUNG

(19) Weltorganisation für geistiges Eigentum
Internationales Büro

(43) Internationales Veröffentlichungsdatum
23. März 2017 (23.03.2017)

WIPO | PCT

(10) Internationale Veröffentlichungsnummer
WO 2017/046417 A1

(51) Internationale Patentklassifikation:
*C07C 63/24* (2006.01) *C07F 15/02* (2006.01)
*C07C 51/41* (2006.01) *B01J 20/22* (2006.01)
*C07F 5/06* (2006.01)

(21) Internationales Aktenzeichen: PCT/EP2016/072152

(22) Internationales Anmeldedatum:
19. September 2016 (19.09.2016)

(25) Einreichungssprache: Deutsch

(26) Veröffentlichungssprache: Deutsch

(30) Angaben zur Priorität:
10 2015 115 738.1
17. September 2015 (17.09.2015) DE

(71) Anmelder: **CHRISTIAN-ALBRECHTS-UNIVERSITÄT ZU KIEL** [DE/DE]; Christian-Albrechts-Platz 4, 24118 Kiel (DE). **FRAUNHOFER-GESELLSCHAFT ZUR FÖRDERUNG DER ANGEWANDTEN FORSCHUNG E. V.** [DE/DE]; Hansastr. 27c, 80686 München (DE).

(72) Erfinder: **FRÖHLICH, Dominik**; Gutleutstr.1, 79115 Freiburg (DE). **HOLZ, Albina**; Elsässerstraße 39, 79110 Freiburg (DE). **HENNINGER, Stefan**; Wilhelmskapelle 38a, 79346 Endingen a. K. (DE). **LENZEN, Dirk**; Dörpacker 34, 24896 Treia (DE). **REINSCH, Helge**; Hanssenstraße 1a, 24106 Kiel (DE). **STOCK, Norbert**; Olshausenstraße 14, 24118 Kiel (DE).

(74) Anwalt: **FUCHS PATENTANWÄLTE PARTNERSCHAFT MBB**; Westhafenplatz 1, 60327 Frankfurt am Main (DE).

(81) Bestimmungsstaaten *(soweit nicht anders angegeben, für jede verfügbare nationale Schutzrechtsart)*: AE, AG, AL, AM, AO, AT, AU, AZ, BA, BB, BG, BH, BN, BR, BW, BY, BZ, CA, CH, CL, CN, CO, CR, CU, CZ, DE, DK, DM, DO, DZ, EC, EE, EG, ES, FI, GB, GD, GE, GH, GM, GT, HN, HR, HU, ID, IL, IN, IR, IS, JP, KE, KG, KN, KP, KR, KW, KZ, LA, LC, LK, LR, LS, LU, LY, MA, MD, ME, MG, MK, MN, MW, MX, MY, MZ, NA, NG, NI, NO, NZ, OM, PA, PE, PG, PH, PL, PT, QA, RO, RS, RU, RW, SA, SC, SD, SE, SG, SK, SL, SM, ST, SV, SY, TH, TJ, TM, TN, TR, TT, TZ, UA, UG, US, UZ, VC, VN, ZA, ZM, ZW.

*[Fortsetzung auf der nächsten Seite]*

(54) **Title**: METHOD FOR PRODUCING METAL-ORGANIC FRAMEWORKS

(54) **Bezeichnung** : Verfahren zur Herstellung von metallorganischen Gerüststrukturverbindungen

Fig. 1

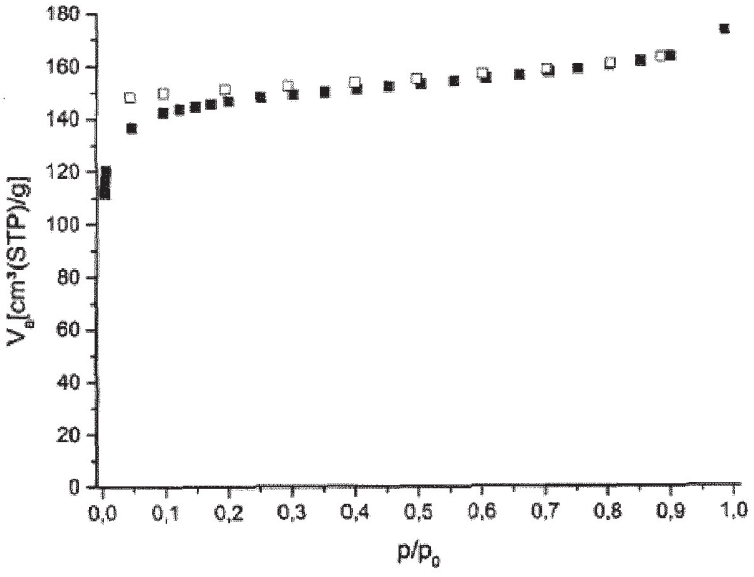


(57) **Abstract**: The present invention relates to a method for producing a metal-organic framework, the metal-organic framework produced by means of this method and the use of the metal-organic framework produced by means of this method as an adsorbent.

(57) **Zusammenfassung**: Die vorliegende Erfindung betrifft ein Verfahren zur Herstellung einer metallorganischen Gerüststrukturverbindung, die so hergestellte metallorganische Gerüststrukturverbindung sowie die Verwendung der so hergestellten metallorganischen Gerüststrukturverbindung als Adsorbens.

WO 2017/046417 A1

(84) **Bestimmungsstaaten** *(soweit nicht anders angegeben, für jede verfügbare regionale Schutzrechtsart)*: ARIPO (BW, GH, GM, KE, LR, LS, MW, MZ, NA, RW, SD, SL, ST, SZ, TZ, UG, ZM, ZW), eurasisches (AM, AZ, BY, KG, KZ, RU, TJ, TM), europäisches (AL, AT, BE, BG, CH, CY, CZ, DE, DK, EE, ES, FI, FR, GB, GR, HR, HU, IE, IS, IT, LT, LU, LV, MC, MK, MT, NL, NO, PL, PT, RO, RS, SE, SI, SK, SM, TR), OAPI (BF, BJ, CF, CG, CI, CM, GA, GN, GQ, GW, KM, ML, MR, NE, SN, TD, TG).

**Veröffentlicht**:

— *mit internationalem Recherchenbericht (Artikel 21 Absatz 3)*

— *vor Ablauf der für Änderungen der Ansprüche geltenden Frist; Veröffentlichung wird wiederholt, falls Änderungen eingehen (Regel 48 Absatz 2 Buchstabe h)*

# Verfahren zur Herstellung von metallorganischen Gerüststruktur-verbindungen

Die vorliegende Erfindung betrifft ein Verfahren zur Herstellung einer metallorganischen Gerüststrukturverbindung, die so hergestellte metallorganische Gerüststrukturverbindung sowie die Verwendung der so hergestellten metallorganischen Gerüststrukturverbindung als Adsorbens.

Adsorptionswärmespeicher bieten die Möglichkeit einer nahezu verlustfreien Speicherung von Wärme, insbesondere im Temperaturbereich bis 250 °C, über lange Zeiträume. Ein Bedarf an solchen Langzeit-Wärmespeichern besteht insbesondere im Zusammenhang mit der solarthermischen Gebäudeheizung in Erdregionen mit starker jahreszeitlicher Schwankung der solaren Einstrahlung, d.h. in allen äquatorfernen Regionen. Hier fällt im Jahresverlauf das größte Angebot der Solarwärme aus thermischen Kollektoren in den Sommer, der Heizwärmebedarf jedoch überwiegend in den Winter. Im Sinne des Aufbaus einer nachhaltigen Energieversorgung, die verstärkt auf erneuerbare Energiequellen setzt, ist die saisonale Wärmespeicherung für die Gebäudeheizung wünschenswert und ist Voraussetzung zur Erreichung hoher solarer Deckungsanteile bei der solarthermischen Gebäudeheizung.

Die Wärmespeicherung im Temperaturbereich bis ca. 250 °C ist auch für viele andere Anwendungen ein wichtiges Thema. So besteht z.B. bei der dezentralen Stromerzeugung in Anlagen mit Kraft-Wärme-Kopplung (KWK) typischerweise das Problem unterschiedlicher zeitlicher Bedarfsprofile für Strom und Wärme. Um diese Anlagen stromgeführt betreiben zu können und die erzeugte Wärme nutzen zu können, muss diese Wärme zwischengespeichert werden, bis sie gebraucht wird. Dazu werden Wärmespeicher mit hoher Energiedichte und hoher Effizienz, d.h. geringen Wärmeverlusten, benötigt.

Adsorptionswärmespeicher haben sich trotz jahrzehntelanger Forschungsanstrengungen bisher nicht am Markt durchgesetzt. Es fehlte bisher vor allem an Adsorptionsmaterialien, die im gewünschten Temperaturbereich einen großen Beladungs- und Wärmeumsatz zeigen. Die vielfach für Wärmespeicheranwendungen untersuchten und eingesetzten Zeolithe, z.B. Zeolithe mit den Strukturtypen LTA und FAU, insbesondere die kommerziell erhältlichen Zeolithe A, X und Y, erfordern typischerweise zur Desorption eine treibende Temperaturdifferenz von mindestens 100 °C zwischen Adsorber und Kondensator, also bei einer Kondensatortemperatur von 35 °C eine Desorptionstemperatur von mindestens 135 °C. Diese Tempe-

ratur kann mit typischen Flachkollektoren nicht oder nur bei sehr geringer Kollektoreffizienz erreicht werden. Es werden daher teurere Vakuumröhrenkollektoren oder strahlungskonzentrierende Kollektoren benötigt. Unter typischen Be- und Entladebedingungen eines saisonalen solaren Speichersystems, wie z.B. beschrieben in Mittelbach et al., *"Solid sorption thermal energy storage for solar heating Systems"* (TERRASTOCK 2000, Stuttgart, 28.8. - 1.9.2000), werden mit den genannten Zeolithen Beladungsumsätze von nicht mehr als 0,18 Gramm Wasser pro Gramm Zeolith erreicht. Bezogen auf die Dichte einer Schüttung des Zeoliths sind damit Speicher-Energiedichten bis etwa 150 kWh/m$^3$ erreichbar (A. Hauer, Dissertation, TU Berlin 2002, *"Beurteilung fester Adsorbentien in offenen Sorptionssystemen für energetische Anwendungen"*).

Mit Silikagelen werden vergleichbare Energiedichten erreicht, hier ist das Hauptproblem der geringe nutzbare Temperaturhub bei der Entladung des Speichers.

Für die saisonale solare Wärmespeicherung wird daher nach Adsorbentien gesucht, deren Wasser-Adsorptionseigenschaften zwischen denen typischer Zeolithe und typischer Silikagele liegen. Insbesondere werden Materialien gesucht, deren Adsorptionsisobaren zu einem Wasserdampfdruck von etwa 56 hPa (entsprechend einem Wasserreservoir bei 35 °C) im Temperaturbereich von etwa 60-110 °C eine Beladungsänderung von mindestens 0,2 g/g zeigen.

Metallorganische Gerüstsubstanzen (Metal-Organic Frameworks, MOFs) wurden im Hinblick auf einen möglichen Einsatz als Hochtemperatur-Wasserstoffspeicher oder generell zur sorptiven Gasspeicherung entwickelt (U. Müller, *"Metal-organic frameworks-prospective industrial applications"*, J. Mater. Chem. 16(2006), S. 626-636). Aufgrund der hohen Porosität und Oberfläche eignen sie sich für vielfältige weitere Einsatzgebiete, die klassischerweise durch Zeolithe abgedeckt werden, wie etwa die heterogene Katalyse oder zur Gasreinigung.

MOFs zeichnen sich durch einen modularen Aufbau aus. Sie bestehen aus anorganischen mehrkernigen Komplexen (Cluster), welche als Konnektoren im Netzwerk dienen. Die Zähligkeit und Topologie des Konnektors wird dabei durch die nach außen gerichteten koordinierenden Liganden bestimmt. Als verknüpfende Bausteine (Linker) werden bi-, tri- und multifunktionale Liganden eingesetzt.

Insbesondere MOFs auf Basis von Aluminium als Metallcluster sind hinsichtlich der technischen Verwendung aufgrund des gut verfügbaren und nicht toxischen Metalls sehr vielver-

sprechend. Für viele Anwendungen ist jedoch die geringe Stabilität gegenüber Wasser und insbesondere Wasserdampf hinderlich.

Beispielsweise ist bei der Methanspeicherung eine Restfeuchte im großtechnischen Maßstab nicht zu verhindern. Für die Verwendung in Wärmepumpen und Kältemaschinen auf Basis der Adsorption von Kältemitteln wie beispielsweise Wasser aber auch Alkoholen oder natürlichen Kältemitteln (Propan etc.) wird ebenfalls eine Stabilität gegenüber Wasserdampf vorausgesetzt.

Während sich die Stabilität gegenüber Wasser bei der Verwendung von Wasser als Kältemittel direkt ergibt, ist die Stabilität gegenüber Wasser aber auch bei den anderen Kältemitteln von Bedeutung, da beispielsweise in einigen Prozessschritten der Kontakt zu Wasserdampf (Luftfeuchte bei der Herstellung) nicht verhindert werden kann. Hierbei zeichnet sich beispielsweise das MOF CAU-10-H als sehr vielversprechend ab, da dieser eine hohe Stabilität bei gleichzeitig guter Adsorptionscharakteristik aufweist.

Für die Synthese von MOFs gibt es unterschiedliche Möglichkeiten; die meisten MOFs sind durch Solvothermalsynthesen zugänglich. Dabei werden ein Metallsalz und eine organische Verbindung in einem Lösungsmittel oder Lösungsmittelgemisch suspendiert und das Reaktionsgemisch in einem Druckreaktor erhitzt. Dies ist auch die in der Literatur zu findende, gängige Synthese für CAU-10-H (H. Reinsch, M. A. van der Veen, B. Gil, B. Marszalek, T. Verbiest, D. de Vos and N. Stock, *Chemistry of Materials,* 2013, **25,** 17-26): Als Reaktionsgemisch dient eine Suspension von Isophthalsäure (1,3-$H_2$BDC) und $Al_2(SO_4)_3$*$18H_2O$ in DMF und Wasser (1:4 Teile). Die Synthese wird in einem Autoklaven mit Teflon-Linern über 12 h bei 135 °C ausgeführt. Es wird berichtet, dass bei der Synthese in einem Glasreaktor eine unbekannte, kristalline Nebenphase erhalten wurde. In dieser Literaturstelle wird CAU-10-H in einem 37 ml Autoklaven hergestellt. Zwar wird erwähnt, dass eine Maßstabsvergrößerung in größeren Autoklaven denkbar ist, der Nachweis wird aber nicht erbracht.

Gerade wasserstabile MOFs, die als Sorptionsmaterial für Wärmetransformationsanwendungen eingesetzt werden sollen, werden mit Wasser bei Überdruck hergestellt, was mit den bekannten, großtechnischen Problemen einhergeht:

1. Aufgrund der typischen Reaktionstemperaturen (>100 °C) muss unter Überdruck und in entsprechenden Gefäßen (Autoklaven) gearbeitet werden.

2. Dies erschwert die Reaktionskontrolle (kein Einblick in die Gefäße) und erhöht den Kostenaufwand enorm, insbesondere dann, wenn Solvothermalsynthesen verwendet werden sollen.

3. Die Verwendung von Glaskolben ist kaum oder nur eingeschränkt möglich.

Für MIL-160, einem zu CAU-10-H isostrukturellen MOF, ist eine drucklose Synthese in wässriger Lösung bekannt geworden, bei der Furandicarbonsäure mit Aluminium(III)chlorid über einen Zeitraum von 24 Stunden umgesetzt wird. Die Aufreinigung erfolgt mittels Zentrifugation. Nachteilig ist einerseits die Verwendung von Aluminium(III)chlorid, welches nicht wasserstabil und korrosiv ist. Die Aufreinigung mittels Zentrifugation ist zeitintensiv und apparativ aufwändig.

DE 10 2014 215 568 A1 offenbart ein Verfahren zur Herstellung eines Adsorbens aus metallorganischen Gerüststrukturen. Die Strukturen sollen bei Atmosphärendruck herstellbar sein. Es wird ein Lösungsmittelgemisch aus DMSO und Wasser verwendet, wobei relativ wenig Wasser und viel DMSO (wenigstens 50 Gew.-%) eingesetzt wird. Ziel ist es, durch das DMSO einen Siedepunkt oberhalb von 100°C zu erreichen. Das Wasser im Reaktionsgemisch spielt eine Nebenrolle und DMSO wird als entscheidend für den erfindungsgemäßen Erfolg angesehen. DMSO hat den Nachteil, dass es mit einigen Metallsalzen, die ebenfalls bei der MOF-Synthese eingesetzt werden, explosive Gemische bildet. Die Reaktionszeiten liegen im Bereich von 24 Stunden und sind damit im Vergleich zur vorliegenden Erfindung sehr lang. Das Dokument offenbart nicht die Verwendung einer wässrigen Lösung für die Synthese.

US 2011/0282071 A1 offenbart fotoaktive Triazolstrukturen. Es wird ein Beispiel für eine aromatische Dicarbonsäure gegeben. Es wird aber nicht die Synthese der aromatischen Dicarbonsäure in wässriger Lösung offenbart.

DE 10 2006 043 648 A1 lehrt ein Verfahren zur Herstellung von MOFs als Adsorbens. Die

Synthese wird in einem organischen Lösungsmittel mit vergleichsweise hohem Siedepunkt durchgeführt, z.B. in DMF. Die Reaktionszeit liegt im Bereich von 5 Tagen.

DE 10 2005 039 654 A1 betrifft mesoporöse MOF-Verbindungen. Es wird als entscheidend beschrieben, dass die strukturellen Merkmale wenigstens eines Stickstoffatoms im Heteroaromaten des Linkers und wenigstens dreier Substituenten X in Form von Carboxylgruppen (bzw. deren Thioderivaten) unbedingt einzuhalten sind. Andernfalls würden die hohen spezifischen Oberflächen und die gewünschte mesoporöse Struktur nicht erreicht. Es wird somit von der Verwendung aromatischer Dicarbonsäuren abgeraten. Die Synthese findet in organischem Lösungsmittel statt. Der Einsatz von Wasser wird nicht empfohlen. Die Reaktionszeiten sind mit 4 Tagen sehr lang. Es wäre ein Herstellungsverfahren für MOFs wünschenswert, das

- im Vergleich zu den Verfahren aus dem Stand der Technik weniger Reaktionszeit erfordert,
- im Hinblick auf die Umwelt unbedenklich ist,
- keine besonderen Anforderungen an die Arbeitssicherheit stellt (z.B. Explosionsgefahr),
- keinen großen apparativen Aufwand erfordert (z.B. Autoklav) und
- MOFs in sehr guter Qualität, insbesondere mit hoher Wasserstabilität und großer spezifischer Oberfläche, erhältlich macht.

Aufgabe der vorliegenden Erfindung war es daher, eine Syntheseroute für CAU-10-H und strukturell verwandte MOFs bereitzustellen, die die Nachteile des Standes der Technik überwindet.

Diese Aufgabe wird in einem ersten Aspekt gelöst durch ein Verfahren zur Herstellung einer metallorganischen Gerüststrukturverbindung, bei dem mindestens ein Metallsalz umfassend ein Metallkation ausgewählt aus der Gruppe bestehend aus den Übergangsmetallen, Mg und Al sowie Kombinationen daraus mit einer Linkerverbindung umgesetzt wird, dadurch gekennzeichnet, dass die Umsetzung in wässriger Lösung bei einem Druck von 1,5 bar oder weniger erfolgt. Dabei ist die Linkerverbindung ausgewählt aus der Gruppe bestehend aus substituierten und unsubstituierten aromatischen Dicarbonsäuren und aromatischen Dicarboxylaten sowie Kombinationen und Mischungen daraus.

Eine „aromatische Dicarbonsäure“ bzw. ein „aromatisches Dicarboxylat“ ist eine Verbindung, die wenigstens einen aromatischen Ring, insbesondere genau einen aromatischen Ring, als Strukturelement aufweist, der mit wenigstens zwei, insbesondere genau zwei, Carboxylgruppen substituiert ist. Der Aromat kann ein Fünfring-Aromat der folgenden Gruppe: Thiophen, Pyrrol, Furan, Imidazol, Pyrazol, Oxazol und Isoxazol, Thiazol; oder ein Sechsring-Aromaten der Gruppe bestehend aus Phenyl, Pyridin, Pyrazin, Pyrimidin und Pyridazin umfassen.

Unter aromatischen Dicarbonsäuren werden erfindungsgemäß bevorzugt Strukturen der allgemeinen Formel 1 verstanden. Unter aromatischen Dicarboxylaten werden erfindungsgemäß bevorzugt Strukturen der allgemeinen Formel 2 verstanden, wobei die Phenylgruppe durch einen anderen aromatischen oder heteroaromatischen Ring ersetzt sein kann, insbesondere einen Fünfring-Aromaten der folgenden Gruppe: Thiophen, Pyrrol, Furan, Imidazol, Pyrazol, Oxazol und Isoxazol, Thiazol; oder einen Sechsring-Aromaten der Gruppe bestehend aus Pyridin, Pyrazin, Pyrimidin und Pyridazin. In bevorzugten Ausführungsformen ist der Phenylring nicht durch andere Gruppen ersetzt, so dass es sich bei der Linkerverbindung vorzugsweise um Isophthalsäure, ein Isophthalat oder ein Derivat davon handelt. In alternativen Ausführungsformen ist die Linkerverbindung ausgewählt aus Trimesinsäure, Thiophen-Dicarbonsäure, Pyridin-Dicarbonsäure und Furandicarbonsäure sowie deren Carboxylaten und Derivaten. Die Carboxylgruppen können wie hier gezeigt in 1- und 3-Position angeordnet sein. Es sind aber auch 1,2- und 1,4-Stellungen erfindungsgemäß.

**Formel 1**

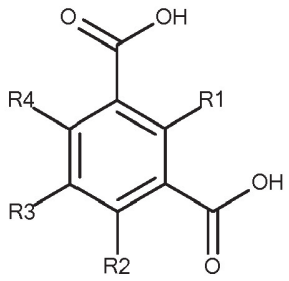

**Formel 2**

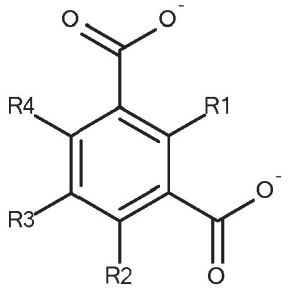


Die Reste R1 bis R4 sind vorzugsweise unabhängig voneinander ausgewählt aus Wasserstoff, Carboxy-, Hydroxy-, Nitro-, Amino-, Methyl-, Ether- und Halogenidgruppen sowie Kombinationen davon. In bevorzugten Ausführungsformen sind alle Reste R1 bis R4 Wasserstoff. In bevorzugten Ausführungsformen ist R3 ausgewählt aus Amino-, Nitro-, Hydroxy-, Methylether- und Methylgruppe.

In bevorzugten Ausführungsformen ist die Linkerverbindung ausgewählt aus Isophthalsäure und Isophthalaten. Erfindungsgemäß umfassen die Begriffe „Isophthalsäure" bzw. „Isophthalate" auch deren Derivate, insbesondere an 2-, 4-, 5- oder 6-Position substituierte Derivate. Als geeignete Substituenten kommen Hydroxy-, Nitro-, Amino-, Methyl-, Ether- und Halogenidgruppen sowie Kombinationen davon in Frage.

Vorzugweise findet die Reaktion in wässriger Lösung statt. Da viele aromatische Dicarbonsäuren in Wasser mitunter schlecht löslich sind, ist es bevorzugt die aromatischen Dicarboxylate zu verwenden. Die Dicarboxylate werden vorzugsweise in Form ihrer Salze, vorzugsweise als Natrium, Kalium oder Ammoniumsalze, eingesetzt.

Bevorzugte Metalle sind Fe, Co, Ni, Zn, Zr, Cu, Cr, Mo, Mg, Mn, Al, Pd und Kombinationen davon, besonders bevorzugt sind Al, Fe, Cu, Cr, Zr sowie Kombinationen davon. In ebenfalls bevorzugten Ausführungsformen sind die Metalle ausgewählt aus Sc, Ti, V, Cr, Mn, Fe, Co, Ni, Cu, Zn sowie Kombinationen davon. In besonders bevorzugten Ausführungsformen ist das Metall ausgewählt aus Al und Fe. Gerade bei Verwendung von Aluminium lassen sich sehr wasserstabile Gerüststrukturverbindungen herstellen. Die Metalle werden vorzugsweise in Form ihrer wasserlöslichen Salze, insbesondere der Sulfate, Nitrate, Carbonate, Oxidchloride oder Halogenide eingesetzt. Besonders bevorzugt ist die Verwendung von Sulfaten und/oder Halogeniden. Es kommen aber auch jeweils andere Salze in Frage.

„Umsetzung in wässriger Lösung" meint erfindungsgemäß bevorzugt, dass im Wesentlichen

keine organischen Lösungsmittel in dem Reaktionsmedium eingesetzt werden. Vorteilhafte wässrige Lösungen umfassen weniger als 10 Vol.-%, insbesondere weniger als 5 Vol.-%, weiter bevorzugt weniger als 2 Vol.-% und besonders bevorzugt weniger als 1 Vol.-% organisches Lösungsmittel wie DMF. In bevorzugten Ausführungsformen enthält das Reaktionsmedium keinerlei organisches Lösungsmittel. Der Anteil an Wasser in der wässrigen Lösung beträgt insbesondere mehr als 50 Vol.-%, mehr bevorzugt wenigstens 70 Vol.-%, insbesondere mehr als 80 Vol.-% und besonders bevorzugt wenigstens 90 Vol.-% oder wenigstens 99 Vol.-%.

In besonderen Ausführungsformen können kurzkettige Alkohole mit Kohlenstoffkettenlängen von 1 bis 4 Kohlenstoffatome, insbesondere Ethanol, in den Reaktionsmedien dieser Erfindung eingesetzt werden. Deren Anteil ist vorzugsweise auf höchstens 20 Vol.-%, mehr bevorzugt höchstens 10 Vol.-% des verwendeten Lösungsmittels beschränkt.

Kernpunkt der vorliegenden Erfindung ist ein neuer Syntheseansatz, bei dem abweichend vom Stand der Technik eine im Wesentlichen drucklose Synthese durchgeführt wird. Die vorliegende Erfindung umfasst vorzugweise als weiteren Aspekt die Verwendung von Lösungen der Edukte und nicht von Feststoffen bzw. Suspensionen. Dies ist insbesondere in Kombination mit der drucklosen Synthese von Vorteil. So kann als Lösungsmittel vorzugsweise Wasser eingesetzt werden, und es ist kein Druckreaktor notwendig.

Daher erfolgt in einer bevorzugten Ausgestaltung des erfindungsgemäßen Verfahrens die Umsetzung bei einem Druck von wenigstens 900 mbar, insbesondere wenigstens 1 bar. In bevorzugten Ausführungsformen beträgt der Druck höchstens 1,2 bar oder höchstens 1,1 bar. Die Reaktion kann also bei Atmosphärendruck durchgeführt werden. Hieraus ergeben sich unmittelbare wirtschaftliche Vorteile bei der großtechnischen Umsetzung des Herstellungsverfahrens. Beispielsweise kann eine kontinuierliche Produktion realisiert werden, indem entstandenes Produkt aus dem Prozess entnommen wird. Dies kann durch Filtration erfolgen. Eine vorteilhafte Ausgestaltung des erfindungsgemäßen Verfahrens umfasst die Isolierung der hergestellten metallorganischen Gerüststrukturverbindung mittels Filtration. Isolierung des Produktes mittels Filtration ist leichter in ein kontinuierliches Verfahren umzusetzen als die Isolierung mittels Zentrifugation.

Weiterhin ist die Aufarbeitung wesentlich einfacher, da nur ein Waschschritt notwendig ist und keine thermische Aktivierung, um beispielsweise Reste von DMF zu entfernen.

Im Ergebnis wird die Recyclingfähigkeit dadurch deutlich erhöht, und die Reste des Syntheseansatzes können ohne weitere Nachbehandlung direkt der Kläranlage zugeführt werden. Auch das Produkt ist somit unmittelbar frei von organischem Lösungsmittel.

In einer bevorzugten Ausgestaltung des erfindungsgemäßen Verfahrens erfolgt die Umsetzung bei einer Temperatur von 80 bis 120°C, insbesondere 90 bis 110°C. In einer Ausführungsform beträgt die Umsetzungstemperatur maximal 100°C. Die Umsetzung erfolgt insbesondere am Siedepunkt des Reaktionsmediums.

Ein weiterer technischer Vorteil der erfindungsgemäßen Synthesemethode liegt darin, dass verglichen mit der schlechten Löslichkeit der aromatischen Dicarbonsäure (z.B. Isophthalsäure) das aromatische Dicarboxylat (z.B. Isophthalat) leicht in Wasser gelöst wird. Das hat insbesondere für eine industrielle Umsetzung Vorteile, da die Reaktionszeit deutlich verkürzt wird, von 12 h wie in der Literatur auf beispielsweise 6 h oder 3 h im Kolben. Damit einhergehend kann ein höherer STY (Raum-Zeit-Ausbeute) erreicht werden. Daher erfolgt in einer bevorzugten Ausgestaltung des erfindungsgemäßen Verfahrens die Umsetzung über einen Zeitraum von 10 Stunden oder weniger, insbesondere von 8 Stunden oder weniger, besonders bevorzugt 6 Stunden oder weniger.

In einer weiteren bevorzugten Ausgestaltung des erfindungsgemäßen Verfahrens erfolgt die Umsetzung unter Bestrahlung der wässrigen Lösung mit Mikrowellen. Es sind aber auch andere dem Fachmann geläufige Verfahren zur Erwärmung des Reaktionsgefäßes erfindungsgemäß.

Im Gegensatz zur literaturbekannten Synthese wird gemäß bevorzugten erfindungsgemäßen Verfahren von aromatischen Dicarboxylaten (z.B. Isophthalaten) ausgegangen und nicht von der in Wasser schwer löslichen aromatischen Dicarbonsäure (z.B. Isophthalsäure). In der literaturbekannten Synthese muss daher wegen der schlechten Löslichkeit DMF als Lösungsmittel und erhöhte Temperatur eingesetzt werden.

Für das erfindungsgemäße Verfahren kann jedes beliebige aromatische Dicarboxylat verwendet werden (z.B. Isophthalat). Bevorzugt verwendet werden Natriumdicarboxylate (z.B. Natriumisophthalate), Kaliumdicarboxylate (z.B. Kaliumisophthalate), Ammoniumdicarboxylate (z.B. Ammoniumisophthalate) und Mischungen daraus.

Für das erfindungsgemäße Verfahren können prinzipiell alle zuvor beschriebenen Metallsalze verwendet werden. Vorzugsweise verwendet werden Eisen- und Aluminiumsalze.

Im Gegensatz zur literaturbekannten Synthese wird vorzugsweise Aluminium-Sulfat in Kombination mit Natriumdicarboxylat (z.B. Natriumisophthalat) sowie gleichzeitig eine anorganische Base, insbesondere Natriumhydroxid, Calciumhydroxid, Kaliumhydroxid, Ammoniak oder Natriumaluminat in einer Lösung und in einem Glasgefäß anstelle eines Teflongefäßes verwendet.

Die Verwendung von Al-Sulfat ist zunächst nicht naheliegend, da die Bildung von Nebenphasen, insbesondere Alunit ($KAl_3[(OH)_6(SO_4)_2]$), deutlich verstärkt auftritt. Um die Bildung dieser Nebenphasen zu unterbinden bzw. zu minimieren wird vorzugsweise Kaliumhydroxid, Natriumhydroxid, Calciumhydroxid, Ammoniak oder Natriumaluminat als Base zugesetzt. Natriumaluminat wird dabei als kombinierte Metallquelle und Base benutzt, was aus der Literatur nicht bekannt ist. Dementsprechend wird in einer bevorzugten Ausgestaltung des erfindungsgemäßen Verfahrens als Metallsalz Aluminiumsulfat eingesetzt. In einer weiteren bevorzugten Ausgestaltung des erfindungsgemäßen Verfahrens wird der wässrigen Lösung eine Base zugesetzt. Vorzugsweise ist die Base ausgewählt aus der Gruppe bestehend aus Ammoniak, Natriumhydroxid, Kaliumhydroxid, Natriumaluminat und Kaliumaluminat. Besonders bevorzugt ist Natriumaluminat.

In einer alternativen bevorzugten Ausgestaltung des erfindungsgemäßen Verfahrens wird als Metallsalz Eisen(III)-chlorid verwendet.

Gegenstand der vorliegenden Erfindung ist auch eine metallorganische Gerüststrukturverbindung hergestellt oder herstellbar durch das hier beschriebene erfindungsgemäße Verfahren. Diese Verbindungen zeichnen sich durch besonders hohe Wasserbeständigkeit aus. Vorzugsweise weist die metallorganische Gerüststrukturverbindung eine spezifische Oberfläche nach BET von 500 $m^2/g$ oder mehr auf.

Gegenstand der vorliegenden Erfindung ist außerdem die Verwendung der metallorganischen Gerüststrukturverbindung als Adsorbens, wobei der adsorbierte Stoff (Adsorbat) vorzugsweise Wasser, Ethanol, Methanol, Methan, $CO_2$, $H_2$ oder eine Mischung daraus ist. Erfindungsgemäß ist insbesondere die Verwendung der hierin beschriebenen metallorganischen Gerüststrukturverbindungen für Anwendungen wie Gasspeicherung, Katalyse, Entfeuchtung und Wärmetransformation (z.B. Wärmepumpen, Kältemaschinen).

Mit dem erfindungsgemäßen Verfahren lassen sich hohe Ausbeuten von über 90 % bezogen auf die Linkerverbindung erzielen. Die mit diesem Verfahren hergestellten metallorganischen

Gerüststrukturverbindungen zeigen die gleichen oder größere Oberflächen, die gleichen oder größere Kapazitäten hinsichtlich Gassorption und damit die gleichen oder bessere technische Eigenschaften als nach einem Verfahren des Standes der Technik hergestellte metallorganische Gerüststrukturverbindungen. Die metallorganischen Gerüststrukturverbindungen, die durch Reaktion in wässriger Lösung hergestellt wurden, zeichnen sich ferner durch die Abwesenheit von Rückständen organischer Lösungsmittel aus.

Die vorliegende Erfindung wird anhand der nachfolgenden Beispiele näher erläutert.

## Beispiele

Für die zu untersuchenden Proben wurde zu Beginn der zyklenunabhängigen Alterung eine Eingangsmessung mit Stickstoff ($N_2$) bei 77 Kelvin an einer NOVA 3000e der Fa. Quantachrome durchgeführt. Über die Stickstoffmessung bei 77 Kelvin lassen sich Aussagen über die Veränderung der Porenstruktur (Porenradienverteilung), Porenvolumen sowie über die innere Oberfläche (BET) treffen. Um die Proben von Feuchte und Fremdgasen zu befreien, wurden diese vor der eigentlichen Messung im Hochvakuum für 24 h bei 120°C ausgeheizt. Danach wurde das Trockengewicht der Probe mit einer Analysenwaage der Fa. Sartorius mit der Genauigkeitsklasse I bestimmt. Anschließend wurden komplette Isothermen in Ad- und Desorption aufgenommen und ausgewertet. Der Relativ-Druckbereich wurde zwischen p/p0 = 0,05-0,999 in Adsorption und p/p0 =0,999-0,1 in Desorption gefahren. Das Porenvolumen wurde nach der Dichte Funktional Theorie (DFT) und nach dem Modell von Dubinin und Astakhov (DA) bestimmt. Die innere Oberfläche wurde nach dem Modell von Brunauer-Emmett-Teller (BET) zwischen p/p0 = 0,05 und 0,15 bestimmt.

**Vergleichsbeispiel**

Synthese: 200 mg 1,3-Isophthalsäure (1,3-$H_2$BDC, 1,20 mmol), gelöst in 1 mL N,N-Dimethylformamid (DMF), wurden mit 800 mg $Al_2(SO_4)_3$*$18H_2O$, gelöst in 4 mL $H_2O$, gemischt und in einem mit Teflon ausgekleideten Stahlautoklaven für 12 Stunden bei 135°C behandelt.

Aufarbeitung: Nach Abkühlenlassen auf Raumtemperatur wurde das Produkt filtriert und im Ultraschallbad mit Wasser gewaschen. Der erhaltene weiße Feststoff wurde getrocknet und danach für 24 Stunden bei 120°C im Vakuum aktiviert.

Die spezifische Oberfläche des Produktes betrug $S_{BET}$ = 525 $m^2/g$ und das Porenvolumen lag

bei 0,27 $cm^3/g$.

**Ausführungsbeispiel 1**

Synthese: Eine Lösung von 0,75 mol (125 g) Isophthalsäure in 600 ml DMF und 2400 ml Wasser und 0,72 mmol (483 g) $Al_2(SO_4)_3*18H_2O$ wurde im 5000-ml-Dreihalskolben auf 135°C erwärmt.

In einem 5L-Kolben wurde 483 g (0,72 mol) $Al_2(SO_4)_3*18H_2O$ in 2,4 L Wasser vollständig gelöst. Zu der Aluminiumsulfat-Lösung wurde 125 g (0,75 mol) Isophthalsäure gelöst in 600 mL DMF portionsweise zugegeben.

Die Lösung wurde für eine Dauer von 48 h unter Rühren refluxiert.

Aufarbeitung: Der entstandene Feststoff wurde über einen Faltenfilter (5 - 13 µm) abfiltriert, in $H_2O$ resuspendiert und für 30 Minuten in ein Ultraschallbad gestellt. Dieser Vorgang wurde 3 Mal wiederholt. Anschließend wurde der weiße Feststoff 5 Tage bei 90°C im Trockenschank und 1 Tag bei 120°C im Vakuumschrank getrocknet.

Nach der Aufreinigung erhielt man 156,8 g eines weißen Feststoffs mit $S_{BET}$ = 578 $m^2/g$. Die einzige kristalline Phase wurde mittels Röntgen-Pulverdiffraktometrie als CAU-10-H identifiziert. Figur 6 zeigt das Pulverdiffraktogramm von CAU-10-H.

**Ausführungsbeispiel 2**

Synthese: Es wurden 5 L einer 0,5 M Natriumisophthalat-Lösung hergestellt, indem Natriumhydroxid (199,99 g; 5 mol) und Isophthalsäure (415,33 g; 2,5 mol) in einem Messkolben mit $H_2O$ auf 5000 ml aufgefüllt wurden. Des Weiteren wurden je 2 L einer 0,5 M Aluminiumsulfat*$18H_2O$-Lösung (666,15 g; 1 mol) und 2 L einer 0,5 M Natriumaluminatlösung (81,79 g; 1 mol), jeweils durch Auffüllen im Messkolben mit $H_2O$ auf 2000 mL, hergestellt. Für die Reaktion wurden 2,16 L Natriumisophthalat-Lösung (0,5 M) und 180 mL Ethanol vorgelegt und unter Rühren 810 mL Aluminiumsulfatlösung (0,5 M) und 540 mL Natriumaluminatlösung (0,5 M) zugegeben. Die Reaktion wurde danach für 6 h unter Rückfluss und Rühren durchgeführt.

Aufarbeitung: Der erhaltene Feststoff wurde abfiltriert, mit reichlich Wasser und Ethanol gewaschen und über Nacht bei 90°C getrocknet. Es wurden 207 g (92% Ausbeute) weißer pulverförmiger Feststoff ($S_{BET}$ = 580 $m^2/g$) erhalten, welcher mittels Röntgenpulverdiffrakto-

metrie als CAU-10-H identifiziert wurde. Die $N_2$-Sorptionsisotherme ist in Fig. 1 gezeigt; ausgefüllte Quadrate beschreiben die Adsorptionskurve und leere Quadrate beschreiben die Desorptionskurve.

**Ausführungsbeispiel 3**

Synthese: Für die Synthese wurden 100 mL einer 0,5 M Natriumisophthalat-Lösung erstellt, indem Natriumhydroxid (3,99 g, 0,1 mol) und Isophthalsäure (8,30 g; 0,05 mol) in einem Messkolben mit $H_2O$ auf 100 ml aufgefüllt wurden. Des Weiteren wurden je 100 mL einer 0,5 M Aluminiumsulfat*18$H_2O$-Lösung (33,308 g; 0,05 mol) und 100 mL einer 2 M Natriumhydroxidlösung (7,99 g; 0,2 mol), jeweils durch Auffüllen im Messkolben mit $H_2O$ auf 100 mL, hergestellt. Für die Reaktion wurden 127,5 mL $H_2O$, 7,5 mL Ethanol und 90 mL Natriumisophthalat-Lösung vorgelegt und unter Rühren 45 mL Aluminiumsulfatlösung und 22,5 mL Natriumhydroxidlösung zugegeben. Die Reaktion wurde danach für 6 h unter Rückfluss und Rühren durchgeführt.

Aufarbeitung: Der erhaltene Feststoff wurde abfiltriert, mit reichlich Wasser und Ethanol gewaschen und über Nacht bei 100°C getrocknet. Es wurde ein pulverförmiger Feststoff ($S_{BET}$ = 573 $m^2/g$) erhalten, welcher mittels Röntgenpulverdiffraktometrie als CAU-10-H identifiziert wurde. Des Weiteren enthält das Reaktionsprodukt eine Nebenphase (Natronalunit, $NaAl_3(OH)_6(SO_4)_2$; #(ICSD) = 44626). Die $N_2$-Sorptionsisotherme ist in Fig. 2 gezeigt; ausgefüllte Quadrate beschreiben die Adsorptionskurve und leere Quadrate beschreiben die Desorptionskurve.

**Ausführungsbeispiel 4**

Synthese: 5,25 mL einer 0,5 M Natriumisophthalat-Lösung wurden mit 4,5 mL Wasser verrührt. Unter Rühren wurden 5,25 mL einer 0,5 M $FeCl_3$-Lösung hinzugefügt. Die Reaktion wurde danach für 6 h bei 95°C in der Mikrowelle unter Rühren durchgeführt.

Aufarbeitung: Der erhaltene Feststoff wurde abfiltriert, mit reichlich Wasser und Ethanol gewaschen und über Nacht bei 90°C getrocknet. Er konnte als Fe-MIL-59 identifiziert werden. Figur 3 zeigt die mit diesem Stoff erhaltene Wasser-Sorptionsisotherme.

**Ausführungsbeispiel 5**

Für eine weitere Synthese von Fe-MIL-59 wurden 100 mL m-$Na_2$-BDC-Lösung (0,5 M) und 50 mL Wasser vorgelegt und unter Rühren 100 mL $FeCl_3$-Lösung (0,5 M) zugegeben. Die

Reaktion wurde unter starkem Rühren und Rückfluss für 6 Stunden durchgeführt. Der erhaltene Feststoff wurde über einen sehr feinen Filter abfiltriert und der Feststoff gründlich mit Wasser gewaschen. Das Produkt wurde für 3 Tage im Trockenofen (90°C) getrocknet. Es wurde ein orangebrauner Feststoff erhalten. Die Ausbeute beträgt 12,55 g (max. 12.8 g, 98%). Das gemessene Pulverdiffraktogramm ist in Figur 4 dargestellt. Als Vergleich dient das Diffraktogramm von Vanadium-MIL-59 welches isostrukturell ist.

**Ausführungsbeispiel 6**

Es wurden 7,5 mL $Na_2TDC$-Lösung (0,5 M) vorgelegt und unter Rühren 5,625 mL $AlCl_3$-Lösung (0,5 M) und 1,875 mL $NaAlO_2$-Lösung (0,5 M) zugegeben. Die Reaktion fand für 3 h bei 95 °C unter Rühren in der Mikrowelle statt. Der erhaltene Feststoff wurde filtriert und mit Wasser und Ethanol gewaschen. Eine Analyse ergab eine Oberfläche (BET) von 1024 $m^2/g$ und ein Porenvolumen = 0,4381 $cm^3/g$. Figur 5 zeigt die $N_2$-Sorptionsisotherme.

In der Zusammenschau des Vergleichsbeispiels mit dem Ausführungsbeispiel 1 ergibt sich, dass das erfindungsgemäße Syntheseverfahren im Vergleich zu herkömmlichen Verfahren, die mit erhöhtem Druck arbeiten, metallorganische Gerüststrukturverbindungen mit größerer spezifischer Oberfläche hervorbringt.

Aus dem Vergleich von Ausführungsbeispiel 1 mit den Ausführungsbeispielen 2 bzw. 3 ist ersichtlich, dass die Verwendung von Isophthalaten in wässrigen Reaktionsmedien die Reaktionszeit wesentlich verkürzt.

Ausführungsbeispiel 4 zeigt, dass die Reaktion nicht nur mit Aluminium als Metallkomponente funktioniert.

Ausführungsbeispiel 6 zeigt, dass die Reaktion in analoger Weise mit anderen aromatischen Dicarbonsäuren durchführbar ist.

## Patentansprüche

1. Verfahren zur Herstellung einer metallorganischen Gerüststrukturverbindung, bei dem mindestens ein Metallsalz umfassend ein Metallkation ausgewählt aus der Gruppe bestehend aus den Übergangsmetallen, Mg und Al sowie Kombinationen daraus mit einer Linkerverbindung umgesetzt wird, dadurch gekennzeichnet, dass die Umsetzung bei einem Druck von weniger als 1,5 bar in wässriger Lösung erfolgt, wobei

   die Linkerverbindung ausgewählt ist aus der Gruppe bestehend aus substituierten und unsubstituierten aromatischen Dicarbonsäuren und aromatischen Dicarboxylaten sowie Kombinationen und Mischungen daraus.

2. Verfahren nach Anspruch 1, dadurch gekennzeichnet, dass die wässrige Lösung weniger als 10 Vol-% organischen Lösungsmittels aufweist.

3. Verfahren nach Anspruch 1 oder 2, dadurch gekennzeichnet, dass die Umsetzung bei einer Temperatur 80 bis 120°C oder mehr erfolgt.

4. Verfahren nach einem der Ansprüche 1 bis 3, dadurch gekennzeichnet, dass die Umsetzung über einen Zeitraum von 10 Stunden oder weniger erfolgt.

5. Verfahren nach einem der Ansprüche 1 bis 4, dadurch gekennzeichnet, dass die aromatischen Dicarbonsäuren Strukturen der allgemeinen Formel 1 sind und die aromatischen Dicarboxylate Strukturen der allgemeinen Formel 2 sind, wobei die Phenylgruppe durch einen anderen aromatischen oder heteroaromatischen Ring ersetzt sein kann

   **Formel 1**

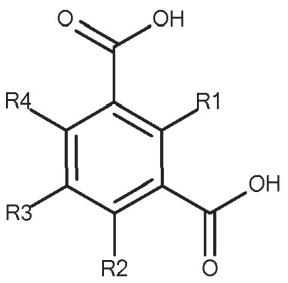

**Formel 2**

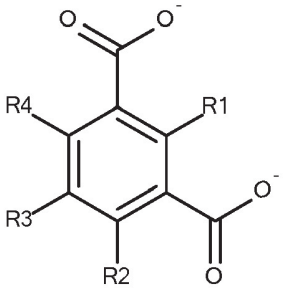


wobei die Reste R1 bis R4 unabhängig voneinander ausgewählt sind aus Wasserstoff, Hydroxy-, Nitro-, Amino-, Methyl-, Ether- und Halogenidgruppen sowie Kombinationen davon.

6. Verfahren nach einem der Ansprüche 1 bis 5, dadurch gekennzeichnet, dass die Linkerverbindung Isophthalsäure, ein Isophthalat oder ein Derivat davon ist.

7. Verfahren nach einem der Ansprüche 1 bis 6, dadurch gekennzeichnet, dass das Metallsalz ausgewählt ist aus der Gruppe bestehend aus Eisen- und Aluminiumsalzen.

8. Verfahren nach einem der Ansprüche 5 bis 7, dadurch gekennzeichnet, dass die Phenylgruppe in Formel 1 und/oder 2 ersetzt ist durch einen Fünfring-Aromaten der Gruppe Thiophen, Pyrrol, Furan, Imidazol, Pyrazol, Oxazol, Isoxazol und Thiazol; oder einen Sechsring-Aromaten der Gruppe Pyridin, Pyrazin, Pyrimidin und Pyridazin.

9. Verfahren nach einem der Ansprüche 2 bis 8, dadurch gekennzeichnet, dass der wässrigen Lösung eine Base zugesetzt wird.

10. Verfahren nach Anspruch 5 bis 9, dadurch gekennzeichnet, dass die Reste R1 bis R4 Wasserstoffsind.

11. Metallorganische Gerüststrukturverbindung hergestellt oder herstellbar durch ein Verfahren nach einem der Ansprüche 1 bis 10.

12. Metallorganische Gerüststrukturverbindung nach Anspruch 11, dadurch gekennzeichnet, dass die Verbindung eine spezifische Oberfläche nach BET von 500 $m^2/g$ oder mehr aufweist.

13. Verwendung einer metallorganischen Gerüststrukturverbindung nach Anspruch 11

oder Anspruch 12 als Adsorbens.

14. Verwendung nach Anspruch 13, wobei das Adsorbat Wasser, Ethanol, Methanol, Methan, $CO_2$, $H_2$ oder eine Mischung daraus ist.

Fig. 1

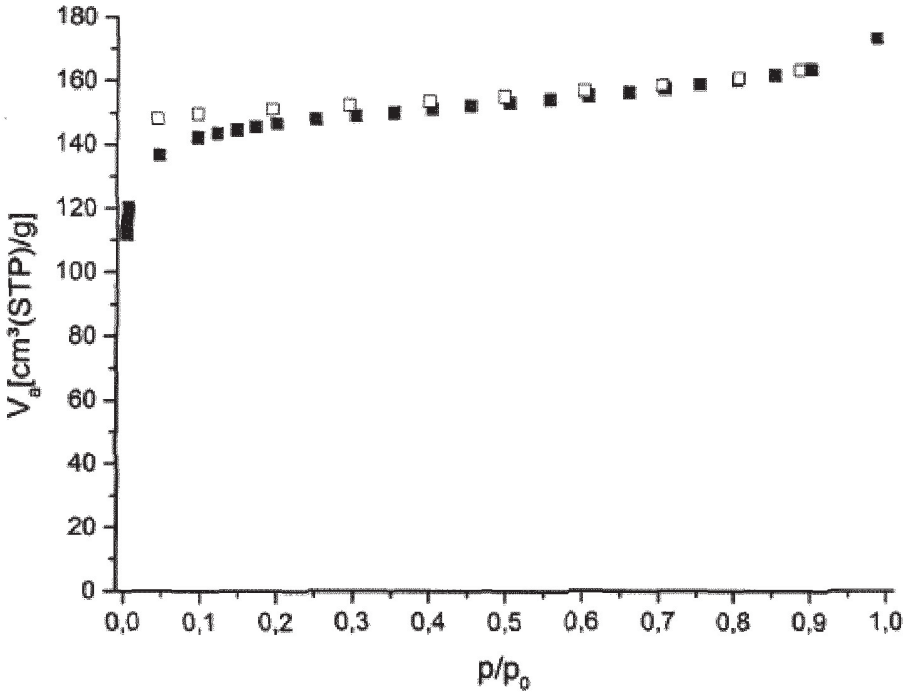
180
160
140
120
100
80
60
40
20
0
$V_a$[cm³(STP)/g]
0,0
0,1
0,2
0,3
0,4
0,5
0,6
0,7
0,8
0,9
1,0
$p/p_0$

Fig. 2

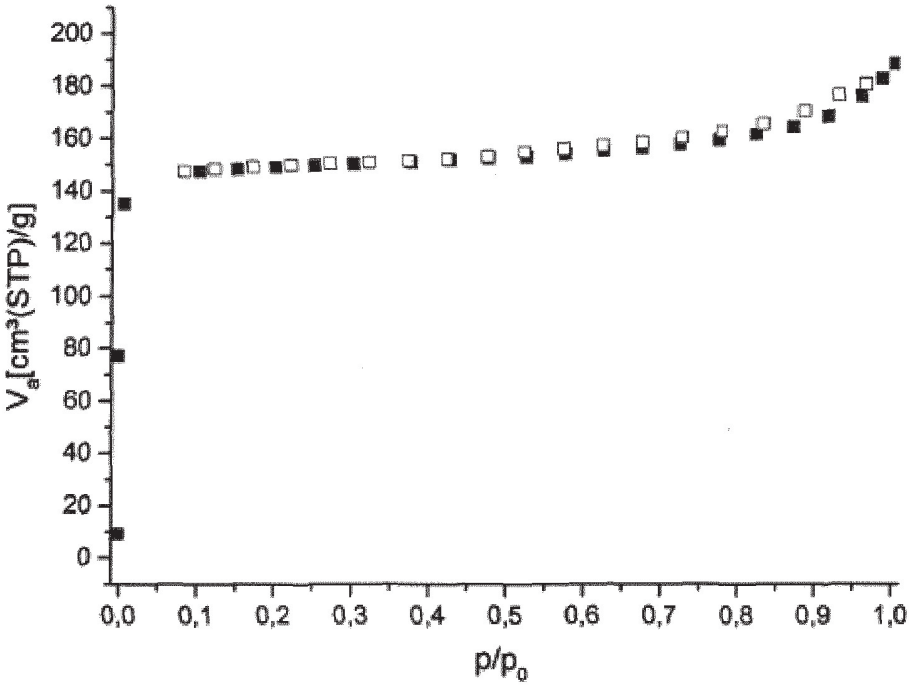
200
180
160
140
120
100
80
60
40
20
0
$V_a$[cm³(STP)/g]
0,0
0,1
0,2
0,3
0,4
0,5
0,6
0,7
0,8
0,9
1,0
$p/p_0$

Fig.3

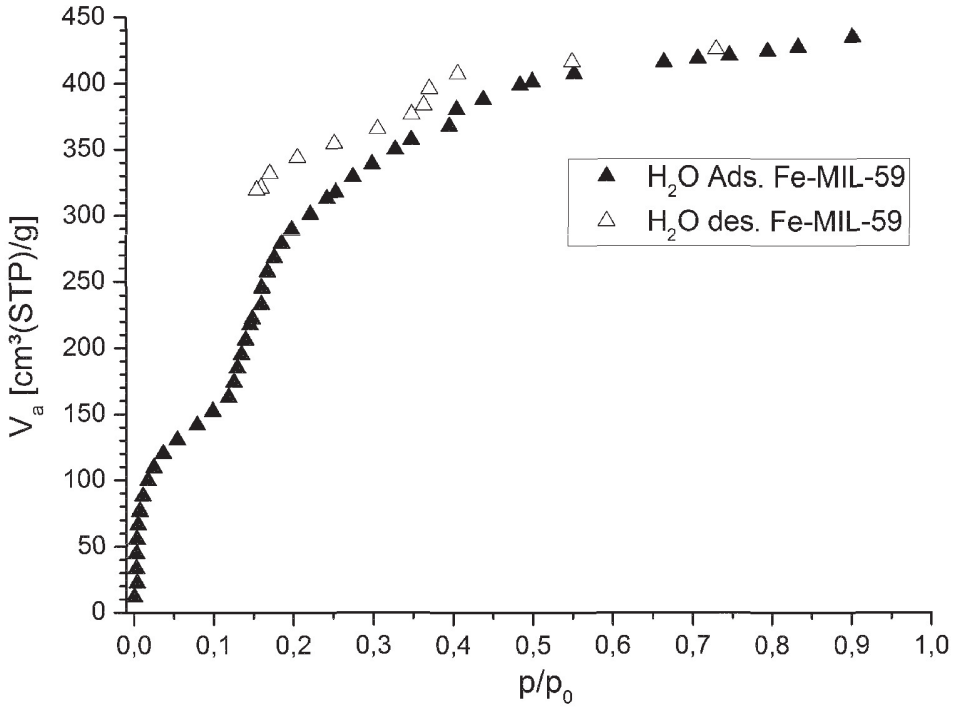
450
400
350
300
250
200
150
100
50
0
$V_a$ [$cm^3$(STP)/g]
0,0
0,1
0,2
0,3
0,4
0,5
0,6
0,7
0,8
0,9
1,0
$p/p_0$
$H_2O$ Ads. Fe-MIL-59
$H_2O$ des. Fe-MIL-59

Fig.4

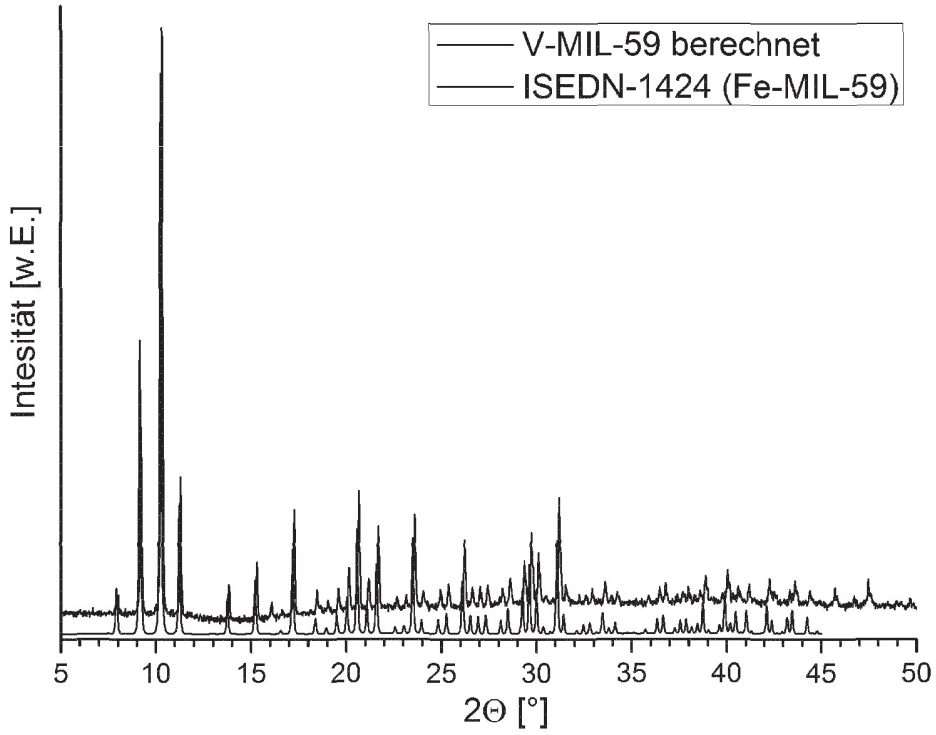
V-MIL-59 berechnet
ISEDN-1424 (Fe-MIL-59)
Intesität [w.E.]
5
10
15
20
25
30
35
40
45
50
2Θ [°]

Fig.5

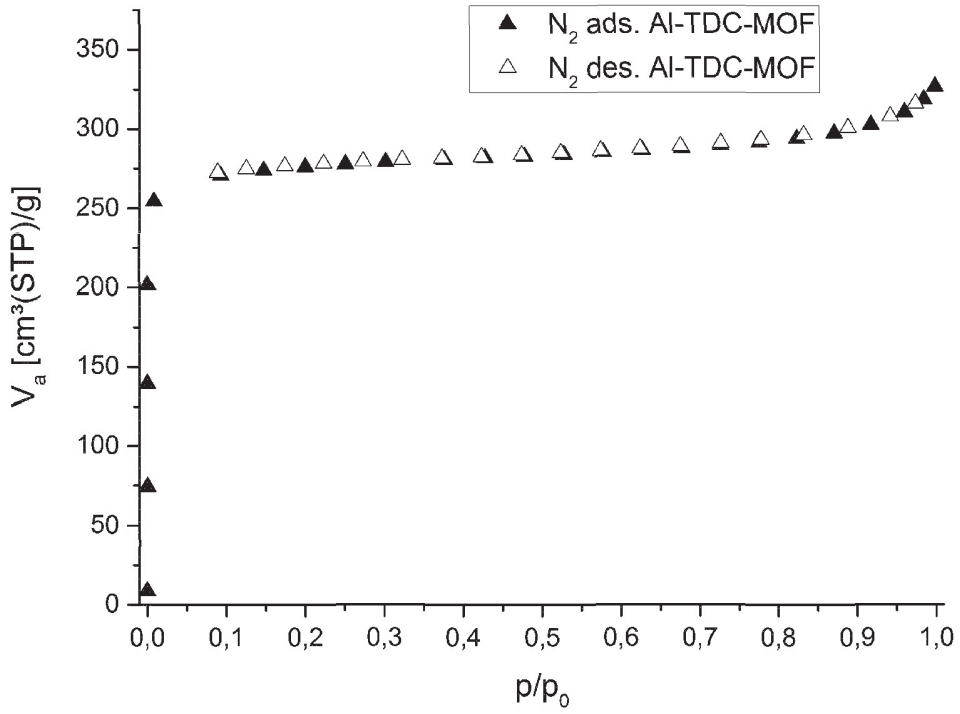
N2 ads. Al-TDC-MOF
N2 des. Al-TDC-MOF
Va [cm³(STP)/g]
p/p0
0
50
100
150
200
250
300
350
0,0
0,1
0,2
0,3
0,4
0,5
0,6
0,7
0,8
0,9
1,0

Fig.6

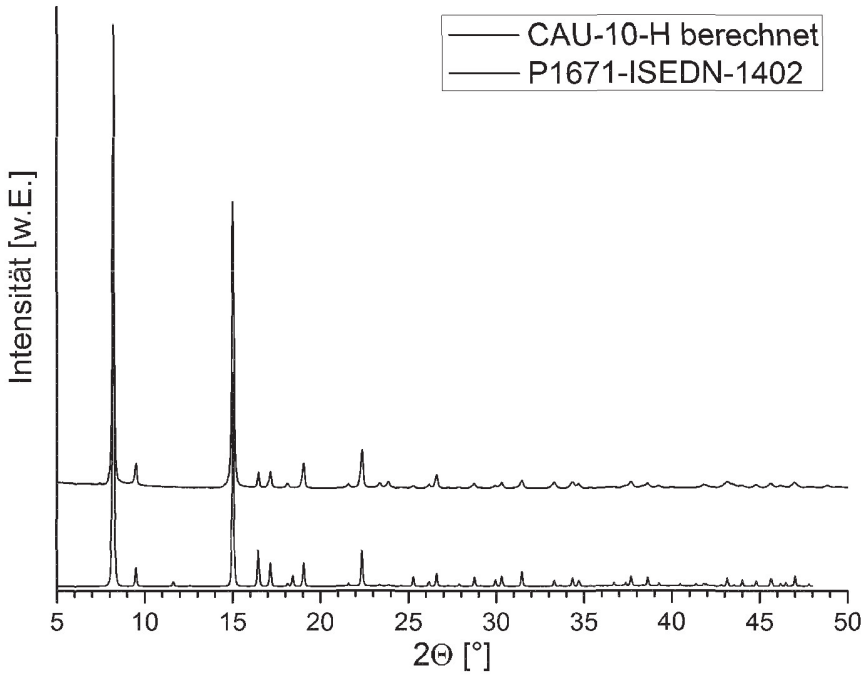
CAU-10-H berechnet
P1671-ISEDN-1402
Intensität [w.E.]
5
10
15
20
25
30
35
40
45
50
2Θ [°]

## 3.5 Oral Presentations

In this section, oral presentations at conferences and non-internal meetings presented by the author are listed in chronological order.

### 3.5.1 MOFs for Heat Pump Applications

Dominik Fröhlich

Christian Albrechts University zu Kiel

June 29. 2015, Kiel, Germany

### 3.5.2 Introduction of MOFs as a Possible Addition in Vulcanisation

Dominik Fröhlich

Continental AG

April 8. 2016, Hannover, Germany

### 3.5.3 Stability Investigations of Porous Materials Under Humid Conditions for Heat Pump Applications

*Oral Presentation*

D. Fröhlich

Material 2016, Perkin Elmer User Meeting

May 7, 2016, Dresden, Germany

### 3.5.4 Functional Full-Scale Heat Exchanger Coated with Aluminum Fumarate Metal-Organic Framework for Adsorption Cooling and Heat Pump Applications

*Oral Presentation*

D. Fröhlich, S. Henninger, H. Kummer, F. Jeremias, R. Gläser, C. Janiak

MOF 2016: 5th International Conference on Metal Organic Frameworks & Open Framework Compounds

September 11 – 15, 2016, Long Beach, United States of America

## 3.6 Conference Poster Contributions

In this section, conference poster contributions presented by the author are listed in chronological order.

### 3.6.1 Multicycle Stability Investigation of Microporous Aluminum Isophthalate

*Poster presentation*

D. Fröhlich, C. Janiak and S. K. Henninger

26. Deutsche Zeolith-Tagung

February 26 - 28, 2014, Paderborn, Germany

### 3.6.2 Aluminum-Fumarate Thick Coating on 3D Metallic Structures

*Poster presentation*

D. Fröhlich, F. Jeremias, H. Kummer, C. Janiak and S. K. Henninger

MOF 2014: 4th International Conference on Metal Organic Frameworks & Open Framework Compounds

September 28 – October 01, 2014, Kobe, Japan

### 3.6.3 Aluminium Based MOFs for Heat Transfer Applications

*Poster presentation*

D. Fröhlich, M. Baumgartner, F. Jeremias, C. Janiak and S. K. Henninger

27. Deutsche Zeolith-Tagung

February 25 – 27, 2105, Oldenburg, Germany

### 3.6.4 Stability Investigations of Porous Materials Under Humid Conditions for Heat Pump Applications

*Poster presentation*

D. Fröhlich, C. Janiak and S. K. Henninger

18th International Zeolite Conference

June 19 – 24, 2016, Rio de Janeiro, Brazil

### 3.6.5 A Robust Scalable Cheap Hydrophilic Al-MOF for Heat Reallocation Applications

*Poster presentation*

A. Permiakova, A. Cadiau, O. Skrylnyk, E. Courbon, J. Seo, A. H. Valekar, J. S. Lee; U-H. Lee, D. Damasceno Borges, M. Afframe, G. Mouchaham, S. Wang, T. Devic, F. Nouar, C. Martineau, D. Froehlich, S. Henninger, J. Gascon, F. Kapteijn, G. Maurin, G. De Weireld, M. Frère, N. Steunou, J. S. Chang, C. Serre

MOF 2016: 5th International Conference on Metal Organic Frameworks & Open Framework Compounds

September 11 – 15, 2016, Long Beach, United States of America

# 4 Unpublished Results

Apart from the results presented in the cumulative part, additional work packages are covered in this thesis, but are not yet published, because some work from coworkers is not finished. These work packages are presented in the current chapter.

## 4.1 Functional Full-Scale Heat Exchanger (HX) Coated with Aluminum Fumarate Metal-Organic Framework for Adsorption Heat Transformation Applications

Felix Jeremias, Harry Kummer, Dominik Fröhlich, Roger Gläser, Christoph Janiak and Stefan K. Henninger

*in preparation*

In this contribution, we present the first coating of a functional, full-scale heat exchanger with 493 g of the microporous aluminum fumarate MOF (Basolite® A520) using a polysiloxane-based binding agent, as well as the functional evaluation of the product: A gross cooling power of 2900 W (at the beginning of the adsorption cycle) or, respectively, 1000 W (at t = 74 s into the adsorption cycle) were achieved under the working conditions of a realistic adsorption chiller of 90 °C - 30 °C - 18 °C (temperature level of heat source, heat rejection/condenser and evaporator).

*Author's share of work:*

- choosing of Al-Fumarate as target MOF,
- Organization of coating work,
- Initiation of measuring the performance,

# A functional full-scale heat exchanger coated with aluminum fumarate metal-organic framework for adsorption heat transformation

# - Research Note -

*Harry Kummer,*[†‡] *Felix Jeremias,*[†] *Alexander Warlo, Gerrit Füldner,*[†] *Dominik Fröhlich,*[†‖] *Christoph Janiak,*[‖] *Roger Gläser*[‡] *and Stefan K. Henninger*[†]*

[†] Fraunhofer Institute for Solar Energy Systems ISE, Division Thermal Systems and Buildings, Heidenhofstr. 2, 79110 Freiburg, Germany. stefan.henninger@ise.fraunhofer.de

[‖] Institut für Anorganische Chemie und Strukturchemie, Universität Düsseldorf, 40204 Düsseldorf, Germany.

[‡] Institut für Technische Chemie, Universität Leipzig, Linnéstr. 3, 04103 Leipzig, Germany.

KEYWORDS

Aluminum fumarate, Adsorption heat transformation, Metal-organic framework.

ABSTRACT

Metal-organic frameworks represent a class of microporous adsorbents with high application potential for adsorption heat transformation. Here, we present a functional, full-scale heat exchanger coated with the microporous aluminum fumarate MOF Basolite® A520 using a polysiloxane-based binding agent. The function of the heat exchanger was evaluated resulting in a gross cooling power of 2900 W (at the beginning of the adsorption cycle) or, respectively an average cooling power of 690 W (up to a limit of 90% equilibrium loading in 7 min) under the working conditions of a realistic adsorption chiller of 90 °C - 30 °C - 18 °C (temperature level of heat source, heat rejection/condenser and evaporator).

## Introduction

Metal-organic frameworks (MOFs) receive continuous attention as microporous adsorbents due to their unsurpassed porosity and chemical variability. MOFs provide an enormous potential for improvement in several fields of application, such as gas storage,[1–8] gas[9–13] and liquid[14–17] separation, heterogeneous catalysis,[18–22] drug delivery[23,24] or sensor applications.[25–27] Based on their favorable water vapor adsorptive properties,[Ref.] they are especially attractive for sorption-based heat transformation.[28–39] Among the different MOFs used for this purpose, microporous aluminum fumarate has proven especially promising because of its comparatively high hydrophilicity, excellent multi-cycle stability[39] (virtually no loss for 4500 ad-/desorption cycles using advantageous water as the working fluid). Moreover, aluminum fumarate is accessible by a cost-efficient synthesis, which can be achieved by precipitation from low-cost bulk chemicals in water at ambient pressure.[40]

Thermally driven adsorption heat pumps (AHPs) can be applied to gain more heating energy from a given amount of fuel than from its mere combustion enthalpy. Thermally driven chillers (TDCs), on the other hand, make use of waste heat (such as heat from combined power and heat cycles, or district heat, during the hot season) for the production of useful cold. The underlying process has been discussed in detail in the literature.[37,39,41–43] However, for the realization of an efficient adsorption heat pump or chiller, the adsorbent has to meet several requirements. Most importantly, the adsorbent must be thermally coupled to the fluid circuit as efficiently as possible, as the adsorption kinetics and hence the power and power density of the unit directly depend on the transfer of heat of adsorption away from and towards the adsorption site.[44–46] Therefore, heat exchangers coated with the adsorbent (HX, in the following referred to as *adsorbers*) are by far superior to packed beds in terms of power delivered per mass of adsorbent.[47–52] Due to the cyclic nature of the process, the overall mass of the adsorber in relation to the adsorption capacity, must be kept as low as possible in order to minimize losses by heating and cooling passive thermal mass. Maximizing the amount of adsorbent coating on a HX and, in addition, achieving fast and efficient heat and mass transfer through the adsorbent, are among the major challenges for the design of adsorbent-coated heat exchangers. Furthermore, the coating has to be mechanically and chemically stable towards thermal stress, due to the cyclic operation, mechanical shocks and vibration, e.g., due to transportation. These issues are addressed in the literature by the development and evaluation of several routes to obtain thick and sturdy binder-based or binder-free coatings, not only for conventional adsorbents, but also for promising MOFs such as CAU-10-H, HKUST-1 or MIL-101(Cr).[39,44,51,53–58] Yet the scale-up towards a functional, fully coated MOF-based HX has not yet been reported so far. This may be attributed to the fact

that the procurement, formulation and deposition of the large amounts of suitable MOFs needed for such applications is arduous on a scale larger than in the laboratory.

In this contribution, we present the fabrication of a functional full-scale HX coated with aluminum fumarate MOF using a polysiloxane binder. Moreover a benchmark evaluation of the HX with respect to adsorption equilibrium and kinetics as well as cooling performance was conducted.

## Experimental procedure

*Procurement:* A state-of-the-art water/air finned HX with aluminum fins pressed onto copper tubes (diameter of copper tubes = 12 mm, aluminum fins with thickness = 0.2 mm, fin spacing = 3.0 mm, total dimensions of 480·160·120 $mm^3$, overall volume filled with lamellas = 385·160·110 $mm^3$ = 6,776 L, total mass 3001 g) was manufactured by WÄTAS Wärmetauscher Sachsen GmbH, Olbernhau, Germany (see Fig. 1a). Microporous aluminum fumarate (Basolite® A520, BET surface of 970 $m^2/g$) was supplied by BASF SE.[40] The polysiloxane binder emulsion (SilRes® MP50 E) was obtained from Wacker Chemie AG.

*Pretreatment:* Prior to application of the coating, the HX was degreased by submersion into a mild alkaline cleaning solution (7 wt% SurTec 140, 0.5 wt% SurTec 089 obtained from SurTec International GmbH) at 80 °C for 5 min, then thoroughly rinsed with deionized water, oxidized by submersion into 13 wt% nitric acid (ACS grade, 69%, Sigma Aldrich), at RT for 2 min and again rinsed with deionized water, then dried at room temperature with compressed air. The cleaned HX is shown in figure 1a. Areas not to be coated were covered using adhesive tape.

*Preparation of the coating dispersion:* In a 25 L stainless steel vat (530·330·200 mm³), 4338 g of microporous aluminum fumarate (5.2 wt% adsorbed water; dry mass content 4121 g) were dispersed in 13.0 L of deionized (DI) water at room temperature using 2 two-bladed propeller stirrers at 500 rpm for 30 min. The dispersion process was assisted by ultrasonic treatment (Elmasonic x-tra basic 800 at 45 kHz and 1000 W) for 30 min, followed by another 45 min of stirring. 2594 g of polysiloxane binder (dry mass content 1258 g) were added, stirring was continued for 60 min.

*Coating process:* The HX was immersed into the freshly prepared dispersion (cf. above) and withdrawn. Excess slurry between lamella was removed by compressed air. The lamellas were put horizontally and dried in air for 60 min, then re-immersed into the dispersion, again withdrawn, excess slurry removed by compressed air and left in air for 6 d at RT. After taking off the adhesive tape, removal of volatile contents of the binding agent was assured by heating the coated HX at 200 °C for 3.5 h in an air ventilated furnace.

Immediately after heating, the dry mass of the coated HX was measured. The mass of the applied coating was determined by subtracting the mass of the cleaned HX before coating from the mass of the hot, dried HX. The adsorbent mass fraction of the dispersion $w_{Ads} = 0.77$, calculated as dry adsorbent mass divided by solid mass of adsorbent and binder in the dispersion. The coating thickness was measured with a digital caliper on 8 different spots of the fins, coated on both sides. The fin thickness was subtracted and the thickness of upper and lower coating averaged.

*Determination of equilibrium adsorption properties:* Water vapor adsorption properties were measured isothermal at 25 °C in a Quantachrome VStar up to a $p/p_0 = 0.99$, after activating the sample at 150°C for 6 h. To crosscheck adsorption properties of the coating adsorbens

approximately 1 g of the coating was scraped off the HX lamellas, slightly grinded and measured in the same way as the original powder.

*Hydrothermal stability* was tested on the sample of the HX coating for 360 cycles in a setup at atmospheric pressure by switching between a cold humidified nitrogen gas stream (25 °C, 80% RH) and a hot dry one (120 °C, ??? %RH). A 25 °C isotherm of the treated sample is compared with the original one.

*Estimation of coefficient of performance (COP) under cooling conditions:* The cooling COP is defined as useful cooling energy output divided by the required regeneration energy input.

$$COP_{cool} = \frac{Q_{evap}}{Q_{regen}}$$

The useful cooling energy is simply the enthalpy achieved in the evaporator $Q_{evap}$ and can be calculated as evaporation enthalpy times the total water uptake. The required regeneration energy consists of a sensible part (for heating up the device) and the desorption enthalpy times the total water uptake. The water uptake was interpolated between the measured data sets as Gaussian approximation of three isotherms (25 °C, 40 °C, and 60 °C). For the sensible part the mass of the height exchanger (3001 g with a specific heat capacity of 900 J $kg^{-1}$ $K^{-1}$) and binder (150 g with a specific heat capacity of 1200 J $kg^{-1}$ $K^{-1}$) has been taken into account, whereas the realized adsorbent mass with 495 g was used and a corresponding heat capacity of 1200 J $kg^{-1}$ $K^{-1}$. Following the COP has been calculated for set of temperatures as follows: evaporator temperature 8 °C to 22 °C, adsorption temperature 25 °C, 30 °C and 35 °C for a fixed desorption temperature of 70 °C. In addition the COP for typical data center cooling condition (65°C-35°C) was calculated. The heat rejection and adsorption temperature were taken as identical. With respect to a necessary temperature difference between adsorbens and fluid circuit to allow heat exchange the COP has been calculated for a minimum mean temperature difference of 4K.

*Dynamic of adsorption and cooling performance testing:* The adsorption and cooling performance of the coated HX was tested in a custom-made apparatus as described earlier.[44] The HX was placed into a vacuum sample chamber, attached to a digital suspension balance and connected to a fluid circuit in such a way that the weight signal was not affected by the tubing. The weight signal was recorded continuously. A sufficiently large evaporator chamber provided a constant, settable water vapor pressure via a solenoid valve. Prior to the adsorption experiment, the adsorber was degassed at a temperature of 90 °C under vacuum (> 0.01 kPa) for 12 h and then preloaded at 0.3 kPa for simulating the preloaded state under field operating conditions (desorbing against a condenser at 30 °C). Adsorption was initiated by opening the connection between the sample chamber and the evaporator chamber. Adsorption kinetics and cooling performance were determined at a HX fluid temperature of 30 °C and a constant water vapor pressure of 1.8 kPa, corresponding to an evaporator temperature (useful cold) of 18 °C.

*The cooling performance of the HX* was calculated from the adsorption kinetic experiments as follows: Under isobaric conditions and constant adsorption temperature, it can be anticipated that the evaporated amount of water equals the adsorbed amount of water at any point of time *t*. Thus, the integral heat of evaporation $Q_{\mathrm{int,evap}}(t)$ that has been provided at any time *t* can be calculated from the adsorbed amount of water $m_{\mathrm{Ads}}(t)$ and the standard evaporation enthalpy of water, $\Delta H^0_{\mathrm{evap}}$ ($H_2O$) = 2230 kJ/kg according to

$$Q_{\mathrm{int,evap}} = m_{\mathrm{Ads}}(t) \cdot \Delta H^0_{\mathrm{evap}}(H_2O)$$

The gross cooling power $P_{\mathrm{cool}}$, provided during adsorption by evaporation, is proportional to the evaporation rate, i.e., also to the adsorption rate, assuming stationary conditions, and equals the time derivative of the integral heat of evaporation:

$$P_{\mathrm{Cool}} = \frac{\mathrm{d}}{\mathrm{d}t} Q_{\mathrm{int,evap}}$$

**Results and Discussion**

After final drying of the coated HX, a smooth, homogeneous MOF-binder surface was obtained (see Figure 1b). The final dry weight of the MOF-coated HX was determined at 3644 g, resulting in 643 g of dried coating being applied and therefore 493 g of aluminum fumarate are coated on the HX. This corresponded to a low adsorbent to sensible mass ratio of 0.135 for the overall adsorber. Assuming an even distribution of the dispersion components, the adsorbent mass fraction of the coating can be taken as identical to the $w_{\mathrm{ads}}$ of the dispersion, therefore the MOF-adsorbent content of the coating is 77 wt%, corresponding to 23 wt% binder in the coating.

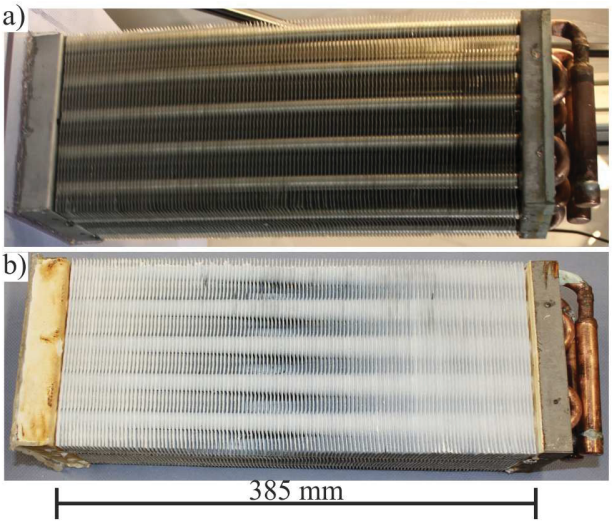


**Figure 1.** a) Heat-exchanger (HX) after cleaning and b) after coating with the aluminum fumarate MOF and drying.

The average thickness of the MOF-containing coating was found to be between 300 and 330 µm, distributed evenly on the aluminum lamellas and copper tubes of the HX. Blocking of the space between the lamellae was not observed. The coating proved mechanically resistant against handling (touchable without flaking) and under conditions of operating during performance testing. After 4 days in climate chamber and 3 days in the closed dynamic setup, the steel plates at the ends of the HX started to corrode by forming brown rust, probably triggered through removing the zinc galvanized protection layer during treatment in $HNO_3$ solution. Also the coating on these steel parts had an orange to brown color, probably caused by diffusion of iron oxide into the coating (see Figure 1b, coated steel part on the left end).

Comparing the equilibrium adsorption isotherms of the coated HX with those of the pure microporous aluminum fumarate (Figure 2), it can be stated that the water loading characteristic

of the MOF has largely been maintained. The original, spray coated material shows an additional arise, starting at $p/p_0$ of 0.6. This is probably induced by early condensation through macro structures of the spray coated particles and result in high hysteresis of the desorption path. At a $p/p_0 = 0.48$ (adsorption point at 30°C against evaporator at 18°C) the equilibrium loading is x = 0.317 $gg^{-1}$. The corrected adsorption loading for the adsorbent in the coating is x = 0.309 $gg^{-1}$, therefore 97 % of the adsorption capacity remained. Also comparing with the equilibrium point out of the kinetic measurement at 30 °C and a $p/p_0 = 0.48$, the loading x is 0.275 $gg^{-1}$, which correspond to 88 % of the original uptake. Taking into account a lower equilibrium loading at higher temperature (25 °C to 30 °C), this is consistent with the isothermal measurements.

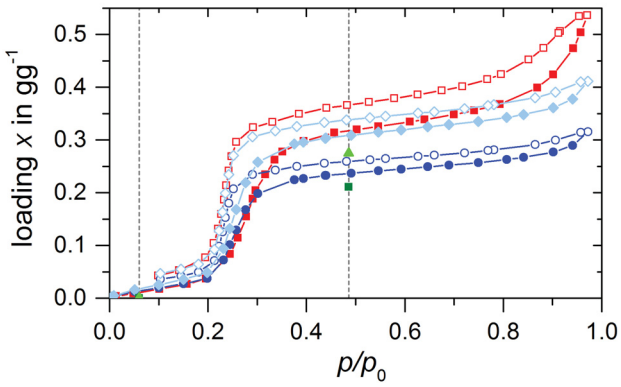


**Figure 2.** Equilibrium isotherms at 25 °C of the aluminum fumarate powder (■), coating (●) and aluminum fumarate (calculated from coating by subtraction of the masses of the binding agent, ◆) in comparison with the 30 °C equilibrium points of the kinetic setup (coating ■ and corrected aluminum fumarate ▲). Adsorption is shown with filled symbols. Grey dotted line shows the operational window of the dynamic measurement.

From published equilibrium data (Lit), an estimation of the achievable COP is possible, taking into account the sensible mass of the HX structure and binder without heat recovery. At operating conditions of 90 °C - 30 °C - 18 °C, the equilibrium COP could reach 0.61 and this holds true for realistic cycle loadings of 90 %.

The strength of this material are operating conditions with low desorption temperatures not more than 65°C, for example data center cooling. The COP variation reveals a maximum COP of ??? at ?????. For data center cooling the with heat rejection at 35 °C and useful cold at 18 °C the COP is at ????.

The kinetics of the mass gain during water sorption at a constant water vapor pressure of 1.8 kPa with a heat rejection temperature of 30 °C is depicted in Figure 3. The equilibrium loading of 0.275 $gg^{-1}$ was determined at $t_{end}$ = 25 min after starting the experiment. After $t_{60}$ = 3 min the adsorber is already loaded to about 60 %, after $t_{90}$ = 7 min it is loaded to 90 % and after 12.5 min, the adsorber is virtually saturated. According to Dawoud[52] the rise-up time $t_{80}$-$t_{15}$ was calculated to $t_r$ = 270 s, the sorption speed $v_s$ = $(x_{50} - x_0)/t_{50}$ = 0.08 g per 100 g adsorbent per s. Adsorption kinetics for a comparable full scale fin heat exchanger coated with the silicoaluminophosphate SAPO-34 (AQSOA-Z02 by Mitsubishi Chemicals) with a thickness of 300 µm was reported before by Dawoud et al[52]. In this study, using operating conditions of 90 °C – 35 °C – 5 °C, 57% of the loading was reached after 10 min. Even when taking into consideration the harsher operating condition at lower adsorption pressure of the SAPO-34-coated HX, the water sorption kinetics for the HX coated with the aluminum fumarate MOF clearly shows the huge potential for this application.

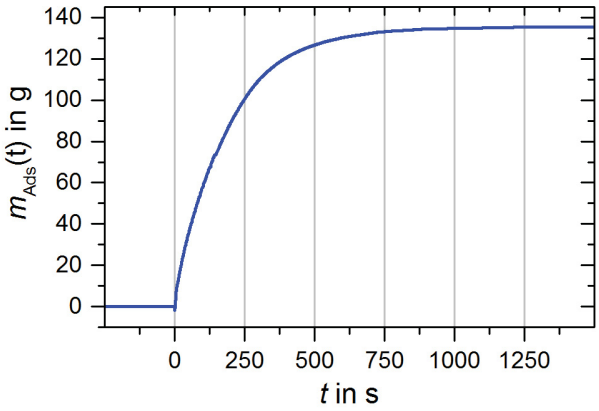


**Figure 3.** Time dependence of the HX mass gain during adsorption for operating condition 90 °C – 30 °C – 18 °C (blue line). Adsorption started with valve opening at $t = 0$ s

According to the mass gain over time (Fig. 3), the calculated integral heat of evaporation and the cooling power are provided in Fig. 4. A maximum performance of 2900 W is achieved at the beginning of the working cycle. Even at $t = 74$ s, the cooling power is still in the range of 1000 W. The average cooling power till reaching a loading of 90% is still at 690 W. Dividing $P_{Cool}$ by the volume of the finned part, the volume specific cooling power (VSCP) of the HX can be calculated. A peak VSCP of $VSCP_{peak} = 430$ W L$^{-1}$ can be achieved and also with realistic cycle loading of 90 %, the $VSCP_{x90}$ amounts to 101 W L$^{-1}$. The achieved specific cooling power (SCP) per kg MOF is a crucial value for estimating the cost of the adsorber. SCP calculated for the peak performance is $SCP_{peak} = 5880$ W kg$^{-1}$, for $x_{90}$ is $SCP_{x90} = 1394$ W kg$^{-1}$. These results show the high potential of this aluminum fumarate coated HX. From the fast adsorption kinetics, it can be deduced that the MOF particles, which are not excluded from adsorption by blocking through the binding agent, are accessible for unhindered and rapid mass transfer. Furthermore,

the steep adsorption isotherm of microporous aluminum fumarate probably also contributes to the fast adsorption and high cooling power, given that pore filling occurs over a small $p/p_0$ range and the driving force for filling the pores remains high as long as unfilled pores are still present.

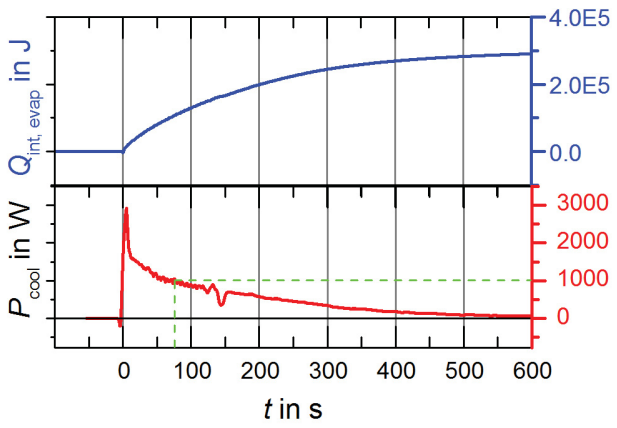


**Figure 4.** Gross cooling power $P_{cool}$ of the aluminum fumarate-coated HX for operating conditions 90 °C – 30 °C – 18 °C (red line, lower part), calculated from the integral heat of evaporation $Q_{int,evap}$ (blue line, upper part). The derivative was calculated using OriginPro and smoothed with the method of Savitzky-Golay using a 2nd order polynome. The green line indicates $P_{Cool}$ = 1000 W for a half cycle time of $t$ = 74 s.

As can be seen in Fig. 5 a broad plateau with a COP of approximately 0.6 is achieved for the given variations.

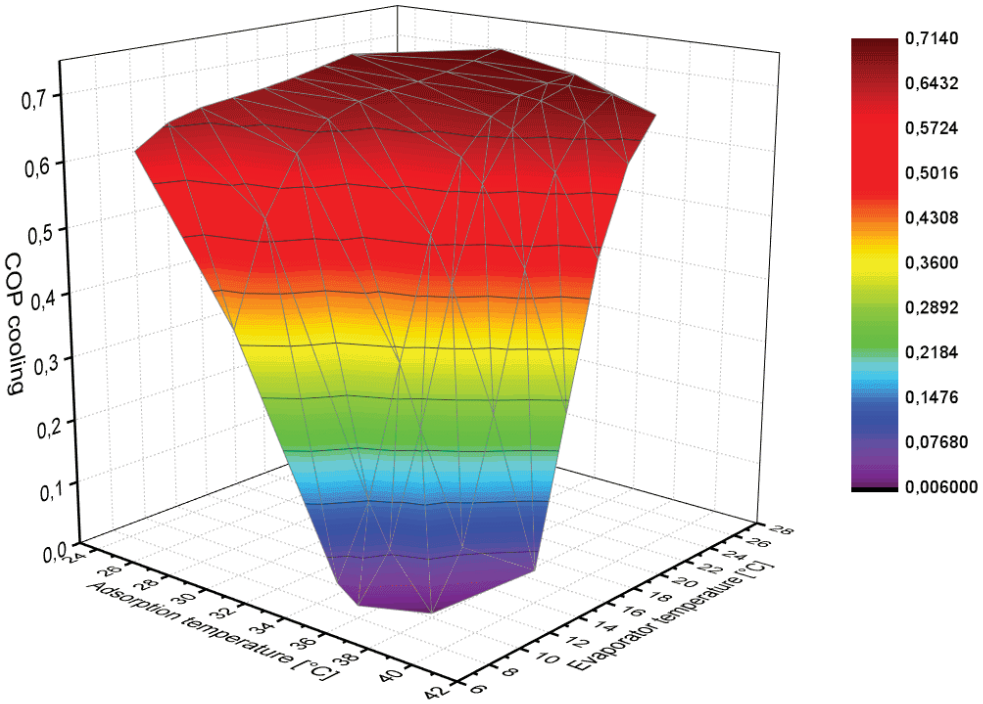


**Figure 5** Calculated cooling COP for different adsorption temperatures and evaporator temperatures for a fix desorption temperature of 70°C . The maximum COP without heat recovery was calculated to 0.7 for the temperature set 70/35/22°C.

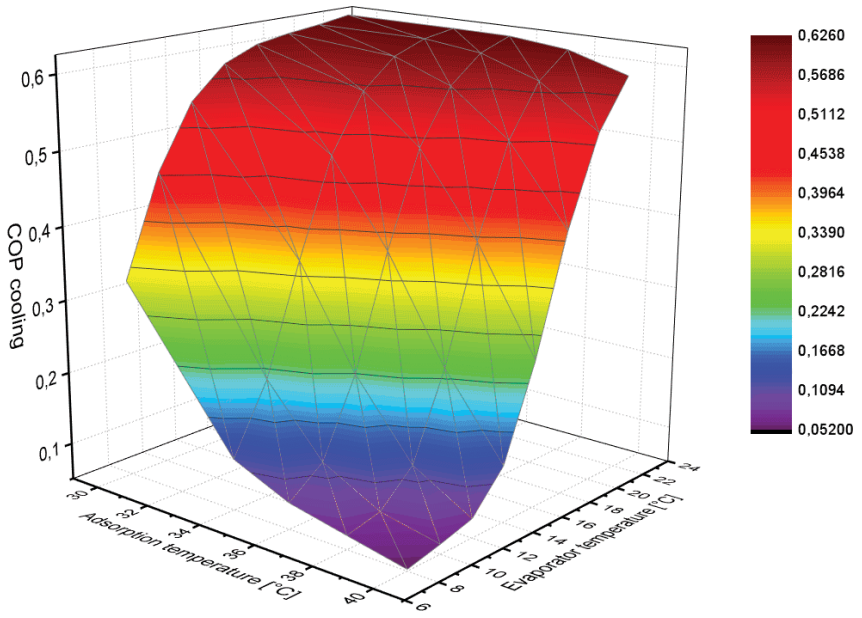


**Figure 6** Calculated cooling COP for different adsorption temperatures and evaporator temperatures and a given desorption temperature of 90°C.

## Summary and Outlook

This work shows that a functional heat exchanger fully coated by the MOF aluminum fumarate can be prepared using a convenient binder-based approach. The coating is evenly distributed among the aluminum fins of the HX and is mechanically stable. The equilibrium adsorption properties of the coating are comparable to those of the pure MOF adsorbent. Adsorption kinetics is very fast compared to conventional adsorbers, and the resulting cooling performance (2900 W at the beginning, 690 W average till 90% loading) is suitable from an industrially point

of view. Together with the inherent multi-cycle stability of microporous aluminum fumarate and the excellent long-term stability of polysiloxane coatings reported in the literature, these results clearly suggest that the technology has the potential for industrial application and can significantly advance sorption-based chilling. Further research should focus on the implementation of the coating process in a technical manufacturing line, corrosion issues and implementation of other MOFs for different boundary conditions, such as CAU-10-H or MIL-100.

## AUTHOR INFORMATION


### Corresponding Author

*stefan.henninger@ise.fraunhofer.de


### Author Contributions

The manuscript was written through contributions of all authors. All authors have given approval to the final version of the manuscript.


### Funding Sources

Funding by the Fraunhofer Society under grant-# MAVO 824 704 is gratefully acknowledged.


### Notes


ACKNOWLEDGMENT

We thank BASF SE for the supply aluminum fumarate and the Group of Lena Schnabel at the Fraunhofer ISE and especially Ursula Wittstadt and Gerrit Füldner for measurements and further support.

ABBREVIATIONS

AHP, adsorption heat pump; HX, heat-exchanger; MOF, metal-organic framework; TDC, thermally driven chiller; SCP, specific cooling power; VSCP, volume specific cooling power;

REFERENCES

## References

(1) Li, Y.; Yang, R. T. Gas Adsorption and Storage in Metal−Organic Framework MOF-177. *Langmuir* **2007**, *23*, 12937–12944.
(2) Alezi, D.; Belmabkhout, Y.; Suyetin, M.; Bhatt, P. M.; Weseliński, Ł. J.; Solovyeva, V.; Adil, K.; Spanopoulos, I.; Trikalitis, P. N.; Emwas, A.-H. *et al.* MOF Crystal Chemistry Paving the Way to Gas Storage Needs: Aluminum-Based soc -MOF for CH 4 , O 2 , and CO 2 Storage. *J. Am. Chem. Soc.* **2015**, *137*, 13308–13318.
(3) Zheng, B.; Yun, R.; Bai, J.; Lu, Z.; Du, L.; Li, Y. Expanded Porous MOF-505 Analogue Exhibiting Large Hydrogen Storage Capacity and Selective Carbon Dioxide Adsorption. *Inorg. Chem.* **2013**, *52*, 2823–2829.
(4) Purewal, J.; Liu, D.; Sudik, A.; Veenstra, M.; Yang, J.; Maurer, S.; Müller, U.; Siegel, D. J. Improved Hydrogen Storage and Thermal Conductivity in High-Density MOF-5 Composites. *J. Phys. Chem. C* **2012**, *116*, 20199–20212.
(5) Suh, M. P.; Park, H. J.; Prasad, T. K.; Lim, D. W. Hydrogen storage in metal-organic frameworks. *Chem. Rev.* **2012**, *112*, 782–835.
(6) Kuppler, R. J.; Timmons, D. J.; Fang, Q.-R.; Li, J.-R.; Makal, T. A.; Young, M. D.; Yuan, D.; Zhao, D.; Zhuang, W.; Zhou, H.-C. Potential applications of metal-organic frameworks. *Coord. Chem. Rev.* **2009**, *253*, 3042–3066.
(7) Mason, J. A.; Veenstra, M.; Long, J. R. Evaluating metal–organic frameworks for natural gas storage. *Chem. Sci.* **2014**, *5*, 32.
(8) Murray, L. J.; Dincă, M.; Long, J. R. Hydrogen storage in metal-organic frameworks. *Chem. Soc. Rev.* **2009**, *38*, 1294–1314.
(9) Zhao, Z.; Ma, X.; Kasik, A.; Li, Z.; Lin, Y. S. Gas Separation Properties of Metal Organic Framework (MOF-5) Membranes. *Ind. Eng. Chem. Res.* **2013**, *52*, 1102–1108.
(10) Wisser, D.; Wisser, F. M.; Raschke, S.; Klein, N.; Leistner, M.; Grothe, J.; Brunner, E.; Kaskel, S. Biological Chitin-MOF Composites with Hierarchical Pore Systems for Air-Filtration Applications. *Angew. Chem. Int. Ed.* **2015**, *54*, 12588–12591.
(11) Verma, P.; Xu, X.; Truhlar, D. G. Adsorption on Fe-MOF-74 for C1–C3 Hydrocarbon Separation. *J. Phys. Chem. C* **2013**, *117*, 12648–12660.

(12) Hu, J.; Cai, H.; Ren, H.; Wei, Y.; Xu, Z.; Liu, H.; Hu, Y. Mixed-Matrix Membrane Hollow Fibers of Cu 3 (BTC) 2 MOF and Polyimide for Gas Separation and Adsorption. *Ind. Eng. Chem. Res.* **2010**, *49*, 12605–12612.
(13) Huang, W.; Jiang, J.; Wu, D.; Xu, J.; Xue, B.; Kirillov, A. M. A Highly Stable Nanotubular MOF Rotator for Selective Adsorption of Benzene and Separation of Xylene Isomers. *Inorg. Chem.* **2015**, *54*, 10524–10526.
(14) Moreira, M. A.; Santos, J. C.; Ferreira, Alexandre F. P.; Loureiro, J. M.; Ragon, F.; Horcajada, P.; Shim, K.-E.; Hwang, Y.-K.; Lee, U.-H.; Chang, J.-S. *et al.* Reverse Shape Selectivity in the Liquid-Phase Adsorption of Xylene Isomers in Zirconium Terephthalate MOF UiO-66. *Langmuir* **2012**, *28*, 5715–5723.
(15) Wang, L.; Li, Y.-A.; Yang, F.; Liu, Q.-K.; Ma, J.-P.; Dong, Y.-B. Cd(II)-MOF: Adsorption, Separation, and Guest-Dependent Luminescence for Monohalobenzenes. *Inorg. Chem.* **2014**, *53*, 9087–9094.
(16) Cychosz, K. A.; Ahmad, R.; Matzger, A. J. Liquid phase separations by crystalline microporous coordination polymers. *Chem. Sci.* **2010**, *1*, 293–302.
(17) Han, S.; Wei, Y.; Valente, C.; Lagzi, I.; Gassensmith, J. J.; Coskun, A.; Stoddart, J. F.; Grzybowski, B. A. Chromatography in a Single Metal−Organic Framework (MOF) Crystal. *J. Am. Chem. Soc.* **2010**, *132*, 16358–16361.
(18) Gole, B.; Sanyal, U.; Banerjee, R.; Mukherjee, P. S. High Loading of Pd Nanoparticles by Interior Functionalization of MOFs for Heterogeneous Catalysis. *Inorg. Chem.* **2016**, *55*, 2345–2354.
(19) Müller, M.; Hermes, S.; Kähler, K.; van den Berg, Maurits W. E.; Muhler, M.; Fischer, R. A. Loading of MOF-5 with Cu and ZnO Nanoparticles by Gas-Phase Infiltration with Organometallic Precursors: Properties of Cu/ZnO@MOF-5 as Catalyst for Methanol Synthesis. *Chem. Mater.* **2008**, *20*, 4576–4587.
(20) Dang, D.; Wu, P.; He, C.; Xie, Z.; Duan, C. Homochiral Metal−Organic Frameworks for Heterogeneous Asymmetric Catalysis. *J. Am. Chem. Soc.* **2010**, *132*, 14321–14323.
(21) Herbst, A.; Khutia, A.; Janiak, C. Brønsted Instead of Lewis Acidity in Functionalized MIL-101Cr MOFs for Efficient Heterogeneous (nano-MOF) Catalysis in the Condensation Reaction of Aldehydes with Alcohols. *Inorg. Chem.* **2014**, *53*, 7319–7333.
(22) Corma, A.; Garcia, H.; Llabres i Xamena, F. X. Engineering metal organic frameworks for heterogeneous catalysis. *Chem. Rev.* **2010**, *110*, 4606–4655.
(23) Bhardwaj, S. K.; Bhardwaj, N.; Mohanta, G. C.; Kumar, P.; Sharma, A. L.; Kim, K.-H.; Deep, A. Immunosensing of Atrazine with Antibody-Functionalized Cu-MOF Conducting Thin Films. *ACS Appl. Mater. Interfaces* **2015**, *7*, 26124–26130.
(24) Horcajada, P.; Gref, R.; Baati, T.; Allan, P. K.; Maurin, G.; Couvreur, P.; Férey, G.; Morris, R. E.; Serre, C. Metal-organic frameworks in biomedicine. *Chem. Rev.* **2012**, *112*, 1232–1268.
(25) Ranft, A.; Niekiel, F.; Pavlichenko, I.; Stock, N.; Lotsch, B. V. Tandem MOF-Based Photonic Crystals for Enhanced Analyte-Specific Optical Detection. *Chem. Mater.* **2015**, *27*, 1961–1970.
(26) Drobek, M.; Kim, J.-H.; Bechelany, M.; Vallicari, C.; Julbe, A.; Kim, S. S. MOF-Based Membrane Encapsulated ZnO Nanowires for Enhanced Gas Sensor Selectivity. *ACS Appl. Mater. Interfaces* **2016**, *8*, 8323–8328.
(27) Cui, L.; Wu, J.; Li, J.; Ju, H. Electrochemical Sensor for Lead Cation Sensitized with a DNA Functionalized Porphyrinic Metal–Organic Framework. *Anal. Chem.* **2015**, *87*, 10635–10641.

(28) de Lange, Martijn F.; Verouden, Karlijn J. F. M.; Vlugt, Thijs J. H.; Gascon, J.; Kapteijn, F. Adsorption-Driven Heat Pumps: The Potential of Metal–Organic Frameworks. *Chem. Rev.* **2015,** DOI: 10.1021/acs.chemrev.5b00059.
(29) Jasuja, H.; Zang, J.; Sholl, D. S.; Walton, K. S. Rational Tuning of Water Vapor and $CO_2$ Adsorption in Highly Stable Zr-Based MOFs. *J. Phys. Chem. C* **2012**, *116*, 23526–23532.
(30) Jeremias, F.; Lozan, V.; Henninger, S.; Janiak, C. Programming MOFs for water sorption: Amino-functionalized MIL-125 and UiO-66 for heat transformation and heat storage applications. *Dalton Trans.* **2013**, *42*, 15967–15973.
(31) Gordeeva, L. G.; Solovyeva, M. V.; Aristov, Y. I. NH2-MIL-125 as a promising material for adsorptive heat transformation and storage. *Energy* **2016**, *100*, 18–24.
(32) de Lange, M. F.; Ottevanger, C. P.; Wiegman, M.; Vlugt, T. J. H.; Gascon, J.; Kapteijn, F. Crystals for sustainability – structuring Al-based MOFs for the allocation of heat and cold. *CrystEngComm* **2015**, *17*, 281–285.
(33) Aristov, Y. I. Novel Materials for Adsorptive Heat Pumping and Storage: Screening and Nanotailoring of Sorption Properties. *J. Chem. Eng. Jpn.* **2007**, *40*, 1242–1251.
(34) Henninger, S. K.; Jeremias, F.; Kummer, H.; Schossig, P.; Henning, H.-M. Novel Sorption Materials for Solar Heating and Cooling. *Energy Procedia* **2012**, *30*, 279–288.
(35) Henninger, S. K.; Jeremias, F.; Kummer, H.; Janiak, C. MOFs for Use in Adsorption Heat Pump Processes. *Eur. J. Inorg. Chem.* **2012**, 2625–2634.
(36) Fröhlich, D.; Henninger, S. K.; Janiak, C. Multicycle water vapour stability of microporous breathing MOF aluminium isophthalate CAU-10-H. *Dalton Trans.* **2014**, *43*, 15300–15304.
(37) Jeremias, F.; Khutia, A.; Henninger, S. K.; Janiak, C. MIL-100(Al, Fe) as water adsorbents for heat transformation purposes—a promising application. *J. Mater. Chem.* **2012**, *22*, 10148–10151.
(38) Jeremias, F.; Fröhlich, D.; Janiak, C.; Henninger, S. K. Water and methanol adsorption on MOFs for cycling heat transformation processes. *New J. Chem.* **2014**, *38*, 1846–1852.
(39) Jeremias, F.; Fröhlich, D.; Janiak, C.; Henninger, S. K. Advancement of sorption-based heat transformation by a metal coating of highly-stable, hydrophilic aluminium fumarate MOF. *RSC Adv.* **2014**, *4*, 24073–24082.
(40) Gaab, M.; Trukhan, N.; Maurer, S.; Gummaraju, R.; Müller, U. The progression of Al-based metal-organic frameworks – From academic research to industrial production and applications. *Microporous Mesoporous Mater.* **2012**, *157*, 131–136.
(41) Aristov, Y. I. Challenging offers of material science for adsorption heat transformation: A review. *Appl. Therm. Eng.* **2013**, *50*, 1610–1618.
(42) Freni, A.; Maggio, G.; Sapienza, A.; Frazzica, A.; Restuccia, G.; Vasta, S. Comparative analysis of promising adsorbent/adsorbate pairs for adsorptive heat pumping, air conditioning and refrigeration. *Appl. Therm. Eng.* **2016**, *104*, 85–95.
(43) Henninger, S. K.; Schmidt, F. P.; Henning, H.-M. Characterisation and improvement of sorption materials with molecular modeling for the use in heat transformation applications. *Adsorption* **2011**, *17*, 833–843.
(44) Wittstadt, U.; Füldner, G.; Andersen, O.; Herrmann, R.; Schmidt, F. A New Adsorbent Composite Material Based on Metal Fiber Technology and Its Application in Adsorption Heat Exchangers. *Energies* **2015**, *8*, 8431–8446.
(45) Chakraborty, A.; Saha, B. B.; Aristov, Y. I. Dynamic behaviors of adsorption chiller: Effects of the silica gel grain size and layers. *Energy* **2014**, *78*, 304–312.

(46) Aristov, Y. I. Adsorptive transformation and storage of renewable heat: Review of current trends in adsorption dynamics. *Renewable Energy* **2016,** DOI: 10.1016/j.renene.2016.06.055.
(47) Frazzica, A.; Füldner, G.; Sapienza, A.; Freni, A.; Schnabel, L. Experimental and theoretical analysis of the kinetic performance of an adsorbent coating composition for use in adsorption chillers and heat pumps. *Appl. Therm. Eng*. **2014**, *73*, 1022–1031.
(48) Jiang, Y.; Ge, T. S.; Wang, R. Z.; Hu, L. M. Experimental investigation and analysis of composite silica-gel coated fin-tube heat exchangers. *Int. J.Refrigeration* **2015**, *51*, 169–179.
(49) Zhao, Y.; Ge, T. S.; Dai, Y. J.; Wang, R. Z. Experimental investigation on a desiccant dehumidification unit using fin-tube heat exchanger with silica gel coating. *Appl. Therm. Eng.* **2014**, *63*, 52–58.
(50) Tu, Y. D.; Wang, R. Z.; Ge, T. S.; Zheng, X. Comfortable, high-efficiency heat pump with desiccant-coated, water-sorbing heat exchangers. *Sci. Rep.* **2017**, *7,* DOI: 10.1038/srep40437.
(51) Freni, A.; Dawoud, B.; Bonaccorsi, L.; Chmielewski, S.; Frazzica, A.; Calabrese, L.; Restuccia, G. *Characterization of Zeolite-Based Coatings for Adsorption Heat Pumps*; SpringerBriefs in Applied Sciences and Technology, 2015.
(52) Dawoud, B. Water vapor adsorption kinetics on small and full scale zeolite coated adsorbers; A comparison. *Appl. Therm. Eng*. **2013**, *50*, 1645–1651.
(53) Kummer, H.; Baumgartner, M.; Hügenell, P.; Fröhlich, D.; Henninger, S. K.; Gläser, R. Thermally driven refrigeration by methanol adsorption on coatings of HKUST-1 and MIL-101(Cr). *Appl. Therm. Eng*. **2016,** DOI: 10.1016/j.applthermaleng.2016.11.026.
(54) Solovyeva, M. V.; Aristov, Y. I.; Gordeeva, L. G. NH2-MIL-125 as promising adsorbent for adsorptive cooling: Water adsorption dynamics. *Appl. Therm. Eng*. **2017**, *116*, 541–548.
(55) Fröhlich, D.; Pantatosaki, E.; Kolokathis, P. D.; Markey, K.; Reinsch, H.; Baumgartner, M.; van der Veen, Monique A.; Vos, D. E. de; Stock, N.; Papadopoulos, G. K. *et al.* Water adsorption behaviour of CAU-10-H: A thorough investigation of its structure–property relationships. *J. Mater. Chem. A* **2016**, *4*, 11859–11869.
(56) Bendix, P. B.; Henninger, S. K.; Henning, H.-M. Temperature and mechanical stabilities and changes in porosity of silicone binder based zeolite coatings. *Ind. Eng. Chem. Res*. **2016,** DOI: 10.1021/acs.iecr.6b00558.
(57) Kummer, H.; Füldner, G.; Henninger, S. K. Versatile siloxane based adsorbent coatings for fast water adsorption processes in thermally driven chillers and heat pumps. *Appl. Therm. Eng.* **2015,** DOI: 10.1016/j.applthermaleng.2015.03.042.
(58) Jeremias, F.; Henninger, S. K.; Janiak, C. High performance metal-organic-framework coatings obtained via thermal gradient synthesis. *Chem. Commun.* **2012**, *48*, 9708–9710.

TOC Artwork:

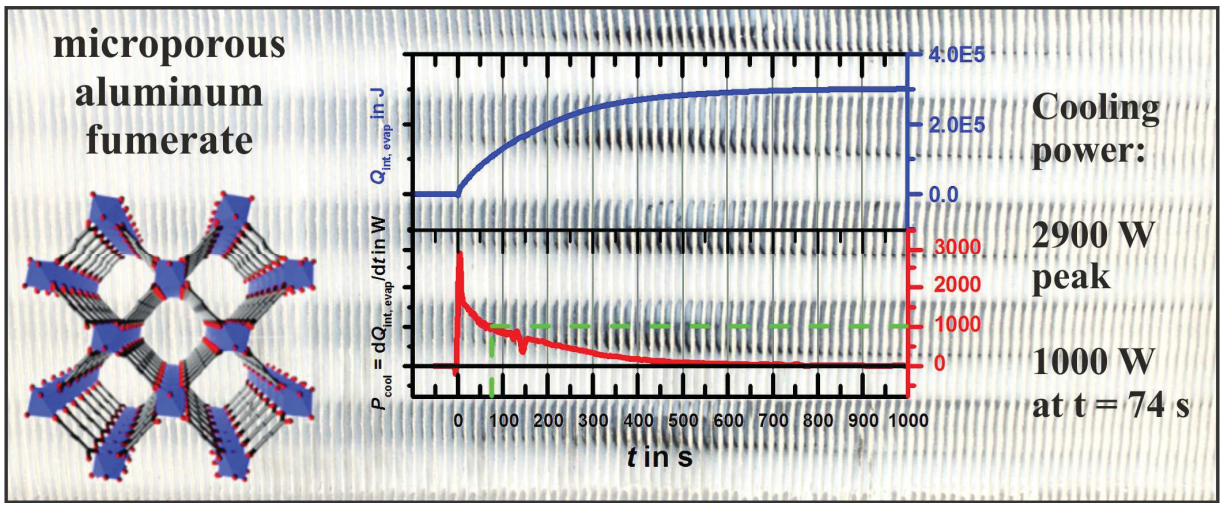
microporous
aluminum
fumerate
$Q_{int,\ evap}$ in J
4.0E5
2.0E5
0.0
$P_{cool} = dQ_{int,\ evap}/dt$ in W
3000
2000
1000
0
0 100 200 300 400 500 600 700 800 900 1000
t in s
Cooling
power:
2900 W
peak
1000 W
at t = 74 s

## 4.2 Three MOFs with UiO-66 structure based on 2,5-pyridinedicarboxilic acid as linker and the influence of the pyridine nitrogen to the properties of the compounds

Steve Waitschat, Dominik Fröhlich, Helge Reinsch, Huayna Terraschke, Dario Broich, Max Baumgartner, Stefan K. Henninger and Norbert. Stock

*In preperation*

Zirconium MOFs are thermal and chemical stable, so they could be interesting for several applications. In this work we present the first synthetic route for a Zr-MOF with pyridine-dicarboxylic acid as a linker. The resulting MOF has the UiO-66 structure. Additionally, the MOF is also synthesized with Cerium and Hafnium. Both metals also build the UiO-66 structure, but with different defect composition in the compound. To show the influence of the additional nitrogen from the pyridine luminescence and sorption measurements were carried out. Also cyclic experiments for water and methanol sorption were tested for a potential application in Heat Transformation.

*Author's share of work:*

- $H_2O$ and MeOH sorption and stability experiments,
- writing of sorption and stability chapters.

Journal Name

ARTICLE

# Water-based synthesis of M-UiO-66 (M = Zr, Ce or Hf) based on 2,5-pyridinedicarboxilic acid as linker: defect chemistry, framework hydrophilisation and water sorption properties

Received 00th January 20xx,
Accepted 00th January 20xx

DOI: 10.1039/x0xx00000x

www.rsc.org/

## Water-based synthesis of hydrophilic UiO-66 with Zr, Hf or Ce: defect chemistry and water sorption properties

S. Waitschat,[a] D. Fröhlich[b], H. Reinsch[a], H. Terraschke[a], K. Lomachenko[c], D. Smazna[d], D. Broich[a], H. Kummer[b], T. Helling[b], M. Baumgartner[b], S. Henninger[b] and N. Stock[a*]

Metal-organic organic frameworks of general composition $[M_6(OH)_4(O)_4(PDC)_{6-x}(Cl)_{2x}(H_2O)_{2x}]$ with M = Zr, Ce, Hf, $PDC^{2-}$ = 2,5-pyridinedicarboxylate and $0 \leq x \leq 2$ were obtained under reflux using water as the solvent. Rietveld-refinements were carried out and confirmed that the MOFs crystallise in the UiO-66 type structure with different defect concentrations. to confof confirmed the were carried out MOFs are thermally and chemically highly stable, therefore they are interesting for several applications. In this work we present the first synthetic route towards a Zr-MOF with 2,5-pyridine-dicarboxylic acid as a linker, exhibiting UiO-66 structure. In addition, the corresponding compounds were also synthesized with cerium and hafnium. Both metals also form the UiO-66 structure but with differing defect composition in the compounds. To highlight the influence of the additional nitrogen atom in the pyridine ring, luminescence and vapour sorption measurements were carried out, including cycling experiments for ad-/desorption of water and methanol vapour to evaluate the MOFs as potential adsorbents in heat transformation applications.

## Introduction

The increasing demand for heating and cooling in the world necessitates the development of new materials and technologies.[1,2] The use of low temperature waste energy in adsorptive heat transformation applications is one promising technology to improve energy efficiency.[3] Water as the working fluid of choice has numerous advantages, not the least in reducing the amount of world-wide used chlorofluorocarbons (CFCs) in the year 2047 as decided in the Montreal protocol of the UN.[4] Thus, adsorptive cooling and heating could replace conventional heat pumps or air conditioning systems, which employ CFCs. As another advantages lowering of $CO_2$ emissions are feasible since low temperature waste energy is employed in this process.[5]

The industrially most relevant method of adsorptive heat transformation is a two-cycle process. Water is preferably employed due to its high enthalpy of evaporation (2500 $kJ \cdot kg^{-1}$), its abundance and its non-toxicity.[5] Furthermore, methanol and ethanol are good candidates as working fluids, especially when the sorption material is not water stable or when low temperatures must be achieved.[6] In the working cycle the dry adsorbent adsorbs a working fluid and the heat of adsorption is released to the environment ($Q_{ads.}$).[5] When the sorption material is saturated with working fluid, the second cycle, the regeneration cycle, is starting. To desorb the working fluid, energy is necessary, which ideally would be waste heat from a different process ($Q_{des.}$). Thus, in this step, energy is consumed from the environment and cold is produced. Due to the condensation of the working fluid in a spatially separated reservoir, heat is produced again ($Q_{con.}$).[3] Hence the machine can work as an adsorption heat pump when the intermediate temperatures ($Q_{ads.}$ and $Q_{con.}$) are used, or as a adsorption chiller when the lower temperature of $Q_{evap.}$ is used.[3] For a good performance, the sorption material should have several properties. It must be stable during thousands of ad-/desorption cycles and should exhibit a high uptake (sorption capacity). Additionally, the isotherm should exhibit no hysteresis and have a sigmoidal shape in a $p/p_0$-range from 0.05 to 0.3.[7] While different adsorbents like silica gels, zeolites or SAPOs have already been employed in commercial cooling systems compounds know as MOFs (metal-organic frameworks) have recently emerged as alternative adsorbents showing superior performance.[3,8,9]

[a] Institute für Anorganische Chemie, Christian-Albrechts-Universität, Max-Eyth-Straße 2, D 24118 Kiel, Germany.
[b] Fraunhofer-Institut for Solar Energy Systems ISE, Heidenhofstrasse 2, 79110 Freiburg, Germany
[c]
[d] D Technische Fakultät. Christian-Albrechts-Universität, Max-Eyth-Straße 2, D 24118 Kiel, Germany.
E-mail: stock@ac.uni-kiel.de

† Footnotes relating to the title and/or authors should appear here.
Electronic Supplementary Information (ESI) available: synthesis optimization, Detailed structure of Zr-UiO-66-PDC, Ce-UiO-66-PDC and Hf-UiO-66-PDC. Also IR, TG, of all compounds. See DOI: 10.1039/x0xx00000x

MOFs are composed of inorganic building units, usually metal ions or metal-oxygen clusters, which are interconnected by organic linker molecules.[10] They exhibit a remarkable structural diversity due to their modular composition.[11,12] The adsorbent with the highest water capacity is Cr-MIL-101 ($[Cr_3F(H_2O)_2O(1,4\text{-}BDC)_3]$, 1,4-$BDC^{2-}$ = 1,4-benzenedicarboxylate, MIL = Material Institute Lavoisier), however, the uptake is in the range $0.3 \leq p/p_0 \leq 0.6$.[13,14] Several thousand cycles of water vapour ad-/desorption without any loss of capacity was demonstrated for MIL-53-Fum ([Al(OH)(Fum)], $Fum^{2-}$ = fumarate)[15] and CAU-10 ([Al(OH)(1,3-BDC)], 1,3-$BDC^{2-}$ = 1,3-benzenedicarboxylate, CAU = Christian-Albrechts-Universität)[16,17] These compounds exhibit high capacities and sigmoidal isotherms below $p/p_0 < 0.3$.[17]

There exist several ways to fully exploit the modular structure of MOFs in order to tailor the water sorption behaviour. Especially the influence of hydrophilic groups on the sorption properties was investigated. Thus, formally replacing a CH group in 2-methylimidazole (HMIM) by N leads to the linker HMTZ (3-methyl-1,2,4-triazole). The resulting compounds $[Zn(MIM)_2]$ and $[Zn(MTZ)_2]$ exhibit very different water sorption properties. While the first compound is not porous, the latter is porous towards water.[18] A similar approach has been reported for the modification of CAU-10. The 1,3-benzenedicarboxylic acid was replaced by 3,5-pyridinedicarboxylic acid or 2,5-furandicarboxylic acid as linker molecules. The incorporation of the more hydrophilic linker molecules lead to a higher uptake of water and to a shift lower $p/p_0$ values compared to parent compound.[19] In addition, the influence of additional amine groups was investigated for UiO-66 ($[Zr_6(O)_4(OH)_4(BDC)_6]$, UiO = University of Oslo).[20] The UiO-66-$NH_2$ shows a shift of the water uptake to lower $p/p_0$-ranges but also a lower total uptake due to the steric demand of the $NH_2$-group.

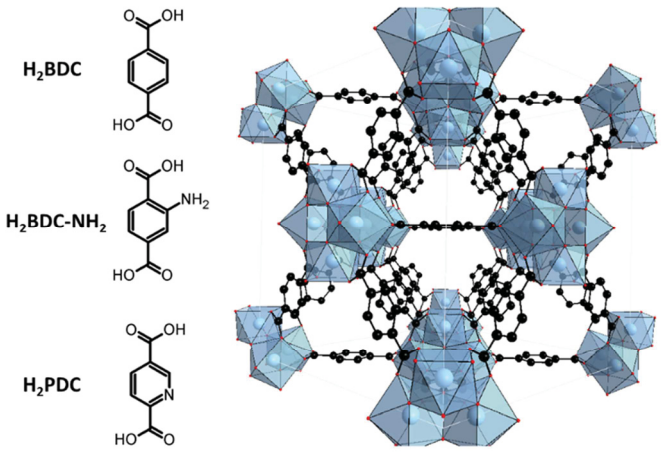


Fig. 1: Three linker molecules (left) that have been used for the synthesis of UiO-66 (right).

Based on these results one could anticipate that the incorporation N-heterocyclic linker molecules into the UiO-66 structure could lead to an increase in the sorption capacity and a shift to lower relative humidity values.

Here, we describe the synthesis and detailed characterisation of three UiO-66-type compounds containing Zr, Ce or Hf in the IBU and 2,5-pyridinedicarboxylate instead of 1,4-benzenedicarboxylate ions, i.e. Zr-, Ce- and Hf-UiO-66-PDC. In addition, the water and methanol sorption properties are reported.

## Experimental

### Materials and methods

All chemicals were used as received. The high throughput powder X-ray diffraction (PXRD) investigations were carried out on a Stoe Stadi P X-ray diffractometer equipped with a xy-stage, in transmission geometry using $MoK_{\alpha1}$ radiation and data collected by a Mythen detector. PXRD patterns for structure determination were measured using a Stoe Stadi P X-ray diffractometer in transmission geometry using $CuK_{\alpha1}$ radiation and data collected by a Mythen detector. Infrared spectra were recorded on a Bruker ALPHA-P A220/D-01 FTIR spectrometer equipped with an ATR unit. NMR spectroscopy was carried out using a Bruker DRX 500 spectrometer. Thermogravimetric analysis was performed using a NETZSCH STA 429 CD analyser with a heating rate of 4 $K \cdot min^{-1}$ under flowing air (flow rate 75 $ml \cdot min^{-1}$). Elemental analysis was performed using a EuroVector Euro EA elemental analyser. Nitrogen and $CO_2$ sorption isotherms were measured at -196 °C and 25 °C, respectively, with a BELSORP-Max apparatus. MeOH sorption isotherms were obtained with a Quantachrome Autosorb and $H_2O$ adsorption with a Quantachrome Hydrosorb at 25 °C. Water cycling stabilities were examined in a Setaram™ TGA-DSC-111 on powdered samples. A humidified argon gas flow (40 °C, 76.3% relative humidity) was generated by a Setaram WetSys humidity controller and passed through the sample chamber, while the temperature of the sample was varied and the mass of the adsorbent was monitored. For the multi-cycle ad-/desorption experiments, the temperature of the sample was varied between 40 °C and 140 °C with a cycle time of 5 h. Methanol cycle stability was examined in a Surface Measurement Systems Ltd. DVS Vacuum. Before and after cycling, the sample was degassed at 90 °C in vacuum and equilibrium points were taken at 25 °C by increasing the pressure of the gas flow 5 ml/min was held constant at 115 hPa while varying the temperature of the sample between 25 °C and 100 °C, which correspondents to a relative pressure p/p0 of 0.671 and 0.033, with cycle times of 1 h while cooling an 1 h when heating. In-situ DRIFTS on Zr-UiO-66-PDC was carried out with a Perkin Elmer Frontier spetrometer, equipped with a Diffuse Reflectance Accessory. A heat chamber with ZnSe window was utilized for the in-situ experiments. The spectra are averaged from 20 scans and recorded between 4000 and 700$cm^{-1}$ with a resolution of 4 $cm^{-1}$. Prior to the measurement the MOF was outgassed at 25 °C and reduced pressure. The experiment was conducted at 25 °C under $N_2$ gas atmosphere with a flow rate of 100 ml/min controlled by a Bronkhorst MassView. To investigate the influence of MeOH on the stability of the MOF, it was subjected 5 times to MeOH dosed $N_2$ for 30 seconds. Thus, the $N_2$ stream was passed through a MeOH bath (298K) with a bubble diffusor. After each treatment the sample was treated with dry $N_2$ until equilibrium and the spectrum was recorded. Luminescence measurements of the solid samples have been carried out in Suprasil A quartz ampoules, at room temperature. For this purpose, a FL-22 Fluorolog3 spectrometer (HORIBA Jobin Yvon GmbH), equipped with a 450 W xenon lamp, a R928P Photomultiplier and an iHR-320-FA triple grating imaging spectrograph was applied. Reflection spectra were also recorded at room temperature from the powdered samples with a Cary 5000 spectrometer (Varian

 

Techtron Pty.) applying BaSO4 as reference and diluting material. A Ce $L_3$-edge XANES spectrum of Ce-UiO-66-PDC was collected at the Southern Federal University (Russia) using Rigaku R-XAS spectrometer.

### Synthesis

The high-throughput investigations for the synthesis of the new compounds were carried out in a steel multiclave equipped with 24 Teflon reactors with a volume of 2 ml each.[21] Different metal salts, solvent combinations as well as modulators were tested. The optimization of reaction time and temperature were performed in Pyrex glass tubes with a volume of 5 ml, which were heated in an aluminium block by a laboratory heating plate. Details of the synthesis optimisation are listed in the supporting information (SI2, SI3, SI4). The optimized reaction conditions for the scale-up to 50 ml reactors is described below.

**Synthesis of Zr-UiO-66-PDC:** 0.733 g (4.4 mmol) $H_2PDC$ and 1.434 g (4.4 mmol) $ZrOCl_2{\cdot}8H_2O$ were mixed in 45 ml formic acid and 5 ml water in a round bottom flask placed in an oil bath. The mixture was heated at 130 °C under reflux for 3 h. The reaction was quenched by placing the round bottom flask under cold water. The suspension separated by centrifugation and subsequently washed twice with water and one time with ethanol (6000 rpm, 30 min, each). The product was dried under ambient conditions. The scale-up to 500 ml using the same reaction conditions is also possible (Fig. SXX) ZAHLEN rein, danach überarbeiten.

**Synthesis of Ce-UiO-66-PDC:** 1.670 g (10 mmol) $H_2PDC$ and 5.480 g (10 mmol) $(NH_4)_2[Ce(NO_3)_6]$ were mixed in 5 ml conc. $HNO_3$ and 45 ml water in a round bottom flask. The mixture was heated at 90 °C under reflux for 30 minutes. The reaction was quenched by placing the round bottom flask under cold water. The suspension separated by centrifugation and subsequently washed twice with water and one time with ethanol (6000 rpm, 30 min, each). The product was dried under ambient conditions.

**Synthesis of Hf-UiO-66-PDC:** 0.835 g (5 mmol) $H_2PDC$ and 1.6 g (5 mmol) $HfCl_4$ were mixed in 25 ml acetic acid and 25 ml water in a round bottom flask. The mixture was heated at 120 °C under reflux for 3 h. The reaction was quenched by placing the round bottom flask under cold water. The suspension separated by centrifugation and subsequently washed twice with water and one time with ethanol (6000 rpm, 30 min, each). The product was dried under ambient conditions.

## Results and discussion

Zr-MOFs with UiO-66 structure have been reported with various dicarboxylate ions.[Zhou] Thus, compounds incorporating nitrogen-containing linkers such as aminoterephthalic acid ($H_2BDC\text{-}NH_2$) 4,4'-azobenzenedicarboxylic acid,[23] or N-heterocyclic linkers (biyridinedicarboxylic acid,[22] pyrazindicarboxylic acid,[28] porphyrintetracarboxylic acid, [Zhou] have been described. Very recently the partial incorporation of 2,5-pyridinedicarboxylate ($PDC^{2-}$) was reported,[24] while the synthesis in DMF leads to Zr-UiO-66-PDC, although no structure determination was carried out in this study.[25]

Using high-throughput methods, we have been able to establish the water-based synthesis of three UiO-66-PDC compounds containing Zr, Ce or Hf on g-scale using reflux conditions. Products of high crystallinity were obtained using different modulators (Zr/fomic acid, Ce/$HNO_3$, Hf/acetic acid).

### Crystallography and defect chemistry

The structure of the three compounds M-UiO-66-PDC (M= Zr, Ce, Hf) were determined from PXRD data using Rietveld methods (SI, Fig. SXX–SYY).[29] All three structures are related to the ideal UiO-66 type framework (Tab. 1) and contain the hexanuclear clusters $[M_6(O_4)(OH)_4]^{12-}$ with M = $Zr^{4+}$ $Ce^{4+}$ and $Hf^{4+}$ respectively. In the ideal structure each cluster is connected by twelve terephthalate ions,[30] however compounds with linker and cluster defects are known.[31–33]

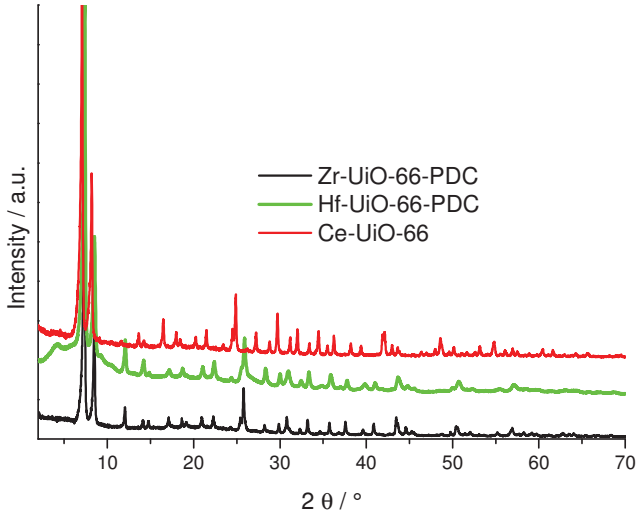


Fig. 2: PXRD patterns of the M-UiO-66-PDC compounds (M = $Zr^{4+}$ $Ce^{4+}$ and $Hf^{4+}$). AKTIVIERT? Additional peaks are marked with an asterisk.

All three MOFs show different types of defect chemistries. The PXRD patterns of Zr- and Ce-UiO-66-PDC exhibits exclusively peaks that are consistent with the fcu topology. Rietveld refinements of the PXRD data of the guest free samples (??? Check) show the absence of linker defects in the Ce-MOF, thus the compound has the ideal composition $[Ce_6(O)_4(OH)_4(PDC)_6]$). The oxidation state of the cerium in the compound was verified by XANES measurements, which confirmed that only $Ce^{4+}$ is present in Ce-UiO-66-PDC (SI Fig.5.13). In contrast, the structure of the Zr-MOF was successfully refined with one statistically missing linker molecule per formula unit. The composition in the product and the presence of $Cl^-$ ions for charge balance were confirmed by TG analysis (Fig. SXY), NMR-spectroscopy (Fig. S6.1) and EDX measurements (ratio Zr : Cl = 3 : 1). Although the localisation of H atoms is not possible and O, OH and $H_2O$ cannot be distinguished, the analytical data confirm the formula of Zr-UiO-66-PDC as $[Zr_6(O)_4(OH)_4(Cl)_2(H_2O)_4(PDC)_5]$.

The PXRD pattern of Hf-UiO-66-PDC shows broad additional peaks that are forbidden for the **fcu** structure of the parent framework. These peaks are due to correlated nanoscale disorder in the crystal structure and are well known for Hf-UiO-66-BDC.[34] In these regions missing linkers and missing clusters result in a structure with **reo**

topology, which is a sub-topology of **fcu**. Detailed characterisation by TG analysis (Fig. SXY), NMR-spectroscopy (SI Fig.6.2) and EDX analysis (ratio Hf : Cl = 3 : 2) excludes the presence of acetate ion and demonstrates the presence of $Cl^-$ ions. The deduced formula is $[Hf_6(O)_4(OH)_4(Cl)_4(H_2O)_8(PDC)_4]$ and a Rietveld refinement, neglecting the additional peaks originating from the **reo** defect topology, also confirmed this composition. The refinement indicates that statistical missing linker defects in the **fcu** framework lead to an identical composition as in the also present defect **reo** domains.

Tab. 1: Space groups and cell parameters of $[Zr_6(O)_4(OH)_4(Cl)_2(H_2O)_4(PDC)_5]$ (Zr-UiO-66-PDC), $[Ce_6(O)_4(OH)_4(PDC)_6]$ (Ce-UiO-66-PDC), $[Hf_6(O)_4(OH)_4(Cl)_4(H_2O)_8(PDC)_4]$ (Hf -UiO-66-PDC).

| MOF | Zr-UiO-66-PDC | Ce-UiO-66-PDC | Hf-UiO-66-PDC |
|---|---|---|---|
| SG | *Fm*-3*m* | *Fm*-3*m* | *Fm*-3*m* |
| a / Å | 20.6819(1) | 21.4579(2) | *20.5841(8)* |
| b / Å | 20.6819(1) | 21.4579(2) | *20.5841(8)* |
| c / Å | 20.6819(1) | 21.4579(2) | *20.5841(8)* |
| α / ° | *90* | *90* | *90* |
| β / ° | *90* | *90* | *90* |
| γ / ° | *90* | *90* | *90* |

**Thermal and chemical Stability**

Thermogravimetric analyses and temperature dependent PXRD experiments were carried out for all three MOFs to verify the deduced formulas and to monitor the thermal stability. According to the PXRD data Zr-UiO-66-PDC is stable up to a temperature of 220 °C (Fig. S9.1). The weight loss in the TG curve corresponding to the framework decomposition starts at approximately 350 °C. These observations indicate, that the structure collapses at lower temperatures while thermal combustion is delayed to higher temperatures. The weight loss corresponds to five linker molecules and two chloride ions per cluster. Thus the postulated sum formula of Zr-UiO-66-PDC is confirmed as $[Zr_6(O)_4(OH)_4(Cl)_2(H_2O)_4PDC)_5]$. A similar behaviour of the thermal stability as observed for Ce- and Hf-UiO-66-PDC. Ce-UiO-66-PDC is stable up to 140 °C but combustion starts only at 250 °C (Fig. SX.X). The TG analysis indicates an ideal composition of six linker molecules per cluster. Thus the deduced formula for Ce-UiO-66-PDC is confirmed as $[Ce_6(O)_4(OH)_4(PDC)_6]$. Hf-UiO-66-PDC is stable up to 150 °C based on the PXRD data (Fig. SXXX) but combustion is delayed to 200 °C (Fig. SYXY). The TG analysis proves the presence of defects in the structure and is in agreement with four linker molecules and four chloride ions per cluster. Thus the postulated sum formula of Hf-UiO-66-PDC is $[Hf_6(O)_4(OH)_4(Cl)_4(H_2O)_8(PDC)_4]$.

The chemical stability of the title compounds was studied by stirring 20 mg of each sample in 1 ml different organic solvents and different concentrations of aqueous HCl and NaOH for 24 hours at room temperature. All three MOFs are stable in a pH-range from 1 to 12, in more basic solutions the MOFs are destroyed. None of the MOFs is stable in a 0.1 M phosphate puffer ($HNa_2PO_4/H_2NaPO_4$). All three MOFs are stable in the tested organic solvents (Fig. S9.5.-Fig.S 9.10.).

**Luminescence Properties**

To study the influence of the N-atom in the aromatic ring on the luminescence properties, emission spectra of Zr-UiO-66-BDC, the title compounds and linker molecules $H_2PDC$ and $H_2BDC$ were carried out applying the excitation energies listed in Table 2 (Fig. 2, Fig. S10.1 – Fig. S10.5). Since radiative electronic transitions in the are not possible in $Zr^{4+}$ and $Hf^{4+}$, the optical properties of these MOFs are caused exclusively by the aromatic units of the organic linker, as often reported for other transition metal MOFs.[35-37] The emission spectrum of the Zr-UiO-66-PDC (Fig. 2, blue curve) consists of a broad band in the UV-blue spectral range with full width at half maximum (FMHM) of 3836 $cm^{-1}$ and maximum at 24752 $cm^{-1}$ (Tab. 2, Fig. S10.1). This band is blue-shifted in comparison to the emission spectrum of the $H_2PDC$ linker, which has an emission maximum located in the green spectral range at 19197 $cm^{-1}$ with a similar FWHM of 3828 $cm^{-1}$ (Fig 2, red curve). Similar values were reported by Sun et al for other MOFs containing $PDC^{2-}$ ions.[38] The blue shift after the incorporation of the organic linker into the MOF structure is explained in the literature by the enhancement of the $\pi \rightarrow \pi^*$ energy due to the weakening effect of the skeleton vibration within the rigid framework.[39] This shift to higher energy is also observed in the emission spectrum of Hf-UiO-66-PDC (Fig 2, black curve), broadly distributed between approximately 15000 $cm^{-1}$ and 26000 $cm^{-1}$ with maximum at 20903 $cm^{-1}$. In addition, the luminescence spectrum of Hf-UiO-66-PDC shows a second emission band of lower intensity with maximum at 24420 $cm^{-1}$. According to the recorded excitation spectra (Fig. S10.3), the energy assigned to this band is self-absorbed by Hf-UiO-66-PDC, decaying radioactively through the emission at ca. 20000 $cm^{-1}$. In contrast, Ce-UiO-66-PDC is not luminescent. Most probably, the blue shift of the emission band in comparison to $H_2PDC$ causes the overlap between the linker-based emission band and the absorbed spectral region of the Ce-UiO-66-PDC, shown by the diffuse reflectance spectra at Fig. S10.6 as previously observed in Ce-CAU-24.

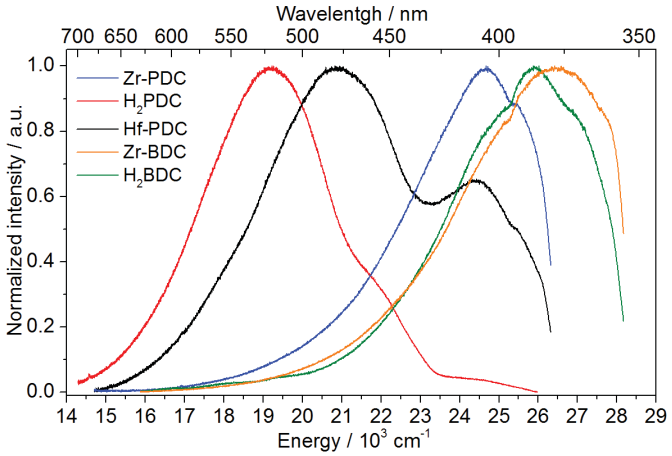


Fig. 2: Emission spectra of Zr-UiO-66-PDC (blue curve), $H_2$PDC (red curve) and Hf-UiO-66-PDC (black curve) as well of $H_2$BDC (green curve) and Zr-UiO-66-BDC (orange curve), applying excitation energies listed on Table 2.

Tab. 2: Emission maximum, excitation energy and FWHM of emission spectra of $H_2$PDC, Hf-UiO-66-PDC, Zr-UiO-66-PDC, Zr-UiO-66-BDC and $H_2$BDC.

| Compound | Emission maximum | Excitation energy | FWHM |
|---|---|---|---|
| $H_2$PDC | 19197 $cm^{-1}$ | 27777 $cm^{-1}$ | 3828 $cm^{-1}$ |
| Hf-UiO-66-PDC | 20903/24420 $cm^{-1}$ | 27777 $cm^{-1}$ | 6885 $cm^{-1}$ |
| Zr-UiO-66-PDC | 24752 $cm^{-1}$ | 27777 $cm^{-1}$ | 3836 $cm^{-1}$ |
| Zr-UiO-66-BDC | 26532 $cm^{-1}$ | 30769 $cm^{-1}$ | 4498 $cm^{-1}$ |
| $H_2$BDC | 25900 $cm^{-1}$ | 30769 $cm^{-1}$ | 4357 $cm^{-1}$ |

The emission spectrum of the Zr-UiO-66-BDC (Fig. 2, orange curve) is located mostly in the UV spectral range with maximum at 26532 $cm^{-1}$ (FWHM = 4498 $cm^{-1}$). In comparison to the $H_2$BDC linker (Fig. 2, green curve) it is also blue-shifted. The same shift in emission axima was reported for Zn teraphthalates (Was gibt es alles für Lumineszenz-Untersuchungen an Zr-UiO-66?).[39] The red shift between the emission spectra of $PCD^{2-}$ to $BDC^{2-}$ based structures has been previously observed for Zn-containing coordination polymers.[38] However, additional experiments are necessary for explaining this effect. According to Yang et al. the additional lone pairs of the nitrogen atoms is important for contributing to the interaction with the π* orbitals of the benzene ring, enhancing the luminescence efficiency of the analogue $H_2$BDC linker.[40] Moreover, the addition of nitrogen atoms to the benzene rings are reported to increase the interaction to guest species within the MOF pores as well as to enhance its luminescence, enabling the application of modified UiO-66 structures as sensor for $Fe^{3+}$,[41] phosphates[40] and biological thiols[42].

**Gas Sorption**

To determine the influence of the N-atom in the aromatic ring on the sorption properties, $N_2$, $CO_2$, $H_2O$ and MeOH isotherms were recorded at -196 and 25 °C for $N_2$ and the other gases, respectively (Fig. 2, SXX-SYY, Tab. SXXX). Whereas Zr-and Ce-UiO-66-PDC were successfully activated at 120 °C for 16 hours under reduced pressure, removal of guest molecules in Hf-UiO-66-PDC, even at ambient temperature and a pressure of 0.1 mbar, lead to the destruction of the structure (Fig. S11.3). Zr- and Ce-UiO-66-PDC show type I isotherms (Fig. 2) and evaluation by the BET method resulted in specific surface areas of $S_{BET}$ = 1380 and 768 $m^2\ g^{-1}$, respectively. The difference is due to the different number of linker of defects and the higher molar masses of the Ce-MOF. Compared to the known Zr- and Ce-UiO-6-BDC structures, the uptake of corresponding PDC-MOFs is higher for the Zr-MOF (Lit.: 1069 $m^2\ g^{-1}$)[28] but lower for the Ce-MOF (Lit.: $S_{BET}$ = 1282 $m^2\ g^{-1}$).[34] These observations also confirm the linker defects observed in Zr-UiO-PDC and Ce-UiO-66-BDC. Both MOFs are also porous towards $CO_2$ (Tab. SXXX).

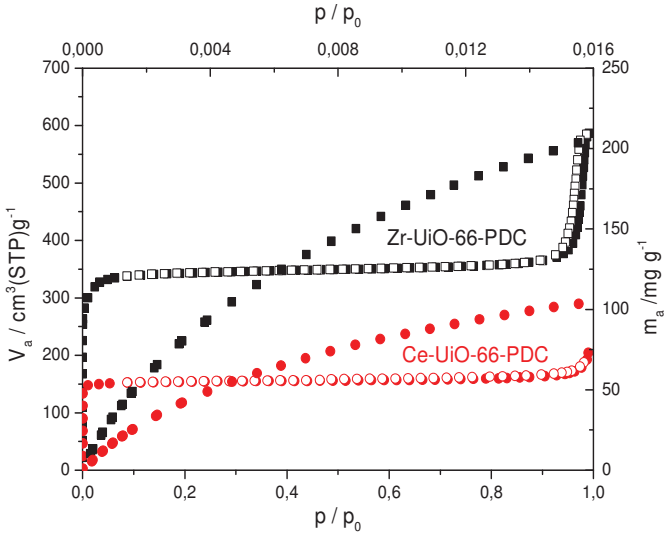


Fig. 2: Nitrogen and $CO_2$ isotherms of the Zr-UiO-66-PDC (black) and Ce-UiO-66-PDC (red) measured at -196 °C and 25 °C respectively.

The volumetric $H_2O$ and MeOH sorption isotherms for Zr-UiO-66-PDC and Ce-UiO-66-PDC are showing a type 1 (b) shape (Fig. 3). Due to the very strong hydrophilic adsorbent-adsorbate interactions uptake at p/p0 < 0.0X takes place. For water as the adsorptive a linear uptake at p/p0 > 0.3 is observed. At this point ($p/p_0$ = 0.3) Zr-UiO-66-PDC adsorbs 0.24XXX g/g and Ce-UiO-66-PDC 0.19XXX g/g water. In comparison to Zr-UiO-66-BDC and –BDC-NH2 UiO-66-BDC shifts the main uptake in the water isotherm from 0.3 p/p0 in Zr-UiO-66-BDC to < 0.2 in Zr-UiO-66-PD.C[18] The absolute amount of vapour adsorbed is comparable.

The affinity of the materials towards MeOH is slightly higher, which is visible by the slightly steeper curves for methanol vapour. The total capacity is for both MOFs similar with 0.25 g/g and 0.23 g/g for Zr-UiO-66-PDC and Ce-UiO-66-PDC respectively, which are relatively high numbers, compared to the values reported in the literature.[4]

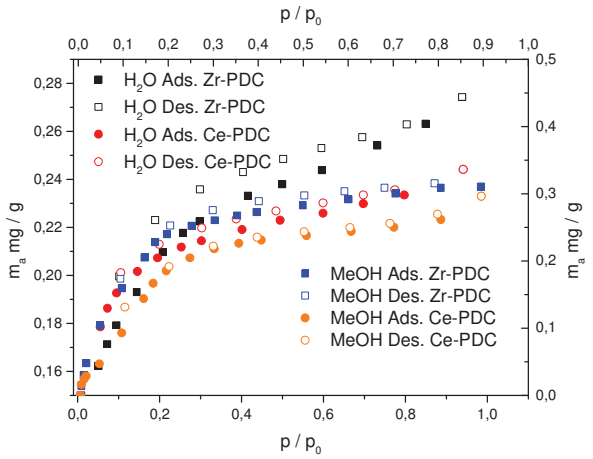


XXX y-Achse auf beiden Seiten bei NULL anfangen. Einfügen H2O und CH3OH/MeOH an den Achsen.Fig. 3: $H_2O$ and MeOH isotherms of the Zr-UiO-66-PDC (black and blue) and Ce-UiO-66-PDC (red and yellow) measured 25 °C.

Due to the shape ? water uptake of 0.2yg/g in the region 0.?<p/p0<0.Y, the compounds M-UiO-66-PDC (M = Zr, Ce) their water stability was tested by a multicycle ad-/desorption experiment in a thermogravimetric analyser (Fig. 4). A humidified argon gas flow of constant relative humidity is passed through the sample chamber and the temperature of the sample was varied (40 and 140°C) and the mass of the adsorbent was monitored. Under cycling conditions, Zr-UiO-66-PDC shows a very small dry mass degradation from 19.22 mg to 18.94 mg (2.5 wt %). During the first cycle starke Abnahme (Zahl) 20 ad-/desorption cycles a decrease in the water uptake capacity from 0.39 to 0.26 g/g is observed (Fig. 4), which levels out to a constant value of 0.25 g/g after additional 20 cylces (im Rahmen der Messfenauigkeit). This degradation is probably due a structural change after the first ad-/desorption, which lowers the adsorption capacity, as the dry mass stays nearly constant but the uptake decrease is already stabilised after this first cycle. Compared Zr-UiO-66-BDC and –BDC-NH2 which show a substantial and continuous loss of water capacity in the cycling experiments, the , it shows a higher stability.

Ce-UiO-66-PDC shows a similar behaviour in the cycling experiments but due its lower thermal stability the degradation is a bit faster (SI Fig.12.1.)

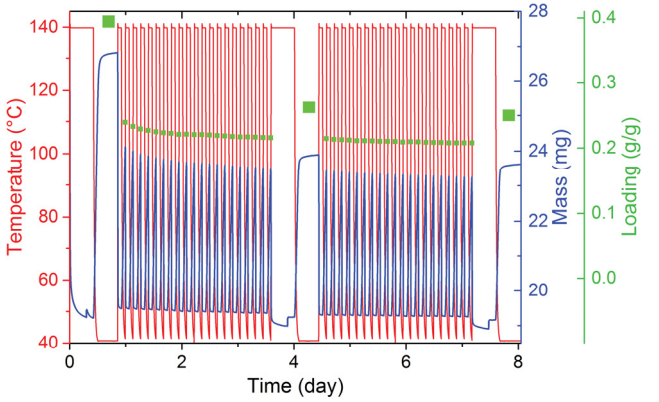


Fig. 4: Thermogravimetric water adsorption/desorption cycling experiments for 20 XXX sind viel mehr! cycles of Zr-UiO-66-PDC. Long segment at the beginning and at the end of each experiment were conducted to determine the equilibrium loading of the sample (red sample temperature, blue mass, green loading).

Additionally the methanol ad-/desorption cycle stability of Zr-UiO-66-PDC was examined in an *in situ* experiment using ?a Surface Measurement Systems Ltd. DVS Vacuum? Parameters were chosen to mimic an adsorption chiller for cooling applications around -10 °C. The material was treated for 100 cycles and exhibits a small constant loss in dry mass. After a fast decline in the methanol uptake during the first cycles the decrease in capacity shows a small but continuous behaviour after XXX (3tage) The total capacity of about 0.35 g/g drops constantly down to about 0.22 g/g after 100 cycles. A plateau could not be reached due to instrumental limits of the set-up. The strong decrease at the beginning can be explained by a postsynthetic exchange of the hydroxide group groups by methoxide groups, which has been reported previously (Yang 2016) and was is confirmed by DRIFTS measurements (Fig. XX). Upon treatment with methanol new bands at 2928 and 2824 $cm^{-1}$ evolve which are assigned to the C-H stretches of methoxy groups. The intensity of the band at 2742 $cm^{-1}$, assigned to the hydrogen-bonded $OH/OH_2$ groups in the hexanuclear cluster node, decreases simultaneously. Zr-UiO-66-PDC exhibits a lower stability compared to other MOFs such as HKUST-1 or MIL-101(Cr) under methanol ad-/desorption conditions.

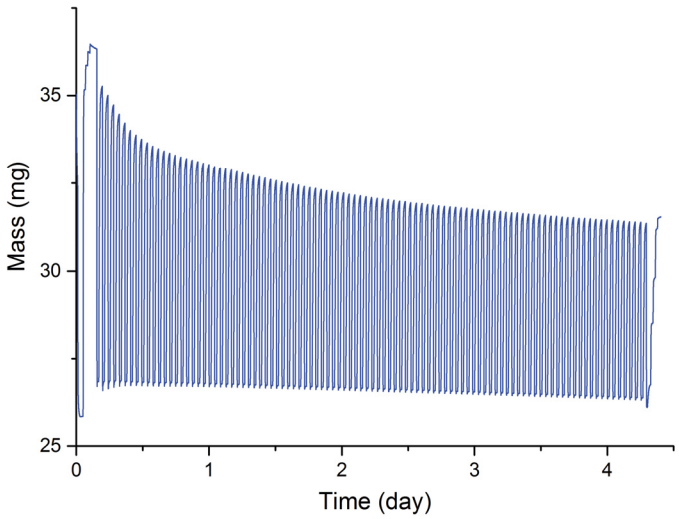


Fig. 10 Thermogravimetric methanol adsorption/desorption cycling experiments for 100 cycles of Zr-UiO-66-PDC (blue mass).

## Conclusions

In conclusion we synthesised three new MOFs with 2,5-pyridinedicarboxilic acid as linker and zirconium, hafnium and cerium respectively as metal. All structures could be determined by Rietveld methods and possesses the UiO-66 structure with different topologies. Additionally the Zr-UiO-66-PDC shows two different polymorph contains to the defects, which we call defect based polymorphism. The influence of the additional nitrogen in the ring was investigated by luminescence spectroscopy and sorption measurements. The water sorption measurements show similar capacity of water compared the UiO-66-BDC but at lower p/p0 values.

## Acknowledgements

We for practical help in the lap and Raphael Zachmann for the TG-DSC.

## Notes and references

1 M. Isaac and D. P. van Vuuren, *Energy Policy*, 2009, **37**, 507–521.
2 M. Sivak, *Energy Policy*, 2009, **37**, 1382–1384.
3 M. F. de Lange, K. J. F. M. Verouden, T. J. H. Vlugt, J. Gascon and F. Kapteijn, *Chem. Rev.*, 2015, **115**, 12205–12250.
4 U. N. E. P. O. Secretariat, *Handbook for the Montreal protocol on substances that deplete the ozone layer*, UNEP/Earthprint, 2006.
5 F. Jeremias, D. Fröhlich, C. Janiak and S. K. Henninger, *New J. Chem.*, 2014, **38**, 1846.
6 M. F. de Lange, B. L. van Velzen, C. P. Ottevanger, K. J. F. M. Verouden, L.-C. Lin, T. J. H. Vlugt, J. Gascon and F. Kapteijn, *Langmuir*, 2015, **31**, 12783–12796.
7 J. Canivet, A. Fateeva, Y. Guo, B. Coasne and D. Farrusseng, *Chem Soc Rev*, 2014, **43**, 5594–5617.
8 S. K. Henninger, F. P. Schmidt and H.-M. Henning, *Appl. Therm. Eng.*, 2010, **30**, 1692–1702.
9 L. W. Wang, R. Z. Wang and R. G. Oliveira, *Renew. Sustain. Energy Rev.*, 2009, **13**, 518–534.
10 S. R. Batten, N. R. Champness, X.-M. Chen, J. Garcia-Martinez, S. Kitagawa, L. Öhrström, M. O'Keeffe, M. Paik Suh and J. Reedijk, *Pure Appl. Chem.*, 2013, **85**.
11 W. Lu, Z. Wei, Z.-Y. Gu, T.-F. Liu, J. Park, J. Park, J. Tian, M. Zhang, Q. Zhang, T. Gentle III, M. Bosch and H.-C. Zhou, *Chem Soc Rev*, 2014, **43**, 5561–5593.
12 N. Stock and S. Biswas, *Chem. Rev.*, 2012, **112**, 933–969.
13 J. Ehrenmann, S. K. Henninger and C. Janiak, *Eur. J. Inorg. Chem.*, 2011, **2011**, 471–474.
14 B. B. Saha, I. I. El-Sharkawy, T. Miyazaki, S. Koyama, S. K. Henninger, A. Herbst and C. Janiak, *Energy*, 2015, **79**, 363–370.
15 F. Jeremias, D. Fröhlich, C. Janiak and S. K. Henninger, *RSC Adv.*, 2014, **4**, 24073.
16 D. Fröhlich, S. K. Henninger and C. Janiak, *Dalton Trans*, 2014, **43**, 15300–15304.
17 D. Fröhlich, E. Pantatosaki, P. D. Kolokathis, K. Markey, H. Reinsch, M. Baumgartner, M. A. van der Veen, D. E. De Vos, N. Stock, G. K. Papadopoulos, S. K. Henninger and C. Janiak, *J Mater Chem A*, 2016, **4**, 11859–11869.
18 J.-P. Zhang, A.-X. Zhu, R.-B. Lin, X.-L. Qi and X.-M. Chen, *Adv. Mater.*, 2011, **23**, 1268–1271.
19 A. Cadiau, J. S. Lee, D. Damasceno Borges, P. Fabry, T. Devic, M. T. Wharmby, C. Martineau, D. Foucher, F. Taulelle, C.-H. Jun, Y. K. Hwang, N. Stock, M. F. De Lange, F. Kapteijn, J. Gascon, G. Maurin, J.-S. Chang and C. Serre, *Adv. Mater.*, 2015, **27**, 4775–4780.
20 F. Jeremias, V. Lozan, S. K. Henninger and C. Janiak, *Dalton Trans.*, 2013, **42**, 15967.
21 N. Stock, *Microporous Mesoporous Mater.*, 2010, **129**, 287–295.
22 L. Li, S. Tang, C. Wang, X. Lv, M. Jiang, H. Wu and X. Zhao, *Chem. Commun.*, 2014, **50**, 2304.
23 A. Schaate, S. Dühnen, G. Platz, S. Lilienthal, A. M. Schneider and P. Behrens, *Eur. J. Inorg. Chem.*, 2012, **2012**, 790–796.
24 L. Chen, J. Ou, H. Wang, Z. Liu, M. Ye and H. Zou, *ACS Appl. Mater. Interfaces*, 2016, **8**, 20292–20300.
25 A. A. Barkhordarian and C. J. Kepert, *J Mater Chem A*, 2017, **5**, 5612–5618.
26 E. E. Sileo, O. E. Piro, G. Rigotti, M. A. Blesa, A. S. de Araujo and E. E. Castellano, *Struct. Chem.*, 2008, **19**, 651–657.
27 P. Silva, L. Cunha-Silva, N. J. O. Silva, J. Rocha and F. A. A. Paz, *Cryst. Growth Des.*, 2013, **13**, 2607–2617.
28 S. Waitschat, H. Reinsch and N. Stock, *Chem Commun*, 2016, **52**, 12698–12701.
29 A. Coelho, *Topas-Academic v5*, Brisbane, Australia, 2012.
30 J. H. Cavka, S. Jakobsen, U. Olsbye, N. Guillou, C. Lamberti, S. Bordiga and K. P. Lillerud, *J. Am. Chem. Soc.*, 2008, **130**, 13850–13851.
31 G. C. Shearer, J. G. Vitillo, S. Bordiga, S. Svelle, U. Olsbye and K. P. Lillerud, *Chem. Mater.*, 2016, **28**, 7190–7193.
32 M. Lammert, M. T. Wharmby, S. Smolders, B. Bueken, A. Lieb, K. A. Lomachenko, D. D. Vos and N. Stock, *Chem Commun*, 2015, **51**, 12578–12581.
33 W. Liang, C. J. Coghlan, F. Ragon, M. Rubio-Martinez, D. M. D'Alessandro and R. Babarao, *Dalton Trans*, 2016, **45**, 4496–4500.
34 M. J. Cliffe, W. Wan, X. Zou, P. A. Chater, A. K. Kleppe, M. G. Tucker, H. Wilhelm, N. P. Funnell, F.-X. Coudert and A. L. Goodwin, *Nat. Commun.*, 2014, **5**.

## 4.3 Stability investigations

The water stability of MOFs is a key issue for various applications like catalysis, gas sensing, gas storage and heat storage.

A frequent and easy to use test for the stability of MOFs is boiling it in water for several hours and analysis of BET surface areas prior and after the treatment. This might give a good indication of the overall stability and a process under liquid conditions.

However, with regard to the use of MOFs in adsorption processes, water is present in the gas phase. The underlying mechanism of ad- and desorption as well as a possible pressure change (PSA) or a temperature change, (TSA) like in pressure/temperature swing adsorption applications, might have a different impact on the structure which is not addressed by a typical boiling test.

Especially in case of the use under pure water vapor atmosphere like in adsorption heat pumps and chillers which are in focus of this work, some candidates, already estimated as stable, failed under hydrothermal cycling tests.

First difference between the test in liquid water and the test under gas water vapor phase is the missing phase change during the repeated ad-/desorption. In addition, boiling in water means that the pores are immediately filled with water molecules in liquid state. These interactions are different compared to the adsorption from gas phase.

However, the underlying mechanism is still not understood. Thus, this contribution aims to provide some additional puzzle pieces to this still open question by a deeper analysis of the cycle stability and decomposition of MOFs under humid conditions. For this, different experimental methods such as boiling in water, temperature and humidity dependent *in situ* DRIFTS and PXRD cycle analysis, were used.

## 4.4 Boiling in water

For the boiling experiments, 0.5 g MOF is refluxed in 100 ml water for a specific time. $N_2$ $S_{BET}$ analysis was done after filtration and vacuum drying at 120°C.

For the very water instable MOFs, like Cu-BTC and MAF-7, it is seen that the after one hour of boiling, nearly the whole surface area is destroyed. For ZIF-8/MAF-4, this is achieved after 24h of cooking, which shows, that ZIF-8 is also not very water stable, only its hydrophobic character gives the stability. The as water stable expected Al-MOFs (Al-Fumarate, CAU-10-H and MIL-160) are showing a small variation of the $S_{BET}$ surface area after 1h and 24h of refluxing. This is probably due to measuring inaccuracy. After 168h/one week of boiling, it's a decrease of around 20 % for Al-Fumarate and CAU-10-H, MIL-160 has a decrease of nearly 50 %.

MIL-100(Fe) shows no decrease of surface area after 24h of cooking, but ~40 % after one week of cooking as well as UiO-66 with a loss of 23 %. The most stable material is MIL-101(Cr) which shows no degradation, even after one week of cooking.

The hydrothermal stability of the MOFs can be proposed as: MIL-101(Cr) > CAU-10-H > Al-Fumarate > UiO-66 > MIL-100(Fe) > MIL-160 > ZIF-8 > MAF-7 > CuBTC. This results agree also with the work of P. van der Voor.[53]

In summary it can be said, that all materials, which still have a surface area after one week of treatment, can be called very stable, due to this harsh conditions.

Table 1 Results of MOF cooking experiments.

| | $S_{BET}$ original | $S_{BET}$ – 1h | $S_{BET}$ – 24h | $S_{BET}$ – 168h |
|---|---|---|---|---|
| Al-Fumarate | 971 | 966 | 914 | 774 |
| CAU-10-H | 628 | 606 | 680 | 506 |
| Cu-BTC | 1633 | 9 | 8 | 6 |
| MIL-100(Fe) | 1827 | 1743 | 1821 | 1135 |
| MIL-101(Cr) | 3460 | 3766 | 3589 | 3388 |
| MIL-160 | 1102 | 1175 | 1106 | 591 |

| | | | | |
|---|---|---|---|---|
| UiO-66 | 1619 | 1641 | 1663 | 1252 |
| MAF-7 | 1665 | 177 | 4 | 2 |
| ZIF-8/MAF-4 | 1865 | 1375 | 6 | 12 |
| MIL-59(Fe) | 1 | 1 | 1 | 2 |

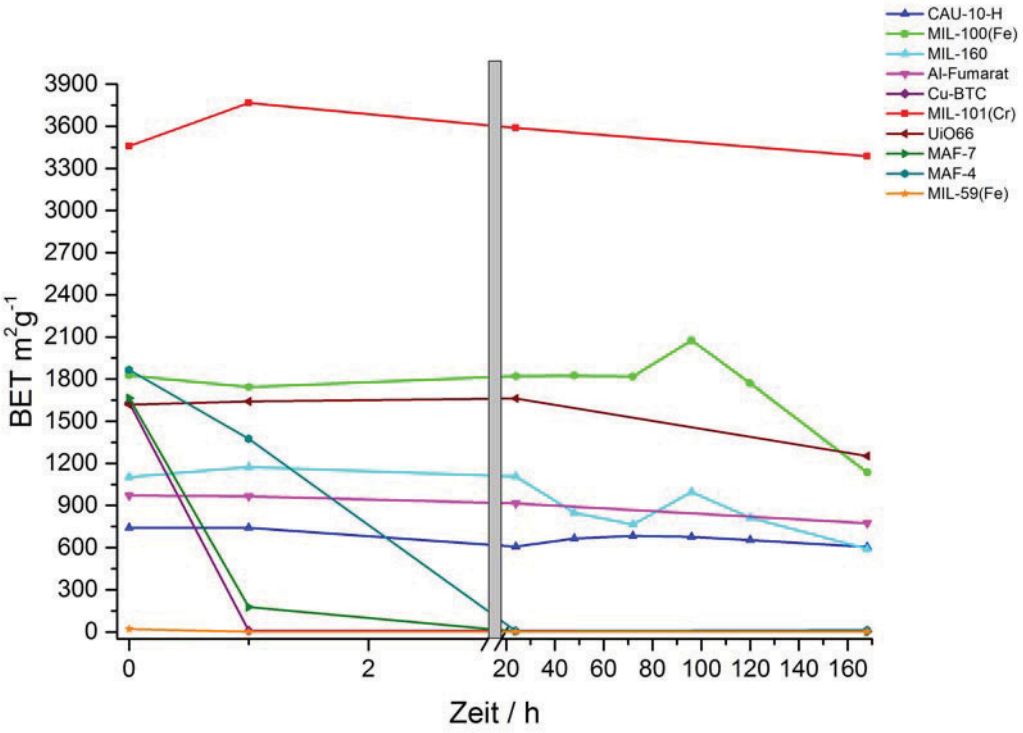


Figure 9 Results of MOF boiling experiments.

## 4.5 DRIFTS setup

The setup for the DRIFTS measurements is a "Frontier MIR Performance System" from Perkin Elmer, equipped with a "Frontier Diffuse IR" and "DiffusIR Env Chamber,900C" from PIKE (Figure 14). The chamber enables the user to expose the sample to different gas atmospheres and to vacuum ($4*10^{-2}$ mbar) ( Figure 12). Equipped with a ZnSe optical window (Edmund optics) allows measuring in humid environment (note, standard KBr is hydrophilic, ZnSe is insoluble in water), as well as nearly all other types of gases ($CO_2$, MeOH, $N_2$, $CH_4$…). The cell can be heated up to ~800°C. Due to the nature of the DRIFTS measuring principle (**Fehler! Verweisquelle konnte nicht gefunden werden.**), it is possible to have *in situ* spectra of the material under different conditions.

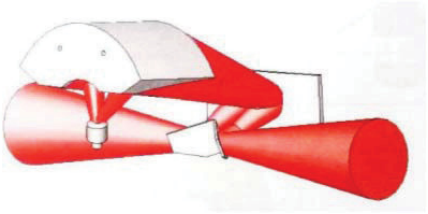

Figure 11 Optical path of DRIFTS cell.

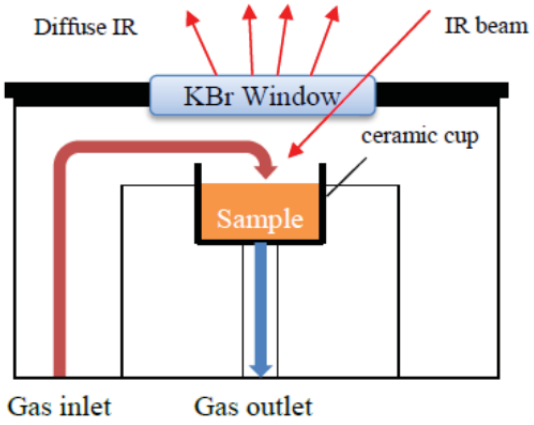


Figure 10 DRIFTS measuring cell.

Nitrogen is bubbled trough a water filled heated flask to obtain a humidified gas stream, which is passed through the environmental cell into the exhaust pipe (Figure 13).

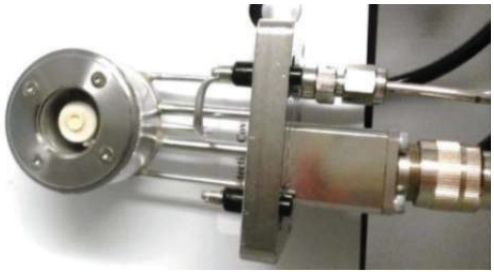

Figure 12 DiffusIR Env Chamber,900C from PIKE.

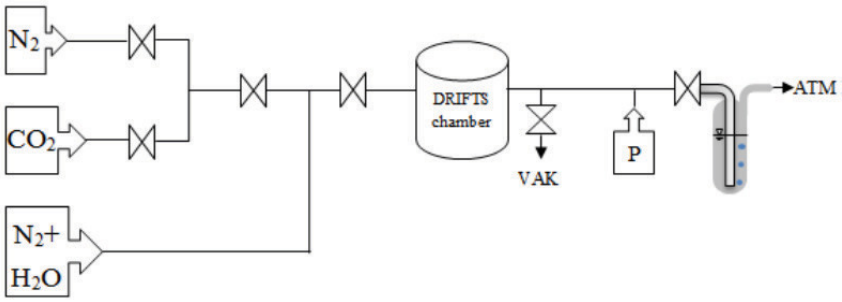


Figure 13 Scheme of the gas connections of the DRIFTS cell.

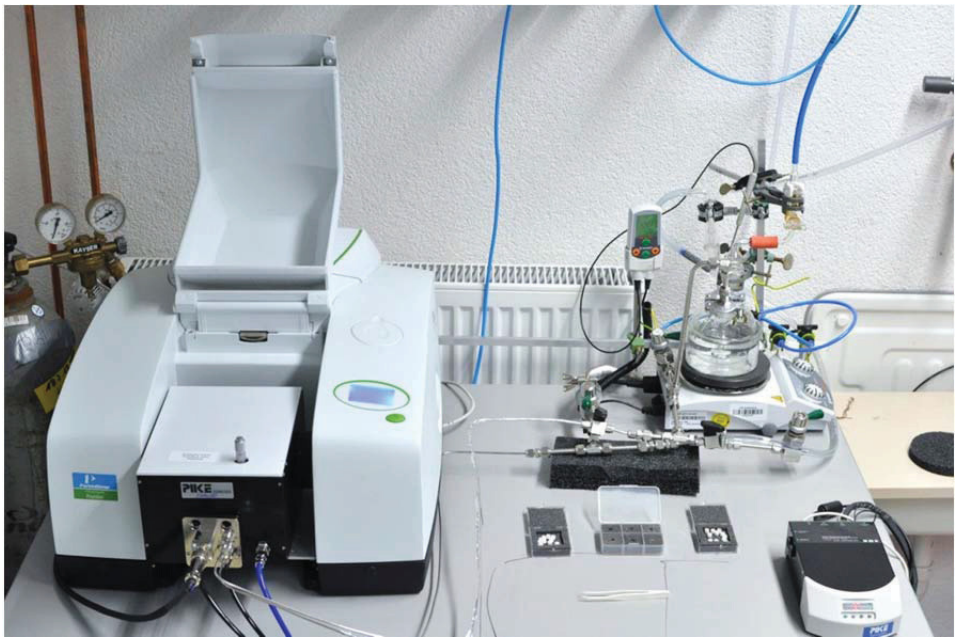


Figure 14 "Frontier MIR Performance System" equipped with "Frontier Diffuse IR" and "DiffusIR Env Chamber,900C"as well as a water reservoir for humidifying the gas stream.

## 4.6 *In situ* DRIFTS Cycles

The DRIFTS cycles had been adapted to the conditions which are present in heat transformations applications. Outgassing for 30 min at 120 °C under vacuum, afterwards a humidified nitrogen stream with 80% r.H. (at 30 °C), heating rate of 5 K/min and 30 min of soak for equilibration in hot (120 °C) and cold state (30 °C). The background is recorded against the humidified argon stream with a ZnSe window. Every 30 seconds is a new scan with 5 accumulations recorded.

In addition to the single spectrum a time profile/RMS intensity plot, of whole experiment, is shown. This enables to see how the MOF varies during the experiment without having to check every single spectrum. It is a graph of absorbance against time, where the average absorbance, over the entire wavenumber range of the spectrum, is a single value. With 35 ad- and desorption cycles in 70 hours, this are around 8000 single spectra per experiment.

### 4.6.1 Al-Fumarate

The Al-Fumarate DRIFT-spectrum (Figure 15) of the desorbed and adsorbed state are clearly distinguishable by the broad –OH band around 3500 $cm^{-1}$. In the desorbed state is a distinct peak at 3705 $cm^{-1}$ caused by the OH vibrations of Al-OH on Al-oxide-hydroxide chains.[54] At 1657 $cm^{-1}$ and 1467 $cm^{-1}$ are the asymmetric vibration of carboxylate visible. At 2672 $cm^{-1}$ and 2455 $cm^{-1}$ are signals which belong to carbonyl group of the fumaric acid. 825 $cm^{-1}$ can be identified to the deformation vibration of the vinylic C-H.

The spectra of the adsorbed Al-Fumarate is relative similar in the finger print, except the rise of the peak at 1034 $cm^{-1}$, which is due to a shift in the hydrogen bonding, from -CO-OH···O-Al to –CO-OH···$OH_2$. The peak at 3705 $cm^{-1}$ is vanishing while adsorption which supports results of a changing environment of the SBU environment.

The ad-/desorbed spectra are the same before and after the cycles, also the RMS intensity (Figure 16) plot shows always the same shape and no degradation over time, which underlines the stability of Al-Fumarate.

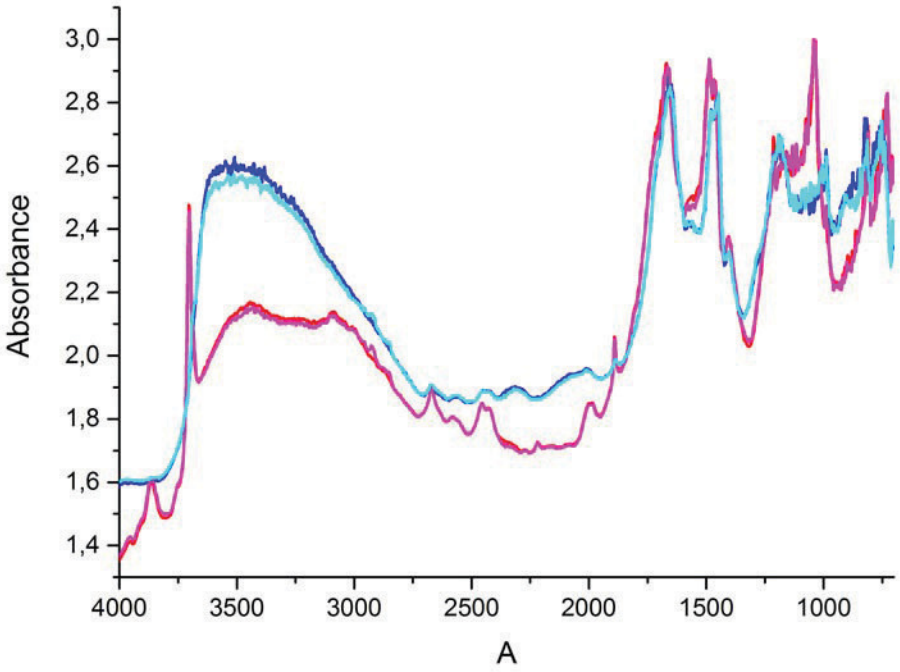


Figure 15 DRIFTS spectrum of Al-Fum. Red first desorption spectra, magenta after 35 cycles; blue first adsorption spectra, pale blue after 35 cycles.

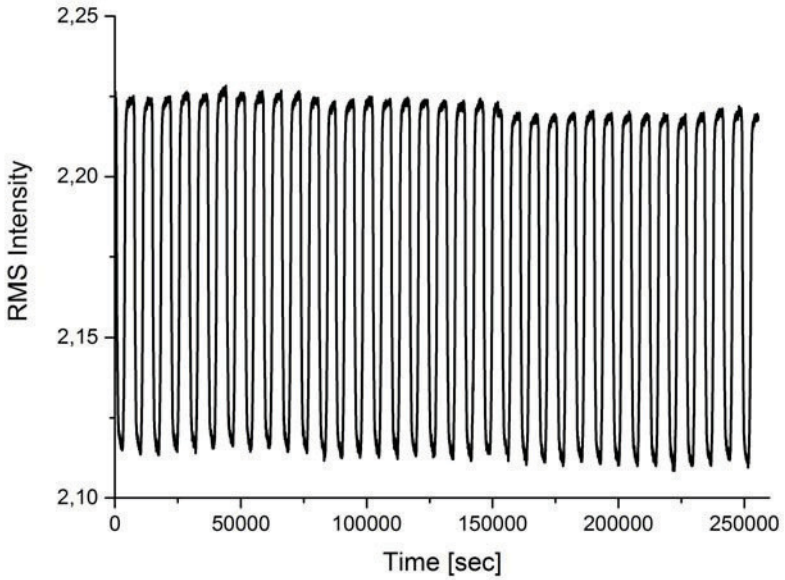


Figure 16 RMS intensity plot of Al-Fumarate DRIFT spectra while hydrothermal cycles.

### 4.6.2 CAU-10-H

The CAU-10-H DRIFT-spectrum (Figure 17) of the desorbed and adsorbed state are clearly distinguishable, because of the broad –OH band around 3500 $cm^{-1}$. In the desorbed state, there is a distinct peak at 3687 $cm^{-1}$ caused by the OH vibrations of Al-OH on Al-oxide-hydroxide chains.[54] At 3074 $cm^{-1}$ is the C-H stretching vibration from the aromatic H. At 1652 $cm^{-1}$ is a C=O stretching vibration, and at 1481 a C=C and C-H stretching vibration from the aromatic system. At 997 $cm^{-1}$ is the signal from the hydrogen bonding.

At adsorption the peak from 3687 $cm^{-1}$ shifts to lower wavenumbers, 3624 $cm^{-1}$, which could indicate a weakening of the Al-oxide-hydroxide bonding. Also the broad uprising of the 3500 $cm^{-1}$ water peak shows clearly the adsorption process. The hydrogen bonding signal at 997 $cm^{-1}$ is shifting to higher wavenumbers of 1137 $cm^{-1}$, which could be interpreted in stronger bonds between the complex and adsorbed water.

The ad-/desorbed spectra are the same before and after the cycles, also the RMS intensity (Figure 18) plot shows always the same shape and no degradation over time, which underlines the stability of CAU-10-H.

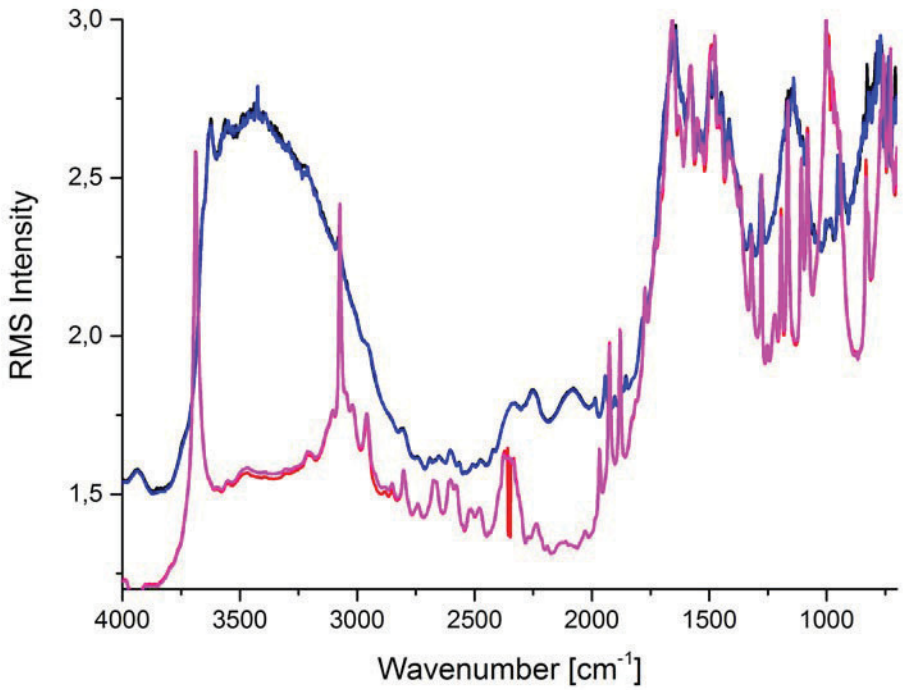


Figure 17 DRIFTS spectrum of CAU-10-H. Red first desorption spectra, magenta after 35 cycles; blue first adsorption spectra, pale blue after 35 cycles.

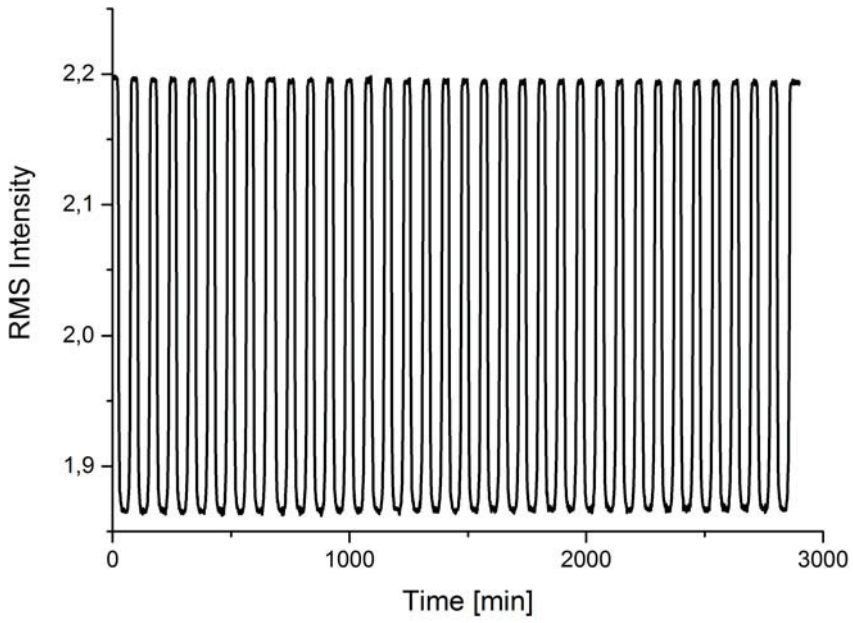


Figure 18 RMS intensity plot of CAU-10-H DRIFT spectra while hydrothermal cycles.

### 4.6.3 MIL-160(Al)

The MIL-160(Al)[55] DRIFT-spectrum (Figure 19) of the desorbed and adsorbed state are clearly to distinguishable, because of the broad –OH band around 3500 $cm^{-1}$. In the desorbed state is a distinct peak at 3689 $cm^{-1}$ caused by the OH vibrations of Al-OH on Al oxide-hydroxide chains.[54] At 1643 $cm^{-1}$ is the asymmetric vibration of carboxylate visible. 1449 $cm^{-1}$ can be identified to the C=C from the furan. The signal from the hydrogen bonding is at 999 $cm^{-1}$.

At adsorption the peak from 3689 $cm^{-1}$ shifts to 3620 and the broad –OH peak around 3500 $cm^{-1}$ is rising. Also the hydrogen peak at 999 $cm^{-1}$ is shifting to 1187 $cm^{-1}$.

The ad-/desorbed spectra are the same before and after the cycles, also the RMS intensity (Figure 20) plot shows always the same shape and therefore no degradation over time, which underlines the stability of MIL-160(Al).

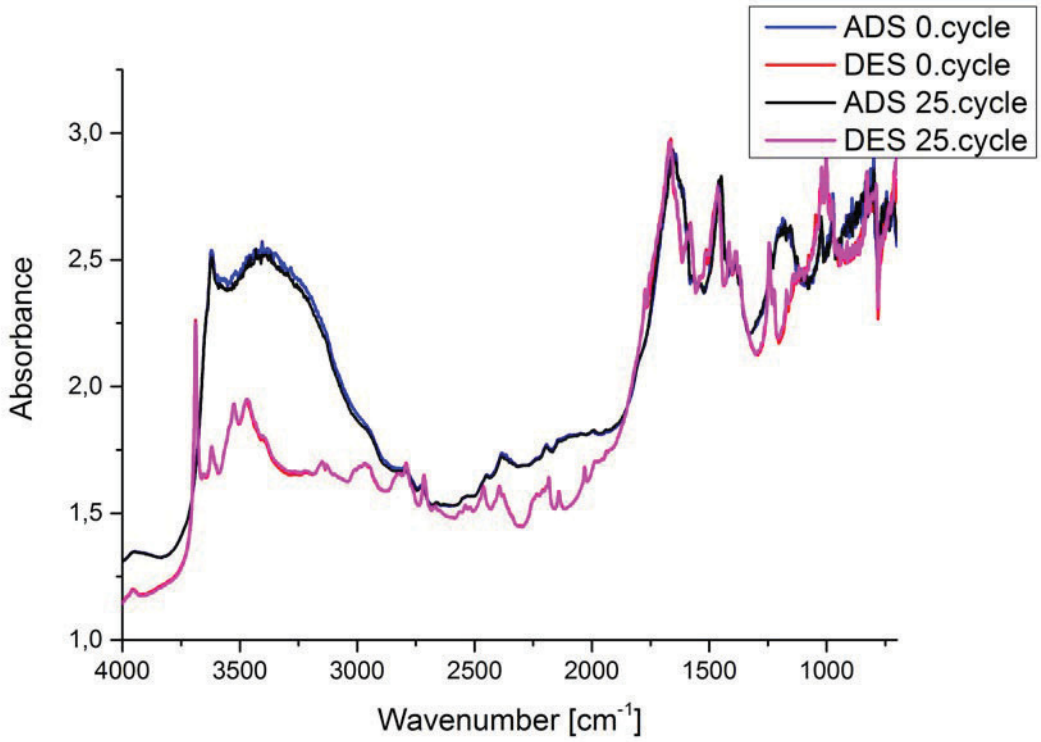


Figure 19 DRIFTS spectrum of MIL-160(Al). Red first desorption spectra, magenta after 25 cycles; blue first adsorption spectra, pale blue after 25 cycles.

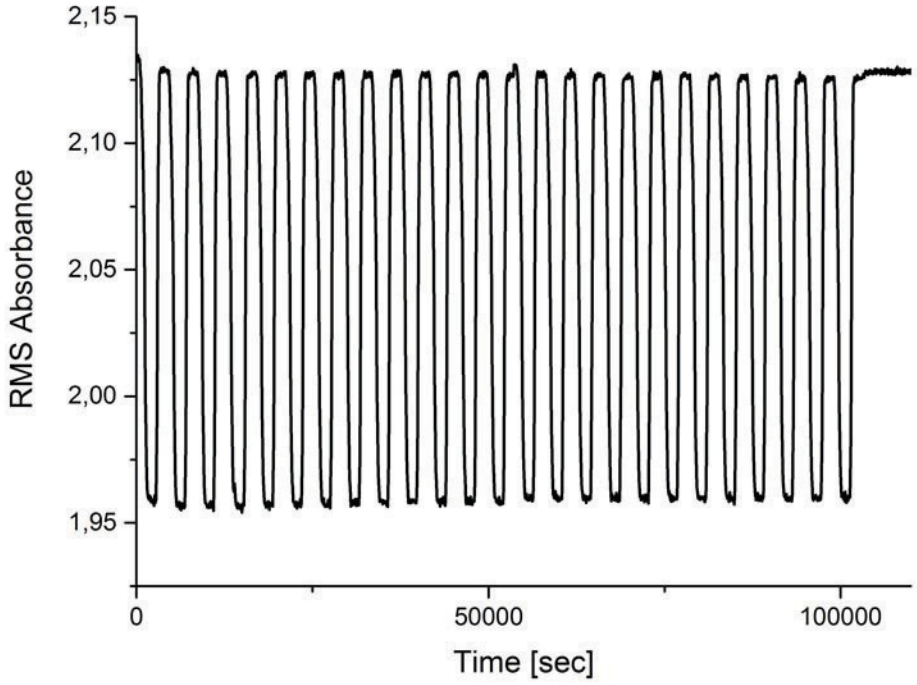


Figure 20 RMS intensity plot of MIL-160 DRIFT spectra while hydrothermal cycles.

### 4.6.4 Cu-BTC

The DRIFT spectra of Cu-BTC (Figure 21) shows a signals from the trimesic acid C-H vibration at 3093 $cm^{-1}$ and 938 $cm^{-1}$, aromatic stretching vibration from C=C at 1466 $cm^{-1}$ and carboxylic stretching at 1892 $cm^{-1}$ as well as a signal from Cu-O at 1401 $cm^{-1}$.

There is not much change while water sorption of the ad- and desorbed spectra, the peaks in the fingerprint stay mostly constant, except that there is a rise around 900 $cm^{-1}$ which is probably from the agglomeration of $H_2O$ in the Cu-O region, and therefor changes the energies of the Cu-paddlewheel bond. There is the common huge rise of the broad water signal during adsorption around 3500 $cm^{-1}$.

Also, the whole spectrum is rising in absorbance over cycles. The rise of the spectra is not yet fully understood. It could be because of a swelling of the material while adsorption, which leads to a different sample height, and therefore a different optical focus. Another explanation could be that Cu-BTC and hydrated Cu-BTC have a different adsorption coefficient, hence the diffuse Kubel-

ka-Munk IR beam penetrates the material different, which leads to a different absorbance.

After the hydrothermal cycle treatment, the desorbed spectra, at 120°C, shows a rise whereby it converges to adsorbed spectra, this means also an average rise in absorbance. The cycled adsorbed spectra shows the convergent opposite behavior, it converges to the desorbed spectra, which means an average lowering in absorbance. The RMS intensity plot (Figure 22) confirms this trend. This trend is also seen in EPR experiments from other groups, where they could find a partial displacement of organic linkers from the copper centers.[56]

From the following trend in the RMS intensity plot, the ad- and desorbed spectra are likely to have converged and will have become nearly equal after many ad-/desorption cycles.

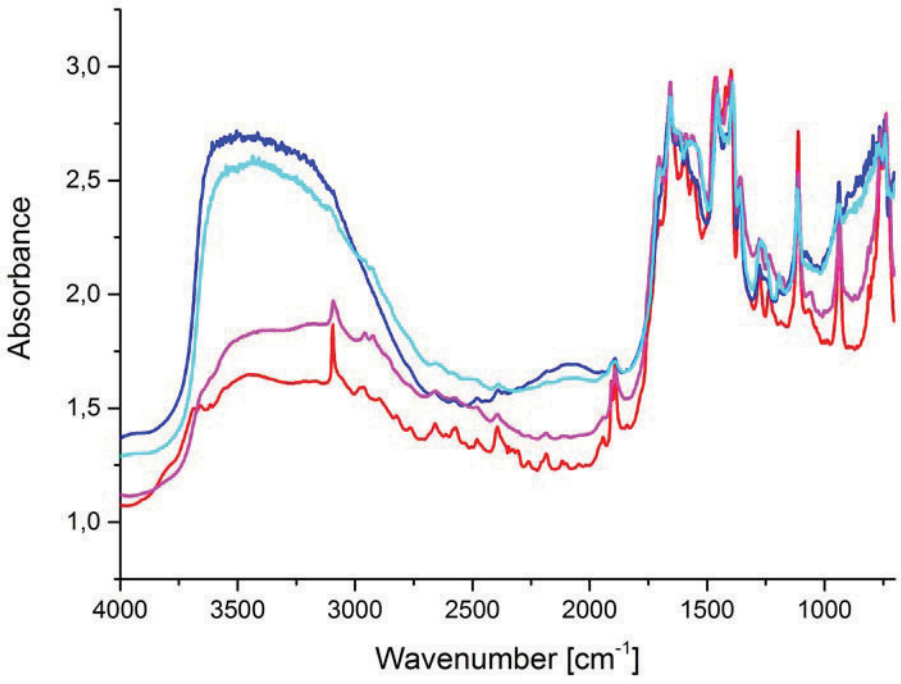


Figure 21 DRIFTS spectrum of Cu-BTC. Red first desorption spectra, magenta after 35cycles; blue first adsorption spectra, pale blue after 35cycles.

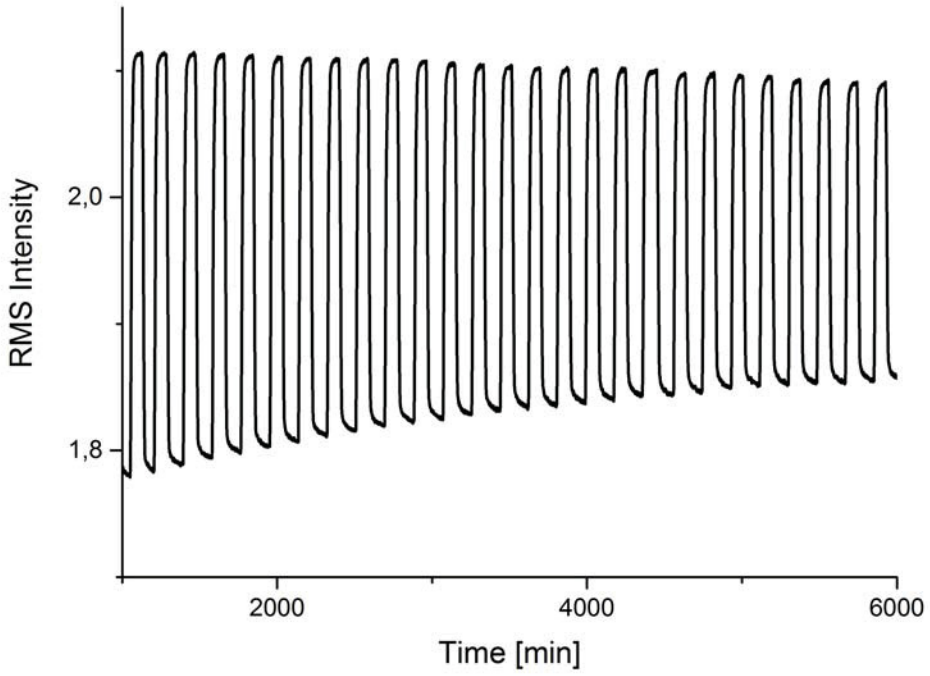


Figure 22 RMS intensity plot of Cu-BTC DRIFT spectra while hydrothermal cycles.

### 4.6.5 Conclusion

Summarizing, it can be said the DRIFTS experiment are beneficial to test the water stability under hydrothermal cyclic stress. This is demonstrated in the Cu-BTC experiment, where a decomposition in the RMS intensity plot is very visible, as well as in the spectra before and after the treatment. Al-Fumarate, CAU-10-H and MIL-160(Al) are showing no degradation.

For these three MOFs, with a SBU of chains of $AlO_6$ octahedra, is in common that the they all have a sharp signal at around 3690 $cm^{-1}$, dedicated to the OH vibrations of Al-OH on Al oxide-hydroxide chains, which shifts to lower wave-numbers (~3620 $cm^{-1}$) while adsorption; for Al-Fumarate it vanishes. Also a sig-

nal at ~998 $cm^{-1}$ is shifting to a higher wavenumber, 1137 $cm^{-1}$ (CAU-10-H), 1187 $cm^{-1}$ (MIL-160(Al)) (for Al-Fumarate 825 $cm^{-1}$ to 1034 $cm^{-1}$). This can be dedicated due a shift in the hydrogen bonding, from -CO-OH···O-Al to –CO-OH···$OH_2$.

This shows, that the Al-MOFs have probably the same sorption mechanism which takes place at the chains of $AlO_6$ octahedra.

## 4.7 XRD setup

To achieve *in situ* measurements, the MTC-LOWTEMP® chamber from Bruker AXS was coupled with a humidity generator. With this setup it is possible to achieve temperatures ranging from -150 °C to 400 °C, in a humid atmosphere (keep in mind freezing under 0 °C). The cooling gets achieved via liquid nitrogen.

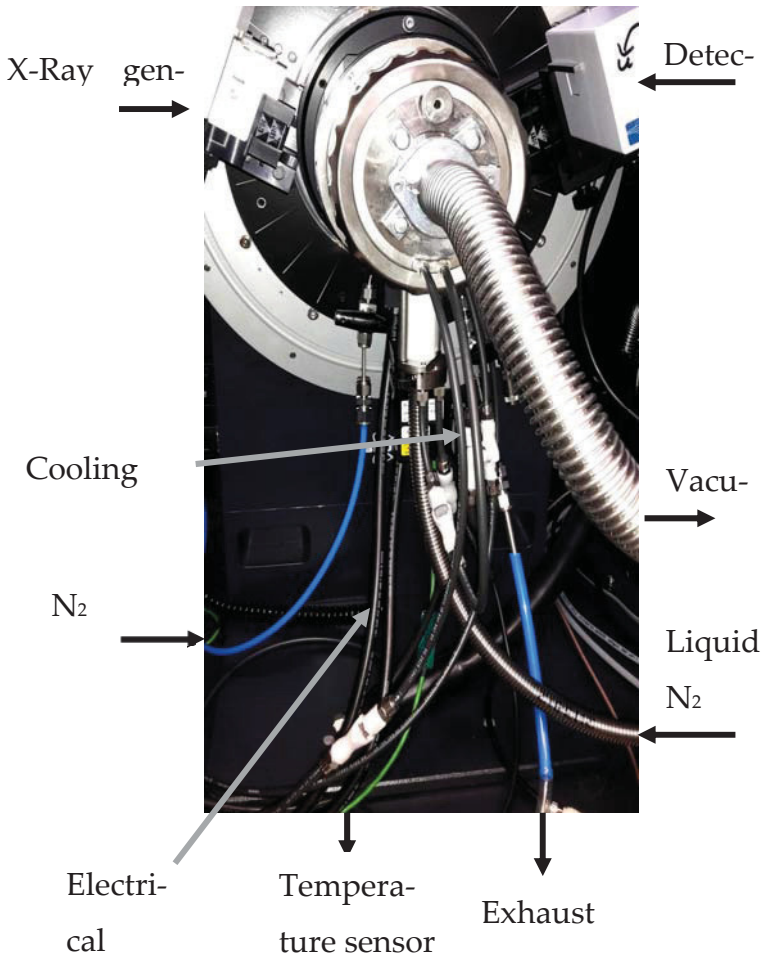


Figure 24 MTC-LOWTEMP® chamber from Bruker AXS

Measurements under vacuum are possible as well as nearly all possible gas mixtures, for example $N_2$, $H_2O$, $CO_2$, $CH_4$, etc. and therefore the environment of the MOF atmosphere, is possible to maintain.

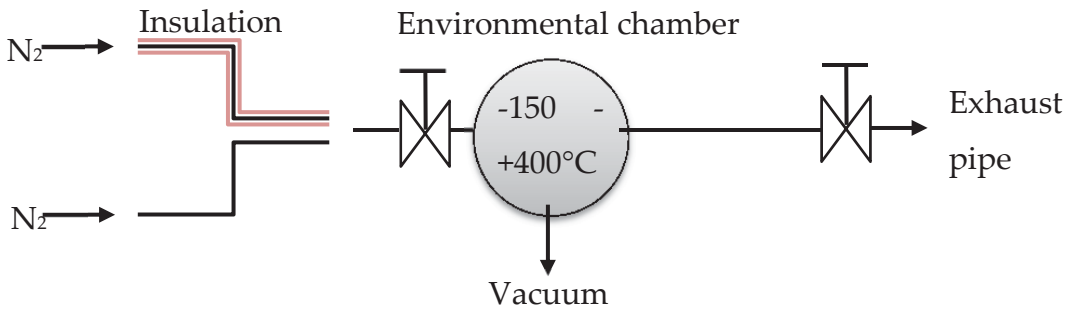


Figure 23 Scheme of XRD environment chamber.

## 4.8 *In situ* XRD cycles

With regard to the known structural change upon adsorption of guest molecules, especially water, adsorption/desorption experiments were conducted under *in situ* PXRD observation.

Powder X-ray diffraction (PXRD) analysis was performed on a Bruker D8 Advance diffractometer with DaVinci™ design, using Cu-K$\alpha$ radiation from a Cu anode tube at 40 kV/40 mA with a Ni filter in Bragg Brentano geometry. An MRI TC-humidity chamber, coupled to a humidified nitrogen flow generated by an Ansyco® humidifier, was used for controlled humidity and *in situ* PXRD cycle experiments. An XYZ Newport stage was used for coated sheets. *In situ* PXRD cycle experiments were done with the sample held at 40 °C and cycled between a wet (40% r.H.) and dry (0% r.H.) nitrogen flow. After every cycle, the powder diffractogram was recorded.

For all the materials 20 adsorption (blue)/desorption (red) cycles where recorded with *in situ* XRD observation. For clarity, only the first 3 cycles and last 3 cycles are shown.

### 4.8.1 Al-Fumarate

During adsorption the intensity of the main reflex at 10.1° decreases, as well as at 20.5°.

After 20 cycles, there are no changes in the PXRD pattern; the reflections of the material show the same intensity as those of the fresh powder. In addition, no increase of amorphous background is visible. This results fit perfectly with other stability investigations which have been undertaken.[32]

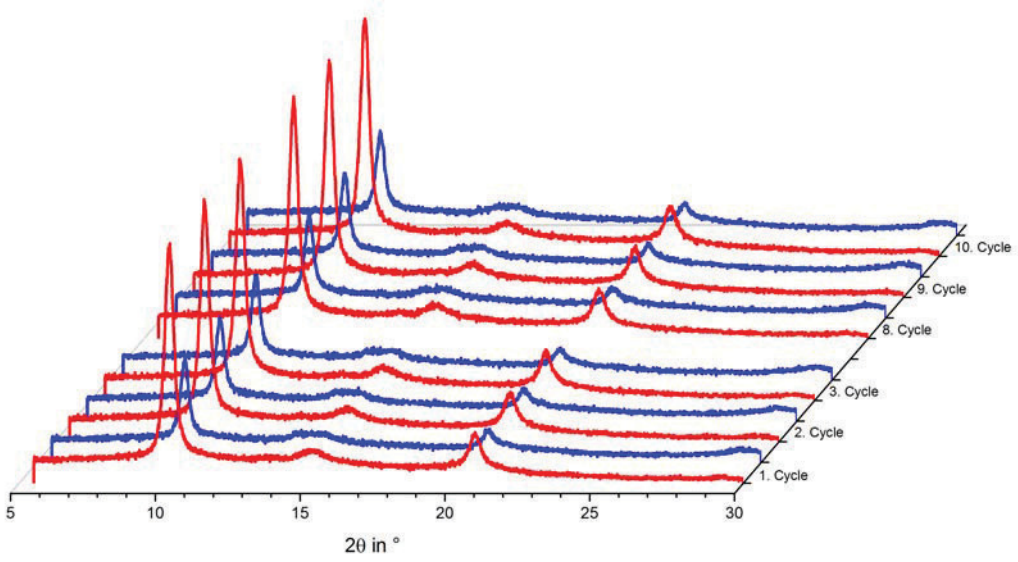


Figure 25 XRD cycles of Al-Fumarate.

### 4.8.2 CAU-10-H

During adsorption the intensity of the main reflex at 7.9° and 14.7 decreases. There a several smaller reflexes which appear, like those at 11.4 or 12.7.

After 20 cycles, there are no changes in the PXRD pattern; the reflections of the material show the same intensity as those of the fresh powder. In addition, no increase of amorphous background is visible. This results fit perfectly with other stability investigations which have been undertaken and already published.[50] Also the crystal structure of the dry and wet phases could be solved.[52]

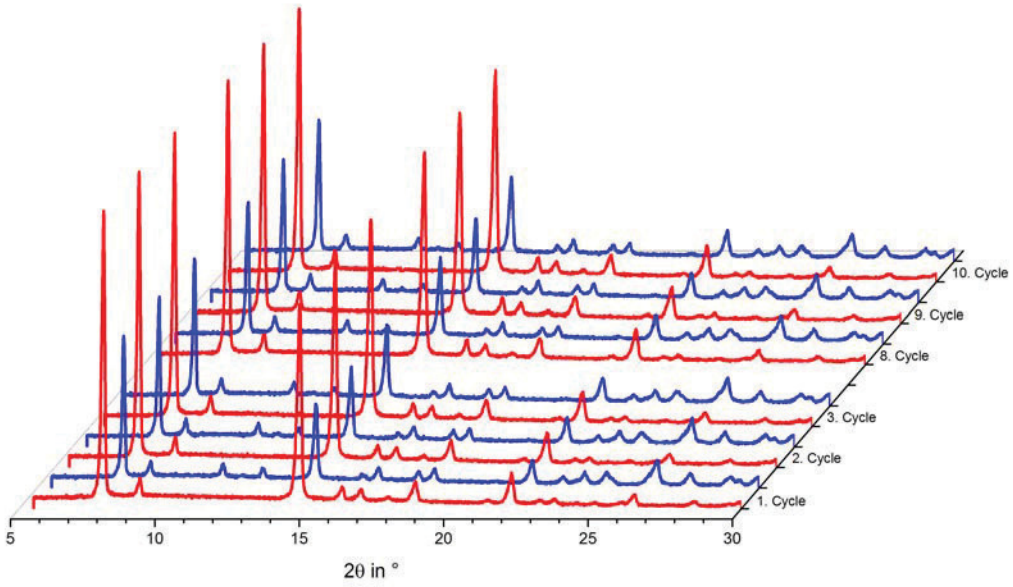


Figure 26 XRD cycles of CAU-10-H.

### 4.8.3 Cu-BTC

During adsorption, there is a decrease in intensity for several reflexes, for example 6.5°, 9.3° or 11.4°

For Cu-BTC it is known, that it is not stable toward water vapor adsorption.[5] This is not obvious in this XRD experiment. Probably the loss of uptake capacity which is visible in *in situ* TG-experiments is not a result of a loss in crystallinity in the first cycles.

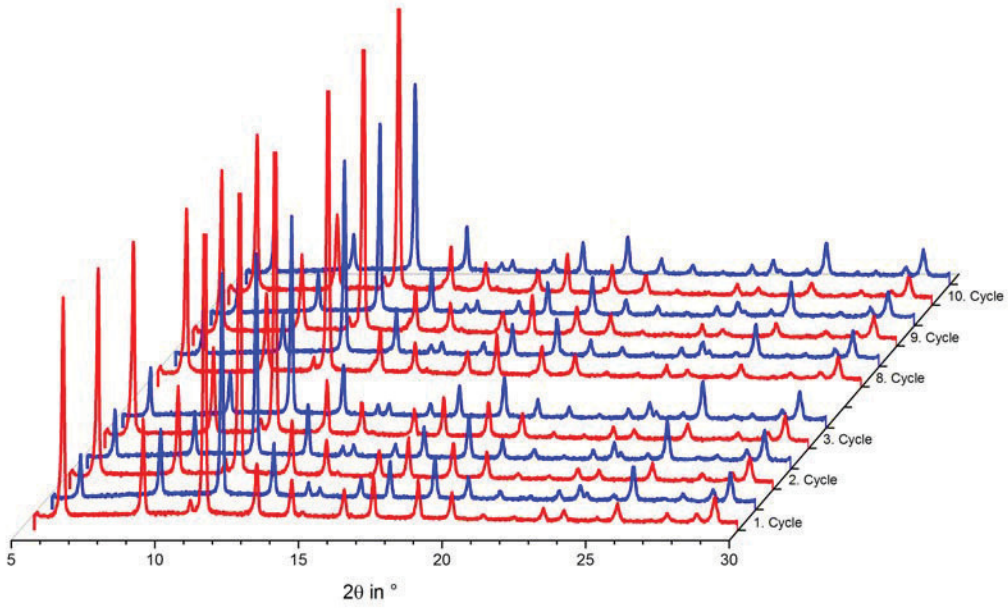


Figure 27 XRD cycles of Cu-BTC.

### 4.8.4 ZIF-8 / MAF-4

ZIF-8/MAF-4 shows no structural change during a cycle where a high water vapor atmosphere is present. This was predictable, because ZIF-8 is a very hydrophilic material. Therefore it also no degradation in this 20 hot and cold cycles is observed.

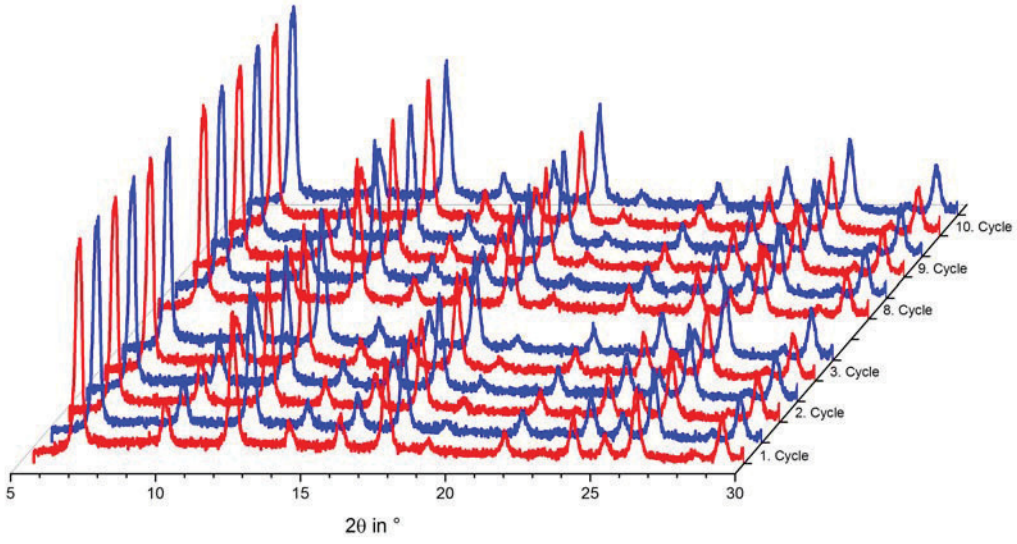


Figure 28 XRD cycles of ZIF-8/MAF-4.

### 4.8.5 MAF-7

Due to the exchange from imidazol to triazol in the MAF materials,[37] MAF-7 is much more hydrophilic than ZIF-8/MAF-4. This is visible in an ad- and desorption difractogram, for example in the decrease of the reflex at 7.0° or 12.4°. Also, there is a dramatic loss in crystallinity, which leads to a nearly amorphous powder after 20 cycles.

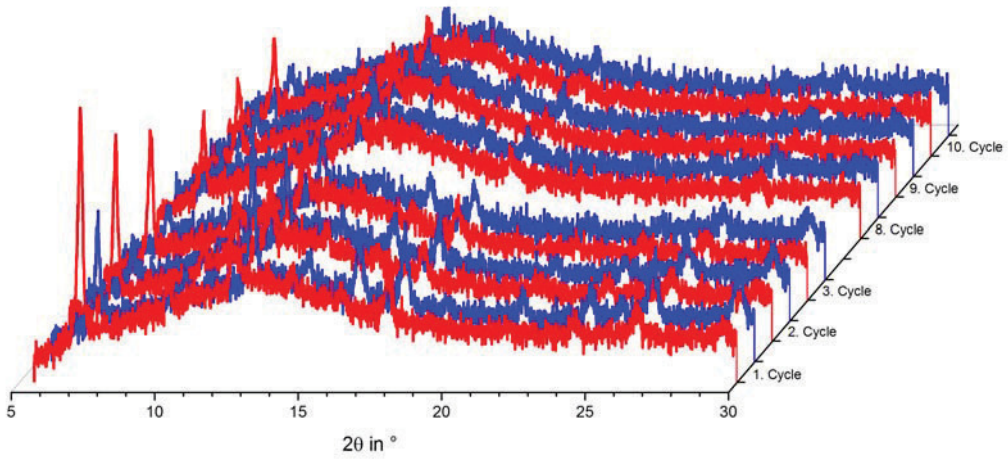


Figure 29 XRD cycles of MAF-7.

### 4.8.6 MIL-100(Fe)

MIL-100(Fe) shows a decrease in intensity for nearly all reflexes while ad-/desorption of water vapor, and no loss in crystallinity after 20 cycles. This matches with other published results, that the material is stable during water adsorption.[21]

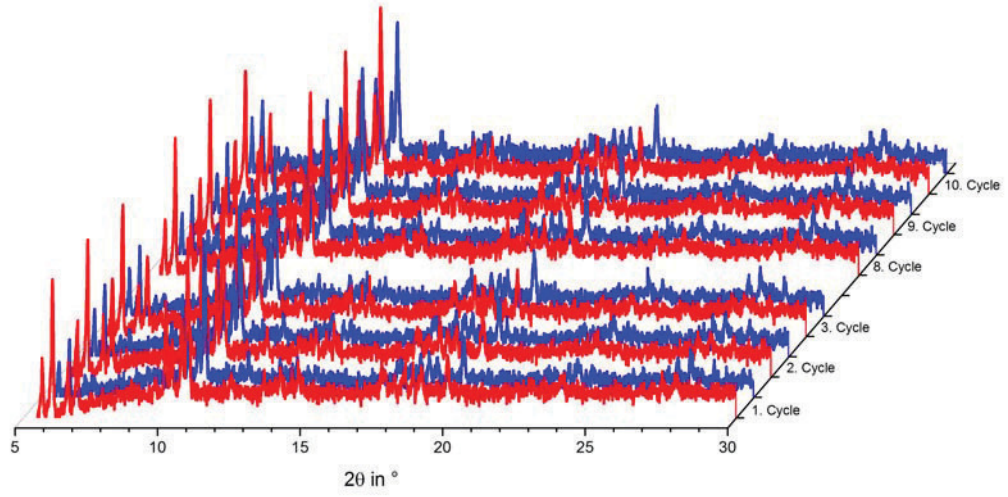


Figure 30 XRD cycles of MIL-100(Fe).

### 4.8.7 MIL-101(Cr)

MIL-101(Cr) shows a decrease in intensity for nearly all reflexes during ad-/desorption of water vapor, and no loss in crystallinity after 20 cycles. This matches with other published results, that the material is stable trough water adsorption.

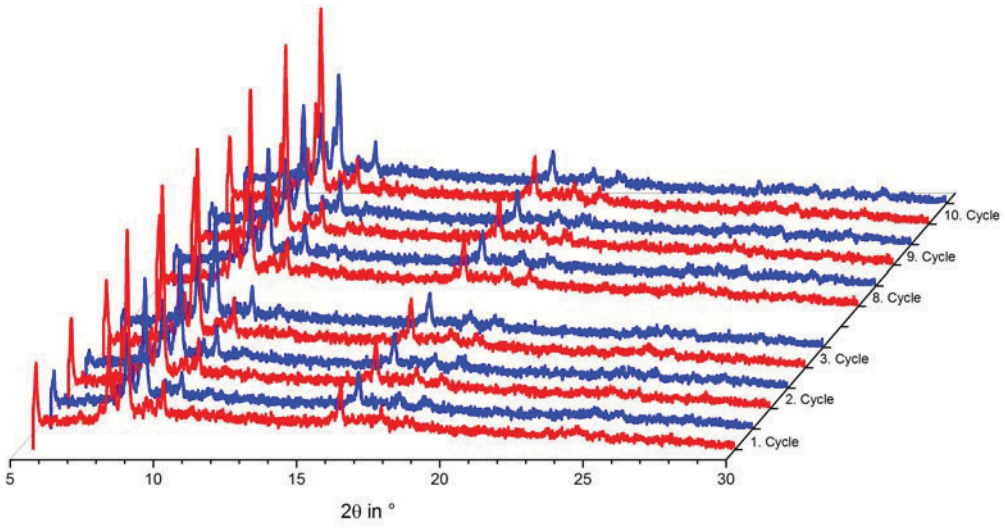


Figure 31 XRD cycles of MIL-101(Cr).

### 4.8.8 Conclusion

The only material which showed a degradation in crystallinity in this study, was MAF-7. Except the hydrophobic ZIF-8, all materials, Al-Fumarate, CAU-10-H, Cu-BTC, MAF-7, MIL-100(Fe) and MIL-101(Cr), show a change in crystal phase or intensity, during water adsorption.

## 4.9 Experimental

In this section, experimental details are given for the processes presented in the current chapter (Unpublished Results). Experimental details of the cumulative part of this paper are given in the respective publications.

### 4.9.1 Reagents and Solvents

*Metal salts, organic linker compounds and other reagents* were used as received.

### 4.9.2 Instrumentation

*$N_2$ adsorption isotherms* were obtained on a Quantachrome® Nova @ 77 K, after vac. degassing (120 °C / 24h).

*$H_2O$ adsorption isotherms* were obtained on a Quantachrome® Hydrosorb, after vac. degassing (120 °C / 24h).

*Powder cycle stabilities* were examined in a Setaram™ TGA-DSC-111. A humidified argon gas flow (40 °C, 76.3 % relative humidity) was generated by a Setaram™ WetSys humidity controller and passed through the sample chamber, while the temperature of the sample chamber itself varied between 40 °C and 140 °C with a cycle time of 5 h.

*Powder X-ray diffractograms* were acquired on a Bruker D8 Advance with DaVinci™, using a Cu anode tube at 40 kV/40 mA, with a Ni filter and constant sample illumination spot size (broadness: 12 mm); step size 0.02°, 1.0 s/step, Cu-K⊚ radiation. A rotating sample holder was used for powders. A Newport stage with three axes was used for coated sheets.

*Multi-cycle tests* of coated sheets were performed in a purpose-made, isobaric testing device. In an evacuated tank filled with ethanol vapor at 3.2 kPa or methanol vapor at 7.5 kPa or water vapor at 1.3 kPa, the sample was attached to a heating/cooling plate and exposed to alternating temperatures of 25 °C or 125 °C for 90 seconds each. This corresponds to relative vapor pressures of $p/p_0 = 0.54$ or 0.006 for ethanol, $p/p_0 = 0.44$ or 0.01 for methanol and $p/p_0 = 0.55$ or 0.006 for water vapor.

# 5 Summary and Outlook

Two aluminum MOFs have been intensively studied. Al-Fumarate and CAU-10-H. They were chosen because of their promising water adsorption characteristics which had been already published. After synthesis, according to literature, they had been intensively tested for their potential in heat pump applications.

Al-Fumarate has distinctive water sorption properties, s-shaped isotherm, narrow hysteresis and a loading of > 0.3 g/g at a relative pressure as low as $p/p_0 = 0.3$ under realistic working conditions, which makes it favorable for heat pump applications. It has a high stability, it can withstand over 4 500 water ad-/desorption cycles, where it shows no loss of crystallinity, which makes it even more feasible for the application. It was possible to coat a 300 µm thick, polycrystalline, thermally well coupled and highly accessible coating via the thermal gradient approach. A heat exchanger (HX) was coated with the binder-based approach with 493 g Al-Fumarate and an average thickness of 300 µm. The coating is evenly distributed among the fins and is mechanically stable. The adsorption kinetic is very fast compared to state of the art materials. The resulting cooling performance is a gross cooling power of 2900 W and 1000 W after 74 seconds.

This is the first functional full-scale HX coated with MOF which is additionally measured under realistic boundary conditions for sorption based chillers.

The water adsorption behavior of CAU-10-H was also intensively studied.

In order to identify the structural features associated with the adsorption behavior, the structural differences between the dry and the water loaded CAU-10-H were studied by Rietveld refinements and second harmonic generation (SHG) microscopy. The observed transition of space group symmetry from $I4_1$ to $I4_1/amd$ between the humid and dry forms is induced by the adsorption/desorption of water into/out of the MOF channels.

For a detailed analysis of the adsorption under hydrothermal stress various *in situ* ad-/desorption cycle experiments under open system conditions have

been carried out. All of them are based on real working conditions, respectively ad-/desorption temperatures between 40 °C and 140 °C and high humidity for a fast equilibration of the sample. This are 100 *in situ* thermogravimetric, 20 *in situ* PXRD (powder X-ray diffraction) and 35 *in situ* DRIFTS (diffuse reflectance infrared fourier transform spectroscopy) ad-/desorption cycles.

To test the long term stability 700 *ex situ* ad-/desorption cycles under open system conditions have been performed. To test CAU-10-H under conditions which are typical for adsorption heat storage (AHS) applications a coating procedure had been developed. A mechanical very stable coating could be developed by a silicophen binder based coating procedure. Thereby 10 000 *ex situ* ad-/desorption cycles could be achieved, under closed system conditions, these are typical lifetimes for adsorption heat storage (AHS) applications.

All this hydrothermal stress tests showed absolutely no sign of degradation of the material, neither in crystallinity nor uptake capacity.

The successful coating procedure, the high stability up to 10 000 cycles under working conditions, the nearly perfect shape of the isotherm and the high uptake capacity make CAU-10-H the best performing and most stable MOF for heat pump applications reported until now.

The synthesis of CAU-10-H was successfully upscaled from the milligram to the kilogram scale, which lead to a patent application.

The adsorption mechanism and stability of several MOFs, was studied in depth by enhanced boiling in water experiments. After 7 days under reflux conditions MIL-101(Cr) showed the best stability by no loss of BET-surface area ($S_{BET}$). For Al-Fumarate and CAU-10-H a $S_{BET}$ loss of 20 % was observed and MIL-160(Al) looses 50 %. Cu-BTC, ZIF-8 and MAF-7 lost all their surface area through the treatment. The hydrothermal stability of the MOFs can be proposed as: MIL-101(Cr) > CAU-10-H > Al-Fumarate > UiO-66 > MIL-100(Fe) > MIL-160 > ZIF-8 > MAF-7 > CuBTC.

With help of newly developed i*n situ* PXRD hydrothermal experiments it is possible to observe a change of the crystal structure during water adsorption. Whereas in case of stable MOFs, like Al-Fumarate and CAU-10-H, this change is fully reversible, i.e. “breathing effect”, irreversible changes are a key indicator

for unstable MOFs. Thus this techniques is a powerful first test to get an information about the stability of a material.

*In situ* DRIFTS experiments could be introduced as a powerful tool for testing the stability of materials, as well as for investigations of the sorption mechanism, because spectra are constantly recorded during ad-/desorptioin. For Al containing MOFs there is strong evidence, that the adsorption takes place at the $AlO_6$-octaeders.

Furthermore MeOH stability investigations had been undertaken on UiO-66 type MOFs, to test them for cooling applications below 0 °C.

*Outlook*

As already very promising results could be achieved by the *in situ* DRIFTS and PXRD experiments, they should be continued. It enables unique insights into mechanism of sorption or degradation and stabilization routes.

Furthermore, coating and probing of real scale heat exchanger, with different MOFs should be done, to get the right material for the right application.

# 6 List of Figures and Tables

# 7 Abbreviations

| | |
|---|---|
| µp-AF | microporous aluminium fumarate |
| AHP | adsorption heat pump |
| AlPO | aluminophosphate |
| bdc | 1,4-benzenedicarboxylate (terephthalate). Sometimes also used for 1,3-benzendicarboxylate (isophthalate) and 1,2-benzendicarboxylate (phthalate) (not in this thesis). |
| bpdc | 4,4′-biphenyl-dicarboxylate |
| BET | adsorption model invented by Brunauer, Emmett and Teller |
| BTB | 4,4′,4′′-benzene-1,3,5-triyl-tribenzoate |
| btc | 1,3,5-benzenetricarboxylate (trimesate) |
| DMF | *N,N*-dimethyl formamide |
| DMSO | Dimethylsulfoxide |
| DRIFTS | englisch diffuse reflectance infrared fourier transform spectroscopy |
| EtOH | ethanol |
| fum | fumarate |
| HKUST-1 | Hong Kong University of Science and Technology |
| IRMOF | isoreticular metal organic framework |
| MeOH | methanol |
| MIL- | Material du Institut Lavoisier |
| mIm | 2-methylimidazolate |
| MOF | metal-organic framework |
| mTz | 3-methyl-1,2,4-triazolate |
| PCP | porous coordination polymer |
| SAPO | silico-aluminophosphate |
| tdc | thermally driven chiller |
| tz | triazolate |
| UiO-… | University of Oslo |
| ZIF | zeolitic imidazolate framework |

# 8 References


1 I. E. Agency, ed., *Key World Energy Statistics*, OECD/IEA, 2013.

2 a) L. Pérez-Lombard, J. Ortiz and C. Pout, *Energy and Buildings*, 2008, **40**, 394–398; b) C. A. Balaras, G. Grossman, H.-M. Henning, C. A. Infante Ferreira, E. Podesser, L. Wang and E. Wiemken, *Renewable and Sustainable Energy Reviews*, 2007, **11**, 299–314.

3 a) L. W. Wang, J. Y. Wu, R. Z. Wang, Y. X. Xu, S. G. Wang and X. R. Li, *Applied Thermal Engineering*, 2003, **23**, 1605–1617; b) Y. Zhong and R. E. Critoph, *Proceedings of the Institution of Mechanical Engineers, Part E: Journal of Process Mechanical Engineering*, 2005, **219**, 285–300; c) S. K. Henninger, M. Schicktanz, P. Hügenell, H. Sievers and H.-M. Henning, *International Journal of Refrigeration*, 2012, **35**, 543–553; d) Z. Tamainot-Telto, S. J. Metcalf, R. E. Critoph, Y. Zhong and R. Thorpe, *International Journal of Refrigeration*, 2009, **32**, 1212–1229.

4 E. J. Hu, *Solar Energy*, 1998, **62**, 325–329.

5 S. K. Henninger, F. Jeremias, H. Kummer and C. Janiak, *European Journal of Inorganic Chemistry*, 2012, 2625–2634.

6 a) E.-P. Ng and S. Mintova, *Microporous and Mesoporous Materials*, 2008, **114**, 1–26; b) J. Jänchen, D. Ackermann, H. Stach and W. Brösicke, *Solar Energy*, 2004, **76**, 339–344; c) Y. I. Aristov, G. Restuccia, G. Cacciola and V. N. Parmon, *Applied Thermal Engineering*, 2002, **22**, 191–204; d) B. B. Saha, S. Koyama, J. B. Lee, K. Kuwahara, K. Alam, Y. Hamamoto, A. Akisawa and T. Kashiwagi, *International Journal of Multiphase Flow*, 2003, **29**, 1249–1263; e) Y. I. Aristov, *Applied Thermal Engineering*, 2013, **50**, 1610–1618.

7 S. K. Henninger, F. P. Schmidt and H. M. Henning, *Applied Thermal Engineering*, 2010, **30**, 1692–1702.

8 a) K. C. Ng, H. T. Chua, C. Y. Chung, C. H. Loke, T. Kashiwagi, A. Akisawa and B. B. Saha, *Applied Thermal Engineering*, 2001, **21**, 1631–1642; b) Y. I. Aristov, M. M. Tokarev, A. Freni, I. S. Glaznev and G. Restuccia, *Microporous and Mesoporous Materials*, 2006, **96**, 65–71; c) L. G. Gordeeva, A. Freni, Y. I. Aristov and G. Restuccia, *Industrial & Engineering Chemistry Research*, 2009, **48**, 6197–6202.

9 B. Dawoud and Y. Aristov, *International Journal of Heat and Mass Transfer*, 2003, **46**, 273–281.

10 a) G. Restuccia, G. Cacciola and R. Quagliata, *Int. J. Energy Res.*, 1988, **12**, 101–111; b) R. E. Critoph and R. Vogel, *International Journal of Ambient Energy*, 1986, **7**, 183–190; c) F. Meunier, *J. Sol. Energy Res.*, 1983, **1**, 23–35; d) E. Dahome and F. Meunier, *Rev. Gen. Therm.*, 1982, **21**, 483–500.

11 S. K. Henninger, F. Jeremias, H. Kummer, P. Schossig and H.-M. Henning, *Energy Procedia*, 2012, **30**, 279–288.

12 a) J. Jänchen, K. Schumann, E. Thrun, A. Brandt, B. Unger and U. Hellwig, *Int. J. Low-Carbon Tech.*, 2012, **7**, 275–279; b) J. Jänchen, H. Stach and U. Hellwig, in *Zeolites and related materials: Trends, targets and challenges, Proceedings of the 4th International FEZA Conference*. *Water sorption in faujasite- and chabazite type zeolites of varying lattice composition for heat storage applications*, ed. J. Jänchen, H. Stach and U. Hellwig, Elsevier, 2008, vol. 174, pp. 599–602; c) S. K. Henninger, F. P. Schmidt and H.-M. Henning, *Adsorption*, 2011, **17**, 833–843; d) K. Schumann, B. Unger, A. Brandt and F. Scheffler, *Microporous and Mesoporous Materials*, 2012, **154**, 119–123; e) K. Schumann, A. Brandt, B. Unger and F. Scheffler, *Chemie Ingenieur Technik*, 2011, **83**, 2237–2243.

13 S. T. Wilson, B. M. Lok, C. A. Messina, T. R. Cannan and E. M. Flanigen, *J. Am. Chem. Soc.*, 1982, **104**, 1146–1147.

14 a) S. Shimooka, K. Oshima, H. Hidaka, T. Takewaki, H. Kakiuchi, A. Kodama, M. Kubota and H. Matsuda, *J. Chem. Eng. Japan / JCEJ*, 2007, **40**, 1330–1334; b) H. Kakiuchi, S. Shimooka, M. Iwade, K. Oshima, M. Yamazaki, S. Terada, H. Watanabe and T. Takewaki, *KAGAKU KOGAKU RONBUNSHU*, 2005, **31**, 361–364; c) H. van Heyden, S. Mintova and T. Bein, *J. Mater. Chem.*, 2006, **16**, 514–518; d) A. Ristić, N. Z. Logar, S. K. Henninger and V. Kaučič, *Adv. Funct. Mater.*, 2012, **22**, 1952–1957.

15 S. G. Izmailova, E. A. Vasiljeva, I. V. Karetina, N. N. Feoktistova and S. S. Khvoshchev, *Journal of Colloid and Interface Science*, 1996, **179**, 374–379.

16 a) J. R. Long and O. M. Yaghi, *Chemical Society reviews*, 2009, **38**, 1213–1214; b) *New J. Chem.*, 2010, **34**, 2353; c) H. C. Zhou, J. R. Long and O. M. Yaghi, *Chemical reviews*, 2012, **112**, 673–674; d) S. Kitagawa and S. Natarajan, *Eur. J. Inorg. Chem.*, 2010, **2010**, 3685.

17 a) C. Janiak, *Dalton Trans.*, 2003, 2781; b) C. Janiak and J. K. Vieth, *New Journal of Chemistry*, 2010, **34**, 2366–2388; c) M. J. Prakash and M. S. Lah, *Chemical communications*, 2009, 3326–3341.

18 A. U. Czaja, N. Trukhan and U. Muller, *Chemical Society reviews*, 2009, **38**, 1284–1293.

19 G. Férey, *Dalton transactions*, 2009, 4400–4415.

20 a) J. R. Li, R. J. Kuppler and H. C. Zhou, *Chemical Society reviews*, 2009, **38**, 1477–1504; b) M. P. Suh, H. J. Park, T. K. Prasad and D. W. Lim, *Chemical reviews*, 2012, **112**, 782–835; c) H. Wu, Q. Gong, D. H. Olson and J. Li, *Chemical reviews*, 2012, **112**, 836–868; d) L. J. Murray, M. Dincă and J. R. Long, *Chemical Society reviews*, 2009, **38**, 1294–1314.

21 F. Jeremias, A. Khutia, S. K. Henninger and C. Janiak, *Journal of Materials Chemistry*, 2012, **22**, 10148–10151.

22 F. Jeremias, V. Lozan, S. Henninger and C. Janiak, *Dalton transactions*, 2013, **42**, 15967–15973.

23 C. Janiak and S. K. Henninger, *Chimia*, 2013, **67**, 419–424.

24 a) G. Akiyama, R. Matsuda, H. Sato, A. Hori, M. Takata and S. Kitagawa, *Microporous and Mesoporous Materials*, 2012, **157**, 89–93; b) E. Biemmi, S. Christian, N. Stock and T. Bein, *Microporous and Mesoporous Materials*, 2009, **117**, 111–117; c) Y. I. Aristov, *Journal of Chemical Engineering of Japan*, 2007, **40**, 1242–1251.

25 J. P. Zhang, A. X. Zhu, R. B. Lin, X. L. Qi and X. M. Chen, *Advanced materials*, 2011, **23**, 1268–1271.

26 J. Ehrenmann, S. K. Henninger and C. Janiak, *European Journal of Inorganic Chemistry*, 2011, 471–474.

27 J. J. Low, A. I. Benin, P. Jakubczak, J. F. Abrahamian, S. A. Faheem and R. R. Willis, *Journal of the American Chemical Society*, 2009, **131**, 15834–15842.

28 F. Jeremias, D. Fröhlich, C. Janiak and S. K. Henninger, *New Journal of Chemistry*, 2014, **38**, 1846–1852.

29 S. K. Henninger, H. A. Habib and C. Janiak, *Journal of the American Chemical Society*, 2009, **131**, 2776–2777.

30 G. Ferey and C. Serre, *Chemical Society reviews*, 2009, **38**, 1380–1399.

31 G. Akiyama, R. Matsuda and S. Kitagawa, *Chemistry Letters*, 2010, **39**, 360–361.

32 F. Jeremias, D. Fröhlich, C. Janiak and S. K. Henninger, *RSC Advances*, 2014, **4**, 24073–24082.

33 a) P. M. Schoenecker, C. G. Carson, H. Jasuja, Flemming, Christine J. J. and K. S. Walton, *Industrial & Engineering Chemistry Research*, 2012, **51**, 6513–6519; b) G. E. Cmarik, M. Kim, S. M. Cohen and K. S. Walton, *Langmuir : the ACS journal of surfaces and colloids*, 2012, **28**, 15606–15613; c) H. Jasuja, J. Zang, D. S. Sholl and K. S. Walton, *The Journal of Physical Chemistry C*, 2012, **116**, 23526–23532.

34 S. Bourrelly, B. Moulin, A. Rivera, G. Maurin, S. Devautour-Vinot, C. Serre, T. Devic, P. Horcajada, A. Vimont, G. Clet, M. Daturi, J. C. Lavalley, S. Loera-Serna, R. Denoyel, P. L. Llewellyn, G. Férey and [Nachname nicht vorhanden], *Journal of the American Chemical Society*, 2010, **132**, 9488–9498.

35 G. Férey, C. Mellot-Draznieks, C. Serre, F. Millange, J. Dutour, S. Surble and I. Margiolaki, *Science*, 2005, **309**, 2040–2042.

36 P. Küsgens, M. Rose, I. Senkovska, H. Fröde, A. Henschel, S. Siegle and S. Kaskel, *Microporous and Mesoporous Materials*, 2009, **120**, 325–330.

37 A.-X. Zhu, R.-B. Lin, X.-L. Qi, Y. Liu, Y.-Y. Lin, J.-P. Zhang and X.-M. Chen, *Microporous and Mesoporous Materials*, 2012, **157**, 42–49.

38 a) T. Birsa Čelič, M. Mazaj, N. Guillou, E. Elkaïm, M. El Roz, F. Thibault-Starzyk, G. Mali, M. Rangus, T. Čendak, V. Kaučič and N. Zabukovec Logar, *J. Phys. Chem. C*, 2013, **117**, 14608–14617; b) H. Jasuja and K. S. Walton, *Dalton transactions (Cambridge, England : 2003)*, 2013, **42**, 15421–15426.

39 M. H. Chahbani, J. Labidi and J. Paris, *Applied Thermal Engineering*, 2002, **22**, 23–40.

40 Y. I. Aristov, *International Journal of Refrigeration*, 2009, **32**, 675–686.

41 a) B. Dawoud, *Applied Thermal Engineering*, 2013, **50**, 1645–1651; b) L. Bonaccorsi, L. Calabrese, A. Freni, E. Proverbio and G. Restuccia, *Applied Thermal Engineering*, 2013, **50**, 1590–1595; c) B. Yilmaz, N. Trukhan and U. Müller, *Chinese Journal of Catalysis*, 2012, **33**, 3–10; d) G. W. Peterson, J. B. DeCoste, T. G. Glover, Y. Huang, H. Jasuja and K. S. Walton, *Microporous and Mesoporous Materials*, 2013, **179**, 48–53.

42 a) S. Kaskel, *Chemie Ingenieur Technik*, 2010, **82**, 1019–1023; b) L. Pino, Y. Aristov, G. Cacciola and G. Restuccia, *Adsorption*, 1997, **3**, 33–40.

43 L. Bastin, P. S. Bárcia, E. J. Hurtado, J. A. C. Silva, A. E. Rodrigues and B. Chen, *J. Phys. Chem. C*, 2008, **112**, 1575–1581.

44 a) A. Atakan, G. Fueldner, G. Munz, S. Henninger and M. Tatlier, *Applied Thermal Engineering*, 2013, **58**, 273–280; b) A. Erdem-Senatalar, M. Tatlıer and M. Ürgen, *Microporous and Mesoporous Materials*, 1999, **32**, 331–343.

45 a) D. Bradshaw, A. Garai and J. Huo, *Chemical Society reviews*, 2012, **41**, 2344–2381; b) A. Bétard and R. A. Fischer, *Chemical reviews*, 2012, **112**, 1055–1083; c) D. Zacher, R. Schmid, C. Wöll and R. A. Fischer, *Angewandte Chemie*, 2011, **50**, 176–199; d) O. Shekhah, J. Liu, R. A. Fischer and C. Wöll, *Chemical Society reviews*, 2011, **40**, 1081–1106; e) D. Zacher, O. Shekhah, C. Wöll and R. A. Fischer, *Chemical Society reviews*, 2009, **38**, 1418–1429.

46 F. Jeremias, S. K. Henninger and C. Janiak, *Chemical communications*, 2012, **48**, 9708–9710.

47 A. Drochner and G. H. Vogel, in *Methods in Physical Chemistry*, ed. R. Schäfer and P. C. Schmidt, Wiley-VCH Verlag GmbH & Co. KGaA, Weinheim, Germany, 2012, pp. 445–475.

48 M. B. Mitchell, in *Structure-Property Relations in Polymers*, ed. M. W. Urban and C. D. Craver, American Chemical Society, Washington, DC, 1993, vol. 236, pp. 351–375.

49 R. Schäfer and P. C. Schmidt, eds., *Methods in Physical Chemistry*, Wiley-VCH Verlag GmbH & Co. KGaA, Weinheim, Germany, 2012.

50 D. Fröhlich, S. K. Henninger and C. Janiak, *Dalton Trans*, 2014, **43**, 15300–15304.

51 H. Reinsch, van der Veen, Monique A., B. Gil, B. Marszalek, T. Verbiest, D. de Vos and N. Stock, *Chemistry of Materials*, 2013, **25**, 17–26.

52 D. Fröhlich, E. Pantatosaki, P. D. Kolokathis, K. Markey, H. Reinsch, M. Baumgartner, van der Veen, Monique A., D. E. de Vos, N. Stock, G. K. Papadopoulos, S. K. Henninger and C. Janiak, *J. Mater. Chem. A*, 2016, **4**, 11859–11869.

53 K. Leus, T. Bogaerts, J. de Decker, H. Depauw, K. Hendrickx, H. Vrielinck, V. van Speybroeck and P. van der Voort, *Microporous and Mesoporous Materials*, 2016, **226**, 110–116.

54 M. F. de Lange, T. Zeng, Vlugt, T. J. H., J. Gascon and F. Kapteijn, *CrystEngComm*, 2015, **17**, 5911–5920.

55 A. Cadiau, J. S. Lee, D. Damasceno Borges, P. Fabry, T. Devic, M. T. Wharmby, C. Martineau, D. Foucher, F. Taulelle, C.-H. Jun, Y. K. Hwang, N. Stock, M. F. de Lange, F. Kapteijn, J. Gascon, G. Maurin, J.-S. Chang and C. Serre, *Advanced materials (Deerfield Beach, Fla.)*, 2015, **27**, 4775–4780.

56 a) N. Al-Janabi, P. Hill, L. Torrente-Murciano, A. Garforth, P. Gorgojo, F. Siperstein and X. Fan, *Chemical Engineering Journal*, 2015, **281**, 669–677; b) M. Todaro, G. Buscarino, L. Sciortino, A. Alessi, F. Messina, M. Taddei, M. Ranocchiari, M. Cannas and F. M. Gelardi, *J. Phys. Chem. C*, 2016, **120**, 12879–12889.